UNIVERSITÉ DE LYON

INSA INSTITUT NATIONAL DES SCIENCES APPLIQUÉES LYON

POLITECNICO MILANO 1863

PHD OF THE UNIVERSITÉ DE LYON

performed within

the Institut National des Sciences Appliquées de Lyon

in an international co-agreement with

the Politecnico di Milano

defended publicly on October 27th, 2017 by

Florian ROUSSET

SINGLE-PIXEL IMAGING: DEVELOPMENT AND APPLICATIONS OF ADAPTIVE METHODS

in front of the jury composed of:

Richard BARANIUK	University of Rice	Reviewer
Charles SOUSSEN	CentraleSupélec	Reviewer
Simon ARRIDGE	University College London	Examinator
Paola TARONI	Politecnico di Milano	Examinator
Cosimo D'ANDREA	Politecnico di Milano	PhD co-director
Nicolas DUCROS	INSA Lyon	PhD co-director
Françoise PEYRIN	INSERM	PhD director

Centre de Recherche en Acquisition et Traitement de l'Image pour la Santé (CREATIS) – Lyon
Dipartimento di Fisica, Politecnico di Milano – Milan

ACKNOWLEDGMENTS

I would first like to express my deepest appreciations to my three supervisors, Françoise Peyrin, Nicolas Ducros and Cosimo D'Andrea.

I thank Françoise for accepting to act as my PhD director. This gave me the opportunity to benefit from her broad experience, her reviews and advices in the progression of my research work. Although setting up the videoconferencing was quite tricky, our meetings were always very constructive and fruitful, which undoubtedly contributed to the success of this thesis.

I express my special thanks to Nicolas who was by my side at CREATIS and always here to answer my questions. His knowledges in optics and image processing in general were a big help throughout these 3 years. His scientific rigor, enthusiasm and passion were a source of motivation and will surely bring success to his accepted project in single-pixel imaging. I also thank him for giving me the opportunity to do some teaching hours at INSA.

I wish to thank Cosimo without who I could not have performed any of the experimental acquisitions presented in this manuscript. My somehow basic knowledge in optics was definitely not enough to understand everything but Cosimo always made things clear with simple yet efficient explanations. I am also grateful for the help Cosimo provided upon my arrival in Milan regarding paperwork and housing.

I would like to express my gratitude to Isabelle Magnin for welcoming me at the CREATIS laboratory, which she managed until 2015, to Olivier Beuf who followed as CREATIS' director and to Franco Ciccacci, head of the Dipartimento di Fisica at the Politecnico di Milano. They all gave me the opportunity to conduct my work in friendly and peaceful environments.

Furthermore I would also like to acknowledge with much appreciation the role of Andrea Farina and David Rousseau. Andrea's help during my time in Milan regarding the setting up of experimental acquisitions was crucial. David provided some optical equipments and knowledge without which the single-pixel camera setup at CREATIS would not have been implemented.

I would like to express my gratitude to the members of the jury for accepting to be part of it. My special thanks go to Richard Baraniuk and Charles Soussen for taking the role of reviewers of this thesis.

I finally give my warmest thanks to everyone I had the opportunity to meet or interact with at CREATIS and at the Politecnico di Milano.

I am grateful to my office mates in Lyon, Anca, Miaomiao, Rémi, Paul, Tom and Matthieu, who were always respectful and quiet which created a very propitious environment for work. I thank Laure, Eric and Simon for nice city sightseeings during ISBI'16 conference in Prague, Pierre for giving me tons of TV series/movies to watch, Juan for offering the opportunity to help for experiments at the European synchrotron (ESRF) and Pierrick for all the paperwork he did for me. I also would like to acknowledge the pleasure I had in teaching practical works alongside Sarah, Thomas, Olivier, Philippe and Nicolas.

On the Italian side, I had the chance to share two offices during two different stays. I thank my first office buddies Sara M., Laura and Sanathana, also known as the three minions, for a very fun 6-month stay, not as quiet as my office in Lyon but still as enjoyable. My second batch of office mates also get my thanks for leaving me the responsibility of the AC remote during the crazy summer heat of Milan : Rebecca, Lina and Marta (for AC) vs Alessia C. and Edo (against AC). I also thank the people often present at the terrace on the 5th floor for lunch : Maurizio, Alessia A., Sara B., Andrea B.. Finally, I give my gratitude to Paola Taroni who made possible the PhD joint agreement and always helped me for paperwork and courses in Milan.

This is also for me the opportunity to thank and acknowledge the numerous sources of fundings for this PhD project whose main grant was provided by the VINCI program of the Université Franco-Italienne. It was also supported in part by Cariplo Foundation under Grant 20130615, LASERLAB-EUROPE under Grant 284464, and ECs Seventh Framework Programme.

I was fortunate to attend and participate to ISBI 2016 and SPIE Photonics West 2017 international conferences thanks to the doctoral school EEA and Labex Primes (ANR-22-LABX-0063) of Université de Lyon ("Investissements d'Avenir", ANR-11-IDEX-0007, operated by the French National Research Agency) which covered my expenses related to these conferences (EEA for ISBI and Primes for SPIE). I further acknowledge the France Life Imaging (FLI) infrastructure, which covered my inscription at the RITS 2015 national congress, the GDR-Isis for my travels to the JIONC (2015, 2016 and 2017) and the CNRS throughout Monopix+ project, which allowed me to attend a summer school on Structured Regularization in Paris and travel to the GRETSI in 2017.

My two stays in Milan were also supported by the région Rhône-Alpes (May to October 2015) and by the PALSE program (June to November 2016). These fundings allowed me to go to Milan twice to conduct the experimental part of this PhD work.

ABSTRACT

SINGLE-PIXEL IMAGING is a recent paradigm that allows the acquisition of images at a reasonably low cost by exploiting hardware compression of the data. The architecture of a single-pixel camera consists of only two elements, a spatial light modulator and a single point detector. The key idea is to measure, at the detector, the projection (i.e., inner product) of the scene under view –the image– with some patterns. The post-processing of a measurements sequence obtained with different patterns permits to restore the desired image.

Single-pixel imaging has several advantages, which are of interest for different applications, especially in the biomedical field. In particular, a time-resolved single-pixel imaging system benefits to fluorescence lifetime sensing. Such a setup can be coupled to a spectrometer to supplement lifetime with spectral information. However, the main limitation of single-pixel imaging is the speed of the acquisition and/or image restoration that is, as of today, not compatible with real-time applications.

This thesis investigates fast acquisition/restoration schemes for single-pixel camera targeting biomedical applications. First, a new acquisition strategy based on wavelet compression algorithms is reported. It is shown that it can significantly accelerate image recovery compared to conventional schemes belonging to the compressive sensing framework. Second, a novel technique is proposed to alleviate an experimental positivity constraint of the modulation patterns. With respect to the classical approaches, the proposed non-negative matrix factorization based technique permits to divide by two the number of patterns sent to the spatial light modulator, hence dividing the overall acquisition time by two. Finally, the applicability of these techniques is demonstrated for multispectral and/or time-resolved imaging, which are common modalities in biomedical imaging.

KEY-WORDS : Single-pixel imaging, wavelets, non-negative matrix factorization, multispectral measurements, time-resolved measurements, fluorescence lifetime imaging.

RÉSUMÉ

L'IMAGERIE MONO-PIXEL est un concept récent qui permet l'obtention d'images à un coût relativement faible par une compression des données durant l'acquisition. L'architecture d'une caméra mono-pixel comprend seulement deux éléments, un modulateur spatial de la lumière et un détecteur ponctuel. L'idée est de mesurer, au niveau du détecteur, la projection de la scène observée –l'image– avec un certain motif. Le post-traitement d'une séquence de mesures obtenues avec différents motifs permet de restaurer l'image de la scène.

L'imagerie mono-pixel possède plusieurs avantages qui sont d'un intérêt pour différentes applications, en particulier dans le domaine biomédical. Par exemple, une caméra mono-pixel résolue en temps bas coût est bénéfique pour l'imagerie de temps de vie de fluorescence. Un tel système peut également être couplé à un spectromètre afin de compléter le temps de vie avec une information spectrale. Cependant, la limite principale de l'imagerie mono-pixel est la vitesse d'acquisition et/ou de l'étape de restauration d'image qui est, à ce jour, non compatible avec des applications temps réel.

Le but de cette thèse est de développer des méthodes rapides d'acquisition et de restauration des images à visée d'applications biomédicales. Tout d'abord, une stratégie d'acquisition basée sur les algorithmes de compression dans le domaine ondelettes est proposée. Celle-ci accélère le temps de restauration de l'image par rapport aux schémas d'acquisition classiques basés sur l'acquisition comprimée. Dans un second temps, une nouvelle méthode pour lever une contrainte expérimentale de positivité sur les motifs est détaillée. Comparée aux approches classiques, cette méthode basée sur une factorisation en matrices non-négatives permet de diviser par deux le nombre de motifs envoyés au modulateur spatial de la lumière, entrainant ainsi une division par deux du temps d'acquisition total. Enfin, l'applicabilité de ces techniques est démontrée pour de l'imagerie multispectrale et/ou résolue en temps, modalités courantes dans le domaine biomédical.

MOTS-CLÉS : Imagerie mono-pixel, ondelettes, factorisation en matrices non-négatives, mesures multispectrales, mesures résolues en temps, imagerie du temps de vie de fluorescence.

N.B. : un résumé étendu en français est donné en Annexe C.

RIASSUNTO

L'ACQUISIZIONE di immagini tramite single-pixel camera è un concetto recente che permette di ottenere immagini ad un costo relativamente basso e di realizzare la compressione dei dati durante l'acquisizione. L'architettura di una single-pixel camera comprende due soli elementi : un modulatore spaziale di luce ed un sensore puntuale. L'idea consiste nel modulare la scena osservata (immagine) con un certo pattern luminoso e di focalizare la luce in uscita dal campione sul sensore. Infine, elaborando la sequenza di misure ottenute con diversi pattern è possibile ricostruire l'immagine desiderata.

L'acquisizione di immagini tramite single-pixel camera presenta diversi vantaggi per varie applicazioni ed in particolare nel campo biomedicale. Ad esempio, permette di realizzare un sistema di imaging risolto nel tempo a basso costo per la mappatura del tempo di vita di fluorescenza. Tale configurazione può anche essere accoppiata ad uno spettrometro aggiungendo, così, l'informazione spettrale. Tuttavia, la limitazione principale della single-pixel camera è la velocità di acquisizione e/o ricostruzione delle immagini che, ad oggi, non è compatibile con le applicazioni che richiedono di essere realizzate in tempo reale.

Lo scopo di questa tesi di dottorato è lo sviluppo di metodi rapidi di acquisizione e ricostruzione delle immagini per applicazioni in campo biomedico. In primo luogo, si propone una strategia di acquisizione delle immagini sulla base di algoritmi di compressione nel dominio wavelet. Questo approccio permette di ricostruire più velocemente l'immagine rispetto ai metodi di acquisizione tradizionali basati sul compressed sensing. In secondo luogo, un altro metodo permette di utilizzare solo patterns positivi. Rispetto agli approcci tradizionali, questo metodo basato sulla fattorizzazione matriciale non-negativa permette di dimezzare il numero di pattern inviati al modulatore spaziale di luce e, quindi, il tempo complessivo di acquisizione. Infine, l'applicabilità di queste tecniche è dimostrata nel campo dell'imaging biomedico tramite misure multispettrali e/o risolte nel tempo.

PAROLE CHIAVE : Single-pixel camera, wavelet, fattorizzazione matriciale non-negativa, misure multispettrali, misure risolte nel tempo, imaging del tempo di vita di fluorescenza.

TABLE OF CONTENTS

List of Figures

LIST OF TABLES

ACRONYMS & ABBREVIATIONS

Abbreviation or acronym	Signification
ABS	Adaptive Basis Scan
ABS-WP	Adaptive Basis Scan by Wavelet Prediction
BS	Basis Scan
ADC	Analog-to-Digital Converter
CCD	Charge Coupled Device
CMOS	Complementary Metal Oxide Semiconductor
CS	Compressive Sensing
DCT	Discrete Cosine Transform
DMD	Digital Micromirror Device
FFT	Fast Fourier Transform
LCD	Liquid Crystal Display
LCoS	Liquid Crystal on Silicon
LED	Light-Emitting Diode
MMA	Metamaterial Absorber
NMF	Nonnegative Matrix Factorization
PMT	Photomultiplier
PSNR	Peak Signal-to-Noise Ratio
PWM	Pulse Width Modulation
RIP	Restricted Isometry Property
SFDI	Spatial Frequency Domain Imaging
SLM	Spatial Light Modulator
SNMF	Semi Nonnegative Matrix Factorization
SNR	Signal-to-Noise Ratio
SPC	Single-Pixel Camera
SPD	Single Point Detector
SPI	Single-Pixel Imaging
TCSPC	Time-Correlated Single Photon Counting
TOF	Time-of-flight
TR	Time-resolved

NOTATIONS & SYMBOLS

General conventions

x and X	are two scalars
$\mathbf{x}$	is a column vector
$\mathbf{X}$	is a matrix

Mathematical sets

$\mathbb{N}$	set of natural elements
$\mathbb{Z}$	set of integers
$\mathbb{R}$	set of real elements
$\mathbb{R}_+$	set of non-negative real elements i.e. $\{x \in \mathbb{R} \quad \text{s.t.} \quad x \geq 0\}$
$\mathbb{R}^{K\times 1}$	set of vectors with K real elements
$\mathbb{R}_+^{K\times 1}$	set of vectors with K non-negative real elements
$\mathbb{R}^{K\times I}$	set of matrices with K rows and I columns of real elements
$\mathbb{R}_+^{K\times I}$	set of matrices with K rows and I columns of non-negative real elements

Vectors and matrices

x_n or $(\mathbf{x})_n$	n-th element of the vector $\mathbf{x}$
$\mathbf{x}_n$	n-th column of the matrix $\mathbf{X}$
$X_{i,j}$ or $(\mathbf{X})_{i,j}$	element at the i-th row and j-th column of $\mathbf{X}$
$\mathbf{X}_{\vert n}$	matrix $\mathbf{X}$ deprived of its n-th column
$\mathbf{X}_{-n}$	matrix $\mathbf{X}$ deprived of its n-th row
$\mathbf{x}^\top$	transpose of the vector $\mathbf{x}$ (row vector)
$\mathbf{X}^\top$	transpose of the matrix $\mathbf{X}$
$\text{tr}(\mathbf{X})$	trace of the matrix $\mathbf{X}$
$\mathbf{X}^{-1}$	inverse of the matrix $\mathbf{X}$

INTRODUCTION

SINGLE-PIXEL IMAGING (SPI) is a trendy paradigm allowing the acquisition of images at a reasonably low cost with hardware compression of the data. The architecture of a *single-pixel camera* (SPC) indeed consists of only two elements, a spatial light modulator and a single point detector. The key idea is to modulate the observed image with a certain pattern and collect the corresponding measurement at the single detector. The desired image can then be restored by post-processing a sequence of measures performed with several patterns.

The probably first concept of modulating a light field and collecting the output light on a single detector was reported in 1982 with the works of Ben-Yosef *et* Sirat. They proposed to use the piezoelectric-elasto-optic effect of crystals for modulation so that the light output is proportional to the Fourier transform of the imaged object. However, back then, building small and numerous crystals was not as accessible as today and Ben-Yosef *et* Sirat only made a proof of concept with few crystals without restoring an image of the object. As a result, the credit of the SPC is attributed to Rice University almost 25 years later where the first SPC images were obtained. At that time, the pioneering idea of *compressive sensing* (CS) proposed by Donoho in 2006 opened a door for Takhar *et al.* in the same year to use the SPC with random patterns and reconstruct an image using a ℓ_1-minimization algorithm. Since then, algorithms have evolved and new acquisition strategies were proposed while the SPC found many different applications.

At first glance, having a single pixel can seem counterproductive since the cameras of today embed several millions pixels. However, several advantages stand out when compared to cameras based on an array of sensors (i.e., CCD or CMOS cameras architecture). First off, single point detectors usually have a high efficiency and are therefore able to detect weak light intensity changes (Hadfield, 2009). In medical application, this can be very useful since tissue absorption is usually quite high (Jacques, 2013). Second, there is an intrinsic compression at the hardware level when using a SPC which hence needs small storage memory. This is a key advantage in applications where the data rate for transmission would be low such as remote imaging applications (e.g. aerospace remote sensing) (Ma, 2009b,a). Finally, a single point sensor imaging device is usually less expensive than a sensor array based camera. The SPC is therefore well suited for infrared imaging (Shin *et al.*, 2016) for which using a conventional imaging system operating at these wavelengths would be costly (Rogalski, 2012).

The latter advantages of SPI and the non-ionizing nature of optical imaging makes the SPC an excellent candidate for biomedical imaging applications. For instance, a low-cost time-resolved

imaging system can benefit to fluorescence lifetime imaging (Becker, 2012) by coupling the point detector with a photon counting board (Pian *et al.*, 2016a; Rousset *et al.*, 2017b). Adding a spectrometer further permits obtaining a complete multispectral time-resolved system (Pian *et al.*, 2016b) to supplement lifetime information of tissues with its spectral content.

The SPC can also be used for imaging through scattering media (Tajahuerce *et al.*, 2014; Duran *et al.*, 2015), for diffuse optics (e.g. skin lesions detection or intraoperative (Gibson *et* Dehghani, 2009)), for ophthalmology (Lochocki *et al.*, 2016, 2017), to characterize tissue properties using near infrared illumination (Torabzadeh *et al.*, 2017) and it has been successfully transposed on a microscope (Studer *et al.*, 2012; Radwell *et al.*, 2014; Rodriguez *et al.*, 2016). Exploiting several SPC images can lead to performing fluorescence molecular tomography or diffuse optical tomography (D'Andrea *et al.*, 2010; Ducros *et al.*, 2013; Pian *et al.*, 2015; Ducros *et al.*, 2016) with application to molecular imaging and oximetry.

The goal of this thesis is to investigate single-pixel imaging for biomedical applications. One of the main limitation of the SPC in the latter cited works regards the speed of the acquisition and/or image restoration. In such cases, real-time applications cannot be considered ruling out interventional imaging (e.g. fluorescence guided surgery) for instance. It is therefore wanted to develop specific techniques for acquisition and/or restoration using a SPC for biomedical imaging.

To meet the goals of this thesis, a new acquisition strategy for SPC to reduce reconstruction time was proposed along with an innovative technique to reduce the acquisition times on the other hand. The applicability of these techniques for medical imaging was demonstrated on multispectral and/or time-resolved measurements.

This work was performed in a joint agreement between INSA Lyon and the Physics department of the Politecnico di Milano (Polimi) to grant PhD of both institutions (PhD in signal/image processing for INSA and PhD in Physics for Polimi). The experimental part was implemented at the Polimi where a SPC setup is available. The algorithms and methodologies were conducted within the CREATIS laboratory that has a long history of dealing with signal processing techniques for medical imaging.

This thesis manuscript is divided in six chapters. The first two expose the general principles in single-pixel imaging with the related state-of-the-art in the field. The remaining four chapters aim to answer to the problematic of this thesis with different contributions. These chapters contain some parts of personal publications listed in Appendix D.

In Chapter I, the SPC concept is detailed with several possible implementations. Many different applications using this device are presented as well as new trends in single-pixel imaging.

In Chapter II, the mathematical formulation of a SPC acquisition is given so as to present the possible acquisition/restoration strategies proposed throughout the years. Two main categories of techniques stand out, the *nonadaptive* one belonging to the CS framework and the *adaptive* methods where some measurements are performed based on previous measures. This chapter ends on a conclusion on the state-of-the-art with respect to this thesis problem.

In Chapter III, two experimental setups involved in the results of the next chapters are presented. One is the optical setup at the Politecnico di Milano to which some improvements were made to control the different instruments. The second system is the one that was implemented at the CREATIS laboratory.

In Chapter IV, our proposed acquisition strategy referred to as *Adaptive Basis Scan by Wavelet Prediction* (ABS-WP) is reported. The wavelet transform for 2D images is detailed before exposing the proposed acquisition strategy based on fast interpolations and multiresolution approximations. Simulated and experimental results show the efficiency of ABS-WP compared to some other SPC acquisition techniques highlighted in Chapter II. This chapter mainly contains an article published in *IEEE Transactions on Computational Imaging* in 2017 (Rousset *et al.*, 2017a).

In Chapter V, a method to divide by a factor of two the number of measurements is proposed. This was designed because patterns having both positive and negative entries cannot be implemented on a spatial light modulator. To deal with this technique, it is common to separate the pattern in its positive part and absolute negative part, the subtraction of two measurements leading to the desired measurement. This however doubles acquisition times as twice measurements should be performed. In this chapter, we formalized the problem and showed that a *semi nonnegative matrix factorization* (SNMF) algorithm can be employed to overcome experimental constraints and therefore lower the common number of measurements. The results presented in this chapter were filed as a patent (Rousset *et al.*, 2017c) and submitted in *IEEE Transactions on Image Processing* (Rousset *et al.*, 2017d).

In Chapter VI, the SPC with the techniques developed in the previous chapters is employed for applications that could benefit to biomedical imaging. A temporal dimension was added to the SPC in order to perform fluorescence lifetime sensing, the lifetime being an important parameter for biologists to assess the tissues' micro-environment (pH for instance). These results were presented at the *SPIE Photonics West* conference in February 2017 (Rousset *et al.*, 2017b). Then, a spectral dimension was further added to obtain multispectral time-resolved measurements. The obtained SPC system coupled to our acquisition strategy of Chapter IV allows to completely differentiate the different components of the imaged object using the spectral and temporal information. These results will soon be submitted for publication in *Optics Express*.

CHAPTER I

SINGLE-PIXEL CAMERA

Contents

CHAPTER I

UNDER the term single-pixel camera are hidden various ideas and possible optical implementations. The goal of this chapter is to give the main concept behind the SPC along with its possible hardware implementations found throughout the years. Some applications where the SPC is a key element are presented as well as new trends in the optical field where the use of a SPC is relevant.

I.1 Concept

The theory and results from Donoho in 2006 on *compressive sensing* (CS) showed that a signal can be recovered from only a small number of projections, revisiting standard Shannon-Nyquist sampling theorem. This enabled Takhar *et al.* to propose the same year a new camera architecture based on a single point detector to build a compressive imaging system (Duarte *et al.*, 2008; Baraniuk *et al.*, 2014; Miao *et* Amirparviz, 2015). Such a system measures 1D data instead of the classical 2D data from a conventional sensor array (e.g. CCD or CMOS cameras). A *spatial light modulator* (SLM) is placed between the scene under view – the image – and the *single point (i.e. pixel) detector* (SPD) so as to modulate the light coming out of the scene and collect the corresponding projection at the sensor. Sequential measurements are taken with different patterns loaded on the SLM and the post-processing of the data permits the image recovery of the scene under view [1].

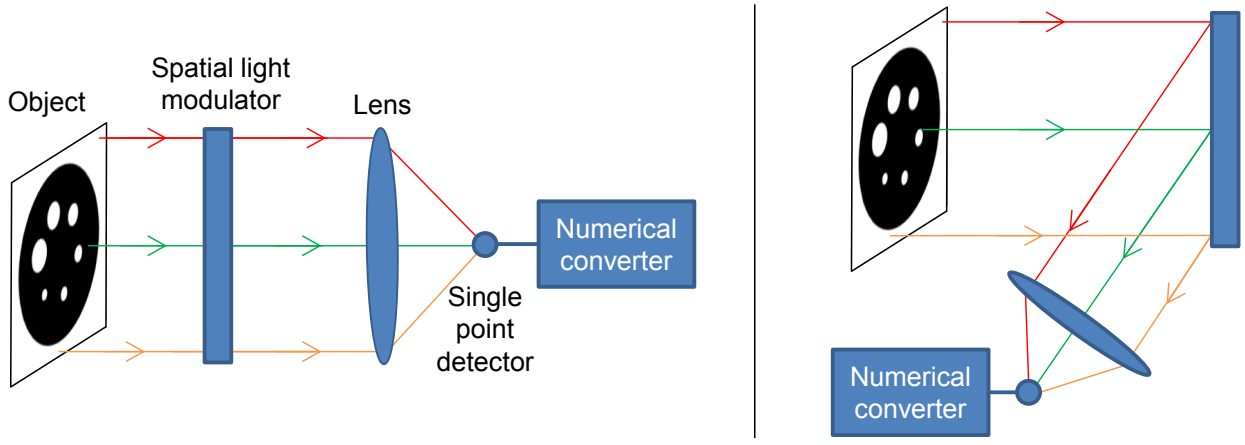

FIGURE I.1 – Single-pixel camera optical setup using a transmissive spatial light modulator (left) or a reflective one (right).

1. The different acquisition/restoration schemes for SPI are detailed in the next chapter.

The simplest implementation of the SPC can be schematized as in Fig. I.1 where the SLM is either a reflective device or a transmissive one depending on the employed technology. The image of the object/scene under view is formed in the SLM plane and a lens is added to focus the modulated light rays on the single point detector. A numerical converter is employed to obtain numerical data from the single point detector. Note that the spatial light modulator and the object are completely interchangeable. If the SLM is placed before [2] the object, it is said to modulate the light in illumination, if placed after, the detection side is modulated.

I.2 Hardware implementation

Throughout the years, many different hardware implementations of the SPC were proposed. Depending on the desired applications, specific technologies should be chosen to draw the best out of it. This section gives some examples [3] of the most employed SLM and SPD technologies as well as the different means to get numerical measurements to process the data.

I.2.1 Spatial light modulator

DMD The original work of Takhar *et al.* and Duarte *et al.* employed a *digital micromirror device* (DMD, Fig. I.2-(a)) invented by Hornbeck at *Texas Instruments* in 1987. Such a device comprises thousands of tiny mirrors arranged in a matrix array of size $H \times W$. The value of H (resp. W) typically ranges from 768 (resp. 1024) to 1600 (resp. 2560) with a mirror pitch of 7 to 14 μm depending on the model. Each of the mirrors are independently controlled and can be tilted in two positions. e At +12°, the so-called ON stat reflects the light towards the detector and is therefore collected by it. At −12°, the OFF state sends the light in the opposite direction. The DMD can hence load binary patterns where a 0 corresponds to the OFF state and a 1 to the ON state. The DMD also offers the possibility to load 8-bit gray level patterns using the principle of *pulse width modulation* (PWM). For this, a single 8-bit pattern is separated in the corresponding 8 binary bit planes. Each of them is associated to a particular display time that is a multiple of a power of 2 in order to recreate an 8-bit pattern. More details about the PWM for DMD are given in Appendix A.

LCD In 2013, Huang *et al.* employed a *liquid crystal display* (LCD, Fig. I.2-(b)) panel as a transmissive [4] spatial light modulator. This kind of device employs polarizing filters and the properties of liquid crystals orientations are tuned by an electric field. Each of the $H \times W$ pixels (crystals) of this system arranged in a matrix can also take two states. The difference with the DMD is that the ON state corresponds to a transparent element letting the light pass to the detector whereas the OFF state represents an opaque element. Values for H and W take a vast variety of range since LCDs are encountered in the everyday life from calculator to TV screens.

2. In the direction of the light.
3. Non-exhaustive list.
4. Reflective LCD devices also exist but are not presented here as they are outperformed by DMDs with their higher refresh rates.

MMA Watts *et al.* in 2014 proposed an in-house SLM defined as a liquid crystal *metamaterial*[5] *absorber* (MMA, Fig. I.2-(c)) SLM. A maximum of 8×8 pixels are available in their design where the properties of the metamaterials are each individually controlled applying a bias voltage. As for the previous DMD, each pixel is reflective and can take two states [0,1]. This setup however permits using patterns with [-1,0,1] values by modulating the pixels $+1$ in phase and the pixels -1 out of phase with a reference. It is shown in Watts *et al.* (2014) that the MMA SLM is well adapted and efficient for terahertz imaging.

LCoS Unlike the previous intensity modulators, a *liquid crystal on silicon* (LCoS, Fig. I.2-(d)) SLM can modulate the light phase. As for the LCD, an electric field tune the crystals to create binary patterns. Such a device is for instance employed in Clemente *et al.* (2013) to perform compressive holography. Note that a LCoS device can be employed along with polarizers to recreate an intensity based SLM if desired.

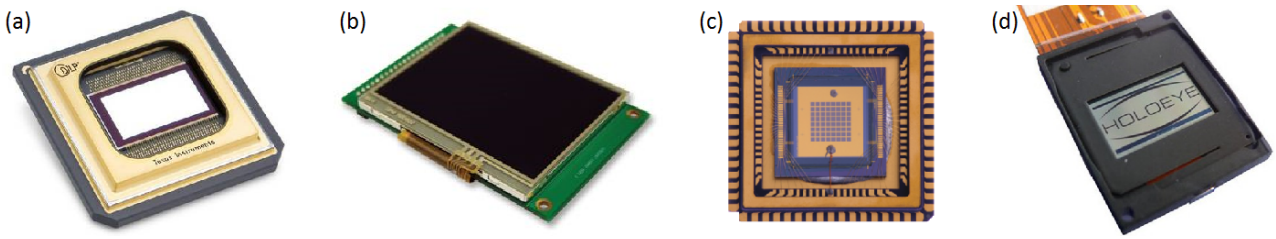

FIGURE I.2 – Example of spatial light modulators. (a) DMD, (b) LCD, (c) MMA, (d) LCoS. Images extracted and adapted from (a) Texas Instruments, (b) STMicroelectronics and (d) Holoeye websites and from (c) Watts *et al.* (2014).

Table I.1 summarizes the principal characteristics of the different SLM technologies. The use of a DMD for SPC is by far the most common as it offers fast refresh rates and is easy to set up.

Technology	Geometry	Modulation	Refresh rate	Number of pixels	Pixel pitch	Active area
DMD	Reflective	Intensity	32 kHz	1600×2560	$7 - 14\,\mu$m	$\sim$ mm^2
LCD	Transmissive	Intensity	$50 - 600$ Hz	4320×7680	~ 50 to $300\,\mu$m	mm^2 to m^2
MMA	Reflective	Intensity	$\sim$ kHz	8×8	$\sim 250\,\mu$m	4.8 mm^2
LCoS	Reflective	Phase	~ 60 Hz	768×1024	$\sim 20\,\mu$m	$\sim$ mm^2

TABLE I.1 – Summary of the main characteristics of different SLM technologies.

I.2.2 Single point detector

Photodiode A photodiode (Fig. I.3-left) is a semi-conductor element able to receive photons and convert them into an electrical current. Its structure is usually made of a PN junction[6] or PIN junction[7]. The photons of the light rays going to the photodiode are absorbed and, if their energy is superior to a certain value, they can move to the conductive band inducing an electric

5. Said for an engineered material whose properties are not found in nature.
6. Junction where the doping changes sharply, going from a positive (P) doped side to a negative (N) one.
7. PN junction with an undoped intrinsic semiconductor in between.

current. Different materials exist to create a photodiode, each of them giving certain properties to the detector, these are summarized in table I.2.

PMT The *photomultiplier* (PMT, Fig. I.3-right) allows the detection of photons to convert them into an electrical current. It comprises a photochatode [8], a focusing electrode, dynodes [9] and a final anode, all embedded in a vacuum tube. When a photon reaches the photochatode, this releases an electron going to the focusing electrode. There, it is accelerated towards the dynodes on which a certain electric tension is applied, multiplying the electron. The bigger the tension applied to the dynodes, the more electrons are multiplied. Finally, the anode collects the electrons as an electrical current.

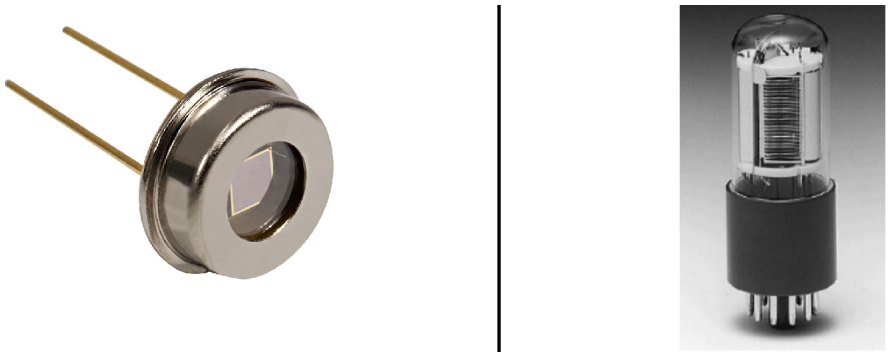

FIGURE I.3 – Example of single-point detectors. Photodiode (left) and photomultiplier (right). Images extracted and adapted from ThorLabs website for the photodiode and Horiba Scientific website for the PMT.

Table I.2 summarizes the principal features of the different single-point detectors [10]. Photodiodes are mostly employed since they are easy to use and cheap while covering wide spectral ranges due to their simple structures.

Technology	Material	Spectral range	Active area	Dark current
Photodiode	Silicon	200 nm - 1100 nm	~mm^2 - cm^2	~ 1 - 600 nA
	Indium Gallium Arsenide	800 nm - 1700 nm	~mm^2	~ 50 nA
	Germanium	800 nm - 1800 nm	~mm^2	~ 1 μA
Photomultiplier	Multialkali	160 nm - 900 nm	~cm^2	~ 3 nA
	Bialkali	185 nm - 650 nm	~cm^2	~ 0.1 nA
	Indium Gallium Arsenide	185 nm - 1010 nm	~mm^2	~ 1 nA

TABLE I.2 – Summary of the main features of different SPD technologies. Data mainly taken from ThorLabs and Horiba Scientific websites.

I.2.3 Numerical converter

No matter the kind of employed detector, the measurement that is wanted by the user should be a numerical measurement in order to process the SPC data. Several technologies can perform such a conversion.

8. Negatively charged electrode covered by a material able to free electrons.
9. Electrodes in a vacuum tube employed to multiply electrons.
10. Non-exhaustive list.

ADC The electrical signal given by the photodiode or PMT can be digitized using an *analog-to-digital converter* (ADC). Such a device samples at a given frequency the current intensity (or tension), the sampled value is proportional to the magnitude of the intensity (or tension). ADCs are widely available and their features (sampling rate, input voltage/intensity, number of bits) should be chosen according to the single point detector.

TCSPC Some single point detectors [11] can be coupled to a *time-correlated single photon counting* (TCSPC) board that should be employed along with a pulsed laser to illuminate the scene under view. A TCSPC counts the number of photons but this is done for different time channels according to the time-of-flight of the photons thanks to the laser pulse reference. In this case, the SPC measurement is not a simple scalar data but a vector of scalar measurements for each time channel.

I.3 Pros and cons

The hardware implementation of the SPC gives some insight and idea about the possible pros and cons of a SPI system. These are detailed in the next paragraphs.

I.3.1 Advantages

As mentioned in introduction, several advantages stand out when employing a SPC as an imaging system compared to a traditional digital camera with an array of sensors.

One of the most important advantage is the optical compression performed at the hardware level. Today's cameras acquire tens of megapixels resulting in huge computer files. As a consequence, most images are compressed to reduce their size on disk and to be suitable for transfer (e.g. email, website). For instance, this throws away roughly 80% of the information that was acquired with the conventional camera. With SPC, the idea is to directly perform the compression during the acquisition so that only the remaining 20% of the useful information is acquired. As well as reducing the storage memory, acquiring only a few number of measurements reduces the consumed energy, by a factor of 5 with the previous example. The small memory storage and power consumption are a key element for devices where the storage unit and the battery life are limited (e.g. robots, cellphones).

As shown in table I.1 and table I.2, the active area of most SLM and SPD are in the mm^2 range that could therefore open the door to a very compact device. In addition, the restoration of SPC images without the lens of Fig. I.1 have been demonstrated by researchers at Bell Labs (Huang *et al.*, 2013) which is a big step for SPC miniaturization.

Last but not least, the price of a SPC can be relatively low compared to traditional cameras. First, while visible CCD or CMOS cameras are inexpensive thanks to the well controlled and cheap silicon technology, silicon sensors are not as efficient outside the visible range and another component should be used. In this sense, the SPC has the huge advantage of using a SPD

11. Mostly PMT or single photon avalanche diodes.

which can have a high efficiency (Hadfield, 2009) and be less costly than a sensor array (Rogalski, 2012) for a system working in the ultraviolet or infrared. Second, a SPC can be easily turned into a hyperspectral/multispectral camera by replacing the detector by a single point spectrometer. Such spectrometers provide nanometer spectral resolution for some thousands of euros, where conventional imaging systems with similar resolution would be about ten times more expensive. Third, the cost gain is also important if the single point detector is coupled to a TCSCP to obtain a *time-resolved* (TR) imaging system. Spectrometer and TCSPC can finally be used in conjunction to build a multispectral/hyperspectral time-resolved device. Hence, SPI facilitates to obtain low cost systems with high spatial, temporal and/or spectral resolutions which can be hardly achieved with conventional array of sensors.

I.3.2 Disadvantages

While a conventional digital camera acquires simultaneously each pixel of the image, a SPC needs to perform sequential measurements making it inevitably slower than traditional cameras. The speed of acquisition is limited by the SLM, the SPD and/or the device to get numerical measurements. For instance, table I.1 shows that, at the date of this manuscript [12], the maximum frame rate for the available SLMs is 32 kHz. If for example a 1024×1024 pixels image is acquired and that 20% of the number of pixels are acquired in terms of measurement, this leads to a minimum of $1024^2 \times 0.2/32000 \approx 6.6$ s for acquisition time where a conventional camera would take a few hundred ms.

A second disadvantage, also linked with the speed of SPI, is the post-processing of the sequence of measurements to obtain the desired image. It will be shown in Chapter II that some image restoration techniques take less than a second but others can take up to minutes, depending on the resolution of the image and the number of sampled measurements.

Overall, SPI is at the moment not well suited for capturing high resolution images since both acquisition times and restoration times increase with the number of measurements.

I.4 Applications

Owing to its numerous advantages, the SPC found several applications since the first recovered images by Takhar *et al.* in 2006. Below are some examples to which one should include the medical applications mentioned in the introduction.

I.4.1 Static imaging

Color imaging Color images were proposed in the first works on SPC by Duarte *et al.* in 2008. For this, the authors employ RGB filters placed in front of the photodiode so as to get three measurements for one pattern. The restoration of the image in each RGB canal leads to a color image. In Welsh *et al.* (2013), a full-color SPC is presented using a dichroic beamsplitter. The latter one

12. The refresh rate of the DMD kept on increasing since its creation.

decomposes the white light in three outputs (red, green, blue) and three photodiodes collect the resulting light. One image per color channel can therefore be restored so as to get a color image (see Fig. I.4-left). In the works of Salvador-Balaguer *et al.* (2016), the same approach as in Duarte *et al.* is employed with one photodetector. The difference lies on the use of a color wheel with RGB filters in the illumination side and not the detection one.

Infrared imaging The works of Radwell *et al.* (2014) (see Fig. I.4-right) design a SPC-based microscope able to image both in the short-wave infrared and the visible spectrum. For this, a short-wave infrared source is employed and the two DMD's arm (ON and OFF states) are coupled to two different detectors, a visible sensitive sensor and an infrared sensitive one. A similar idea is employed in Edgar *et al.* (2015) where visible and infrared images are recorded. The light emitted from the DMD is split in a short-wave dependent beam and a visible beam thanks to a hot-mirror [13]. In Shin *et al.* (2016), the authors illuminate the object with a near-infrared tunable continuous-wave laser coupled to a single-mode fiber to illuminate the object with random speckle patterns [14](Shin *et al.*, 2017). A sensitive infrared photodiode is employed as a detector so as to get an image of the object in the infrared. Recently, methane gas leaks were observed using an infrared SPI system in Gibson *et al.* (2017), showing the potential of infrared imaging based on SPC.

Ghost imaging Ghost imaging systems usually combines a CCD camera that does not see the object (hence the term *ghost*) with a single-point detector on the object's path to get the image of the observed object. In 2008, with the advances on SPC, Shapiro showed that ghost imaging was possible using only the SPD. The idea of using simply the SPC arm is taken over by Aßmann *et* Bayer (2013) and then Yu *et al.* (2014a) with different computational approaches. In Onose *et al.* (2016), a new hardware technology is employed for ghost imaging with an array of *light-emitting diode* (LED) lights performing the modulation in illumination to recreate a SPI system.

Terahertz imaging Shortly after the first SPC images, Chan *et al.* in 2008 showed that the ideas of SPI could be applied to terahertz imaging. A terahertz transmitter is used to illuminate the object,

13. Mirror reflecting the infrared light and letting pass the visible light.
14. Note that in this particular design, no SLM is employed.

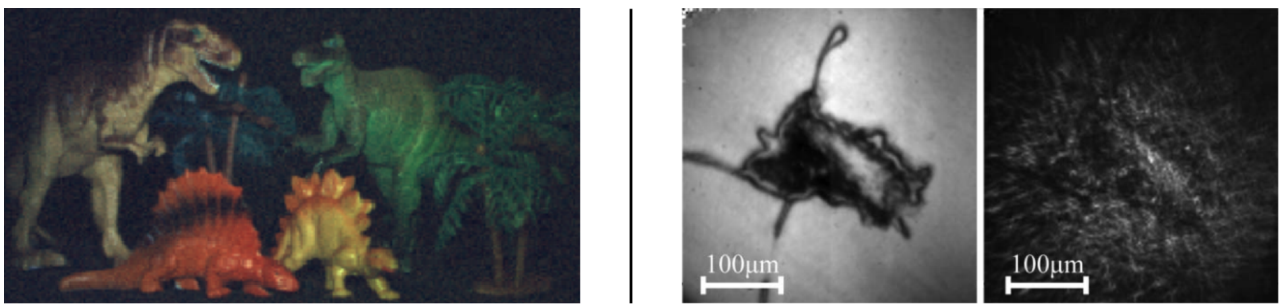

FIGURE I.4 – Example of static imaging using a SPC. Left : color image of a dinosaur scene adapted from Welsh *et al.* (2013), right : visible (left) and short-wave infrared (right) images obtained from the SPC-based microscope of Radwell *et al.* (2014).

the SPC patterns are printed on printed-circuit boards and a single terahertz receiver serves as a detector. Ma *et al.* (2012) considers the use of a Nipkow disk to create a SPC-based imaging system suited for terahertz imaging. A terahertz SLM is created in Shrekenhamer *et al.* (2013) by photoexcitation of semiconductors, that is employed, coupled to a classic DMD, to obtain a SPC terahertz imaging system. The same authors in Watts *et al.* (2014) slightly change their design to use the single MMA SLM presented in I.2.1 as a proof for a terahertz SLM. In Fursich *et al.* (2016), a system based on a single terahertz detector and frequency modulated continuous wave radar is reported. This SPC-based imaging system radar can be used in airport security for weapon detection. A single-pixel terahertz system based on a metal mask structure is also presented in Duan *et al.* (2016) allowing to image at 1.75 THz.

Microscopy In Studer *et al.* (2012), a conventional microscope is transformed into a compressive microscope using the principles of CS that is shown to successfully image fluorescent beads, cells or tissues. In the works of Rodriguez *et al.* (2016), a microscope able to image in both reflective and transmissive geometries based on SPC is created. A DMD is employed for illumination and two PMTs serve to create two SPC, one in reflection and one in transmission. The dual infrared/visible SPC of Radwell *et al.* presented for infrared imaging was also mounted on a microscope to image object of a few hundreds μm (see Fig. I.4-right).

Telescopic imaging A telescopic system is used in Yu *et al.* (2014b) to image an object from 2 km far away. They show that a reduction of the measurements can be achieved using both arms of the employed DMD (the ON and OFF beams) with two PMTs. Their setup has the advantage of having large field of views over a long distance and could be employed for applications in remote target imaging.

Digital holography Digital holography is reported by the authors in Martínez-León *et al.* (2017) using phase-structured illumination and bucket detection, allowing them to image complex amplitude objects. Advantages in this design regard the use of only one phase SLM and an improvement by a factor of two of the signal-to-noise ratio.

I.4.2 Multidimensional imaging

Multispectral/Hyperspectral imaging In Magalhaes *et al.* (2012), a hyperspectral imaging system based on SPC is proposed. The single-point detector of the SPC is replaced by a spectrum analyzer able to reach spectral resolution of 10 pm. A hyperspectral spectrometer coupled to a SPC is also employed in Hahn *et al.* (2014) with a different acquisition strategy at the software level. A patent for a dual spectral SPC acquisition setup has also been filed by Xerox Corporation (Bernal *et al.*, 2015). The same corporation also filed a patent for hyperspectral imaging using a fabry perot filter and a single point detector (Nystrom *et al.*, 2016). In the recent works of Bian *et al.* (2016b), a multispectral imaging system employing a single bucket detector is reported giving a high sensitivity imaging system (see Fig. I.5-(a) and (b)). The authors employ a classical SPC

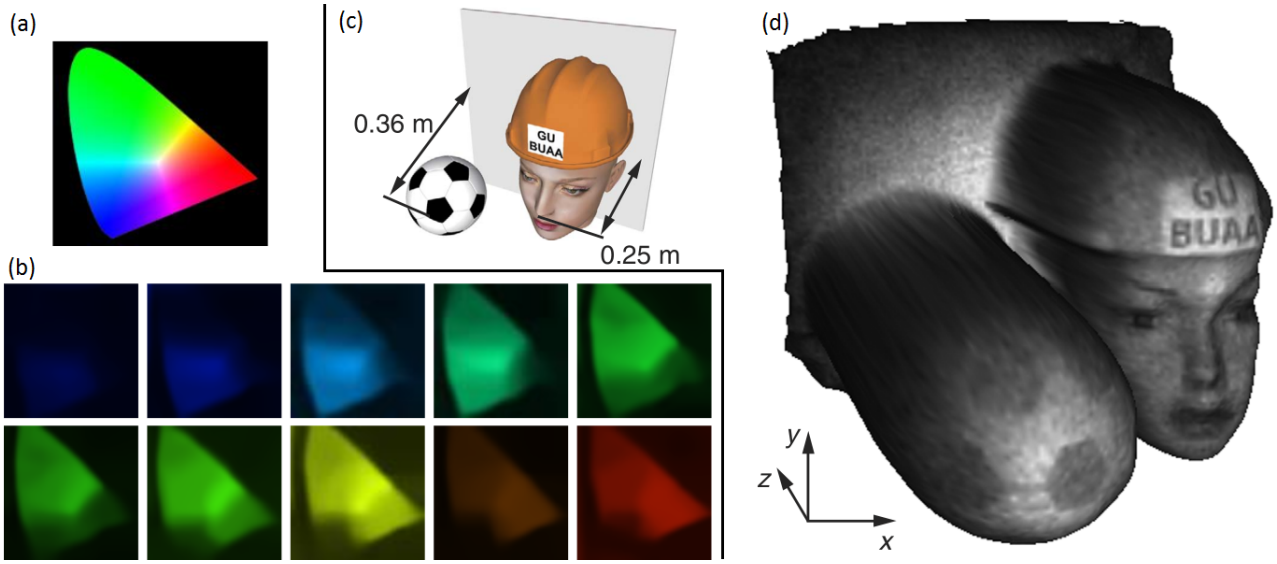

FIGURE I.5 – Example of multidimensional imaging using a SPC. (a) Object employed for multispectral imaging in Bian *et al.* (2016b) and the corresponding (b) 10 SPC restored images in different spectral channels from 450 nm to 650 nm. (c) Scene imaged in Sun *et al.* (2016a) and (d) recovered 3D image from the SPC measurements.

architecture with a DMD but further modulate their data with a rotating film allowing for sinusoidal modulation in the spectral dimension. A spectrometer based on SPC is reported in Starling *et al.* (2016) where their design is able to measure both absorption and emission spectra with 90% reduction of the data-set employed by commercial spectrometer. In Li *et al.* (2017), a system employing only one photodiode is presented for multispectral imaging. In their setup, the light emitted from the object goes to a spectral splitter creating 8 different beams going to 8 different areas of the SLM and then everything is collected on the photodiode. The areas of the SLM being encoded with its own particular patterns, post-processing of the measurements allows to recreate the 8 images in 8 different spectral channels.

3D imaging In Sun *et al.* (2013) a projector illuminates the scene with random speckle patterns and four photodetectors placed at different angles collect the outgoing light. Post-processing of the data from the four single-point detectors allows to reconstruct a 3D image of the scene. The same group extends their results to 3D video imaging in Zhang *et al.* (2016) and Sun *et al.* (2016a) (see Fig. I.5-(c) and (d)). In Yu *et al.* (2015), the depth information and 3D reflectivity of the scene are reconstructed using simple algebra. A Fourier-based technique to retrieve 3D information is presented in Zhang *et* Zhong (2016). The depth information is modulated by well-chosen patterns in illumination and collected by the SPD enabling 3D reconstruction of the object with Fourier analysis. The works of Salvador-Balaguer *et al.* (2016) perform stereoscopic color imaging using a color projector [15] for illumination from two different angles creating a stereoscopic pair.

Time-resolved imaging A time-resolved photodetector is employed in Kirmani *et al.* (2011) to perform *time-of-flight* (TOF) measurements using a SPC. The exploitation of this TOF for each

15. Most projector produced nowadays employ DMDs.

pixel of the image leads to the obtainment of a depth map for the scene under view. The same idea is presented in the works of Howland *et al.* (2013) using a SPC with a PMT as a detector coupled to a TCSPC board. In Dai *et al.* (2016), the same technology is employed with a different acquisition strategy to obtain both the reflectivity and depth map.

I.4.3 Video acquisition

A growing application for SPC concerns video imaging judging by the number of publications in the last years. A recent review of state-of-the-art compressed video sensing techniques is given in Baraniuk *et al.* (2017). Although SPC acquisition and restoration schemes can be quite slow, the idea is to exploit temporal redundancy so as to reduce the number of measurements, speeding up both acquisition and restoration times. Such approaches therefore makes video recovery computationally more demanding than static image restoration.

To compress further exploiting temporal redundancy, different techniques have been proposed e.g. methods based on motion estimation in Sankaranarayanan *et al.* (2015, 2016) (see Fig. I.6) and Goldstein *et al.* (2015), minimization of the image spatial-curvature in Edgar *et al.* (2015), techniques mimicking animal imaging in Phillips *et al.* (2016). A different approach for image acquisition/restoration is employed in Zhang *et al.* (2016) that allows faster image recovery. The same group proposed a similar approach for video surveillance of methane gas leaks in Gibson *et al.* (2017). A time-varying 2D ultrasonic field was encoded in Huynh *et al.* (2016) to enable video rate imaging of ultrasound fields.

FIGURE I.6 – Example of video imaging of a red toy car moving from left to right using a SPC adapted from Sankaranarayanan *et al.* (2015). Ground truth images (top row) and SPC recovered video images (bottom row).

FIGURE I.7 – Lensless SPC image adapted from Huang *et al.* (2013) (left) and SPC image obtained with a carbon nanotube photodetector adapted from Chen *et al.* (2014) (right).

I.5 New trends in SPC optical methods

In the last years, some new ideas and optical system designs were reported in the optical field to simplify imaging system or draw the best out of new materials. The use of a SPC for some of these new trends can be relevant and is presented in the next paragraphs.

I.5.1 Lensless imaging

Lensless imaging has become an important topic in optics in the last decade since it offers large field of views with compact imaging systems (Allier *et al.*, 2010; Ozcan *et* McLeod, 2016; Boominathan *et al.*, 2016). New imaging systems without focusing lens where designed such as the PicoCam (Stork *et* Gill, 2013) or the FlatCam (Asif *et al.*, 2015b,a; Boominathan *et al.*, 2016).

In 2013, Bell Labs proposed a SPC architecture without a lens in Huang *et al.* (see Fig. I.7-left). Their designed comprises an LCD screen as SLM and a photovoltaic sensor. In their work, no physical image is formed before it is digitally captured. The use of a SPI in this design reduce the size, cost and complexity of the final camera architecture.

I.5.2 Emerging photodetectors

In the last decade, new technologies and materials allowed for the creation of new photodetectors with improved features. For instance, carbon nanotube (Chen *et al.*, 2011, 2014) and more recently graphene (Li *et al.*, 2016) have been used as photodetectors to enhance some or several SPC possibilities.

Owing to its optoelectronic properties, *carbon nanotube* (CNT) can be used as a photodetector outperforming most infrared detectors. The high surface-to-volume ratio of CNT can increase the signal-to-noise ratio and the phonon scattering suppression and size shrinking can reduce the noise for such detectors (Kuo *et al.*, 2001). Fabricating large scale CNT photodetectors being difficult, the authors in Chen *et al.* (2011, 2014) (see Fig. I.7-right) proposed to employ the sensor in a SPI system, extending the possible applications of the SPC with classic photodetectors.

Since its first discovery in 2004, graphene has been more and more investigated by laboratories due to its remarkable properties. Among them, graphene is stronger than any steel and

is as good an electricity conductor as copper. Graphene can be made luminescent, its transmittance is almost wavelength-independent and it can be used as a saturable absorber (Bonaccorso *et al.*, 2010). Combining its electronic and optical properties, graphene-based photodetector can convert received light in voltage in an extremely short time (Xia *et al.*, 2009). Li *et al.* proved in 2016 that such a detector can be used for SPI. This showed the potential of graphene that could allow in the future high speed imaging thanks to its ability to convert light in voltage at high frequency.

I.6 Conclusion

This chapter presented the main idea behind the SPC and its possible hardware implementations that can take various forms, both in transmissive and reflective geometries. The many advantages of the simple setup, particularly the low cost aspect of using a single-point detector, made SPI an emerging imaging technique in the last decade. Based on the numerous applications presented in this chapter, the SPC should still remain an attractive topic in the future years.

While this chapter presented the hardware side of the SPC, several essential questions related to its software side remain unanswered however : how does one can obtain an image from single-point measurements ? What are the mathematical tools and concepts behind it ? These questions are addressed in the following chapter with the possible acquisition/restoration scheme for SPC that have been proposed since 2006.

CHAPTER II

ACQUISITION/RESTORATION SCHEMES FOR SPI

Contents

CHAPTER II

UNLIKE for CCD or CMOS cameras, hardware acquisition of an image in single-pixel imaging is linked to its software restoration. With an array of sensors, one measure acquires in parallel each pixel of the image which is impossible to perform with a single-pixel camera. A sequence of SPC measurements with different SLM patterns are thus performed and the post-processing of these measurements leads to the image. This chapter aims to answer to the following two questions : how to choose the SLM patterns? Knowing the SLM patterns and the measurements, how to recover the image?

The first part of this chapter describes the mathematical formulation of a SPC acquisition. Then, state-of-the art acquisition/restoration schemes are reported. Two main categories of approaches stand out, the *nonadaptive* and *adaptive* techniques. The first considers a fixed set of patterns regardless of the image whereas the second *adapts* the set of patterns based on previous SPC measurements. Finally, hybrids methods combining different approaches are presented.

II.1 Mathematical formulation

II.1.1 Simple modeling

As mentioned in Section I.1, a SPC acquisition consists in modulating the light field emitted by the object (i.e. the image) with a given SLM pattern. The single-point detector then integrates the modulated light rays (see Fig. I.1), i.e., the inner product of the image with the SLM pattern is measured at the SPD. Let us note $\mathbf{f} \in \mathbb{R}^{D\times 1}$ the image of the object with $D = H \times W$ the size of the image. We note $\mathbf{p}_k \in \mathbb{R}^{D\times 1}$ a pattern loaded on the SLM and m_k the measure collected by the single sensor :

$$m_k = \sum_{i=1}^{D} \left(\mathbf{p}_k\right)_i (\mathbf{f})_i = \mathbf{p}_k^\top \mathbf{f}, \tag{II.1}$$

with $\left(\mathbf{p}_k\right)_i$ (resp. $(\mathbf{f})_i$) the i-th element of the vector $\mathbf{p}_k$ (resp. $\mathbf{f}$), $i \in [1, D]$.

As mentioned before, recovering the image of the object with a single measurement is impossible, sequential measurements with different SLM patterns $\mathbf{p}_k$ are therefore performed. Let $\mathbf{P} = (\mathbf{p}_1, \ldots, \mathbf{p}_K)^\top \in \mathbb{R}^{K\times D}$ be the matrix containing K SLM patterns sequence. The measurement vector $\mathbf{m} = (m_1, \ldots, m_K)^\top \in \mathbb{R}^{K\times 1}$ containing the corresponding sequence of measures is mathematically modeled by

$$\mathbf{m} = \mathbf{P}\mathbf{f}. \tag{II.2}$$

II.1.2 Real measurement modeling

In practice, the measure obtained at the SPD is collected over a certain integration time Δt (in s). A light source emitting a certain number of photons per seconds N_0 (in ph/s) is also employed to illuminate the object. If $\mathbf{f}$ and $\mathbf{p}$ (no units) are normalized, then the measurement is obtained as a number of photons and (II.1) becomes

$$m_k = \Delta t N_0 \mathbf{p}_k^\top \mathbf{f}. \tag{II.3}$$

A final component should be added to (II.3). If one switches off the light source, i.e. $N_0 = 0$ ph/s, the measurement m_k is not null. This is mainly because of the dark current of the SPD, i.e., an electric current is induced even when no photons reach the device. In addition to the SPD's dark current, even when acquisitions are performed in the dark [1], there is always a remaining small amount of light creating a non zero measure at the SPD. To account for all of this, let us note α (in ph/s) a single component regrouping the data read by the SPD when $N_0 = 0$. This component will be referred to as the *dark current* of the SPC system. Hence, the final measure can be modeled (Takhar *et al.*, 2006; Duarte *et al.*, 2008) as

$$m_k = \left(N_0 \mathbf{p}_k^\top \mathbf{f} + \alpha\right) \Delta t. \tag{II.4}$$

Including the previous results, the matrix equation (II.2) for sequential measurements becomes

$$\mathbf{m} = \left(N_0 \mathbf{P}\mathbf{f} + \alpha \mathbf{1}_K\right) \Delta t \tag{II.5}$$

where $\mathbf{1}_K = (1, \ldots, 1)^\top \in \mathbb{R}^{K \times 1}$.

Note that in all the above equations, the sign equal is used but should be understood as proportional. The measurements are indeed collected by the SPD and are then converted into scalars by one of the devices of Section I.2.3. Conversions also appear in the SPD to convert photons to electrical current or tension. The measurements given by (II.4) and (II.5) models the number of photons reaching the single-point detector and not exactly the final numerical data given to the user.

II.1.3 Problem

As mentioned in the introduction of this chapter, the acquisition/restoration schemes for SPI induce two problems. The last equation (II.5) indeed suggests that a SPC acquisition requires to answer to the two following points :

1. **Acquisition :** how to design and/or choose the sequence of SLM patterns $\mathbf{P}$?
2. **Restoration :** knowing the patterns $\mathbf{P}$ and the measurements $\mathbf{m}$; how to restore the image $\mathbf{f}$?

1. Note that this is not required as SPC acquisitions can be performed with the ambient light.

For the sake of simplicity, in the rest of the chapter, equation (II.2) is employed. As a first approximation, the additive component $\Delta t \alpha \mathbf{1}_K$ of (II.5) can simply be measured by setting $N_0 = 0$ ph/s and then it can be deducted to each SPC measurement [2]. Regarding the term $\Delta t N_0$, being a constant for each measurement, equation (II.2) remains valid up to a scaling factor.

II.2 Compressive sensing

The first category of algorithms that provided the first SPC images in 2006 are based on the compressive sensing (CS) paradigm. The next sections give the mathematical tools behind it as well as some examples of CS-based SPC acquisitions.

II.2.1 Acquisition/restoration in the CS framework

CS theory The first works on the SPC in 2006 by Takhar *et al.* took advantage of the recent CS paradigm (Donoho, 2006; Candes *et al.*, 2006; Baraniuk, 2007; Baraniuk *et al.*, 2010). The idea is that most signals are compressible in a certain basis and can hence be recovered from only a small (sub Nyquist) number of projections (i.e., measurements). Let us note $\mathbf{\Lambda} \in \mathbb{R}^{D\times D}$ a transform operator for which the image $\mathbf{f}$ has a sparse representation. Mathematically,

$$\mathbf{f} = \mathbf{\Lambda s} \tag{II.6}$$

where $\mathbf{s} \in \mathbb{R}^{D\times 1}$ is L-sparse which means that $\mathbf{s}$ only has L nonzero entries. In other words, the image $\mathbf{f}$ can be restored from only L basis vectors and an optimal basis would be the one for which $L \ll D$ with the smallest possible value. Wavelets, Fourier and *discrete cosine transform* (DCT) basis are common choices for $\mathbf{\Lambda}$.

The L basis vectors being unknown, the idea of CS is to acquire $K < D$ projections of the image $\mathbf{f}$ with a collection of vectors $\mathbf{p}_k$ arranged in a matrix $\mathbf{P}$ and the corresponding SPC measurement vector is given by

$$\mathbf{m} = \mathbf{Pf} = \mathbf{P\Lambda s} = \mathbf{\Psi s} \qquad \text{with} \quad \mathbf{\Psi} = \mathbf{P\Lambda} \in \mathbb{R}^{K\times D} \tag{II.7}$$

Acquisition The problem now lies in the design of the matrix $\mathbf{P}$ so that it captures enough information to restore the image of size D from only K measurements. Since we assumed that the signal has an L-sparse representation in some basis $\mathbf{\Lambda}$, K must be superior or equal to L. It was shown that to obtain a good estimate of $\mathbf{f}$, the matrix $\mathbf{\Psi}$ must satisfy the so-called *restricted isometry property* (RIP) (Donoho, 2006) :

$$(1-\epsilon)\|\mathbf{b}\|_2^2 \leq \|\mathbf{\Psi b}\|_2^2 \leq (1+\epsilon)\|\mathbf{b}\|_2^2 \tag{II.8}$$

where $\mathbf{b} \in \mathbb{R}^{D\times 1}$ is any vector having the same L nonzero entries as $\mathbf{s}$ for some $\epsilon > 0$. It has been shown that selecting $\mathbf{P}$ as a random matrix can ensure the RIP property for $\mathbf{\Psi}$ (Donoho, 2006;

2. Different strategies to deal with this component are exposed throughout this manuscript, mostly in Chapter V.

Baraniuk *et al.*, 2007). For instance, an independent identically distributed Gaussian matrix has the RIP with high probability if

$$K \geq cL\log\left(\frac{D}{L}\right) \tag{II.9}$$

for some values of c typically ranging in $1-100$ (Donoho, 2006; Candes *et al.*, 2006; Baraniuk *et al.*, 2007). Hence, the elements of $\mathbf{P}$ for SPC are generally chosen (Candes *et* Tao, 2006; Takhar *et al.*, 2006; Duarte *et al.*, 2008) as

$$(\mathbf{P})_{i,j} \sim \mathscr{B}(\mu = 0, p = 1/2) \tag{II.10}$$

where $\mathscr{B}(\mu, p)$ accounts for the Bernoulli distribution with probability p and mean μ. Such a distribution is often chosen since the resulting patterns with ± 1 entries are well suited to any SLM technology.

Restoration To find the image $\mathbf{f}$ from the measurement $\mathbf{m}$ of (II.7), one must solve the following optimization problem

$$\mathbf{s}^* = \arg\min \|\mathbf{s}\|_p \quad \text{such that} \quad \mathbf{\Psi s} = \mathbf{m}. \tag{II.11}$$

with $\|\mathbf{x}\|_p = \left(\sum_{i=1}^{D} |x_i|^p\right)^{\frac{1}{p}}$ the ℓ_p norm of vector $\mathbf{x} \in \mathbb{R}^{D\times 1}$ and $0 \leq p \leq 1$. The image is finally restored in the original domain according to (II.6), i.e.,

$$\mathbf{f}^* = \mathbf{\Lambda s}^* \tag{II.12}$$

However, many $\mathbf{s}^*$ that are L-sparse signals are solutions of $\mathbf{\Psi s} = \mathbf{m}$ in (II.11) since we chose $K < D$. The norm should therefore be carefully chosen in order to obtain the best solution $\mathbf{s}^*$.

ℓ_0 "norm" Given that we search for a L-sparse vector, it is intuitive to employ the ℓ_0 "norm" [3] in (II.11) as $\|\mathbf{x}\|_0$ counts the number of nonzero elements in $\mathbf{x}$. This sparsity measure based minimization is however a NP-complete problem that is numerically unstable. It therefore requires many computations to find the possible locations of the nonzero entries in $\mathbf{s}$.

ℓ_2 norm As it is commonly employed in several optimization problems, the ℓ_2 norm can be set to solve (II.11). The advantage is that one can directly find a closed-form solution by simple algebra, i.e., $\mathbf{s}^* = \left(\mathbf{\Psi}^\top\mathbf{\Psi}\right)^{-1}\mathbf{\Psi}^\top\mathbf{m}$. However, with this norm, the energy is minimized and the found solution will almost never be a L-sparse vector $\mathbf{s}$ which is therefore not the best solution.

ℓ_1 norm It was shown that, under the conditions that $K \geq cL\log(D/L)$, the image can be exactly or closely recovered in the transform domain by solving the problem (II.11) with the ℓ_1 norm (Donoho, 2006). Different algorithms (Candes *et* Romberg, 2005; Candes *et al.*, 2006; Foucart *et* Rauhut, 2013) can efficiently solve this convex optimization problem.

3. This is not exactly a norm in the mathematical sense of the term.

TV minimization In the context of single-pixel imaging, it is classical to obtain $\mathbf{f}$ directly in the image domain using Total Variation (TV) minimization (Li, 2009) instead of the ℓ_1-minimization and (II.12). Although the CS theory is not applicable in this case, TV-minimization is a popular alternative since it allows for much faster image restoration while being almost similar to performing ℓ_1-minimization in the wavelet domain (Candes *et al.*, 2006). The problem is hence formulated as below

$$\mathbf{f}^* = \arg\min \|\mathbf{f}\|_{\text{TV}} \quad \text{such that} \quad \mathbf{Pf} = \mathbf{m}. \tag{II.13}$$

If $\mathbf{F} \in \mathbb{R}^{H\times W}$ represents the 2D version of $\mathbf{f} \in \mathbb{R}^{D\times 1}$, $D = H \times W$, then the TV norm of $\mathbf{f}$ can be defined in its isotropic or anisotropic versions as

$$\begin{cases} \|\mathbf{f}\|_{\text{TV}}^{\text{iso}} = \|\mathbf{F}\|_{\text{TV}}^{\text{iso}} = \sum_{h=1}^{H-1}\sum_{w=1}^{W-1} \sqrt{|F_{h+1,w} - F_{h,w}|^2 + |F_{h,w+1} - F_{h,w}|^2} \\ \|\mathbf{f}\|_{\text{TV}}^{\text{aniso}} = \|\mathbf{F}\|_{\text{TV}}^{\text{aniso}} = \sum_{h=1}^{H-1}\sum_{w=1}^{W-1} |F_{h+1,w} - F_{h,w}| + |F_{h,w+1} - F_{h,w}| \end{cases} \tag{II.14}$$

Depending on the problem to solve, anisotropic TV can be easier to minimize and is often preferred. This kind of minimization works well if the gradient of $\mathbf{f}$ is sparse, i.e., if $\mathbf{f}$ is a piecewise constant image.

In summary, the acquisition/restoration scheme using CS is referred to as a *nonadaptive* acquisition strategy in the sense that the matrix $\mathbf{P}$, for a given size D and number of measurements K, can be used for different objects to image. Figure II.1 gives the main scheme of such an acquisition strategy.

FIGURE II.1 – Scheme of a nonadaptive acquisition framework for single-pixel camera.

II.2.2 Examples of CS-based SPC

Figure II.2 gives an example of CS-based SPC acquisitions from the first works of Takhar *et al.* (2006) and Duarte *et al.* (2008). The authors image the black-and-white letter R using random patterns and ℓ_1-minimization or TV-minimization for image restoration. It can be seen that the TV-minimization leads to the creation of spots and works well for this image that is piecewise constant.

CS-based SPC has been widely applied to various applications presented in Section I.4 (Chan *et al.*, 2008; Ma, 2009b,a; Magalhaes *et al.*, 2011; Studer *et al.*, 2012; Magalhaes *et al.*, 2012; Welsh *et al.*, 2013; Tajahuerce *et al.*, 2014; Duran *et al.*, 2015; Edgar *et al.*, 2015; Zhang *et al.*, 2016; Rodriguez *et al.*, 2016) since the patterns are very easy to create and open source codes are available for ℓ_1 or TV minimization.

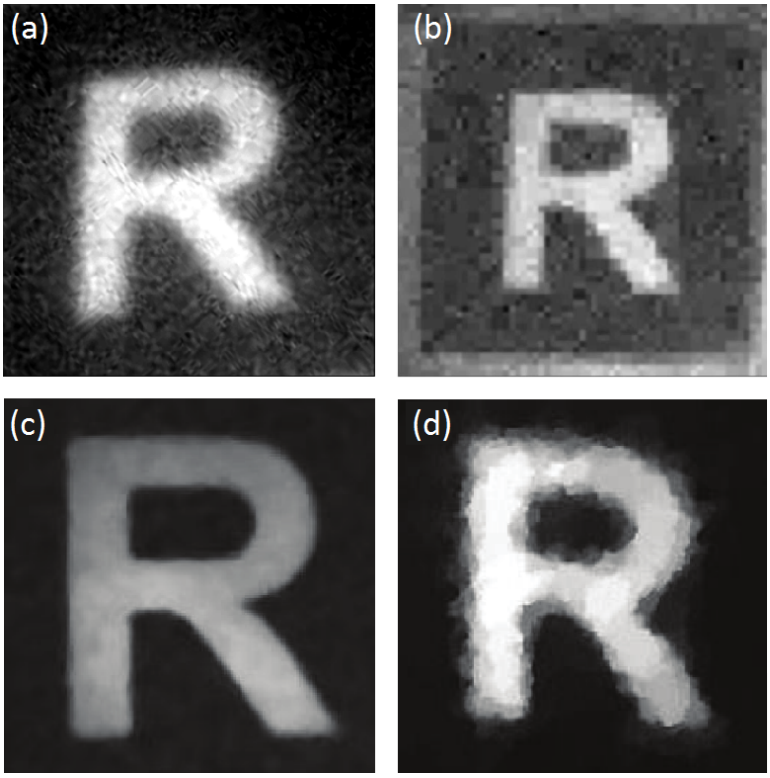

FIGURE II.2 – Example of SPC images obtained using the CS paradigm. (a) Image of the object on the SLM and (b) 64×64 SPC image recovered from 1600 measurements using ℓ_1-minimization. (c) CCD image of the object and (d) 256×256 SPC image recovered from 1300 measurements using TV-minimization. Images extracted and adapted from Takhar *et al.* (2006) (a-b) and Duarte *et al.* (2008) (c-d).

II.2.3 Pros and cons

Advantages The simple design of the matrix $\mathbf{P}$ with random ± 1 variables is an advantage since, for a given size D and number of measurements K, one can create this matrix once and for all. The second advantage is that most signal being L-sparse in a basis, the number of measurements K can be rather small compared to the number of pixels D of the restored image. For instance, in Fig. II.2-(d) only 1300 measurements are acquired for a 256×256 image thus giving a compression ratio of 98%.

Disadvantage The biggest drawback with CS is the restoration step based on ℓ_1-minimization. Such an optimization process indeed needs some heavy computation and the reconstruction time deeply suffers when D and K increase, taking from seconds to minutes. It is hence quite difficult to consider real time applications needing high resolution images with CS.

II.3 Basis scan

In order to have a straightforward image recovery without ℓ_1 or TV minimization, a *basis scan* (BS) approach can be employed, i.e., the SPC progressively acquires the scene under view in a user chosen basis. The next sections give the mathematical tools behind BS-based acquisition as well as some examples and advantages/disadvantages of this technique.

II.3.1 Acquisition/restoration in the BS framework

Acquisition As mentioned earlier, a basis scan acquires the image directly in the chosen orthonormal basis. Let us note $\mathbf{B} \in \mathbb{R}^{D\times D}$ the transform operator of a given basis and $\widetilde{\mathbf{f}} \in \mathbb{R}^{D\times 1}$ the image $\mathbf{f}$ in the basis $\mathbf{B}$. Each element of $\widetilde{\mathbf{f}}$ therefore represents a coefficient in that basis and corresponds to the inner product of a row of $\mathbf{B}$ with image $\mathbf{f}$. A basis scan acquisition can hence be formalized as :

$$\mathbf{m} = \mathbf{P}\mathbf{f} \qquad \text{with} \quad \mathbf{P} = \mathbf{B} \quad \text{s.t.} \quad \mathbf{m} = \widetilde{\mathbf{f}} \tag{II.15}$$

Possible choices for $\mathbf{B}$ consist in a natural, Hadamard, wavelet, Fourier, discrete cosine transform basis, etc.

Restoration Using (II.15) and if $\mathbf{B}$ is invertible, the image recovery of $\mathbf{f}$ from its coefficients $\widetilde{\mathbf{f}}$ in basis $\mathbf{B}$ is straightforward :

$$\mathbf{f} = \mathbf{B}^{-1}\widetilde{\mathbf{f}} = \mathbf{B}^{-1}\mathbf{m} \qquad \text{or} \qquad \mathbf{f} = \sum_{k=1}^{K} m_k \mathbf{p}_k \tag{II.16}$$

$\mathbf{B}^{-1}$ accounts for the inverse basis transform of the chosen basis, e.g., inverse Fourier transform.

As we will show in the examples of BS-based SPC, it is in practice time-consuming to send the complete basis $\mathbf{B}$ as the number of patterns is equal to the number of pixels D of the desired image. A subset of $\mathbf{B}$ noted $\mathbf{B}_K$ having $L < K \leq D$ patterns is considered for which the choice of these K patterns is decided before acquisition no matter the object to image. The image restoration (II.16) is still valid provided that the elements of $\widetilde{\mathbf{f}}$ that were not acquired are set to 0.

As for the compressive sensing technique presented in Section II.2, the basis scan approach therefore lies in the category of nonadaptive approaches outlined in Fig. II.1 since the matrix $\mathbf{P} = \mathbf{B}$ or $\mathbf{P} = \mathbf{B}_K$ is the same regardless of the object to image.

II.3.2 Examples of BS-based SPC

Hadamard basis The Hadamard basis (Pratt *et al.*, 1969) is well suited for implementation on a SPC as the corresponding patterns have [-1,0,1] values. Such a basis is considered in Welsh *et al.* (2015) with a fully sampled Hadamard space that allows for near video-rate restoration of the image. Application is demonstrated for colour imaging and Stokes parameters are obtained using photodetector signals from orthogonal linear polarization states. The same group recently reported in Sun *et al.* (2016b) a way to improve the signal-to-noise ratio of the measurement when a DMD is considered as SLM. Their solution consists in spatially slightly shifting each pattern in the x, y and x/y (diagonal) direction so as to obtain four different measurements for a similar pattern. The approach is shown using a Hadamard basis scan where the four measurements are finally combined. Repeating the approach for each pattern, an improved image quality can be obtained.

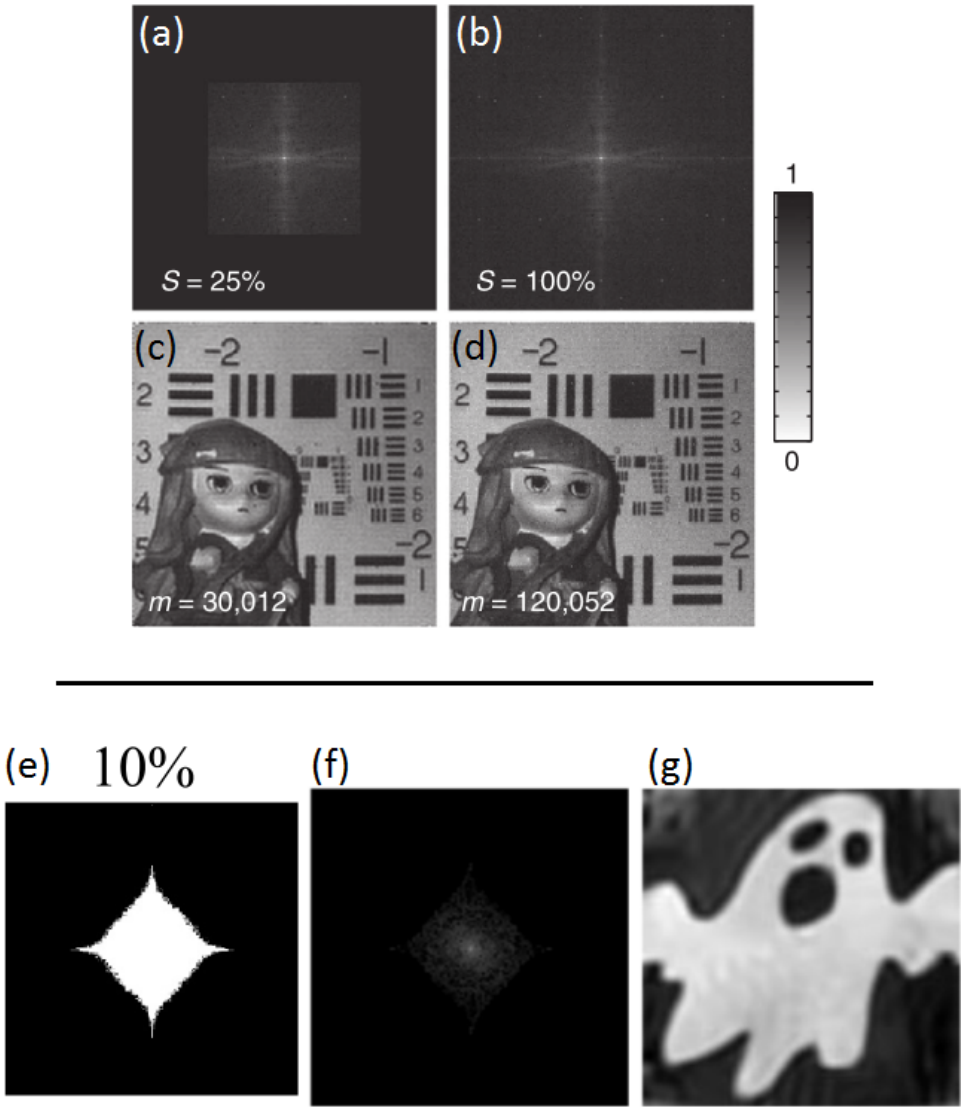

FIGURE II.3 – Example of SPC acquisitions with a basis scan approach in the Fourier domain. Sampled Fourier transform with a subset corresponding to (a) 25% of the (b) full spectrum and corresponding SPC restored images (c) with $K = 25\% \times D$ and (d) $K = D$, images extracted and adapted from Zhang *et al.* (2015). (e) Fourier subspace with 10% of the full spectrum, (f) sampled coefficients and (g) image obtain from the sampled coefficients, images extracted and adapted from Bian *et al.* (2016a).

Fourier basis In Zhang *et al.* (2015), the authors employ the Fourier basis to restore an image with *fast Fourier transform* (FFT) algorithms. They illuminate the scene with phase-shifting sinusoids in order to assemble the Fourier coefficients. Since a basis scan approach generally acquires the D coefficients of the image, Zhang *et al.* propose to use a subset $K < D$ of the patterns corresponding to the low frequencies of the Fourier domain as shown in Fig. II.3 (top). In Zhang *et* Zhong (2016), the same authors employ their Fourier strategy (Zhang *et al.*, 2015) with a more complex experimental setup allowing them to obtain depth information. They show that by estimating a fringe phase map, the height information of the scene under view can be exploited to obtain a 3D image. Fourier patterns are also employed in Bian *et al.* (2016a) with a different choice of the subset $K < D$. To create this subspace, the authors take the Fourier transform of a database of 44 natural images and compute the average magnitude map of these spectra. Thresholding

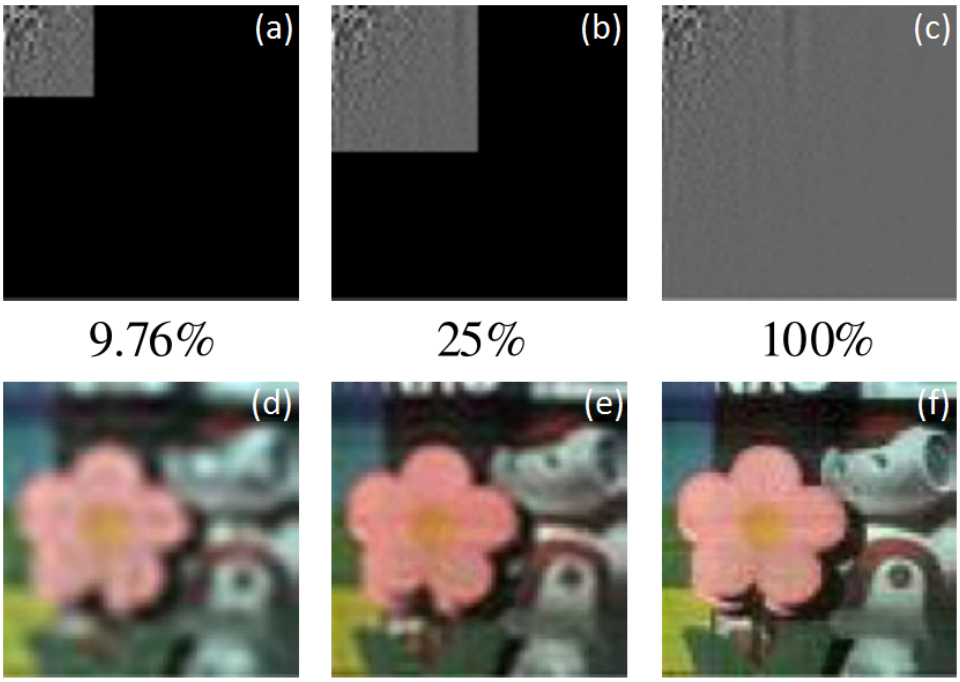

FIGURE II.4 – Example of SPC acquisition with a basis scan approach in the DCT domain. Coefficients acquired in the DCT domain with a sampling rate of (a) 9.76%, (b) 25%, (c) 100% and (d-f) corresponding restored SPC images. Images extracted and adapted from Liu *et al.* (2017).

this map for different values of threshold yields to different subspaces of the Fourier space (see Fig. II.3-bottom). Then SPC acquisitions are performed with the corresponding patterns belonging to the Fourier subspace no matter the image of the scene.

DCT basis The discrete cosine transform basis is considered in Liu *et al.* (2017). The full set of the D DCT patterns can be sent for acquisition or subsets $K < D$ of the DCT domain are also considered. Results for full-color imaging are given in Fig. II.4.

II.3.3 Pros and cons

Advantage The most notorious advantages of BS-based SPI is the inverse basis transform for image restoration. The matrix computation of (II.16) is quite rapid and for some well chosen basis, fast algorithms exist such as the FFT or the filter banks [4] for wavelet basis. For such algorithms, the complexity ranges from $O(D\log(D))$ to $O(D)$ which is much better than a CS algorithm for which complexity can reach $O(D^3)$ (Foucart *et* Rauhut, 2013).

Disadvantage In a basis scan approach, the matrix $\mathbf{P}$ of (II.15) becomes $\mathbf{B}$ leading to $K = D$, i.e., D measurements are acquired for an image of D pixels. The acquisition time is hence dramatically increased compared to a CS-based approach for which $K \ll D$. No compression is performed and acquisition times increase linearly with the number of pixels, making it again not practicable for real time applications needing high resolution images. When a subset of the full basis domain is

4. This will be detailed in Chapter IV.

considered, this allows to lower the number of measurements. However, such an approach relies on an a-priori from a database of images that is not necessarily representative of the scene under view. For instance, in the Fourier example of Fig. II.3, no coefficients corresponding to the high frequencies are acquired. This could be a problem if the scene under view has lots of high frequencies that would therefore not be well restored by this approach.

II.4 Adaptive basis scan

The number of measurements in a basis scan being a big limit to its employment, the idea of an *adaptive basis scan* (ABS) approach is to sample only the K useful elements in the basis $\mathbf{B}$, i.e., the K significant coefficients in that basis. In Section II.2, it was said that most signals have a sparse representation in a well chosen basis, therefore having L non-zeros entries. An ABS strategy therefore tries to search for these L entries using $K \geq L$. The following section presents the general framework of an ABS strategy with some examples of ABS-based SPC.

II.4.1 Acquisition/restoration in the ABS framework

Finding the sparse coefficients in a basis $\mathbf{B}$ is easy when the whole image is known. One can simply compute $\widetilde{\mathbf{f}} = \mathbf{B}\mathbf{f}$ and search the locations of the K significant coefficients. For this, the D coefficients of $\widetilde{\mathbf{f}}$ can be sorted in order of decreasing magnitude [5] and the first K coefficients of the sorted vector are retained. In SPI however, the whole image of the object is unknown and each value of the coefficients in $\widetilde{\mathbf{f}}$ cannot be computed.

Acquisition The principal idea of an adaptive basis scan approach is to acquire first some of the coefficients of the basis and, based on these measurements, predict the next coefficients to sample. Once the new coefficients are added, the total set of measurements can be further analysed to predict again the next elements to sample and so on. Hence, the acquisition step of an ABS strategy consists of an iterative process with a prediction technique deciding which are the next coefficients of $\widetilde{\mathbf{f}}$ that should be sampled, i.e., which coefficients are *predicted* to be significant.

Let us note J the maximum number of iterations and $j \in [1, J]$ the iteration index. The set of predicted significant coefficients is noted $\mathcal{I}$:

$$\mathcal{I} = \left\{ i \in [1, D] \quad \text{s.t.} \quad \tilde{f}_i \text{ is significant} \right\} \tag{II.17}$$

The set $\mathcal{I}$ is therefore constructed with the J iterations with subsets noted $\mathcal{I}^{(j)}$ so that

$$\bigcup_{j=1}^{J} \mathcal{I}^{(j)} = \mathcal{I} \quad \text{and} \quad \bigcap_{j=1}^{J} \mathcal{I}^{(j)} = \varnothing \tag{II.18}$$

with

$$\text{card}\,(\mathcal{I}) = \sum_{j=1}^{J} \text{card}\left(\mathcal{I}^{(j)}\right) = \sum_{j=1}^{J} K^{(j)} = K. \tag{II.19}$$

5. Value of the coefficient taken in absolute value.

Note that the cardinality of $\mathcal{I}$ depends on the metric employed to judge if $\tilde{f}_i$ is significant or not and is detailed in the next section. The non-acquired coefficients are neglected and set to 0, i.e., $\tilde{f}_i = 0 \quad \forall i \notin \mathcal{I}$.

The formulation of an ABS acquisition scheme for SPC can be expressed by algorithm 1 where $\bigoplus_{l=1}^{L} \mathbf{1}_l$ denotes the concatenation of the L vectors $\mathbf{1}_l$.

Algorithm 1 Adaptive Basis Scan acquisition

Initialization : Set $\widetilde{\mathbf{f}} = \mathbf{0} \in \mathbb{R}^{D\times 1}$ so that $\forall i \in [1, D] \quad \tilde{f}_i = 0$
for $j = 1$ **to** J **do**
1. Compute $\mathcal{I}^{(j)}$ with the chosen prediction method and set $K^{(j)} = \text{card}\left(\mathcal{I}^{(j)}\right)$
2. Compute $\mathbf{P}^{(j)} = \bigoplus_{i\in\mathcal{I}^{(j)}} \mathbf{b}_i$ with $\mathbf{b}_i$ the i-th row of $\mathbf{B}$
3. Acquire $\mathbf{m}^{(j)} = \mathbf{P}^{(j)}\mathbf{f}$ with the SPC
4. Update $\widetilde{\mathbf{f}}$:
    for $k = 1$ **to** $K^{(j)}$ **do**
    4.1. Set $i = \mathcal{I}_k^{(j)}$ where $\mathcal{I}_k^{(j)}$ is the k-th value of $\mathcal{I}^{(j)}$
    4.2. Set $\tilde{f}_i = m_k^{(j)}$
    end for
end for

Restoration During the ABS acquisition presented in algorithm 1, $\widetilde{\mathbf{f}}$ is partially filled with some coefficients that were predicted to be significant, i.e., for coefficients at index $i \in \mathcal{I}$. The image $\mathbf{f}$ can therefore simply be restored as in the basis scan scheme, i.e.,

$$\mathbf{f} = \mathbf{B}^{-1}\widetilde{\mathbf{f}} \qquad \text{or} \qquad \mathbf{f} = \sum_{j=1}^{J}\sum_{k=1}^{K_j} m_k^{(j)}\mathbf{p}_k^{(j)}. \tag{II.20}$$

Fig. II.5 gives the general framework of the adaptive idea that, compared to the nonadaptive scheme of Fig. II.1, adds a prediction step performed J times.

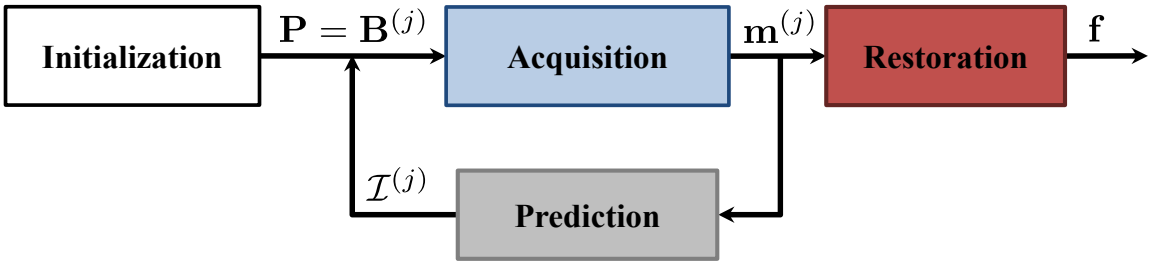

FIGURE II.5 – Framework of an adaptive single-pixel imaging acquisition strategy.

II.4.2 Examples of ABS-based SPC

ADS In Deutsch *et al.* (2009), it was proposed to use a Haar[6] wavelet basis with an adaptive technique referred to as *adaptive direct sampling* (ADS). The authors considered a father-son

6. Such a wavelet is well adapted to the ON/OFF technology of SLM since the patterns only have [-1,0,1] values.

relationship between wavelet coefficients based on the tree structure of the wavelet decomposition (Mallat, 1989; Shapiro, 1993; Mallat, 2008). The wavelet decomposition of an image is indeed structured in J levels as can be seen in Fig. II.6 (arrows in colour except the blue ones) and this relationship means that a coefficient at j has four sons at the next scale $j-1$ [7]. In their technique, Deutsch *et al.* employed a thresholding strategy based on the Lipschitz exponent (Mallat, 2008) to predict the relevant coefficients at finer and finer scales. If a father coefficient is found to be significant, then its 4 sons at the next scales are considered for acquisition. The use of the father-son relationship in their strategy is justified by the fact that wavelet coefficients tend to persist through scale, i.e., a significant coefficient at j may have four significant sons at the scale $j-1$.

ADS using dictionaries Similarly to what they had done in 2009 with ADS, the same authors proposed to change their prediction strategy using dictionaries in Averbuch *et al.* (2012). The technique, refereed to as *adaptive direct sampling* using dictionaries, employs statistical modeling of images found in compression algorithms. Discrete probability distributions are estimated and the mutual information between a pair of two wavelet coefficients can be evaluated. A predictor to estimate the absolute value of a wavelet coefficient is also proposed so that this value can be compared to a threshold and the evaluated mutual information to decide whether the coefficient is significant or not.

ADS with red-black tree The ADS strategy with Haar wavelet is derived in Hahn *et al.* (2014) with a threshold-free prediction strategy. Instead, Hahn *et al.* choose the coefficients whose parents have the largest absolute value using an ordered queue implemented by a red-black tree. This particular kind of binary tree [8] allows for a somewhat self-adapting approach that does not sample coefficients up to a certain detail level. Overall, this overcomes the choice of thresholds that can impact the quality of the restored image in ADS if they are badly chosen. A demonstration for hyperspectral imaging using Haar wavelet is proposed.

EWT-ACS Dai *et al.* reported an ABS strategy in 2014 refereed to as *extended wavelet trees adaptive compressed sampling* (EWT-ACS). This approach is closed to ADS as the technique is derived from the Haar wavelet and makes use of the father-son relationship. The difference lies in a more refined thresholding strategy showed to outperform ADS (Deutsch *et al.*, 2009). This strategy not only uses the father-son relationship but also the sibling relationship. This information, depicted in Fig. II.6 (arrows in blue), links the information between wavelet coefficients at the same scale since it comes from the same area of the image. In addition, Dai *et al.* show that there is some redundancy in the sampled SPC measurement when Haar is considered and some acquisitions are not necessary to get certain wavelet coefficients. This allows them to further compress the number of measurements for a same number of sampled wavelet coefficients.

Guided coefficients In the recent works of Huo *et al.* (2017), the strategy of EWT-ACS (Dai *et al.*, 2014) in the Haar domain is derived using what the authors call guided coefficients. These ele-

7. We take the convention of arranging scales in a decreasing order from J to $j=1$ with $J \geq 1$.
8. Particular type of containers to store data and mostly employed to implement dynamic sets.

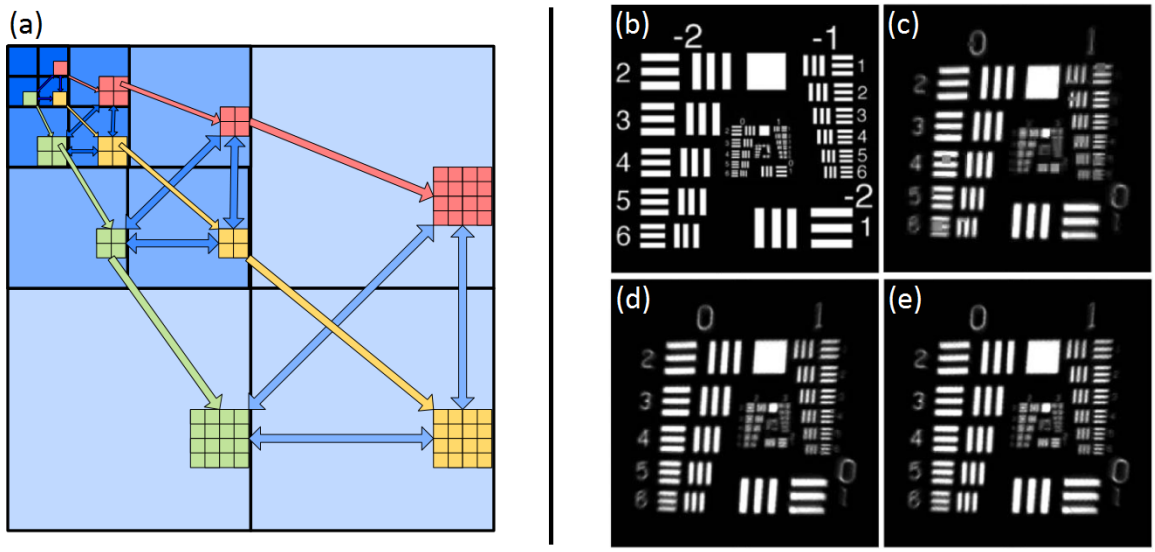

FIGURE II.6 – Wavelet tree and results of EWT-ACS acquisitions. (a) Structure of the wavelet tree, (b) ground truth image, SPC acquisitions with EWT-ACS for a compression rate of (c) 90%, (d) 67% and (e) 58%. Images extracted and adapted from Dai *et al.* (2014).

ments correspond to some unsampled sibling coefficients in EWT-ACS which are localized by a same-scale prediction method based on thresholding. They further show that Dai *et al.* did not completely make use of the redundancy using Haar wavelet to compute the wavelet coefficients. Overall, their technique needs less measurement for a same image quality compared to EWT-ACS by sampling more efficiently the significant Haar elements.

II.4.3 Pros and cons

Advantages The most notorious advantage of an adaptive basis scan approach regards the image restoration that can still be performed as in the basis scan framework with an efficient inverse transform. This allows to use fast algorithms making possible to consider high resolution images for which the reconstruction time does not suffer much since the complexity of these algorithms can reach $O\big(D\log(D)\big)$. The second advantage is the small number of measurements that can be performed. In theory, if the prediction step is perfect, one could obtain $K = L$ and acquire only the L significant coefficients therefore reducing drastically the number of measurements compared to a basis scan approach. In practice, reaching $K = L$ is close to impossible since a perfect prediction without knowing the entire image is hardly achievable.

Disadvantages A disadvantage of an ABS approach is that it does not allow for a perfectly restored image. When the term L-sparse is employed, this is up to a certain threshold. This means that the $D - L$ zero coefficients in a given basis are not exactly equal to zero and they therefore contribute to the final quality of the restored image. Of course most of the features of the restored image come from the L significant coefficients so the prediction step should be good enough to at least sample these coefficients. The latter stage should also be rather rapid since it is applied between two SPC acquisitions and thus increases the overall acquisition time. A fast and efficient prediction step is hence needed.

II.5 Hybrid methods

Some acquisition/restoration schemes for SPI combine the use of compressive sensing, basis scan and/or adaptive basis scan. In this section, we review some of these techniques that we refer to as hybrid methods.

II.5.1 Examples of hybrid techniques

Wavelet combined with CS In Yu *et al.* (2014a), a partial wavelet transform of the scene under view is built from CS measurements. Random patterns (i.e., chosen as in (II.10)) are first sent for acquisition of a coarse image (recovered with TV-minimization) that is one level wavelet transformed. Using a thresholding strategy and the idea of the ADS scheme presented in Section II.4.2, the authors decide the next 4 coefficients to sample at a finer scale. To acquire them, random CS patterns are again considered with a different structure size to get finer information. These steps are then repeated to build the wavelet transform of the image, image that can be quickly obtained by the corresponding inverse transform.

Wavelet combined with Hadamard In Soldevila *et al.* (2015) (see Fig. II.7), several basis scans at different resolutions with Hadamard patterns are performed to build the wavelet transform of the image. The authors start by acquiring a coarse image of the scene with a complete set of Hadamard patterns and a one level wavelet transform is applied on this coarse image. A search for the quadrants with higher density of borders is performed and if one quadrant does not show borders then it is discarded at the next stage. For the remaining quadrants, another basis scan with Hadamard patterns of a finer resolution and localized on the remaining quadrants is performed and so on. This adaptive technique therefore enables to build a wavelet transform to have a fast image restoration.

Noiselets with CS In the works of Zhao *et al.* in 2015, a noiselet sensing matrix (Coifman *et al.*, 2001) is considered. Noiselet functions are related to the wavelet functions in the sense that they can be used in compressive sensing as a sensing matrix to restore a signal having a sparse representation in the wavelet domain [9]. If 100% of the noiselet sensing basis is taken for acquisition, then the inverse noiselet transform can be applied resulting in a fast image recovery. In their design, in order not to sample the $K = D$ coefficients, Zhao *et al.* randomly choose some of the noiselet patterns for acquisition. In this case, a basis pursuit denoising algorithm is applied similarly to what can be done in the CS framework.

Hadamard combined with CS In Radwell *et al.* (2014), a method referred to as *evolutionary CS* is briefly reported. In this technique, the authors use information from a previous frame to decide which Hadamard patterns should be sent to the SLM by simply sorting the measurements of the previous frame in order of magnitude. The K Hadamard patterns corresponding to the highest responses are then chosen for acquisition of the current frame. Among these K patterns, 70%

9. Noiselet functions are for instance perfectly incoherent with the Haar functions.

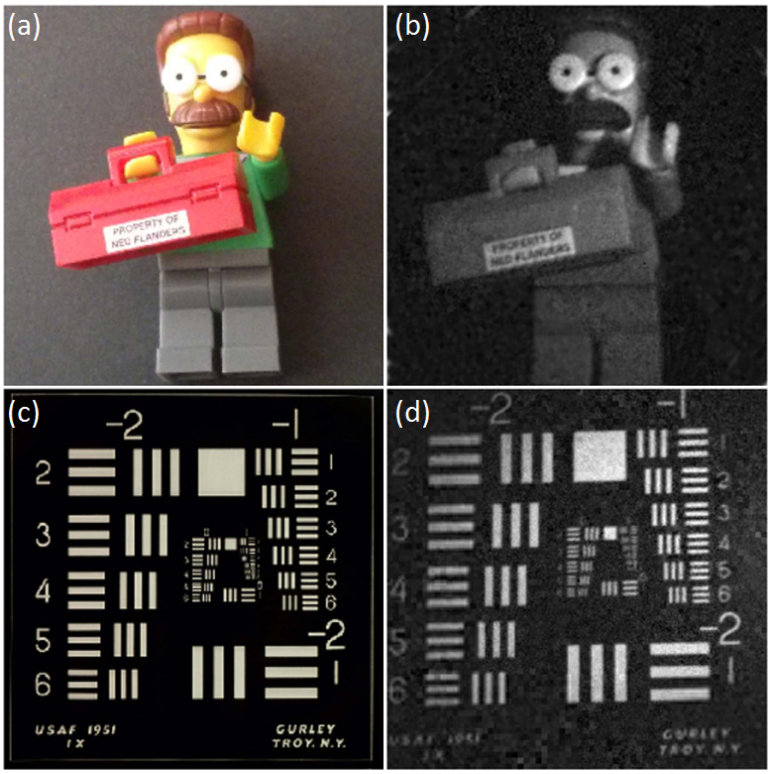

FIGURE II.7 – Example of a hybrid acquisition technique employing wavelets and Hadamard basis. (a) (resp. (c)) Ground truth 256×256 (resp. 512×512) image, (b) (resp. (d)) corresponding SPC image obtained with $K = 88\% \times D$ (resp. $K = 55\% \times D$) measurements using the hybrid method proposed in Soldevila *et al.* (2015). Images extracted and adapted from Soldevila *et al.* (2015).

are retained and 30% are randomized showing a good balance between image quality and the image restoration speed based on the subset of Hadamard patterns. Instead of sampling with the complete Hadamard basis, the authors in Herman *et al.* (2015) and Sankaranarayanan *et al.* (2016) propose to employ Hadamard patterns as patches on the image. For instance, if the scene under view is 768×1024 and 8×8 Hadamard patterns are considered, this results in 64 Hadamard patterns that can be sent to 96×128 positions in the image to obtain 64 images of size 96×128 that are images filtered with the Hadamard patterns. In order not to sample each coefficient, some of the 64 Hadamard patterns scan the full scene but others only scan randomly chosen positions with scrambled Hadamard patterns, i.e., random patterns as in CS-based SPC. In the end, a TV-minimization algorithm can be used to restore the image of the scene under view.

CS with sinusoidal mask Random patterns in illumination are considered in Torabzadeh *et al.* (2017) along with a *spatial frequency domain imaging* (SFDI) technique. To perform SFDI, the light composed of 3 different LEDs is modulated by a linear stage with a sinusoidal mask before reaching the DMD. Several images corresponding to different phase-shifted sinusoidal projections are classically recovered using a CS algorithm. A reflecance image can finally be estimated using temporal frequency domain analysis.

Adaptivity in CS In the context of CS, it is worth noting that adaptivity have also been examined out of the scope of SPI. Some authors argued that the benefit is rather small (Donoho, 2006) while

others claimed an improvement of the measurements accuracy (Davenport *et* Arias-Castro, 2012; Malloy *et* Nowak, 2014) and/or that the number of measurements can be reduced (Indyk *et al.*, 2011). Moreover, CS with non-uniform sampling has recently been considered in Petrovici *et al.* (2016) where the authors select samples in the contour vicinity.

II.5.2 Pros and cons

For a given hybrid technique, it entails both pros and cons of the techniques reported earlier in this chapter that it combines. Below are given some examples of advantages and disadvantages of some hybrid approaches for SPI.

Advantages The works of Yu *et al.* (2014a) and Soldevila *et al.* (2015) allow for a fast image recovery since only an inverse wavelet transform is needed. These methods are partially *adaptive* in the sense that the locations of the patterns to send to the SLM are decided based on previous measurements. However the set of patterns (CS for Yu *et al.* (2014a) and Hadamard for Soldevila *et al.* (2015)) is the same regardless of the object as opposed to an ABS strategy. In Zhao *et al.* (2015) it is claimed that employing deterministic noiselet matrices for acquisition instead of the random patterns involved in CS yields better results. The *evolutionary CS* of Radwell *et al.* (2014) allows to dispose of the reconstruction algorithm of CS by employing a sort of partially random basis scan approach based on data collected from a previous frame. Image restoration is therefore faster and video applications are within reach.

Disadvantages In the design of Soldevila *et al.* (2015), if an object falls into a quadrant without touching a border, this quadrant will be discarded for acquisition and no information about this object will be collected. Furthermore, the basis scan with Hadamard acquires in someway insignificant wavelet coefficients since whole quadrants are acquired. This induces a higher number of samples (see Fig. II.7) compared to what can be achieved using an adaptive basis scan approach. The sampling of insignificant coefficients also happens in the strategy of Yu *et al.* (2014a) that employs CS patterns instead of Hadamard patterns to sample coarse images. The approaches described in Yu *et al.* (2014a); Herman *et al.* (2015); Sankaranarayanan *et al.* (2016) and Torabzadeh *et al.* (2017) are computationally demanding for the image restoration step since they are based on CS recovery algorithms.

II.6 Conclusion

This chapter reported the acquisition and restoration schemes found in the literature for acquisitions of images using a single-pixel imaging device. These are mainly divided into four approaches whose main features are summarized in table II.1.

The compressed sensing approach is efficient since it requires few measurements K (about L for a L-sparse signal in a given basis). However, the heavy computational cost of the restoration process oriented researches towards faster image recovery schemes. Basis scan strategies are a

Approach	**Adaptivity**	**Patterns**	**# of patterns K**	**Image restoration**
Compressed Sensing	No	Random	$L < K \ll D$	ℓ_1/TV minimization
Basis Scan	No	Basis	$L < K \leq D$	Inverse transform
Adaptive Basis Scan	Yes	Basis	$L \leq K \ll D$	Inverse transform
Hybrid	Yes/no	Random/Basis	$L < K < D$	ℓ_1/TV or inverse transform

TABLE II.1 – Comparison of the main characteristics of the four major categories of acquisition/restoration schemes for SPI.

solution since they benefit from fast inverse transform, which allows for an almost instant image recovery. This approach is yet not practical due to the large number of measures that is required (i.e., the number D of pixels of the desired image). To fill this gap, adaptive basis scan techniques have been proposed. The number of measurements can be as low as in the CS paradigm while having a straightforward image recovery. Finally, hybrid methods combine features of the three strategies.

Overall, the *adaptive basis scan* strategy is very attractive since it permits to reduce both the number of measurements, i.e., acquisition time, and the restoration time. This is the reason why such an approach is considered in this thesis that is reported in Chapter IV.

The end of this chapter marks a rupture with the bibliography in single-pixel imaging presented at the hardware (Chapter I) and software (Chapter II) levels and the contributions of this thesis reported in the following chapters. Before detailing the adopted adaptive technique, the employed experimental setups on which the developed techniques have been tested are presented in the next chapter.

CHAPTER III

EXPERIMENTAL SYSTEMS

Contents

CHAPTER III

EXPERIMENTAL data acquisition are essential to the design of new algorithms as it allows to validate and/or adjust the developments. Most algorithms rely on assumptions on a system which work in theory. However, when moving to experimental acquisitions, these relying assumptions can be proved wrong. This is especially true in the case of SPI where some experimental constraints limit the applicability of certain techniques [1].

This chapter describes the two employed experimental systems since the proposed techniques of this thesis are tested experimentally. One is the optical setup existing at the Politecnico di Milano to which some improvements were made to control the different devices. The second system is a new setup that was implemented at the CREATIS laboratory. The hardware design of these systems are presented as well as the softwares to control them and perform SPC measurements with an *adaptive* approach.

The system of the Politecnico was described in Rousset *et al.* (2017a) and in Rousset *et al.* (2017b) for time-resolved measurements.

III.1 Politecnico di Milano setup

Most of the experiments presented in the following chapters were obtained at the Politecnico di Milano where a single-pixel camera setup is available. This setup was initially designed to perform fluorescence tomographic imaging (D'Andrea *et al.*, 2010; Ducros *et al.*, 2013, 2016) using a DMD for structured illumination and a CCD instead of the single-point detector. A second DMD was then added along with a single-point detector to obtain the SPC setup schematized in Fig. III.1.

The contributions of this thesis on this particular system are twofold. First, a spectrometer was added to the already existing time-resolved SPC in order to obtain multispectral time-resolved measurements. Second, a way to control the different devices with an *adaptive* strategy was implemented within the existing programs.

III.1.1 Setup overview

Light source The experimental setup at the Politecnico di Milano is composed of a supercontinuum pulsed white laser source. Two options are possible for the source. The first option is the

1. These constraints are addressed in Chapter V.

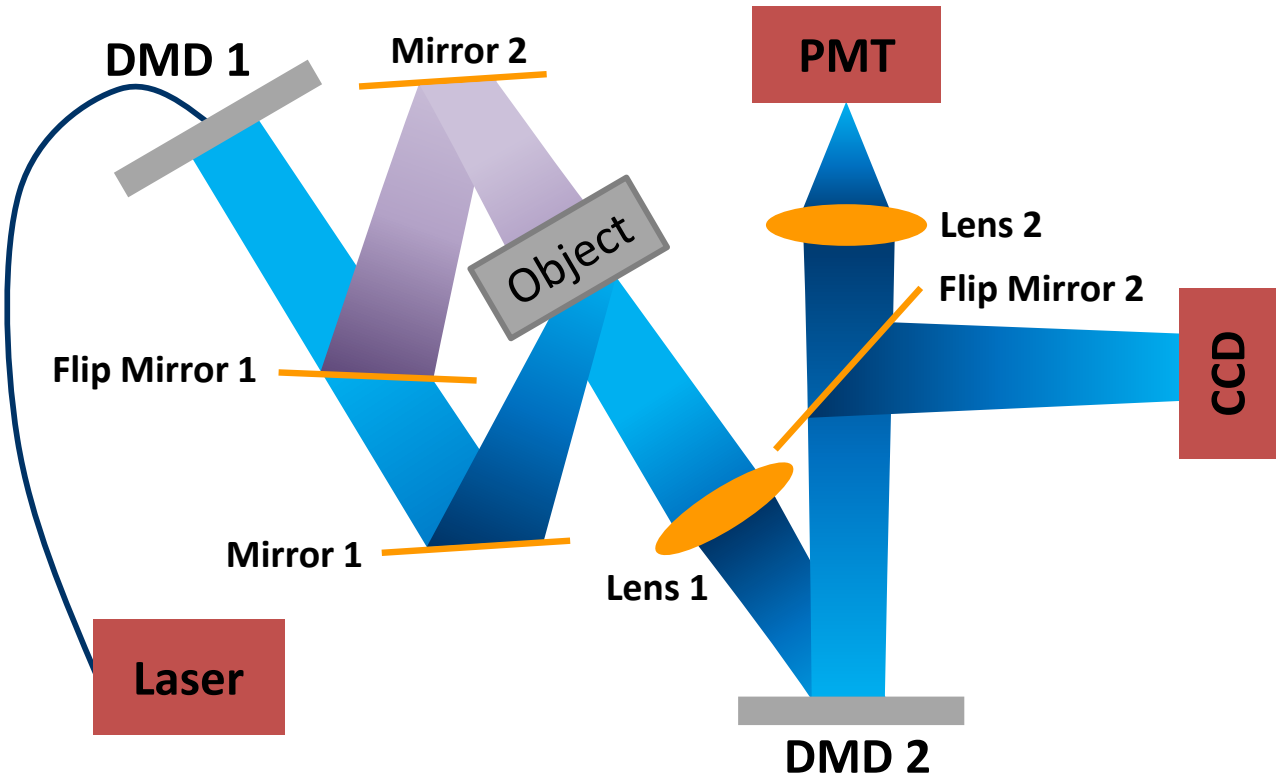

FIGURE III.1 – Experimental setup at the Politecnico di Milano.

SC-450 from Fianium and the second is the SuperK Extreme EXW-12 from NKT Photonics. Both have adjustable repetition rates up to 80 MHz and visible power up to 1200 mW. The object being usually illuminated in a certain spectral band, a bandpass filter (ThorLabs) is added on the laser path when the SC-450 is employed. If the other laser is used, a tunable wavelength filter (SuperK Select, NKT Photonics) is coupled to the laser to choose one or several[2] spectral bands.

Light modulation A first 768 × 1024 DMD (DLP7000-V7001, Vialux GmbH) is employed for illumination of the imaged object. The light can brighten the object either in transmittance or reflectance thanks to a set of mirrors (mirror 1, 2 and flip mirror 1). The image of the object is then formed on a second 768 × 1024 DMD (DLP7000-V7001, Vialux GmbH) via the first lens (lens 1, $f = 60$ cm). This particular geometry with two DMDs permits to either modulate the light in illumination (DMD 1) or detection (DMD 2). If the first (resp. second) DMD is used for modulation, then the pattern on the second (resp. first) one is a completely white pattern[3]. For each of these DMDs, it is possible to load 8-bits patterns. This is performed by the DMD software (ALP Controller Suite, Vialux GmbH) which splits each 8-bit patterns and assigns to them a particular display time on the DMD which is a multiple of a power of 2 so as to recreate the 8-bit pattern. Further explanations about this are given in Appendix A. Although two DMDs are present in this setup, note that in the experiments proposed in the next chapters, DMD 1 always displays a white image so as to obtain a uniform illumination of the object. The modulation is hence performed on DMD 2 only.

2. Up to eight.
3. The DMD is therefore equivalent to a mirror.

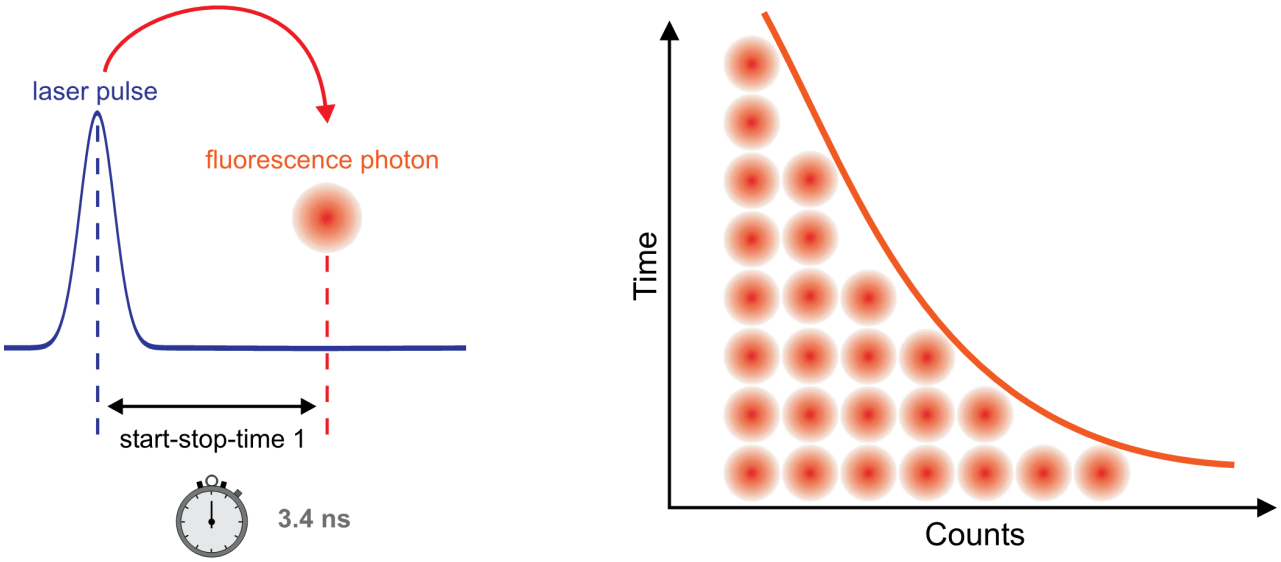

FIGURE III.2 – Principal of a photon counting (TCSPC) board. The board measures the time-of-flight of each photon thanks to the sync with the pulse of the laser. A histogram of the number of photons for different time channels is finally built. Images extracted and adapted from Wahl (2014).

Detection Finally, the light reflected from the second DMD can be imaged either on a 16-bit cooled CCD (Versarray 512, Princeton Instruments) or a single point detector thanks to the second flip mirror (flip mirror 2). The SPD consists of a long-working-distance objective 10 × /0.25 (noted lens 2 in Fig. III.1), which focuses the light onto an optical fiber. The light exiting the fiber is finally collected by a PMT (HPM-100-50, Becker & Hickl GmbH).

III.1.2 Time-resolved measurements

In order to obtain a time-resolved system, a *time-correlated single photon counting* (TCSPC) board (SPC-130 or SPC-630, Becker & Hickl GmbH) is connected to the PMT. Such a device is synchronized with a pulsed laser so that the TCSPC board can assess the time-of-flight of each of the detected photons (Fig. III.2-(left)). Depending on the assessed time-of-flight, the board updates the number of counts in the corresponding time bin. This process is repeated for each photon reaching the board and allows to construct the histogram of the photons' time of flight, i.e., it gives the number of photons detected in T time channels (Fig. III.2-(right)).

The time step that can be achieved with a TCSPC mostly depends on the employed detector. In our setup, a time step of about 3 ps per time channel can be reached for $T = 4096$ channels. Instead of the single scalar measurement by a classical SPC, a vector of size T is now directly obtained when one pattern is sent to the SLM. This results in the possibility of restoring one image per time-channel [4].

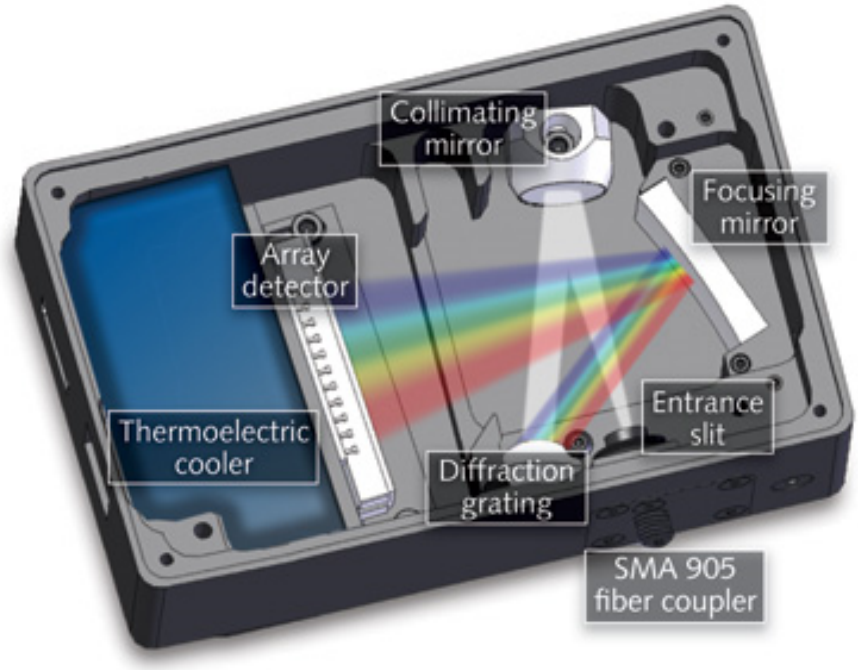

FIGURE III.3 – Example of a spectrometer and its components. Image extracted from http://www.laserfocusworld.com.

III.1.3 Multispectral measurements

Multispectral measurements can be easily performed by the SPC replacing the single-point detector by a spectrometer. The principle is schematized in Fig. III.3. The spectrometer is usually composed of a slit coupled to the fiber where the light comes from. That light is then collimated on a mirror before being dispersed at different angles thanks to a grating. Finally, a second focusing mirror sends the different light rays to an array of Λ single-point detectors.

In our system, the array of detectors is a $\Lambda = 16$-channel PMT (PML-16-1, Becker & Hickl GmbH). Then, the detector is still coupled to the TCSPC board (SPC-630, Becker & Hickl GmbH) that allows to get one time-of-flight histogram for the Λ spectral channels. For this, the TCSPC is employed in its routing mode which permits to determine in which of the Λ detectors a photon was detected. Overall, the simple scalar measurement of a classical SPC system becomes a vector measurement of size $(\Lambda \times T)$ for one pattern sent to the SLM [5].

III.2 CREATIS setup

A simpler experimental setup was built at the CREATIS laboratory during this thesis in order to validate the tools developed in Chapter V. To our knowledge, except for the work of Studer *et al.* dating back to 2012, no SPC platform is available in France. This recently built setup is outlined in Fig. III.4.

4. The mathematical formulation of such acquisitions is formalized in Chapter VI.
5. This mathematical formulation is also formalized in Chapter VI.

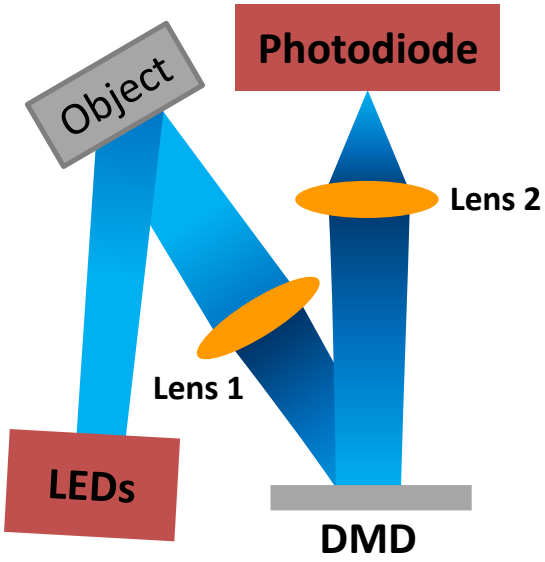

FIGURE III.4 – Experimental setup at CREATIS.

Light source The experimental setup at the CREATIS laboratory is composed of a white LED array (LIUCWHA, ThorLabs) for illumination of the object. A wheel with absorptive filters of different optical densities (NEXXB, ThorLabs) is placed in front of the LED array to control the illumination intensity (parameter N_0 introduced in (II.5)).

Light modulation The image of the object is formed by the lens 1 ($f = 75$ mm) on the SLM plane. The latter is a 768×1024 DMD (DLP700-V7001, Vialux) able to load 8-bits patterns.

Detection The light exiting the DMD converges onto the sensitive area of a photodetector (PDA36A-EC, ThorLabs) by means of lens 2 ($f = 25$ mm). The detector is finally coupled to an analog-to-digital converter (USB-6210, National Instruments).

III.3 Software control

As mentioned in the conclusion of Chapter II, an *adaptive* approach is considered in this thesis, which means that the patterns sent to the SLM are chosen based on previous measurements. A communication between the control of the instruments using Labiew and the adaptive algorithm in Matlab is hence needed. This section details the Labview software to control the SPC and the main features of the Matlab algorithm before giving an operation mode to implement an automatic feedback between the two programs.

III.3.1 Labview for instrumentation

As is often the case for optical and electronic devices, they can be controlled through Labview. During this PhD, an easy-to-use and intuitive application was therefore implemented to command the DMD, the CCD and the single-point detector (PMT+TCSPC at Polimi or photodiode+ADC at CREATIS). The graphical user interface allows to perform acquisitions manually by

tuning the main parameters :

- Path of the folder containing the patterns;
- Number of DMD patterns to send;
- DMD refresh rate;
- Integration time Δt of the detector;
- Frame rate of the CCD if the CCD is employed;
- ADC sampling frequency;
- Path of the folder where the measurements are saved;
- Name of the measured data set.

Note that the power N_0 of the light source is controlled directly from the laser (Polimi setup) itself or by using a special absorptive filter in front of the LED array (CREATIS setup).

Once the parameters have been set, one can manually start a sequence of measurements : the software reads the first pattern from the given folder, loads it on the DMD which launches the measure during Δt and the data is finally stored in the given saving folder. The second pattern is then automatically read and so on until reaching the number of patterns that was set on the user interface. In addition, the software shown in Fig. III.5, displays the pattern that is currently loaded on the DMD as well as the current measurement.

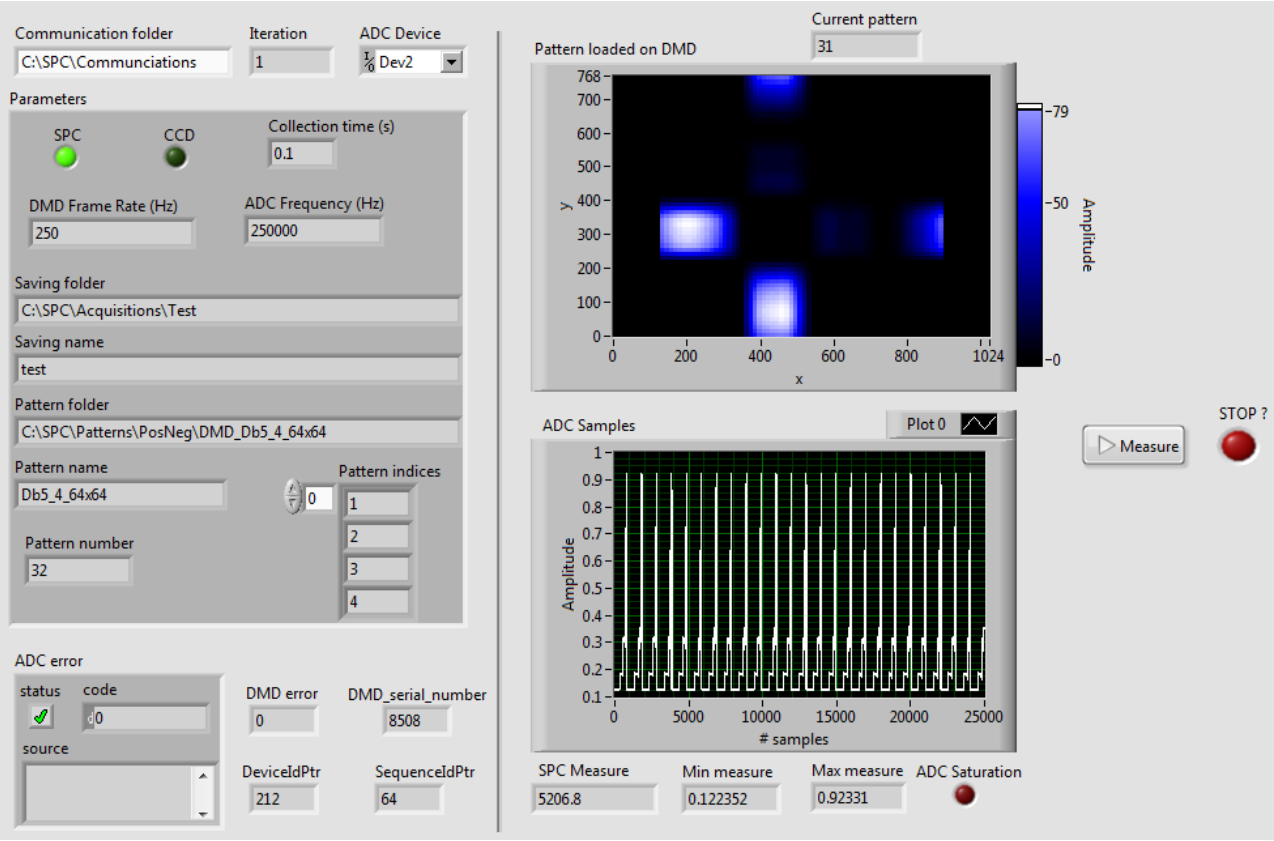

FIGURE III.5 – Graphical user interface of the Labview software to control the different instruments.

III.3.2 Matlab for data processing

Matlab is employed to create the patterns, implement the acquisition and restoration techniques by processing the data saved by the Labview software. Some parameters are also tuned in the Matlab script :

- Number of iterations J if an *adaptive* scheme is considered;
- Path of the folder where the measurements are stored;
- Name of the acquired data set;
- Pattern type/basis;
- Total number of patterns, i.e., compression rate;
- Path of the folder where the patterns are stored;
- Parameters of the acquisition/reconstruction algorithm.

Once some measurements have ben performed by the Labview software, Matlab can start processing them to either restore an image or decide the next measurements to be performed.

III.3.3 Matlab/Labview communication

The two programs presented in the previous two sections work independently and should be started manually one after the other to perform a complete set of measurements and restore an image. In order to further implement an *adaptive* scheme for acquisition/restoration, a Matlab/Labview communication was put in place so to have automatic feedbacks between the two softwares. If we look at the list of parameters that were given for both programs, it can be seen that some are redundant. A choice was therefore made to only tune all the necessary parameters from Matlab. In other words, in our final implementation, Matlab is the master and Labview is the slave since it follows Matlab's orders.

The general framework of this implementation is outlined in Fig. III.6 where two different computers are employed, one to control the instruments with Labview and another one with Matlab for the processing. The operation works as follows :

1. The user set all the needed parameters through Matlab. In particular, three folders are created on a common network, the pattern and measurement folders and a communication folder. The value j (iteration index) is set to 1.
2. The path to the *Communication folder* is set in the Labview interface.
3. Matlab and Labview programs are manually launched in any order. If Labview is started first, it goes in an infinite loop (i.e., wait mode) waiting for Matlab.
4. Matlab creates the necessary patterns on the *Pattern folder* and a parameter file called *Parameters_j.txt* is written in the *Communication folder*. Once this is done, a file *Matlab_done.txt* is created and Matlab enters its wait mode.

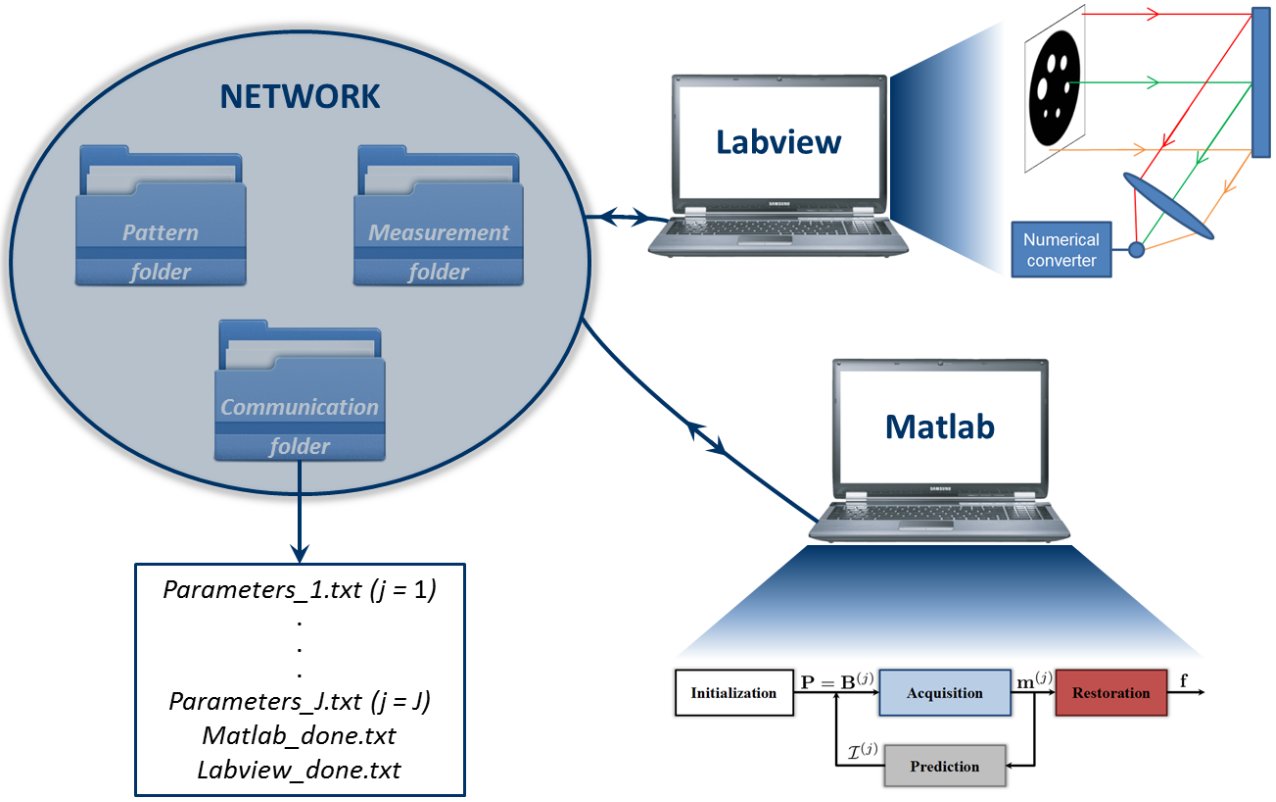

FIGURE III.6 – Scheme of the communication implemented between Matlab and Labview.

5. In its infinite loop, Labview tries to open *Matlab_done.txt*. If this opening fails, Labview stays in its loop. Once the file is created by Matlab, Labview is aware that Matlab has finished its processing and it therefore goes out of its wait mode. The file *Matlab_done.txt* is deleted by Labview.
6. Labview reads the j-th acquisition parameter file and starts the acquisition and pick up the patterns in the *Pattern folder*.
7. Once the measurements are performed, Labview saves them in the *Measurement folder* and a file *Labview_done.txt* is created on the *Communication folder*.
8. Matlab, in its wait mode tries to open *Labview_done.txt*. If this opening fails, Matlab stays in its loop. Once the file is created by Labview, Matlab is aware that Labview has finished the measurements and it therefore goes out of its wait mode. The file *Labview_done.txt* is deleted by Matlab.
9. Matlab performs the data analysis from the measurements in *Measurement folder* according to the chosen acquisition/restoration scheme. It hence decides the next patterns to send for acquisition with the corresponding parameters for the iteration $j = j+1$.
10. Steps 4 to 9 are repeated until $j = J$.

The advantage of such a communication process is that it can be done from two different computers as long as they can access to a common network. This allows to remotely control the instrumentation from another room that the laboratory where the optical setup is present. Note that this implementation can also be done using only one computer running both programs without the use of folders on a network but local folders instead.

III.4 Conclusion

This chapter presented the experimental setups that are employed for the acquisition of experimental data in the next chapters. The setup at the Politecnico di Milano is very complete as it implements a multispectral time-resolved single-pixel camera. The object can also be illuminated in reflection or transmission which enables to consider different applications. At CREATIS, the newborn setup consists in a basic SPC implementation though the only of its kind in France [6]. For both setups, a Labview program permits to control the optical instruments while Matlab is employed for data processing. A communication between the two softwares is possible using a common network and writing of different files. A possible improvement would be to write everything in *C/C++* in order to gain time on both sides. For instance, in the acquisition side in Labview, if the collection time at the detector is set to $\Delta t = 1$ s, a single acquisition is actually around 1.2 s due to the reading of the pattern, initialization of the DMD, etc. A cleaner implementation that would prepare the next acquisition during the previous one could allow to be closer to 1 s, saving 20% of time.

As mentioned at the end of Chapter II, *adaptive basis scans* strategies are very effective acquisition/restoration schemes in terms of both number of patterns and image restoration time. The setups and software described in this chapter allow to implement the proposed ABS approach reported in the following chapter.

6. To the best of our knowledge.

CHAPTER IV

ADAPTIVE BASIS SCAN BY WAVELET PREDICTION

Contents

CHAPTER IV

ADAPTIVE acquisitions for single-pixel imaging exploit the set of previously obtained measurements to decide the next SLM patterns for a new set of measurements. In particular, as it was highlighted in Chapter II, *adaptive basis scan* (ABS) schemes are powerful since the number of measurements can be rather small and quick image recovery techniques are available.

In this chapter, we report our novel ABS strategy that we refer to as *adaptive basis scan by wavelet prediction* (ABS-WP). Some of the material of this chapter comes from two conferences proceedings, *IEEE EMBC 2015* (Rousset *et al.*, 2015) where a slightly different prediction strategy was reported and *IEEE ISBI 2016* (Rousset *et al.*, 2016) where a comparison with CS was given. It also mostly contains an article published in *IEEE Transactions on Computational Imaging* in 2017a (Rousset *et al.*, 2017a).

IV.1 Introduction

In most ABS schemes, wavelet basis are often employed since most images are known to have a sparse representation in the wavelet domain and to recover the image, fast inverse transform algorithms are available (Mallat, 2008). These are the main reasons why wavelets have been and always are important in compression algorithms such as JPEG2000 (Taubman *et* Marcellin, 2001). The ABS schemes proposed in the literature and detailed in Chapter II with wavelet basis show two main drawbacks. The first one is that these techniques usually employ thresholding which is image-dependent and the algorithms are therefore not so easy to tune. The second limitation regards the employed wavelet; experimental acquisitions have only been demonstrated for Haar's wavelet [1] which is not necessarily the best wavelet to draw the best compression ratio out of it depending on the image.

In this chapter, we propose an entire framework for single-pixel imaging using our new ABS technique ABS-WP. Our approach comprises two main characteristics. First off, we report a threshold-free prediction strategy based on the non-linear wavelet approximation. The second characteristic is the possibility to employ any desired wavelet for acquisition. We show that other wavelets than Haar's can provide an improved image quality. To begin with, the wavelet transform is detailed before reporting our acquisition and prediction strategy. The conditions in which the experiments were performed are then reported as well as the results on simulated and experimental acquisitions. ABS-WP is compared to the conventional CS framework and another ABS strategy before discussing about the results.

1. Haar's wavelet is well suited for the DMD ON/OFF states.

IV.2 Wavelet transform

The wavelet transform is a very powerful and popular tool (Taubman *et* Marcellin, 2001; Mallat, 2008). This transform allows one to interpret the signal as a superposition of oscillating functions called wavelets, localized both in time and frequency. Since we are interested in the wavelet transform of 2D images with dyadic wavelet, our image $\mathbf{f}$ is now considered as a $D = N \times N$ vector with N a power of 2. We describe in this section the wavelet decomposition with the corresponding equations leading to the obtainment of the different wavelet coefficients via filter banks. A simplification of the notation is then giving before showing that the non-linear approximation of the wavelet transform leads to extremely good image quality with few coefficients.

IV.2.1 Wavelet decomposition

The so-called scaling function $\phi : \mathbb{R} \to \mathbb{R}$ and mother wavelet function $\psi : \mathbb{R} \to \mathbb{R}$ are defined as follow :

$$\phi(x) = \sqrt{2} \sum_{i \in \mathbb{Z}} h_i \phi(2x - i) \qquad \psi(x) = \sqrt{2} \sum_{i \in \mathbb{Z}} g_i \phi(2x - i) \tag{IV.1}$$

with $\mathbf{h}$ a low-pass filter and $\mathbf{g}$ a high-pass filter with coefficients chosen such that $g_i = (-1)^i h_{1-i}$, $i \in \mathbb{Z}$. The multiresolution analysis (Mallat, 1989) with dyadic wavelets is made possible by means of the functions $\phi_{j,i}$ and $\psi_{j,i}$, corresponding to dilated and translated version of ϕ and ψ :

$$\phi_{j,i}(x) = 2^{-j/2} \phi\left(2^{-j}x - i\right) \qquad \psi_{j,i}(x) = 2^{-j/2} \psi\left(2^{-j}x - i\right) \tag{IV.2}$$

The function $\phi_{j,i}(x)$ is the function $\phi(x)$ dilated of a scale factor 2^j with a translation of $2^j i$. The set of functions $\phi(2x - i)$ generates a subspace V_{-1} that includes functions of another resolution that the ones from the set V_0 generated by $\phi(x - i) : V_0 \subset V_{-1}$. This inclusion of subspaces can be generalized and is the key to the multiresolution analysis.

When image processing is considered, equations (IV.1) and (IV.2) can easily be generalized to the 2D case considering separable functions. Such a function is defined as $\mathbf{\Phi} : \mathbb{R}^2 \to \mathbb{R}$ so that $\Phi(\mathbf{x}) = \Phi(x_1, x_2) = \phi(x_1)\phi(x_2)$ with $\mathbf{x} = (x_1, x_2)^\top$. The tensor product between two 1D-subspaces generates four functions, the scaling function $\mathbf{\Phi}_{j,\mathbf{i}}$ and three wavelet functions $\mathbf{\Psi}^1_{j,\mathbf{i}}$, $\mathbf{\Psi}^2_{j,\mathbf{i}}$ and $\mathbf{\Psi}^3_{j,\mathbf{i}}$ defined as :

$$\begin{cases} \Phi_{j,\mathbf{i}}(\mathbf{x}) = \phi_{j,i_1}(x_1)\phi_{j,i_2}(x_2) \\ \Psi^1_{j,\mathbf{i}}(\mathbf{x}) = \phi_{j,i_1}(x_1)\psi_{j,i_2}(x_2) \\ \Psi^2_{j,\mathbf{i}}(\mathbf{x}) = \psi_{j,i_1}(x_1)\phi_{j,i_2}(x_2) \\ \Psi^3_{j,\mathbf{i}}(\mathbf{x}) = \psi_{j,i_1}(x_1)\psi_{j,i_2}(x_2) \end{cases} \quad \text{with} \quad \mathbf{i} = (i_1, i_2)^\top. \tag{IV.3}$$

Using those functions, any image $\mathbf{f}$ can be decomposed into approximation and detail coefficients. These coefficients are obtained as projections of the image on one of the four functions. Some are called approximation coefficients, $\boldsymbol{\beta}_j$, since they result from a low-pass filtering. The

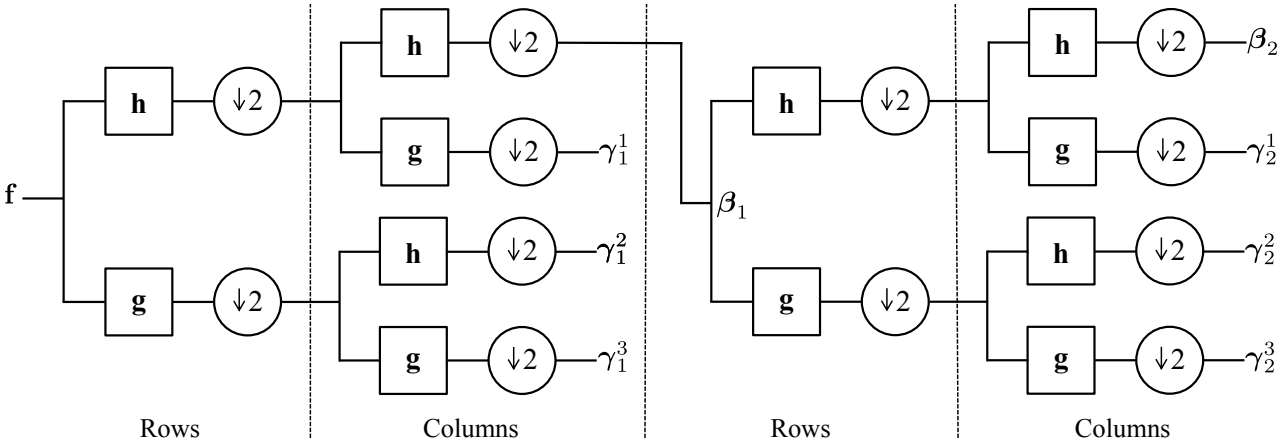

FIGURE IV.1 – Filter banks representation of a 2-level wavelet decomposition.

others, $\boldsymbol{\gamma}_j^o$, represent the vertical ($o = 1$), horizontal ($o = 2$) or diagonal ($o = 3$) coefficients after a high-pass filtering. It can be shown that the coefficients can be calculated as follow :

$$\begin{cases} \beta_{j,\mathbf{i}} = \langle \mathbf{f}, \boldsymbol{\Phi}_{j,\mathbf{i}} \rangle = \sum_{m_1 \in \mathbb{Z}} \sum_{m_2 \in \mathbb{Z}} h_{m_1-2i_1} h_{m_2-2i_2} \beta_{j-1,\mathbf{m}} \\ \gamma^1_{j,\mathbf{i}} = \langle \mathbf{f}, \boldsymbol{\Psi}^1_{j,\mathbf{i}} \rangle = \sum_{m_1 \in \mathbb{Z}} \sum_{m_2 \in \mathbb{Z}} h_{m_1-2i_1} g_{m_2-2i_2} \beta_{j-1,\mathbf{m}} \\ \gamma^2_{j,\mathbf{i}} = \langle \mathbf{f}, \boldsymbol{\Psi}^2_{j,\mathbf{i}} \rangle = \sum_{m_1 \in \mathbb{Z}} \sum_{m_2 \in \mathbb{Z}} g_{m_1-2i_1} h_{m_2-2i_2} \beta_{j-1,\mathbf{m}} \\ \gamma^3_{j,\mathbf{i}} = \langle \mathbf{f}, \boldsymbol{\Psi}^3_{j,\mathbf{i}} \rangle = \sum_{m_1 \in \mathbb{Z}} \sum_{m_2 \in \mathbb{Z}} g_{m_1-2i_1} g_{m_2-2i_2} \beta_{j-1,\mathbf{m}} \end{cases} \tag{IV.4}$$

with $\mathbf{m} = (m_1, m_2)^\top$. The multiresolution analysis allows one to study the image at different scales, a small value of j will give fine details whereas a bigger value gives coarser details. The coefficient computation in (IV.4) shows two convolutions and two decimations, one of each applied on the rows of the image and then on the columns. This can be sketched as in Fig. IV.1 using filter banks.

Given the decimation by two on the rows and the columns, the discrete wavelet of an image $N \times N$ can be arranged in a $N \times N$ image as can be seen in Fig. IV.2-(a). With orthogonal wavelets (Daubechies, 1992), one can perfectly recover the image from its coefficients using the inverse wavelet transform :

$$\mathbf{f} = \sum_{\mathbf{i} \in \mathbb{Z}^2} \beta_{J,\mathbf{i}} \boldsymbol{\Phi}_{J,\mathbf{i}} + \sum_{o=1}^{3} \sum_{j=1}^{J} \sum_{\mathbf{i} \in \mathbb{Z}^2} \gamma^o_{j,\mathbf{i}} \boldsymbol{\Psi}^o_{j,\mathbf{i}} \tag{IV.5}$$

where J is the chosen decomposition level with $1 \leq J \leq \log_2(N) = R$. When $J = R$, the approximation is reduced to only one coefficient.

IV.2.2 Notation simplification

For the sake of simplicity, in the rest of this thesis, we note $\widetilde{\mathbf{f}} \in \mathbb{R}^{D \times 1}$ the wavelet coefficients of $\mathbf{f}$ for a given wavelet. The vector $\widetilde{\mathbf{f}}$ hence regroups the different coefficients of (IV.4) and represents $\mathbf{f}$ in the wavelet domain (see Fig. IV.2-(c)). The value $j = 1 \dots J$ represents the scale at which the

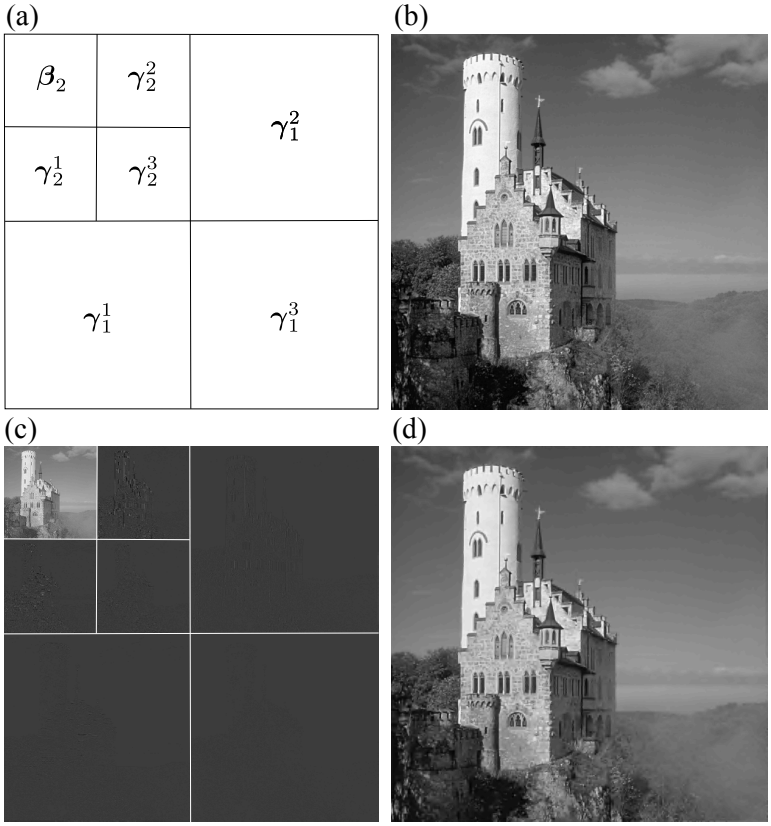

FIGURE IV.2 – Example of a 2-level wavelet transform on a 512 × 512 pixels image. (a) Disposition of the wavelet coefficients, (b) ground truth image of the Lichtenstein castle, (c) 2-level wavelet transform of (b) and (d) recovered image with only 10% of the largest coefficients in (c).

image $\mathbf{f}$ is observed with J the decomposition level. A location is specified by the vector $\mathbf{i}$ so that

$$\mathbf{i} = (i_1, i_2)^\top \in \left\{1, \ldots, 2^\ell\right\}^2 \quad \text{with} \quad \ell = R - j \tag{IV.6}$$

The wavelet transform of $\mathbf{f}$ depicted by $\widetilde{\mathbf{f}}$ is given by :

$$\widetilde{\mathbf{f}} = \mathbf{B}\mathbf{f} \tag{IV.7}$$

with $\mathbf{B} \in \mathbb{R}^{D \times D}$ an orthonormal operator (Daubechies, 1992). Each element of $\widetilde{\mathbf{f}}$ may be fully identified and located by its unique triplet k :

$$k = \{o, j, \mathbf{i}\} \tag{IV.8}$$

where $o = 0$, 1, 2 or 3 corresponds to the approximation, vertical, horizontal and diagonal coefficients, respectively. In addition, each row of $\mathbf{B}$ corresponds to a unique triplet k. The image $\mathbf{f}$ can be perfectly recovered from $\widetilde{\mathbf{f}}$, similarly to (IV.5), using the inverse wavelet transform :

$$\mathbf{f} = \mathbf{B}^{-1}\widetilde{\mathbf{f}} \tag{IV.9}$$

IV.2.3 Non-linear approximation

The wavelet transform was shown to give sparse signals, allowing one to discard many coefficients at the recovery step. The best possible approximation of the wavelet transform is the

non-linear one where a number $K \ll D$ of the largest coefficients are retained among all scales. The other elements are set to 0 and the image restoration using (IV.5) shows excellent image quality (Mallat, 2008). It therefore simply consists of hard-thresholding the elements of $\widetilde{\mathbf{f}}$ for a given threshold γ to give the non-linear approximation image $\mathbf{f}_\gamma$ of $\mathbf{f}$:

$$\mathbf{f}_\gamma = \mathbf{B}^{-1}\widetilde{\mathbf{f}}_\gamma \quad \text{with} \quad \left(\widetilde{\mathbf{f}}_\gamma\right)_n = \begin{cases} \left(\widetilde{\mathbf{f}}\right)_n & \text{if} \quad \left|\left(\widetilde{\mathbf{f}}\right)_n\right| \geq \gamma \\ 0 \quad \text{otherwise.} \end{cases} \tag{IV.10}$$

This approximation is non-linear [2] since the set $\Gamma = \left\{n \,:\, \left|\left(\widetilde{\mathbf{f}}\right)_n\right| \geq \gamma\right\}$, with $\text{card}(\Gamma) = K$, changes with the image $\mathbf{f}$. Figure IV.2 shows an example of a non-linear approximation with only 10% of the largest coefficients. This approximation is non-linear in the sense that the set of retained coefficient is different for each image.

IV.3 ABS-WP method : prediction strategy

IV.3.1 Idea

Our method ABS-WP aims to record a non-linear approximation of the wavelet transform. Our goal is to acquire the significant wavelet coefficients and it is therefore wanted to predict the triplets k for each of these elements. The endgame consists in filling the matrix $\mathbf{P} = \left(\mathbf{p}_1, \ldots, \mathbf{p}_k, \ldots, \mathbf{p}_K\right)^\top$ of (II.5) with the rows of $\mathbf{B}$ corresponding to the predicted triplet k, noted $\bar{k}$. When a SPC acquisition is considered, the whole wavelet transform of the image is unknown. Hence, the idea is to perform several non-linear approximations iteratively on the different scales of the wavelet decomposition.

IV.3.2 Strategy

For the sake of simplicity and to better understand the sizes of the images involved in our ABS-WP scheme, the vector notation of the image $\mathbf{f} \in \mathbb{R}^{D\times 1}$, $D = N \times N$, is temporarily replaced by the matrix notation $\mathbf{F} \in \mathbb{R}^{N\times N}$. Similarly, $\widetilde{\mathbf{F}} \in \mathbb{R}^{N\times N}$ represents the wavelet transform of $\mathbf{F}$.

Our strategy can be decomposed into five steps. Step 1 is the initialization where a predefined set of patterns is sent for acquisitions. Steps 2 to 4 predict the next coefficients to sample, i.e., the next wavelet patterns to send to the SLM. Step 5 consists in the experimental acquisition of the predicted significant wavelet elements :

1. The approximation image $\mathbf{A}_j$ at the coarse scale $j = J$ is completely acquired. This is a $2^\ell \times 2^\ell$ image with $\ell = R - j$. To be precise, this approximation image is obtained with the corresponding set of patterns at the coarse wavelet scale J. This can therefore be seen as a basis scan sampling the $2^{2\ell}$ coefficients.
2. $\mathbf{A}_j \in \mathbb{R}^{2^\ell \times 2^\ell}$ is oversampled by a factor of two using an interpolation operator [3] $\mathcal{S}$. This leads

2. The linear approximation of the image is the one retaining the first K coefficients of $\widetilde{\mathbf{f}}$, i.e., taking all elements of the wavelet decomposition starting from the largest scale J to $J-1$ and so on.

3. The influence of the choice of the interpolation operator is reported in the results.

to the high resolution image $\mathbf{H}_j = \mathcal{S}(\mathbf{A}_j) \in \mathbb{R}^{2^{\ell+1}\times 2^{\ell+1}}$.

3. This image $\mathbf{H}_j$ is one-level wavelet transformed to give $\widetilde{\mathbf{H}}_j \in \mathbb{R}^{2^{\ell+1}\times 2^{\ell+1}}$. This provides the *predicted* wavelet detail coefficients at scale j.
4. To obtain the triplets $\bar{k}$ of the largest predicted elements, a non-linear approximation is performed by retaining a percentage p_j of the largest detail coefficients of $\widetilde{\mathbf{H}}_j$. This leads to the obtainment of the predicted significant elements and their corresponding predicted triplets $\bar{k}$.
5. The coefficients are finally experimentally acquired by employing the patterns matching the rows of $\mathbf{B}$ corresponding to the triplets $\bar{k}$.

The above description works for one scale of the wavelet transform but can easily be extended to the other scales. For the step 1, instead of the whole sampling of the coarse image at scale $j = J$, the approximation image $\mathbf{A}_j$ is retrieved by inverse wavelet transforming the coefficients acquired so far. Steps 2 to 5 are unchanged, only a different value of p_j is used for each scale giving the overall set of percentages

$$\mathcal{P} = \{p_J, p_{J-1}, ..., p_1\}. \tag{IV.11}$$

This strategy hence alternates between acquisition of the wavelet coefficients on the real image (i.e., experimentally) and prediction using an interpolation technique. A sketch of the algorithm of ABS-WP is given in Fig. IV.3 where the number for each step corresponds to the above steps. The image $\mathbf{F}$ (or $\mathbf{f}$) is obtained by (IV.5) by inverse wavelet transforming the elements acquired up to scale $j = 1$.

IV.3.3 Compression rate

The whole acquisition at scale $j = J$ of the approximation image $\mathbf{A}_j$ leads to the sampling of $n_0 = 2^{2L} = 4^L$ wavelet coefficients with $L = R - J$. Then, a percentage p_j of the strongest predicted detail coefficients is acquired. Hence, the number of measurements at each scale j is given by

$$n_j = 3 \times 4^{R-j} \times p_j \tag{IV.12}$$

The total number of elements n acquired for each decomposition level is therefore controlled by modulating the set of percentages $\mathcal{P}$ in (IV.11). Using (IV.12), it can be shown that

$$n = 4^L \left[1 + 3 \sum_{j=1}^{J} 4^{J-j} p_j \right] \tag{IV.13}$$

The compression rate (CR) is defined as

$$\mathrm{CR} = 1 - \frac{n}{D} \tag{IV.14}$$

which corresponds to a normalized quantity ranging from 0 to 1.

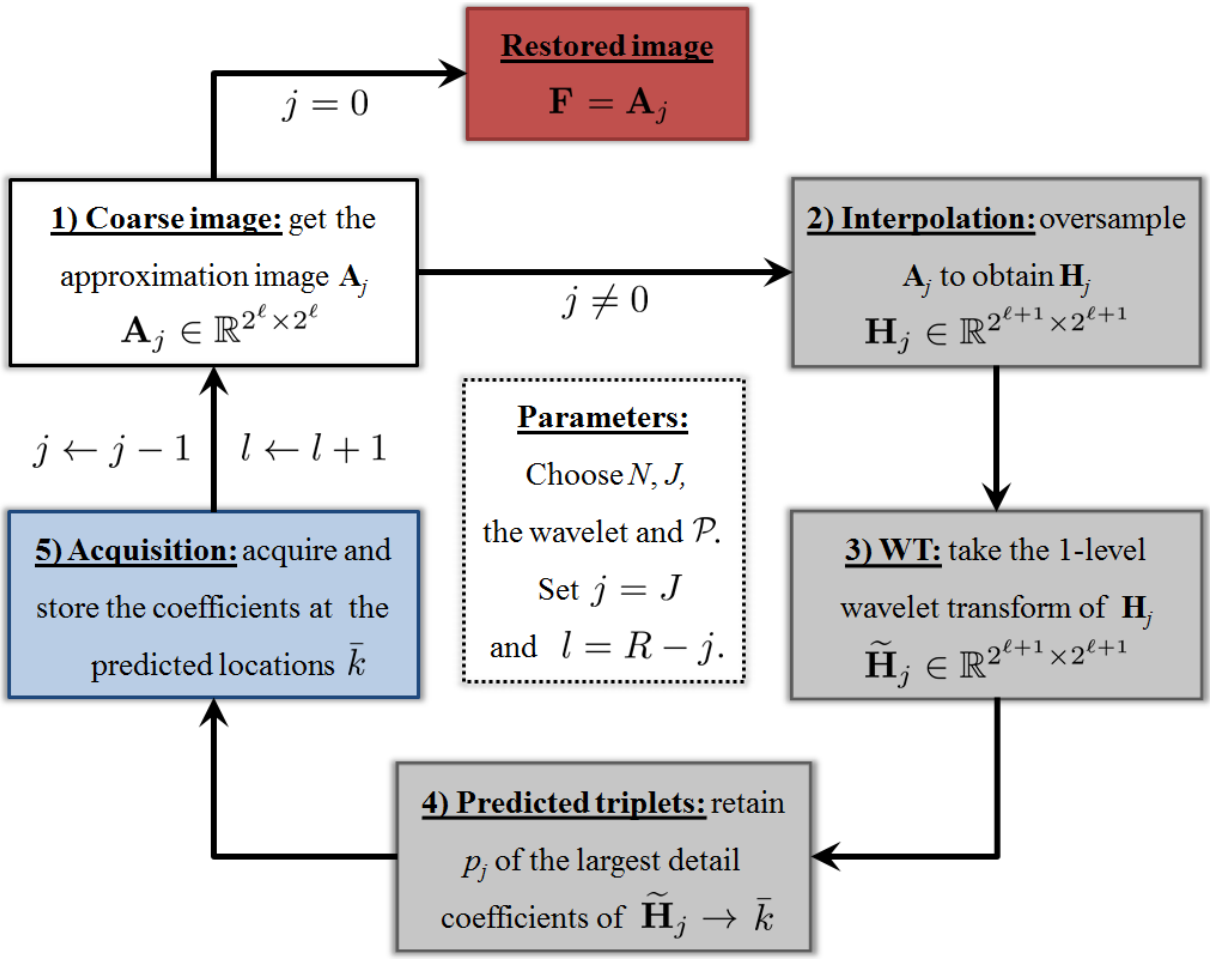

FIGURE IV.3 – Summary of the acquisition and prediction strategies of our technique *Adaptive Basis Scan by Wavelet Prediction*. The blue box corresponds to the acquisition step, the gray boxes to the prediction and the red one is the image recovery. White boxes regards initialization or general processes.

IV.4 Experiments overview

IV.4.1 Pattern creation

Generation To perform the acquisition, the set of patterns $\mathbf{P} = \left(\mathbf{p}_1, \ldots, \mathbf{p}_k, \ldots, \mathbf{p}_K\right)^\top$ that will be sent to the DMD have to be generated. One pattern can be obtained as :

$$\mathbf{p}_k = \mathbf{B}^{-1}\mathbf{v}_k \tag{IV.15}$$

with $\mathbf{v}_k$ a unit vector that is chosen from the canonical basis $\{\mathbf{e}_k\}$. In practice, one can create a null image and set to 1 the only pixel located at the triplet k. Taking the inverse wavelet transform of this image leads to the corresponding pattern to acquire the wavelet coefficient located at the triplet k.

Two practical problems however arise to send such images to any SLM : the created patterns have floating values and present both negative and positive elements that cannot be physically implemented on any SLM.

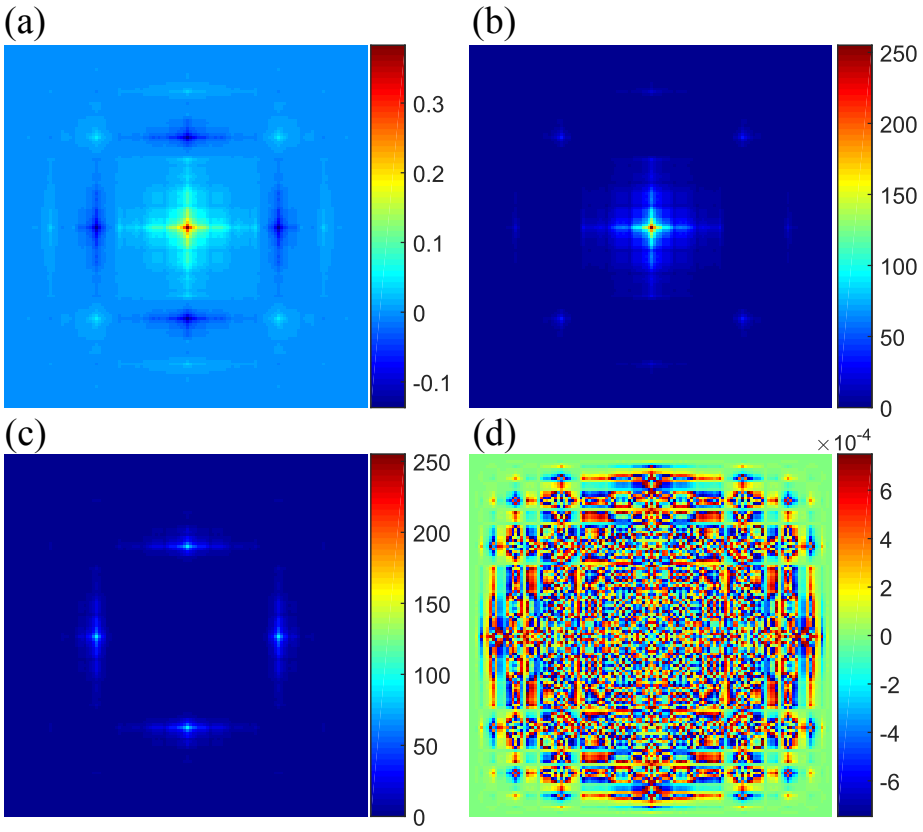

FIGURE IV.4 – Before and after quantization of one of Le Gall's wavelet pattern for $b = 8$ bits. (a) Real wavelet pattern $\mathbf{p}_k$, (b) positive quantized part $\widehat{\mathbf{p}}_k^+$, (c) negative quantized part $\widehat{\mathbf{p}}_k^-$ and (d) quantification error pattern $\widehat{\mathbf{e}}_k$.

Positive/negative separation To deal with the positivity problem [4], $\mathbf{p}_k$ is separated in its positive and absolute negative parts so that $\mathbf{p}_k = \mathbf{p}_k^+ - \mathbf{p}_k^-$. Equation (II.4) being linear, the final measurement m_k can be obtained numerically as

$$m_k = m_k^+ - m_k^- \tag{IV.16}$$

with

$$m_k^+ = \left(N_0 \mathbf{f}^\top \mathbf{p}_k^+ + \alpha\right)\Delta t \qquad \text{and} \qquad m_k^- = \left(N_0 \mathbf{f}^\top \mathbf{p}_k^- + \alpha\right)\Delta t \tag{IV.17}$$

two experimental measures by the SPC. Note that in (IV.16), the additive component $\alpha\Delta t$ is canceled by the subtraction which is convenient since it flaws the measurement [5].

Quantization In order to use any kind of wavelet and to deal with the floating values of the patterns, an uniform quantization is performed to convert the patterns to b-bits patterns, 2^b being the employed dynamic range of the SLM [6]. The following transform is applied to each pattern to realize this uniform quantization :

$$\widehat{\mathbf{p}}_k = \left\lfloor \frac{1}{q_k}\mathbf{p}_k \right\rfloor \qquad q_k = \frac{\max\left(|\mathbf{p}_k|\right)}{2^b - 1} \tag{IV.18}$$

4. This problem is detailed in the next chapter with a proposed technique to deal with this constraint.
5. Again, the next chapter gives more detail about this problem.
6. For a DMD, b ranges from 4 to 12 depending on the model.

where $\lfloor . \rfloor$ corresponds to a rounding operation. Since the patterns $\mathbf{p}_k$ depend on the triplet k of (IV.8), the quantization factor noted q_k also depends on the same triplet. Figure IV.4 displays an example of pattern quantization using Le Gall (CDF 5/3) biorthogonal wavelet (Gall *et* Tabatabai, 1988; Cohen *et al.*, 1992). This quantization step leads inevitably to an irreversible loss of information which can be depicted by the quantization error pattern $\widehat{\mathbf{e}}_k = q_k \widehat{\mathbf{p}}_k - \mathbf{p}_k$.

If this quantization error can be neglected, the measurement m_k in (IV.16) is obtained numerically by applying the quantization factor to the measures :

$$m_k = q_k \left(\hat{m}_k^+ - \hat{m}_k^- \right) \tag{IV.19}$$

where

$$\hat{m}_k^+ = \left(N_0 \mathbf{f}^\top \widehat{\mathbf{p}}_k^+ + \alpha \right) \Delta t \qquad \text{and} \qquad \hat{m}_k^- = \left(N_0 \mathbf{f}^\top \widehat{\mathbf{p}}_k^- + \alpha \right) \Delta t \tag{IV.20}$$

are two experimental measurements acquired by the SPC. The value of $q_k \Delta t = \Delta t_k$ can also be directly employed as an integration time so as to obtain correctly-scaled measurements (i.e., without post-processing) :

$$m_k^+ = q_k \left(N_0 \mathbf{f}^\top \widehat{\mathbf{p}}_k^+ + \alpha \right) \Delta t = \left(N_0 \mathbf{f}^\top \widehat{\mathbf{p}}_k^+ + \alpha \right) \Delta t_k \quad \text{and} \quad m_k^- = \left(N_0 \mathbf{f}^\top \widehat{\mathbf{p}}_k^- + \alpha \right) \Delta t_k \tag{IV.21}$$

are directly experimentally acquired by the SPC with Δt_k as integration time and the final measurement is numerically computed as in (IV.16).

IV.4.2 Numerical experiments

To perform simulations, images showing different features have been employed. Commonly used in image processing, the well known images of Lena and the peppers have been employed for a test on natural images. An image of vertebral bone tissue of a fetus obtained by optical microscopy and displayed in Fig. IV.5 serves as an indicator for textured images. Fluorescence imaging being a target application, a bioluminescence image of a mouse (Keramidas *et al.*, 2010) superimposed to its ambient light image is finally considered and shown in Fig. IV.6.

Our ABS-WP method is compared to the use of the compressive sensing (CS) presented in Section II.2 which is the reference *nonadaptive* approach. For CS simulations, we directly reconstructed the image $\mathbf{f}$ from the measurements $\mathbf{m}$ using Total Variation (TV) minimization (II.13) via TVAL3 (Li, 2009) as done in Takhar *et al.* (2006) and Duarte *et al.* (2008). Regarding the parameters of such an approach, they were tackled to give the best results in most cases. Among them, anisotropic TV with positivity was employed.

Our results are also compared to the *adaptive* method EWT-ACS proposed by Dai *et al.* and described in Section II.4.2. As a reminder, this *adaptive* technique is derived from Haar's wavelet and a threshold has to be chosen to predict the relevant coefficients to sample. For each of the proposed image and compression rate, this threshold was tackled experimentally to lead to the best possible PSNR [7] of the restored image.

7. Peak signal-to-noise ratio between the reference image $\mathbf{f}$ and image $\mathbf{g}$ defined as $\mathrm{PSNR}(\mathbf{f},\mathbf{g}) = 10\log_{10}\left(\frac{\max(\mathbf{f})^2}{\mathrm{MSE}(\mathbf{f},\mathbf{g})}\right)$ in dB with $\mathrm{MSE}(\mathbf{f},\mathbf{g}) = \frac{1}{D}\sum_{i=1}^{D}(f_i - g_i)^2$.

Noisy simulations are also reported in which the measurements are corrupted by Poisson noise, noise generally present when an optical measurement with photon is considered [8]. Experimentally, this noise affects the number of photons read by the single-point detector, numerically it is hence applied on the two measurements of (IV.21), i.e., this equation becomes

$$m_k^+ = \mathscr{P}\left(q_k\left(N_0\mathbf{f}^\top\widehat{\mathbf{p}}_k^+ + \alpha\right)\Delta t\right) \quad \text{and} \quad m_k^- = \mathscr{P}\left(q_k\left(N_0\mathbf{f}^\top\widehat{\mathbf{p}}_k^- + \alpha\right)\Delta t\right) \tag{IV.22}$$

where $\mathscr{P}$ is the Poisson distribution. Changing N_0 and/or Δt in (IV.22) permits to simulate several levels of noise for a given image $\mathbf{f}$. When the values of N_0 are small, the Poisson noise has indeed a greater effect since less photons are received by the detector.

IV.4.3 Experimental acquisitions

The setup at the Politecnico di Milano described in Section III.1 was employed. It comprised the supercontinuum pulsed white laser source (SC-450, Fianium) followed by a filter with center wavelength at 650 nm for uniform illumination of the object. The one-channel PMT (HPM-100-50, Becker & Hickl GmbH) coupled to the TCSPC board (SPC-130, Becker & Hickl GmbH) is employed as a detector. Only time-resolved measurements are therefore considered in this chapter with the use of the TCSPC. For the given acquisitions however, this information is not exploited, the different measurements in the time channels are integrated (i.e., summed) to give only scalar measurements equivalent to a system with an ADC instead of the TCSPC [9].

Two Jaszczak phantoms commonly used in computerized tomography are chosen as objects. These targets were printed on white paper with a diameter of about 22 mm. Figure IV.7-(a) and Fig. IV.8-(a) display the corresponding experimental CCD image of these targets.

For the two proposed experimental acquisitions, 128×128 pixels patterns were used thus giving 128×128 restored SPC images. In order to use most of the DMD's height in our setup, the patterns were further resized as 640×640 patterns. A box-shaped kernel was employed to perform the resizing operation, meaning that no pixel values other than those in the patterns were added. An area of 5×5 ($640/128 = 5$) DMD mirrors was employed to represent one pixel of the 128×128 pattern in other words. After acquisition, SPC images are compared to their reference CCD image. For visual comparison, the dynamic of the SPC images has been rescaled to the dynamic range of the CCD image.

IV.4.4 Integration time

Regarding the integration time Δt at the detector, it is, in most SPC architecture, only limited by the DMD's frequency. However, as mentioned earlier, a TCSPC board is employed in our setup. The statistics constraints of photon counting of the board restricts the use of the DMD at its highest speed. To work properly while having a correct SNR [10], the board indeed requires integration times of a few hundred milliseconds in standard illumination conditions. The integration

8. Other sources of noise exist but the predominant one is the Poisson noise.
9. The time information is exploited for applications such as fluorescence lifetime imaging in Chapter VI.
10. Signal-to-noise ratio defined as $\text{SNR} = 10\log_{10}\left(\frac{P_{\text{signal}}}{P_{\text{noise}}}\right)$ in dB where P_{signal} (resp. P_{noise}) is the power of the observed signal (resp. noise).

time Δt at the single-point detector, in this particular case, is hence always greater that the integration time without the TCSPC. As a result, Δt was kept constant for each case of the following simulations and experimental results. The different techniques (CS, EWT-ACS or ABS-WP) are therefore fairly comparable for a given number of measurements. Once the set of measurements $\{\hat{m}_k\}$ of (IV.20) were acquired, to obtain correctly-scaled measurements according to (IV.19), they were post-processed with their quantization factor $\{q_k\}$.

IV.5 Results

IV.5.1 Numerical experiments

Influence of the interpolation technique As was mentioned in our acquisition strategy, an interpolation operator $\mathcal{S}$ is employed to predict the locations of the significant coefficients of the wavelet transform. Among many existing interpolation techniques, we tried out the bicubic interpolation (Keys, 1981), the *Fourier zero padding* (FZP) technique, the *new-edge directed interpolation* (NEDI) (Li *et* Orchard, 2001) and the *cycle-spinning wavelet zero padding* method (CS-WZP) (Temizel *et* Vlachos, 2005) for their easy implementation and fast computation time. It is indeed wanted for the prediction to be very fast so that the prediction is as quick as possible. To judge which technique allows one to predict with the best accuracy the coefficient locations, a series of simulations were performed. The produced images can be compared at several points in our acquisition strategy. If we refer to Fig. IV.3, the interpolated image $\mathbf{H}_j$ in point 2 *before* acquisition of the predicted coefficients can be compared to the ground truth high resolution image. The latter image would be the one obtained without prediction but with knowledge of the complete wavelet transform until level j. Then, *after* acquisition of the details in point 5, we can compare the restored approximation image $\mathbf{A}_j$ of point 1 with the same ground truth high resolution image as previously. The two comparisons *before* and *after* acquisition can be done for any scale $1 \leq j \leq J$. These results are summarized in table IV.1 considering the four different test images for a CR of 85% obtained with $\mathcal{P} = \{0.90, 0.80, 0.45, 0.019\}$ and Le Gall's wavelet.

In the rest of this manuscript, ABS-WP is always employed with the bicubic interpolation since table IV.1 shows that this interpolation technique predicts with better accuracy the significant wavelet coefficients and its computation times are very fast.

Influence of the quantization Simulation results on two images showing the quantization effect are presented in table IV.2 with our method ABS-WP using Le Gall's wavelet. One pattern of this particular wavelet can be seen in Fig. IV.4. In these simulations, the wavelet coefficients were computed exactly as they would be by the SPC : using the dot product between the image and the corresponding quantized patterns. The set of percentages employed for these experiment is $\mathcal{P} = \{0.90, 0.80, 0.71, 0.02\}$ giving a CR of 80%.

Image	**Technique**	**PSNR** (dB)								**Time** (s)
		$j = J = 4$		$j = 3$		$j = 2$		$j = 1$ / Global		
		Before	*After*	*Before*	*After*	*Before*	*After*	*Before*	*After*	
Lena	Bicubic	16.92	**34.09**	19.62	**34.10**	22.72	**31.73**	26.25	**29.59**	**0.43**
	FZP	18.00	31.11	20.77	30.07	23.85	28.64	27.00	27.59	**0.43**
(256 × 256)	NEDI	**18.23**	30.32	**21.63**	29.22	**24.26**	28.20	26.97	27.30	6.46
	CS-WZP	18.13	31.45	21.22	31.11	24.25	29.84	**27.80**	28.30	1.02
Peppers	Bicubic	20.16	**37.95**	22.97	**38.60**	26.26	**37.50**	30.44	**34.83**	**0.43**
	FZP	21.19	36.40	24.34	35.46	28.06	33.69	31.93	32.66	**0.43**
(256 × 256)	NEDI	**21.43**	36.19	**25.05**	36.29	**28.44**	33.96	32.09	32.70	6.36
	CS-WZP	21.15	34.91	24.62	34.66	28.28	34.02	**32.10**	32.72	1.00
Bones	Bicubic	18.21	30.86	21.32	**30.72**	24.87	**30.13**	28.52	**30.29**	**0.43**
	FZP	18.33	**31.18**	22.44	30.46	26.30	29.81	**29.77**	29.96	**0.43**
(256 × 256)	NEDI	**19.14**	29.74	**22.72**	28.53	25.87	28.02	28.16	28.34	6.46
	CS-WZP	18.61	30.40	22.59	29.90	**26.40**	29.43	29.55	29.60	1.00
Mouse	Bicubic	20.53	65.77	25.27	66.86	31.38	61.76	37.57	**49.13**	**0.22**
	FZP	**22.95**	53.57	**28.57**	42.21	36.67	45.71	43.40	45.03	**0.22**
(128 × 128)	NEDI	21.41	**76.55**	27.92	**71.97**	35.80	**63.03**	44.90	47.72	1.94
	CS-WZP	22.38	53.30	28.47	54.48	**37.16**	55.14	**46.52**	49.04	0.48

TABLE IV.1 – Effect of the interpolation technique in our ABS-WP method for different test images. Obtained PSNRs *before* and *after* acquisition of the significant predicted coefficients during ABS-WP for different interpolation methods. Le Gall 128 × 128 patterns were employed with a CR of 85%. The computation time given in the last column includes the prediction and restoration of the image.

Influence of the prediction strategy The accuracy of the prediction strategy for our technique ABS-WP and EWT-ACS (Dai *et al.*, 2014) at identifying the significant wavelet coefficients is reported in table IV.3. For each case, since EWT-ACS is derived from Haar's wavelet, it was also employed for our technique. Moreover, the set of percentages for each image in our technique was obtained from EWT-ACS's number of sampled wavelet elements at each scale in order to compare fairly the influence of the prediction. Then, the locations of the true significant wavelet coefficients (obtained from the ground truth images) were compared to the locations of the found coefficients for ABS-WP and EWT-ACS. This leads to the prediction accuracy in percentages in table IV.3.

Image	**PSNR** (dB)					
	$b = 4$	$b = 6$	$b = 8$	$b = 10$	$b = 12$	$b \to \infty$
Bones (256 × 256)	24.73	29.98	30.87	31.18	31.18	31.18
Mouse (128 × 128)	33.20	43.80	47.82	49.18	49.23	49.23

TABLE IV.2 – Quantization effect in ABS-WP for Le Gall's wavelet for a CR of 80% and different number of bits b. The last column is equivalent to simulate the strategy without quantization.

Image	**CR**	**Correctly matched wavelet coefficients** (%)	
		Dai	*ABS-WP*
Bones	80	62	**69**
(256 × 256)	85	59	**65**
Mouse	80	82	**85**
(128 × 128)	85	79	**84**

TABLE IV.3 – Accuracy of the prediction strategy for EWT-ACS (Dai *et al.*, 2014) technique and our ABS-WP framework. The table displays the percentages of the wavelet coefficients that were correctly predicted as significant compared to the true significant wavelet coefficients.

Influence of the acquisition/restoration technique Visual simulated results for CS, EWT-ACS and ABS-WP are given in Fig. IV.5 for the bone image. For our technique ABS-WP, Le Gall's wavelet was employed since, in several cases, it proved to be the most efficient wavelet. Obtained PSNRs for these SPC frameworks at two compression rates are presented in table IV.4 and table IV.5 gives the associated average computation times.

Influence of the image As mentioned earlier, four different test images were considered : Lena and peppers as natural images, a textured image with the bone picture of Fig. IV.5 and a smooth image with the mouse picture depicted in Fig. IV.6. Note that the mouse image is pretty smooth compared to the high-frequency bone image.

Influence of noise The above presented results were conducted in a noise-free setting. Table IV.6 compares the performance of CS, EWT-ACS and ABS-WP strategies considering noisy measurements as given by (IV.22). Figure IV.6-(a) serves as a test image for different levels of noise simulated by several values of N_0 for $\Delta t = 1$ s. A low value of N_0 leads to a low average of photons received by the single-point detector and makes the noise effect greater.

Image	**CR**	**PSNR** (dB)			**Dai's thresholds**
		CS	*EWT-ACS*	*ABS-WP*	
Lena (256 × 256)	80	29.55	29.90	**30.33**	11.52
	85	27.89	28.49	**29.59**	16.63
Peppers (256 × 256)	80	34.70	35.06	**35.35**	7.71
	85	32.96	33.42	**34.83**	11.77
Bones (256 × 256)	80	29.38	30.24	**31.18**	12.89
	85	28.14	28.59	**30.29**	17.61
Mouse (128 × 128)	80	45.36	47.65	**49.23**	385.65
	85	42.18	45.83	**49.13**	851.10

TABLE IV.4 – Obtained PSNRs for different SPC acquisition techniques at two compression rates on several test images in a noise-free setting. The thresholds used for Dai's method are given in the last column. For ABS-WP, Le Gall patterns were employed with $\mathcal{P} = \{0.90, 0.80, 0.71, 0.02\}$ and $\mathcal{P} = \{0.90, 0.80, 0.45, 0.019\}$ to give CRs of 80% and 85%.

Image size	**CR**	**Time** (s)		
		CS	*EWT-ACS*	*ABS-WP*
256 × 256	80	267.37	**0.12**	0.43
	85	213.62	**0.09**	0.42
128 × 128	80	15.50	**0.02**	0.19
	85	13.18	**0.02**	0.18

TABLE IV.5 – Average computation time for the different SPC acquisition techniques for the results of table IV.4. The time includes the image restoration for CI and prediction + restoration for Dai's method and our technique. Acquisition times are not counted since they are the same for each technique (fixed compression rate).

$N_0(ph/s)$	**PSNR** (dB)			
	CS	*EWT-ACS*	*ABS-WP (Haar)*	*ABS-WP (Le Gall)*
58072	38.99	45.72	46.05	**47.20**
43554	39.29	45.61	45.98	**46.88**
29036	39.04	45.48	45.91	**46.54**
14518	38.47	45.31	45.71	**45.90**
5807	37.06	44.72	**45.01**	43.99

TABLE IV.6 – Noisy simulations for different acquisition strategies at a CR of 85% for different values of N_0 on the mouse image of Fig. IV.6-(a). For ABS-WP, the set of percentages used for Haar's wavelet was $\mathcal{P} = \{0.77, 0.42, 0.24, 0.1\}$ and $\mathcal{P} = \{0.90, 0.80, 0.45, 0.019\}$ for Le Gall.

IV.5.2 Experimental acquisitions

Real SPC acquisitions of a Jaszczak target with ABS-WP and CS are presented in Fig. IV.7. In the case of our technique, both Haar and Le Gall wavelets were employed to show the ability of the DMD to handle 8-bits patterns [11].

Figure IV.8 displays acquisitions of another target with our technique and permits to judge the ability of the SPC setup to discern small dots depending on the compression rates. The smallest dots have a diameter of about 1 mm whereas the biggest one is about 3 mm. In our setup, a pixel size of 210 µm was measured which can easily be changed by adjusting optics and/or modify the patterns' size.

IV.6 Discussion

Our ABS-WP acquisition/restoration scheme presented in this chapter was mainly designed to overcome the limits of ℓ_1-minimization based image restoration in the CS framework. Instead, the image is acquired directly in a wavelet basis for which fast inverse transform exist. In addition,

11. The library controlling our DMD model (DLP7000-V7001, Vialux GmbH) can load patterns coded on up to 8-bits.

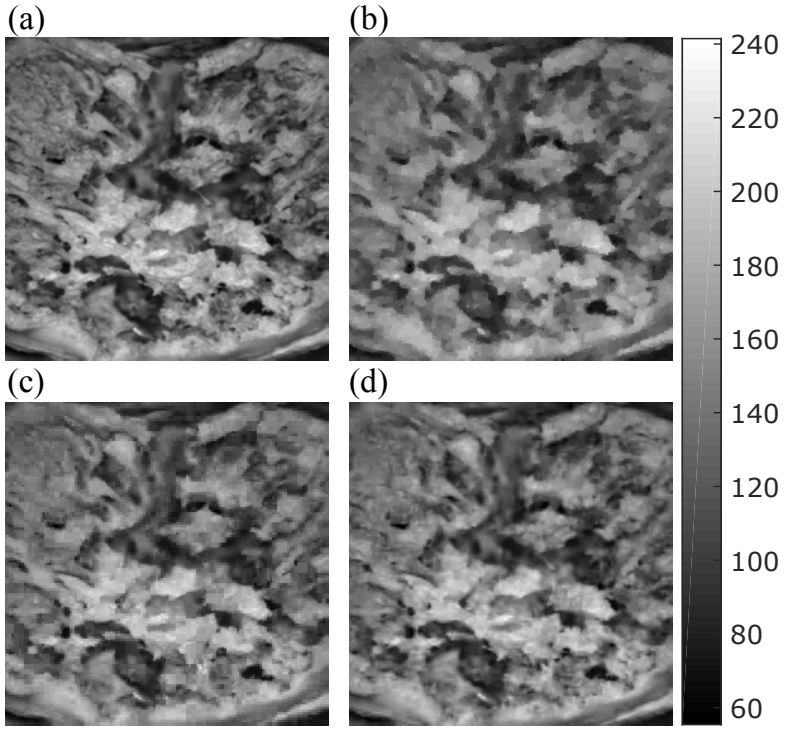

FIGURE IV.5 – Noise-free simulation of different SPC acquisition techniques on a 256 × 256 image of bones with a CR of 80%. (a) Ground truth image, images restored with (b) CS, (c) EWT-ACS method and (d) our ABS-WP technique. The PSNRs and parameters associated with these results are given in table IV.4.

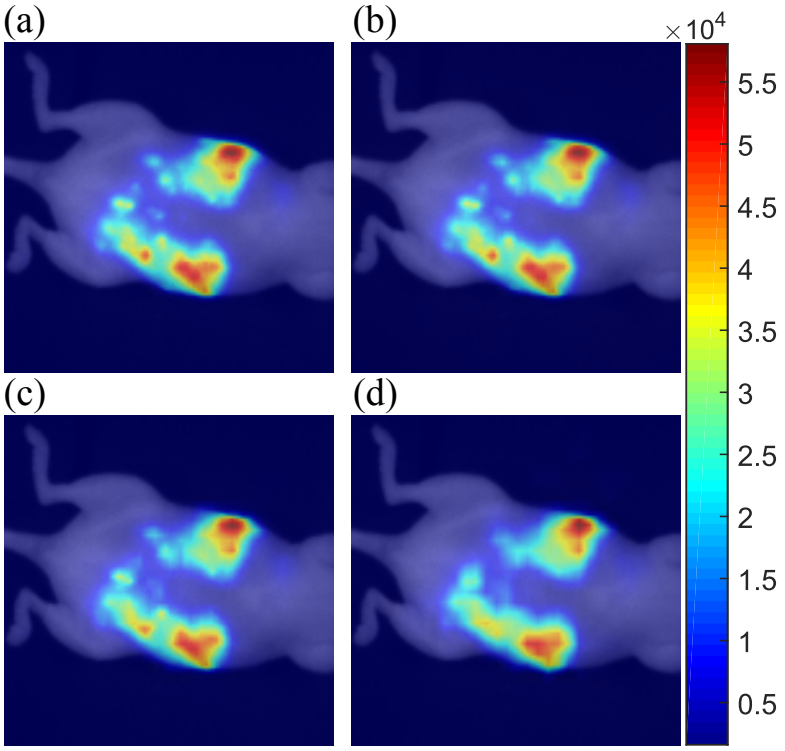

FIGURE IV.6 – Noise-free simulation of our acquisition strategy on a 128 × 128 bioluminescence image of a mouse. The bioluminescence images have been overlaid on the ambient light image of the mouse. (a) Ground truth image, images restored using Le Gall's wavelet for a CR of (b) 90%, (c) 95% and (d) 98%. Respectively, PSNRs compared to the ground truth image are 48.25 dB, 41.48 dB and 35.37 dB.

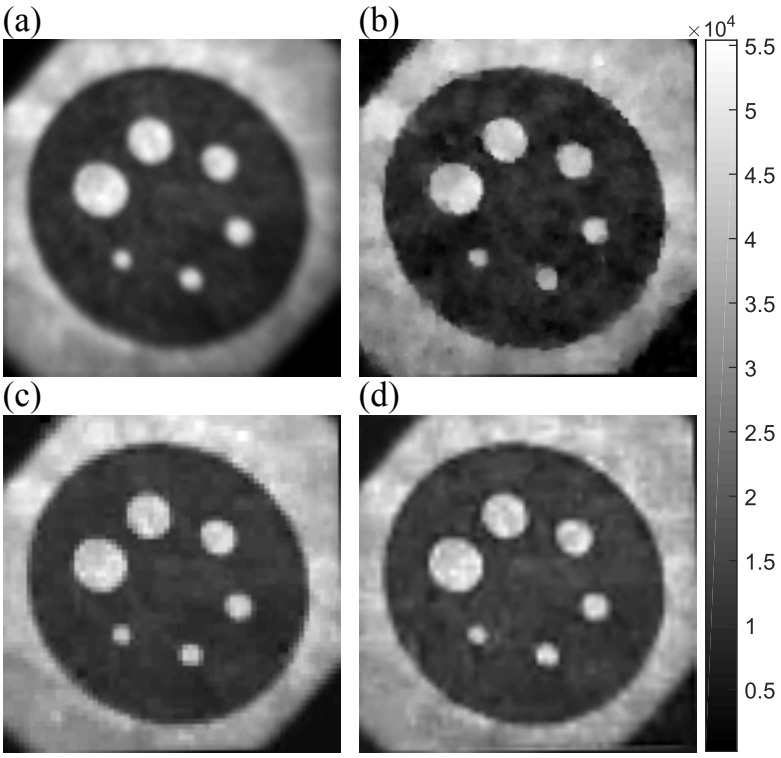

FIGURE IV.7 – Experimental acquisitions with the SPC on the Jaszczak target. (a) Experimental CCD image of the target, recovered 128 × 128 pixels images with a CR of 85% (b) using CS and for ABS-WP with (c) Haar,and (d) Le Gall wavelets. Respectively, the obtained PSNRs compared to the CCD image after registration are 21.20 dB, 21.99 dB and 21.65 dB.

our technique presents the advantage of being threshold-free by employing non-linear approximations [12] as defined in (IV.10). Uniform quantization of the patterns is performed in order to use any possible wavelet to obtain the best possible compression ratio.

By looking at the results of table IV.1, it can be seen that the bicubic interpolation seems to perform the best to predict the significant wavelet coefficients. The second to last column indeed presents the final obtained PSNR of the restored image and is always higher for this interpolation technique. However, it can be noted that, *before* the acquisition of the coefficients, the other three techniques perform better in general. This performance is not abnormal since the NEDI or WZP-CS methods were designed to best interpolate the edges in images and the bicubic interpolation tends to smooth edges. With the latter techniques, we could assume that the locations of the significant coefficients should be better predicted as in general, the highest wavelet coefficients are in the vicinity of the edges (Mallat, 2008). In spite of the smoothness of the bicubic interpolation, it still performs better to locate the researched elements which is why this technique is now considered in the rest of the proposed experiments. Given the endless number of existing interpolation or super-resolution techniques (Park *et al.*, 2003), we can not insure that the bicubic is the best possible method. However, it has the advantage of being extremely fast and parameter-free while providing efficient results.

12. Threshold-free in comparison to other ABS techniques for which a threshold has to be chosen before acquisition. In our ABS-WP framework, using the set of percentages $\mathcal{P}$, a threshold at each scale is automatically chosen.

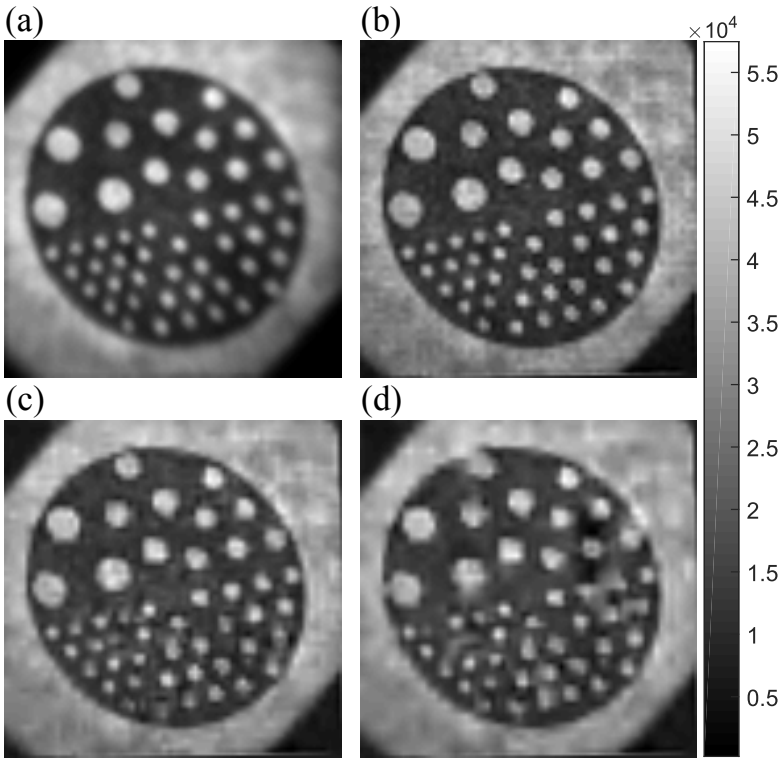

FIGURE IV.8 – Ability of the system to distinguish dots whose diameters range from 1 mm to 3 mm. (a) Experimental CCD image of the target, recovered 128 × 128 pixels images with ABS-WP with Le Gall for a CR of (b) 75%, (c) 85% and (d) 90%. Respectively, the obtained PSNRs compared to the CCD image after registration are 22.35 dB, 21.51 dB and 20.85 dB. A pixel size of 210 µm was measured.

As it was shown in Section II.4.2, when an adaptive basis scan approach is considered, Haar wavelet is often employed (Deutsch *et al.*, 2009; Dai *et al.*, 2014; Averbuch *et al.*, 2012; Yu *et al.*, 2014a; Huo *et al.*, 2017). This is because, up to a scale factor, the patterns have only 0 or 1 and hence the image quality is not impacted by the quantization process. Nevertheless, in the case of our proposed technique ABS-WP with another wavelet, as shown by the results of table IV.2, the quantization impacts the quality of the restored SPC images. For values of $b \leq 10$, the recovered images have indeed a smaller PSNR than the ones restored with the real patterns (results of the last column with $b \to \infty$). The irreversible rounding operation in (IV.18) clearly explains this difference. When $b \geq 10$, the grayscale is extended and the quantization error can be considered as negligible. As mentioned earlier, the quantization factor q_k has an impact on the effective integration time $\Delta t_k = q_k \Delta t$ at the single-point detector. In the proposed experiments in this chapter, Δt was always kept constant and the measurements were post-processed by applying q_k as depicted by (IV.19) and (IV.20). To obtain the best possible SNR, this is not the finest possible solution. The optimum one would be to increase or decrease, according to the pattern and its quantization factor, the integration time. In other words, $\Delta t_k = q_k \Delta t$ would act as the new integration time as in (IV.21).

Looking at the results of table IV.3 giving the prediction accuracy of EWT-ACS (Dai *et al.*, 2014) and ABS-WP, our prediction strategy based on a simple bicubic interpolation performs better at

identifying the true significant wavelet coefficients. These results are provided for the Haar wavelet since EWT-ACS is derived from it. However, the possibility to employ another wavelet in the case of our technique can greater improve the image quality provided that the wavelet was correctly chosen.

In light of the results of table IV.4 where ABS-WP is compared to CS and EWT-ACS, numerically close or better results are achieved by our technique. Visually, as can be seen in Fig. IV.5, the TV-minimization creates some spots/patches in the case of a high-frequency image such as the textured image of the bone. For EWT-ACS, because of the employment of Haar's wavelet, some pixelation is present in the SPC restored image that cannot be seen in our method with Le Gall's wavelet. Computation times of table IV.5 also show the improvement of considering an adaptive basis scan approach. When bigger images are acquired, this improvement is again greater. ABS-WP takes however a little bit more time than EWT-ACS for which only thresholding operations are extremely fast.

For EWT-ACS, the thresholds presented in table IV.4 reveal their image dependency and should be adjusted for each image. In comparison, for ABS-WP and a fixed CR, a common set of percentages $\mathcal{P}$ was employed for each image. Our strategy still recovers good quality images despite the clear difference of the involved imaged in table IV.4. ABS-WP therefore adapts to the image and no threshold should be adjusted. To obtain fairly good set of percentages, they have been learned from several test images. In practice, in simulation one can apply the non-linear approximation of the wavelet transform for a given CR on several images. Then, the number of retained coefficients at each level j can be obtained. Averaging the collected values between the images leads to a good candidate for $\mathcal{P}$. In the case of CS, many parameters have to be tackled for the TV-minimization. Depending on the choice of parameters, the quality of the SPC restored image can dramatically change.

Even with a CR as high as 98%, the results of Fig. IV.6 demonstrate that one can restore an excellent image using ABS-WP for smooth images. For this kind of images, only a few wavelet coefficients are indeed needed to recover the principal features of the image. The decomposition level value J can hence be set closed to the limit $R = \log_2(N)$. In addition, for small values of j, the percentages p_j can be set to 0, i.e., no high-frequency details are needed. This is because smooth images only have very few details and the coarser coefficients can be sufficient enough to restore a good quality image. On the contrary, one should choose high values for p_1 to obtain the finest details in the case of images with high frequency components. Both choices of J and $\mathcal{P}$ are hence linked with the aimed application and the type of object to image.

In a real-world setting, the noisy simulations of table IV.6 show that ABS-WP still perform close or better than CS or EWT-ACS. It is worth noting however that the measurements, in the case of ABS-WP with Le Gall's wavelet, are more rapidly corrupted by noise. This can be explained by the fact that, compared to patterns obtained with Haar, Le Gall's patterns have less elements

whose value is one and so such patterns send less light to the single-point detector. The value of the measurements of (IV.22) are hence bigger for Haar than Le Gall leading to a lower impact of the Poisson noise in the Haar case (last column of table IV.6). If extremely low-light scenarios are considered, one should therefore better use the simple Haar wavelet. In the next chapter, a strategy to modify any wavelet pattern is proposed which reduces the effect of the noise in such cases.

Moving on to the experimental results, a more sophisticated wavelet such as Le Gall's can be used for real acquisition using ABS-WP as proved by the results of Fig. IV.7. It even gives visually better result compared to Haar with a smoother image. The TV-minimization of CS creates, as for the textured image of Fig. IV.5, spots on the restored image. The Haar case of ABS-WP shows some pixelation since p_1 was set to a small value, only few high frequency coefficients were sampled. In our ABS-WP strategy, an important feature therefore regards the choice of the wavelet. Depending on the object to image, some wavelets are better at sensing the scene than others, i.e., they capture the information in fewer coefficients, giving a sparser wavelet transform in one wavelet basis compared to another. For instance if a very smooth object is considered, a Battle wavelet would be much more appropriate than Haar's wavelet and fewer Battle coefficients would be needed compared to using Haar. With ABS-WP, one can choose any wavelet best adapted to the desired application and object to be acquired.

Finally, some insights about the system's possibilities with ABS-WP are provided with the results of Fig. IV.8. In the actual configuration of the setup at the Politecnico di Milano, objects of at least 1 mm can be discerned provided that the CR is well chosen. For instance, the small dots are all visible for a CR of 80% and 85% but not for 90% since not enough elements were sampled to restore the dots. A great feature of an adaptive basis scan approach and ABS-WP is that several passes of the algorithm can be performed to add more wavelet coefficients and therefore more details. In other words, a first pass with a certain CR can be done and, if the image quality is not judged sufficient, acquisitions of new wavelet coefficients can be added by lowering the CR and doing a second pass. A new restored image can easily be obtained with the quick inverse wavelet transform.

Concerning the limitation of our technique, the employment of 8-bit patterns in ABS-WP is one since it reduces the maximum possible acquisition frame rate. The DMD in the setup at the Politecnico di Milano can work at a maximum frequency of 290 Hz in 8-bit mode but it can reach 22 kHz in the 1-bit mode. Employing 8-bit patterns is therefore slower than limiting the use to the ON/OFF states which can be a problem depending on the application. The possibility to reach the maximum DMD's frame rate is however practically limited by different issues such as the weak SNR in low-light scenarios. In the field of biomedical optics, this can be particularly true, e.g., specific dyes emit weak fluorescence signals. Based on the results of Fig. IV.7 and table IV.6, if fast measurements are required in any case, one can still use the Haar wavelet with ABS-WP and obtain better results compared to CS or EWT-ACS thanks to a better prediction (results of table IV.3).

Overall, the proposed acquisition/restoration scheme ABS-WP is fast, threshold-free and easy to adjust with few parameters to tune. The perfect recovery of the signal is however not guaranteed unlike for the CS approach [13]. One can nevertheless refine the recovered image in ABS-WP with a second pass of the algorithm to complete the set of sampled wavelet coefficients. Such a process is more complex in the CS case since the ℓ_1 or TV minimization which is time consuming have to be started from scratch again.

IV.7 Conclusion

In this chapter, we reported a new framework for single-pixel imaging. The non-linear approximation of the wavelet transform inspires the philosophy of our approach. Significant wavelet coefficients that should be experimentally acquired are predicted via an interpolation operator, while the other coefficients are discarded in the restoration process. The main advantage of ABS-WP is the fast image recovery based on inverse wavelet transform with filter banks. It hence disposes of the computational overhead of ℓ_1 or TV minimization required by the compressed sensing theory.

To the best of our knowledge, experimental data in an *adaptive* strategy had never been acquired with a wavelet other than Haar's. This is made possible by quantization of the patterns so that more sophisticated wavelets can be employed and chosen according to the desired application and object to image. Both good visual and quantitative results of ABS-WP were proposed in simulation and for experimental acquisitions. The technique was moreover proven to adapt to different kinds of images with a same set of parameters.

As mentioned earlier in the chapter, a common problem regards the negative values in a pattern that cannot physically be implemented on any SLM. No matter the chosen acquisition and restoration scheme employed, most patterns present both positive and negative values. In this chapter, the acquisitions were performed using a separation of the patterns in their positive and absolute negative part which doubles acquisition times. In the next chapter, another method is presented as well as a proposed general way to transform any pattern into a combination of positive patterns to deal with this problem.

13. Under certain assumptions, see Chapter II.

CHAPTER V

PATTERN GENERALIZATION

Contents

CHAPTER V

NO MATTER the kind of acquisition and restoration techniques employed for single-pixel imaging, the patterns that should be sent to the SLM usually require both positive and negative values which is physically impossible to achieve since photons number cannot be negative. A second constraint is the dark current α presented in Section II.1 that flaws the measurements.

In this chapter, we report a general way to deal with these experimental constraints. The materials of this chapter were filed as a patent (Rousset *et al.*, 2017c) and submitted to *IEEE Transactions on Computational Imaging* (Rousset *et al.*, 2017d).

V.1 Introduction

Two constraints arise for the experimental implementation of SPC image acquisition and restoration : patterns positivity and dark current rejection. The positivity limitation and dark current rejection are often overcome by splitting (i.e., separating) patterns in their positive and negative part (Dai *et al.*, 2014; Rousset *et al.*, 2017a). Subtracting the two measurements leads to the desired measurement, i.e., the measurement that would have been acquired with the desired SLM pattern having both positive and negative values. While this approach is straightforward, it requires to double the number of measurements which also doubles the total acquisition time. A second approach is pattern shifting. It consists in adding the same background value to all the patterns such that they become positive (Duarte *et al.*, 2008). The desired measurements are then obtained by subtracting a measurement acquired for the background value to all the measurements. Only one additional measurement is required, but pattern shifting is very sensitive to noise. Efficient strategies to get rid of the dark current are essential to restoration algorithms. Although these two constraints are of particular importance for experimental data acquisition and image restoration, they have not been addressed from a general perspective.

In this chapter, we propose to tackle the experimental limitations by seeking positive patterns that are related to the desired SLM patterns through linear combinations. Image acquisition by means of an SPC being linear, the measurements obtained using the positive patterns can be linearly combined to provide the desired measurements. The *ad hoc* solutions based on pattern splitting or shifting can be seen as two particular cases of this approach, which we refer to as pattern generalization.

By formalizing the problem, we show that pattern generalization can be related to nonnegative matrix factorization (NMF), which is the process of factorizing a matrix in a product of two

matrices having positive only entries (Paatero *et* Tapper, 1994; Lee *et* Seung, 1999, 2001). NMF algorithms have found various applications including image analysis (Lee *et* Seung, 1999), text mining (Wang *et al.*, 2008), blind source separation (Cichocki *et al.*, 2006), video tracking (Bucak *et* Gunsel, 2007), financial data analysis (de Fréin *et al.*, 2008). Several algorithms can address this problem, e.g., alternating least squares algorithms (Paatero *et* Tapper, 1994), multiplicative update algorithms (Lee *et* Seung, 1999) and gradient descent algorithms (Lee *et* Seung, 2001; Lin, 2007). We refer the reader to the reviews Berry *et al.* (2006); Wang *et* Zhang (2013); Gillis (2014) for extensive explanations on NMF and the different algorithms. More recently, NMF has been extended to semi NMF (SNMF) that decomposes a matrix in a product of two matrices with one having nonnegative entries (Ding *et al.*, 2010).

It is demonstrated in this chapter that the single-pixel experimental constraints can be efficiently addressed through pattern generalization using a semi nonnegative matrix factorization (SNMF) algorithm. We also show that, for a given number of patterns, only one additional measurement has to be performed. Compared to the classical positive/negative pattern splitting method, this leads to a reduction of the number of measurements by a factor of two. To the best of our knowledge, this is the first time that this pattern generalization problem is addressed in single-pixel imaging.

In this chapter, we first present the conventional SPC used technique to deal with the experimental constraints. Then, our proposed pattern generalization problem is detailed and a way to solve it using a SNMF algorithm is given. A particular constraint linked to the dark current rejection is added in this algorithm. The conditions in which the experiments were made are then reported with the associated results in simulations and for experimental data. Finally, we discuss our findings and give our conclusions.

V.2 *Ad hoc* methods for experimental constraints

Different approaches have been proposed to design the set of patterns $\mathbf{P}$ and recover the image $\mathbf{f}$ from the measurements $\mathbf{m}$ as mentioned in Chapter II. It is important to note that most of them consider patterns with negative values. Patterns are indeed chosen in bases such as Fourier (Zhang *et al.*, 2015; Zhang *et* Zhong, 2016), discrete cosine transform (Liu *et al.*, 2017), wavelets (Deutsch *et al.*, 2009; Averbuch *et al.*, 2012; Dai *et al.*, 2014; Hahn *et al.*, 2014; Huo *et al.*, 2017; Rousset *et al.*, 2017a) or Hadamard (Radwell *et al.*, 2014). In addition, it is common to assume that no dark current is present so that the image formation model classically considered for image restoration is

$$\check{m} = N_0 \check{\mathbf{p}}^\top \mathbf{f} \, \Delta t \tag{V.1}$$

where $\check{\mathbf{p}} \in \mathbb{R}^{D\times 1}$ is a SLM pattern with positive and negative values. From now on, we will refer to $\check{\mathbf{p}}$ (resp. $\check{m}$) as the desired SLM pattern (resp. measurement vector). As a reminder, the real physical

measurement is obtained as in (II.4) :

$$m = \left(N_0 \mathbf{p}^\top \mathbf{f} + \alpha\right) \Delta t. \tag{V.2}$$

with $\mathbf{p} \in \mathbb{R}_+^{D\times 1}$. Unfortunately patterns $\check{\mathbf{p}}$ cannot be physically implemented on a SLM and the absence of the dark current α is unrealistic. However, two *ad hoc* methods are (implicitly) used to correct for the two problems.

V.2.1 Pattern splitting

This natural method consists in separating each desired pattern $\check{\mathbf{p}} \in \mathbb{R}^{D\times 1}$ in its positive $\mathbf{p}_+ \in \mathbb{R}_+^{D\times 1}$ and absolute negative part $\mathbf{p}_- \in \mathbb{R}_+^{D\times 1}$ (Dai *et al.*, 2014; Rousset *et al.*, 2017a), i.e.,

$$\check{\mathbf{p}} = \mathbf{p}_+ - \mathbf{p}_- \quad \text{with} \begin{cases} \mathbf{p}_+ = \max\left(\mathbf{0}_D, \check{\mathbf{p}}\right) \\ \mathbf{p}_- = \left|\min\left(\mathbf{0}_D, \check{\mathbf{p}}\right)\right| \end{cases} \tag{V.3}$$

where the $\max(.)$ and $\min(.)$ functions are applied to each entry of both vectors, $\mathbf{0}_D$ being the null vector of size D. Then, the measurements m_+ and m_- acquired using the patterns $\mathbf{p}_+$ and $\mathbf{p}_-$, respectively, are subtracted to give $\check{m}$. Indeed, we have

$$\begin{aligned} m_+ - m_- &= \left(N_0 \mathbf{p}_+^\top \mathbf{f} + \alpha\right) \Delta t - \left(N_0 \mathbf{p}_-^\top \mathbf{f} + \alpha\right) \Delta t && \text{(V.4)} \\ &= N_0 \left(\mathbf{p}_+ - \mathbf{p}_-\right)^\top \mathbf{f} \, \Delta t && \text{(V.5)} \\ &= \check{m}. && \text{(V.6)} \end{aligned}$$

It is important to note that the dark current α cancels out. The drawback of this natural solution is, if I is the number of desired measurements, $2I$ SPC measurements are needed to obtain them, leading to an increased acquisition time.

V.2.2 Pattern shifting

A second approach consists in shifting the pattern $\check{\mathbf{p}} \in \mathbb{R}^{D\times 1}$ towards the positive values (Duarte *et al.*, 2008). Mathematically

$$\check{\mathbf{p}} = \mathbf{p}_\mathrm{s} - \mathbf{p}_\mathrm{b} \quad \text{with} \begin{cases} \mathbf{p}_\mathrm{s} = \check{\mathbf{p}} + \mathbf{p}_\mathrm{b} \in \mathbb{R}_+^{D\times 1} \\ \mathbf{p}_\mathrm{b} = (b, \ldots, b)^\top \in \mathbb{R}_+^{D\times 1} \end{cases} \tag{V.7}$$

where b is a background value chosen so that $b \geq \left|\min\left(\check{\mathbf{p}}\right)\right| \in \mathbb{R}_+$. As for the positive/negative separation, the subtraction of the two corresponding SPC measurements gives the desired measurement by canceling the dark current :

$$\check{m} = m_\mathrm{s} - m_\mathrm{b}. \tag{V.8}$$

Contrary to pattern splitting, it is *not* mandatory to double the number of measurements. Indeed, choosing b large enough, the background value b can be the same for all the desired measurements. Therefore, if I measurements are desired, only $K = I + 1$ measurements are to be acquired. However, as will be shown later, this method dramatically suffers from noise.

V.3 Pattern generalization

V.3.1 Patterns as linear combinations

We note $\check{\mathbf{P}} = (\check{\mathbf{p}}_1, \dots, \check{\mathbf{p}}_I)^\top \in \mathbb{R}^{I \times D}$ the set of I desired patterns and $\check{\mathbf{m}} = (\check{m}_1, \dots, \check{m}_I)^\top$ the vector containing the corresponding desired measurements. Applying (V.1) to the collection of patterns $\check{\mathbf{P}}$ leads to

$$\check{\mathbf{m}} = N_0 \check{\mathbf{P}} \mathbf{f} \, \Delta t. \tag{V.9}$$

To acquire $\check{\mathbf{m}}$, which is infeasible in practice, our idea is to generalize the approaches described in Section V.2 looking for a collection of positive patterns $\mathbf{P} \in \mathbb{R}_+^{K \times D}$ such that

$$\check{\mathbf{P}} = \mathbf{T}\mathbf{P} \tag{V.10}$$

where $\mathbf{T} \in \mathbb{R}^{I \times K}$ is a transformation matrix. Applying $\mathbf{T}$ to the measurements $\mathbf{m}$ of (II.5) acquired with the patterns $\mathbf{P}$ leads to

$$\mathbf{T}\mathbf{m} = \mathbf{T}(N_0 \mathbf{P}\mathbf{f} + \alpha \mathbf{1}_K) \, \Delta t \tag{V.11}$$

$$= (N_0 \check{\mathbf{P}}\mathbf{f} + \alpha \mathbf{T}\mathbf{1}_K) \, \Delta t \tag{V.12}$$

We can notice that the desired measurements $\check{\mathbf{m}}$ of (V.9) can be obtained transforming the acquired measurements $\mathbf{m}$ as in (V.12), provided that

$$\mathbf{T}\mathbf{1}_K = \mathbf{0}_I \tag{V.13}$$

where $\mathbf{0}_I = (0, \dots, 0)^\top \in \mathbb{R}^{I \times 1}$. If (V.13) is satisfied, then the desired measurements $\check{\mathbf{m}}$ of (V.9) are directly obtained as

$$\check{\mathbf{m}} = \mathbf{T}\mathbf{m} \tag{V.14}$$

In summary, for a given $\check{\mathbf{P}} \in \mathbb{R}^{I \times D}$, the pattern generalization problem we address is the following :

$$\text{Find } \mathbf{T} \in \mathbb{R}^{I \times K} \text{ and } \mathbf{P} \in \mathbb{R}^{K \times D} \text{ s.t. } \begin{cases} \check{\mathbf{P}} = \mathbf{T}\mathbf{P} \\ \mathbf{P} \geq 0 \\ \mathbf{T}\mathbf{1}_K = \mathbf{0}_I \end{cases} \tag{V.15}$$

where $\mathbf{P} \geq 0$ is a shorthand for $(\mathbf{P})_{k,n} \geq 0$, $\forall (k,n)$. The framework of the proposed pattern generalization method is presented in Fig. V.1.

V.3.2 Link with *ad hoc* methods

The pattern splitting method described in (V.3) is equivalent to choosing $\mathbf{T}$ and $\mathbf{P}$ in (V.15) as

$$\mathbf{T} = \begin{pmatrix} 1 & -1 & 0 & \dots & & 0 \\ 0 & 0 & 1 & -1 & \dots & 0 \\ \vdots & \vdots & \vdots & \vdots & \ddots & \vdots \\ 0 & \dots & & 0 & 1 & -1 \end{pmatrix} \in \mathbb{R}^{I \times 2I} \qquad \mathbf{P} = \begin{pmatrix} \mathbf{p}_1^\top \\ \mathbf{p}_2^\top \\ \vdots \\ \mathbf{p}_{2I-1}^\top \\ \mathbf{p}_{2I}^\top \end{pmatrix} = \begin{pmatrix} \max(\mathbf{0}_D, \check{\mathbf{p}}_1)^\top \\ |\min(\mathbf{0}_D, \check{\mathbf{p}}_1)|^\top \\ \vdots \\ \max(\mathbf{0}_D, \check{\mathbf{p}}_I)^\top \\ |\min(\mathbf{0}_D, \check{\mathbf{p}}_I)|^\top \end{pmatrix} \in \mathbb{R}_+^{2I \times D}. \tag{V.16}$$

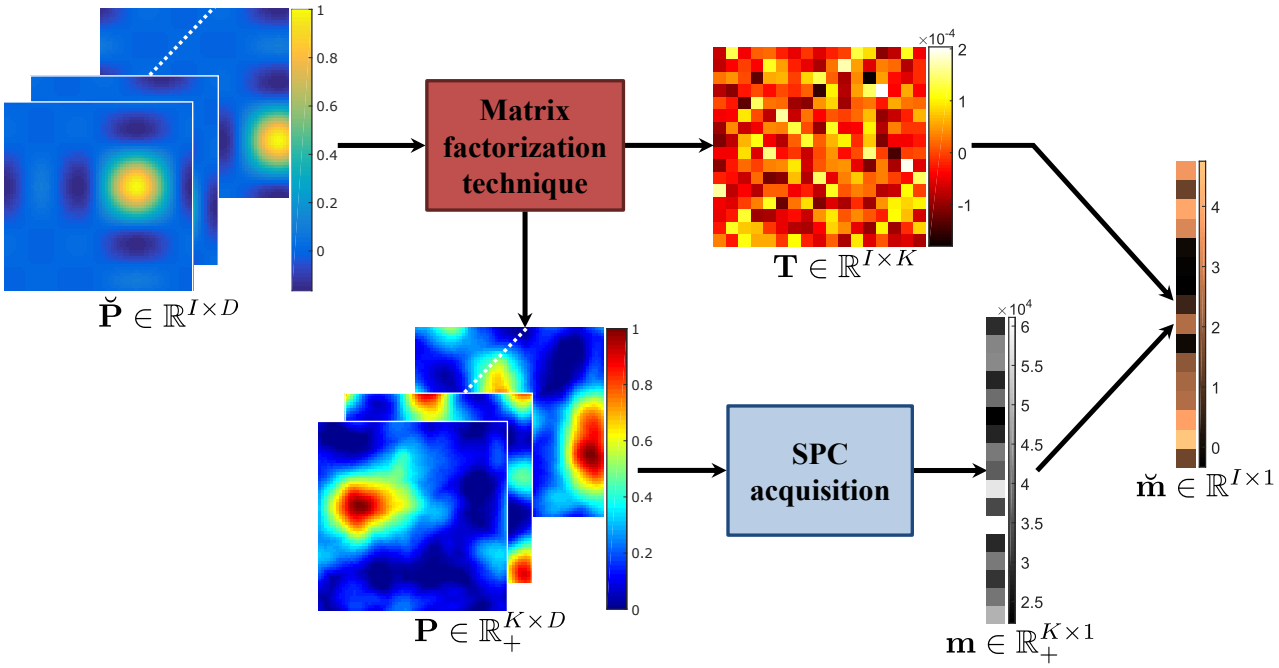

FIGURE V.1 – Framework of the proposed pattern generalization method.

The number of SLM patterns is $K = 2I$, where I is the number of desired patterns

For the pattern shifting method described in (V.7), $\mathbf{T}$ and $\mathbf{P}$ are given by the following formulas :

$$\mathbf{T} = \begin{pmatrix} 1 & \dots & 0 & -\frac{1}{M} & \dots & -\frac{1}{M} \\ \vdots & \ddots & \vdots & \vdots & \ddots & \vdots \\ 0 & \dots & 1 & -\frac{1}{M} & \dots & -\frac{1}{M} \end{pmatrix} \in \mathbb{R}^{I \times (I+M)} \qquad \mathbf{P} = \begin{pmatrix} \mathbf{p}_1^\top \\ \vdots \\ \mathbf{p}_I^\top \\ \mathbf{p}_{I+1}^\top \\ \vdots \\ \mathbf{p}_{I+M}^\top \end{pmatrix} = \begin{pmatrix} (\check{\mathbf{p}}_1 + \mathbf{p}_\mathrm{b})^\top \\ \vdots \\ (\check{\mathbf{p}}_I + \mathbf{p}_\mathrm{b})^\top \\ \mathbf{p}_\mathrm{b}^\top \\ \vdots \\ \mathbf{p}_\mathrm{b}^\top \end{pmatrix} \in \mathbb{R}_+^{(I+M) \times D}. \tag{V.17}$$

The number of SLM patterns is given by $K = I + M$ in this case. Setting M to one reduces the number of measurements. However, when it comes to noisy experimental measurements, it is better to average several measurements acquired with the same pattern $\mathbf{p}_\mathrm{b}$.

V.3.3 Optimization problem

To find two matrices $\mathbf{T}$ and $\mathbf{P}$ satisfying (V.15), a possibility is to seek two matrices that minimize the squared Frobenius norm of $\check{\mathbf{P}}$ minus $\mathbf{TP}$. Adding the positivity constraint on $\mathbf{P}$ and the condition (V.13) leads to the following optimization problem :

$$\min_{\mathbf{T},\,\mathbf{P}} \left\| \check{\mathbf{P}} - \mathbf{TP} \right\|_\mathrm{F}^2 \quad \text{such that} \quad \mathbf{P} \geq 0 \text{ and } \mathbf{T}\mathbf{1}_K = \mathbf{0}_I \tag{V.18}$$

V.4 Proposed SNMF algorithm

V.4.1 Algorithm overview

The minimization problem (V.18) can be solved adapting algorithms designed for semi non-negative matrix factorization (SNMF), which usually solve (V.18) with the constraint $\mathbf{P} \geq 0$ but without the constraint on $\mathbf{T}$. Most SNMF methods are iterative and alternate between the minimization of $\left\|\check{\mathbf{P}} - \mathbf{TP}\right\|_{\mathrm{F}}^2$ for $\mathbf{P}$ and for $\mathbf{T}$ (Berry *et al.*, 2006; Wang *et* Zhang, 2013; Gillis, 2014). Herein, we propose a similar approach where each of the two minimization steps is solved with its respective constraint. An overview of our two-step iterative algorithm is given in algorithm 2.

Algorithm 2 Solve the pattern generalization problem (V.15) as (V.18)

Initialization : $\mathbf{P} = \mathrm{rand}(K, D)$
while $\left\|\check{\mathbf{P}} - \mathbf{TP}\right\|_{\mathrm{F}}^2 > \epsilon$ **do**
  Step 1 : Minimize $\left\|\check{\mathbf{P}} - \mathbf{TP}\right\|_{\mathrm{F}}^2$ w.r.t. $\mathbf{T}$ such that $\mathbf{T}\mathbf{1}_K = \mathbf{0}_I$
  Step 2 : Minimize $\left\|\check{\mathbf{P}} - \mathbf{TP}\right\|_{\mathrm{F}}^2$ w.r.t. $\mathbf{P}$ such that $\mathbf{P} \geq 0$
end while

For each of the two steps in algorithm 2, different resolution methods are available, including alternating least squares algorithms (Paatero *et* Tapper, 1994), multiplicative update algorithms (Lee *et* Seung, 1999) and gradient descent algorithm (Lee *et* Seung, 2001; Lin, 2007). For fast computation and guaranteed convergence, we investigate methods based on alternating least squares to solve (V.18).

V.4.2 Solution for T

Assuming $\mathbf{P}$ is fixed, the following subproblem must be solved :

$$\min_{\mathbf{T}} \left\|\check{\mathbf{P}} - \mathbf{TP}\right\|_{\mathrm{F}}^2 \quad \text{such that} \quad \mathbf{T}\mathbf{1}_K = \mathbf{0}_I \tag{V.19}$$

In standard SNMF problems where no constraint acts on $\mathbf{T}$, the subproblem (V.19) has a straightforward solution $\mathbf{T} = \check{\mathbf{P}}\mathbf{P}^\top \left(\mathbf{P}\mathbf{P}^\top\right)^{-1}$ when $\mathbf{P}\mathbf{P}^\top$ is invertible. In our case, the constraint (V.13) makes it an equality constrained optimization problem. Nevertheless, we showed in Appendix B that it can still be solved analytically using the duality property. We have

$$\mathbf{T} = \check{\mathbf{P}}\mathbf{P}^\top \left(\mathbf{P}\mathbf{P}^\top\right)^{-1} \left(\mathbf{I} - \frac{1}{\mathbf{1}_K{}^\top \left(\mathbf{P}\mathbf{P}^\top\right)^{-1} \mathbf{1}_K} \mathbf{1}_{K\times K} \left(\mathbf{P}\mathbf{P}^\top\right)^{-1}\right) \tag{V.20}$$

with $\mathbf{I}$ the identity matrix of size $K \times K$ and $\mathbf{1}_{K\times K} = \mathbf{1}_K \mathbf{1}_K{}^\top$ is the matrix of size $K \times K$ with all entries equal to one. If $\mathbf{P}\mathbf{P}^\top$ is not invertible, one can instead employ the Moore-Penrose pseudoinverse.

V.4.3 Solution for P

Assuming $\mathbf{T}$ is fixed, the following subproblem must be solved :

$$\min_{\mathbf{P}} \left\|\check{\mathbf{P}} - \mathbf{TP}\right\|_{\mathrm{F}}^2 \quad \text{such that} \quad \mathbf{P} \geq 0 \tag{V.21}$$

This problem is a non-negative least square problem which does not have an explicit solution as is. Gillis proposed a block coordinate descent method that leads to a closed-form solution for each block and to a fast computation (Gillis *et* Kumar, 2015). Moreover, this method was shown to give a very low factorization error using only $K = I + 1$ (Gillis *et* Kumar, 2015). For this block coordinate method, the cost function $\mathcal{F}(\mathbf{P}) = \left\|\check{\mathbf{P}} - \mathbf{TP}\right\|_{\mathrm{F}}^2$ is rewritten as

$$\mathcal{F}(\mathbf{P}) = \mathcal{F}(\mathbf{P}_{-k}, \mathbf{p}_k) = \left\|\check{\mathbf{P}} - \mathbf{T}_{|k}\mathbf{P}_{-k} - \mathbf{t}_k\mathbf{p}_k^\top\right\|_{\mathrm{F}}^2 \tag{V.22}$$

where $\mathbf{T}_{|k}$ (resp. $\mathbf{P}_{-k}$) is the matrix $\mathbf{T}$ (resp. $\mathbf{P}$) deprived of its column (resp. row) k and $\mathbf{t}_k \in \mathbb{R}^{I\times 1}$ (resp. $\mathbf{p}_k^\top \in \mathbb{R}^{1\times D}$) is the k-th column (resp. row) of $\mathbf{T}$ (resp. $\mathbf{P}$). A partial solution of the problem (V.21) is obtained by minimizing $\mathcal{F}(\mathbf{P})$ w.r.t. $\mathbf{p}_k$ and iterating over the K rows of $\mathbf{P}$ (Gillis *et* Kumar, 2015). Hence, at each iteration, the following problem has to be solved

$$\min_{\mathbf{p}_k} \mathcal{F}(\mathbf{P}_{-k}, \mathbf{p}_k) \quad \text{such that} \quad \mathbf{p}_k \geq 0, \tag{V.23}$$

Interestingly, it admits an analytical solution :

$$\mathbf{p}_k = \max\left(\mathbf{0}_D, \frac{\left(\check{\mathbf{P}} - \mathbf{T}_{|k}\mathbf{P}_{-k}\right)^\top \mathbf{t}_k}{\|\mathbf{t}_k\|_2^2}\right) \tag{V.24}$$

where the $\max(.)$ function is applied entrywise and $\mathbf{0}_D$ is the null vector of size D. For consistence, the demonstration of (V.22) is provided in Appendix B.

V.4.4 Proposed algorithm

Using the closed-formula (V.20) and (V.24) permits to completely write algorithm 2 as in algorithm 3 to solve for $\check{\mathbf{P}} \approx \mathbf{TP}$ with only $K = I + 1$.

Algorithm 3 Solve $\check{\mathbf{P}} \approx \mathbf{TP}$ as in (V.18)

Initialization : Set $K = I + 1$ and $\mathbf{P} = \mathrm{rand}(K, D)$
while $\left\|\check{\mathbf{P}} - \mathbf{TP}\right\|_{\mathrm{F}}^2 > \epsilon$ **do**
  1 : Update $\mathbf{T}$ using (V.20)
  2 : Update $\mathbf{P}$
    for $k = 1 : K$ **do**
      2.1 : $\mathbf{p}_k \leftarrow \max\left(\mathbf{0}_D, \frac{\left(\check{\mathbf{P}} - \mathbf{T}_{|k}\mathbf{P}_{-k}\right)^\top \mathbf{t}_k}{\|\mathbf{t}_k\|_2^2}\right)$
      2.2 : Update the k-th row of $\mathbf{P}$ with $\mathbf{p}_k^\top$
    end for
end while

As mentioned earlier, (V.24) gives a partial solution to (V.21) if the update of the rows of $\mathbf{P}$ is only performed once. To get a solution of (V.21), the state 2 of algorithm 3 should be within another while loop. However, for faster computation, the update of $\mathbf{P}$ is only performed once as seen in algorithm 3. When the algorithm starts to converge, $\mathbf{T}$ does not change much and a minimizer of (V.21) is thus obtained by several consecutive iterations of the update of $\mathbf{P}$.

V.5 Experiments overview

V.5.1 Pattern quantization

To be implemented on the DMD or any other SLM, the patterns should be quantized since real-valued patterns cannot be sent directly to a SLM. A uniform quantization of the patterns on b-bits is therefore performed, 2^b being the maximum available dynamic range of the DMD. To realize this quantization, we apply the following transform to the set of patterns $\mathbf{P}$:

$$\widehat{\mathbf{P}} = \left\lfloor \frac{1}{q}\mathbf{P} \right\rfloor \qquad q = \frac{\max(\mathbf{P})}{2^b - 1} \tag{V.25}$$

where $\lfloor . \rfloor$ denotes a rounding operation. Assuming the quantization errors can be neglected (Rousset *et al.*, 2017a), the desired measurement vector $\breve{\mathbf{m}}$ of (V.14) can be obtained as

$$\breve{\mathbf{m}} = q\left(N_0\mathbf{T}\widehat{\mathbf{P}}\mathbf{f} + \alpha\mathbf{T}\mathbf{1}_K\right)\Delta t = \widehat{\mathbf{T}}\widehat{\mathbf{m}} \tag{V.26}$$

where

$$\widehat{\mathbf{m}} = \left(N_0\widehat{\mathbf{P}}\mathbf{f} + \alpha\mathbf{1}_K\right)\Delta t \qquad \text{and} \qquad \widehat{\mathbf{T}} = q\mathbf{T} \tag{V.27}$$

V.5.2 Numerical experiments

Our numerical simulations are based on the computation of the forward model (II.4). The imaged object $\mathbf{f}$ is chosen as the Jasczak target, which is classically considered to assess the resolution of an imaging device.

The measurements $\mathbf{m}$, which are the numbers of photon collected at the single detector, are necessarily corrupted by Poisson noise [1]. Mathematically, the following noise model is used :

$$\mathbf{m} = \mathscr{P}\left(\left(N_0\mathbf{P}\mathbf{f} + \alpha\mathbf{1}_K\right)\Delta t\right) \tag{V.28}$$

where $\mathscr{P}(.)$ is the Poisson distribution applied on each entry of the vector. Changing N_0 and/or Δt in (V.28) allows to simulate several levels of noise. The larger N_0 and Δt, the larger the number of collected photon, hence, the better the signal-to-noise ratio of the measurements.

The proposed SNMF method is compared to the pattern splitting and the pattern shifting methods presented in Section V.2. The same matrix $\breve{\mathbf{P}}$ was considered for both factorizations of Section V.3.2 and for the SNMF algorithm 3. The stopping criterion for the SNMF method is set to $\epsilon = 10^{-6}$. For pattern shifting, we choose $M = 10$ in (V.17) in order to reduce the influence of noise and better estimate the background value.

Different acquisition scenarios are considered for the numerical experiments, which correspond to different values for the parameters of (II.4). In particular, varying light power N_0 is considered. A low N_0 indicates a low-light scenario, while large N_0 simulates a very bright object. Varying dark current α is also considered since each specific optical setup has its own value depending on the employed single-point detector, the illumination conditions, etc. The integration time Δt, which scales the measurements linearly, is set to one. The CCD image of the Jaczczak target

1. Other sources of noise exist but the predominant one is the Poisson noise.

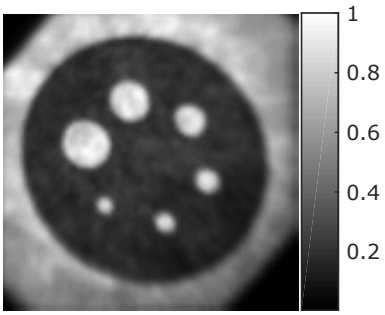

FIGURE V.2 – CCD image of the Jaszczak target employed for the numerical experiments.

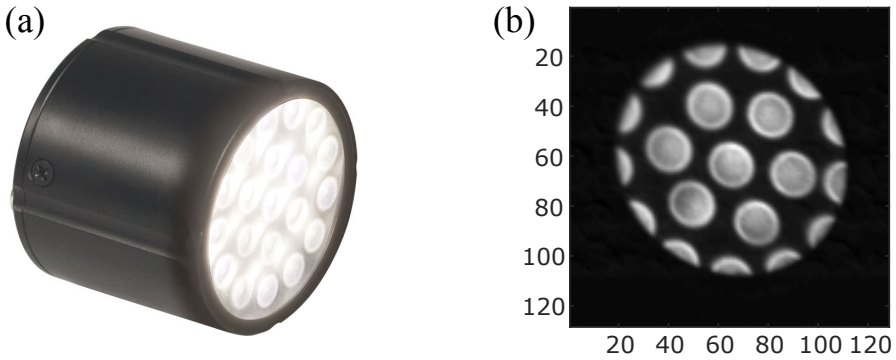

FIGURE V.3 – (a) Lamp used as an object in the setup at CREATIS and (b) SPC reference image of it obtained with a basis scan of a 128 × 128 Hadamard basis.

displayed in Fig. V.2 serves as the reference image. Image acquisition is simulated for N_0 ranging from 100 ph/s to 3600 ph/s and α ranging from 500 to 80000 ph/s. Different values for N_0 account for laser power variability that can start from milliwatts to a few watts. The dark current α, which regroups all the components read by the single-point detector when $N_0 = 0$, can be quite low if acquisitions are performed in the dark but high if they are taken in a luminous environment with undesirable photons reaching the detector.

V.5.3 Experimental acquisitions

To complete the numerical results of the previous section, experimental data were acquired using the setup at CREATIS presented in Section III.2. The lamp used in the setup was directly imaged so as to see its LED structure. Figure V.3 displays this object as well as the SPC reference image obtained from a basis scan of Hadamard 128 × 128 patterns. To recreate three values of N_0, different optical density (OD) filters from ThorLabs have been placed in front of the lamp (none - $OD = 0$, NE01B - $OD = 0.1$, NE02B - $OD = 0.2$). The collection time Δt at the photodetector was kept constant at $\Delta t = 100$ ms.

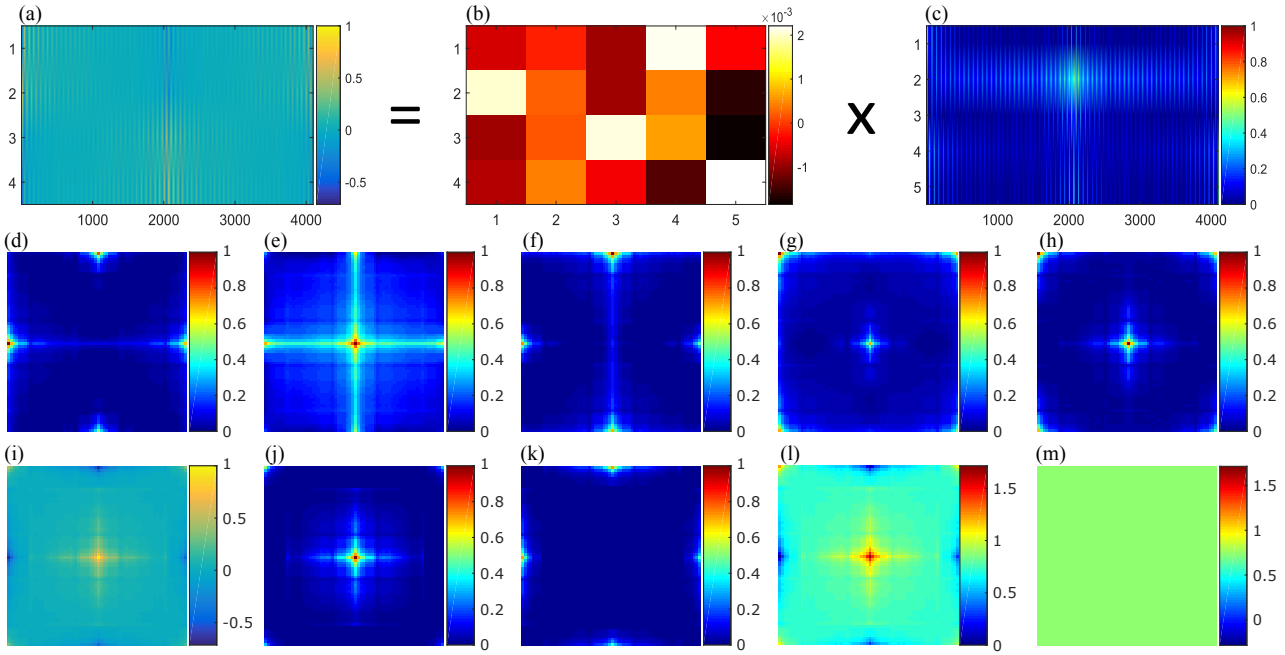

FIGURE V.4 – Example of created patterns with the proposed matrix factorization algorithm using Le Gall wavelet patterns. (a) Sequence matrix $\check{\mathbf{P}}$ of $I = 4$ desired SLM patterns of size $D = 64 \times 64 = 4096$, obtained (b) transformation matrix $\mathbf{T}$ and (c) sequence matrix $\mathbf{P}$ of $K = I + 1 = 5$ positive SLM patterns. (d-h) 5 SNMF patterns of $\mathbf{P}$ (rows of image (c)), (i) example of a desired pattern $\check{\mathbf{p}}$ (4th row of image (a)), (j) positive part $\mathbf{p}_+ = \max(\mathbf{0}_D, \check{\mathbf{p}})$, (k) negative part $\mathbf{p}_- = |\min(\mathbf{0}_D, \check{\mathbf{p}})|$, (l) shifted pattern $\mathbf{p}_\text{s} = \check{\mathbf{p}} + \mathbf{p}_\text{b}$ and (m) background pattern $\mathbf{p}_\text{b}$.

V.6 Results

V.6.1 Numerical experiments

Convergence of the proposed algorithm Figure V.4 illustrates the typical positive patterns obtained using the proposed SNMF method and using the *ad hoc* methods. Le Gall's wavelet (CDF 5/3 biorthogonal) patterns of size $D = N \times N = 64 \times 64 = 4096$ are considered. The top row of Fig. V.4 displays the pattern generalization $\check{\mathbf{P}} = \mathbf{TP}$ obtained using our SNMF approach. In this example, the matrix $\check{\mathbf{P}}$ contains a sequence of $I = 4$ desired patterns while the matrix $\mathbf{P}$ contains $K = I + 1 = 5$ (positive) patterns, which are also displayed in the middle row of Fig. V.4. The positive patterns obtained using the pattern splitting and the pattern shifting methods, for one of the desired patterns of $\check{\mathbf{P}}$, are given in the bottom row of Fig. V.4. As can be seen, the proposed SNMF method generates SLM patterns whose main structures and shapes are those of the desired patterns. The desired pattern Fig. V.4-(i) indeed has a star shape in its center that is also visible in the created SLM patterns Fig. V.4-(d)–(h).

The decrease of the pattern generalization error $\left\|\check{\mathbf{P}} - \mathbf{PT}\right\|_\text{F}^2$ during the SNMF iterations is presented in Fig. V.5. The SNMF method is evaluated for several matrices $\check{\mathbf{P}}$ containing different numbers of patterns I and pattern sizes D. The resulting computation times and number of iterations are reported in table V.1.

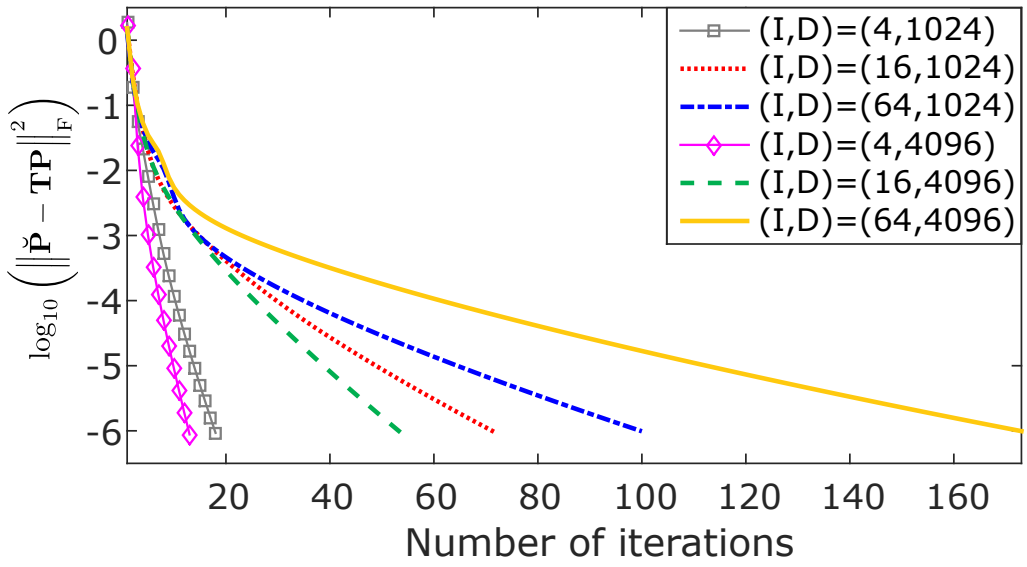

FIGURE V.5 – Logarithm (in base 10) of the error $\left\|\check{\mathbf{P}}-\mathbf{TP}\right\|_{\mathrm{F}}^{2}$ during the iterations of algorithm 3 for different values of desired patterns I and pattern sizes D. The convergence criterion ϵ was set to 10^{-6}.

Value of (I,D)	**Number of iterations**	**Computation time** (s)
$(4,1024)$	18	0.01
$(16,1024)$	72	0.10
$(64,1024)$	100	0.68
$(4,4096)$	13	0.02
$(16,4096)$	54	0.25
$(64,4096)$	173	3.58

TABLE V.1 – Number of iterations and computation time for the proposed SNMF algorithm 3 to converge for several values of (I,D). The convergence criterion ϵ was set to 10^{-6}.

Influence of the conditions for acquisition SPC recovered images of size 64×64 for four different couples (N_0,α) are displayed in Fig. V.6. Le Gall's wavelet was employed and each wavelet coefficient from scale $J=4$ to $j=2$ was acquired ($CR=75\%$) in order to only compare the influence of the splitting, shifting and SNMF methods[2]. The peak signal-to-noise ratio (PSNR) of the restored images is displayed as a function of N_0 for two values of α (20000 ph/s and 80000 ph/s) in Fig. V.7-(a) and as a function of α for two values of N_0 (600 ph/s and 1600 ph/s) in Fig. V.7-(b). The larger the PSNR, the better the image quality. The PSNR of the restored images for all (N_0,α) couples and pattern generalization methods is reported in table V.2.

All the three pattern generalization methods are found to perform better for increasing N_0 (see Fig. V.7-(a)) and decreasing α (see Fig. V.7-(b)). In all cases, pattern shifting is found to provide the the lowest PSNR. For low values of α, pattern splitting gives the best image quality. However, the pattern splitting image quality is found to degrade dramatically in low light scenarios for increasing α (see Fig. V.7-(b)). Overall, the proposed SNMF algorithm performs better in most of the assessed scenarios.

2. The prediction step of ABS-WP would indeed have a different outcome since the values of the wavelet coefficients acquired by each technique can be different.

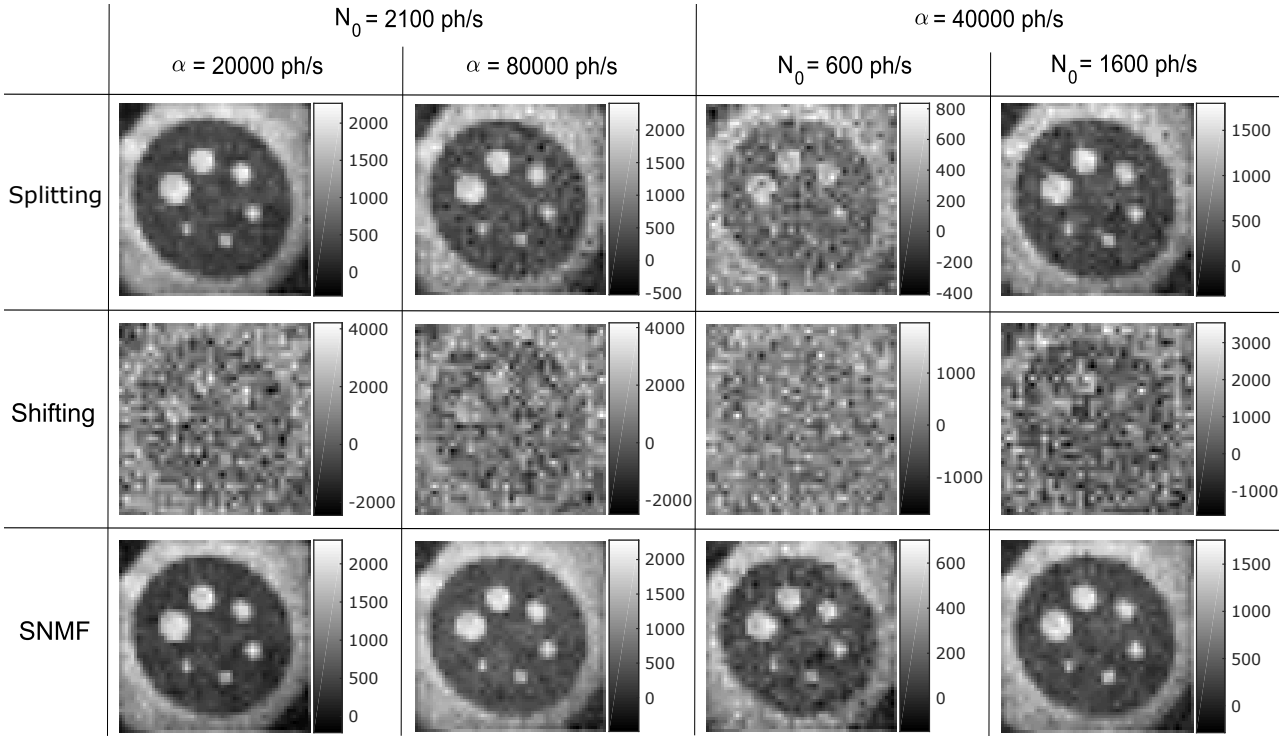

FIGURE V.6 – SPC restored images using ABS-WP for the three matrix factorization techniques for different values of N_0 and α on the test image of Fig. V.7. Corresponding PSNR compared to the ground truth image (displayed in Fig. V.7) can be read from Fig. V.7 and table V.2.

Influence of the constraint on T To motivate the introduction of the transformation matrix constraint (V.13), the SNMF pattern generalization is performed for all of the previously described scenarios without the constraint $\mathbf{T}\mathbf{1}_K = \mathbf{0}_I$. Table V.2 reports PSNR of the images restored with no constraint on $\mathbf{T}$. The image quality is found to be dramatically improved when the equality constraint is added if α is big enough. For the cases of table V.2 when α is small (i.e. 500 and 5000 ph/s), results are close or even better without the constraint. As a reminder, this constraint is equivalent to saying that the sum on each row of $\mathbf{T}$ equals 0. If $\mathbf{T}$ is obtained as $\mathbf{T} = \check{\mathbf{P}}\mathbf{P}^\top \left(\mathbf{P}\mathbf{P}^\top\right)^{-1}$ (no constraint), the sum on the rows of $\mathbf{T}$ is around 10^{-4}. This is therefore sufficient enough to cancel small dark current values in this case. With the constraint, this sum is lowered to about 10^{-18} which cancels any value of dark current.

V.6.2 Experimental data

Experimental data have been acquired using 128×128 patterns from Daubechies' wavelet with 5 vanishing moments (Db5) by means of the CREATIS setup. Wavelet coefficients from scale $J = 4$ to $j = 3$ ($CR = 93.75\%$) were acquired in order to only judge the influence of the splitting, shifting and SNMF methods. For the pattern shifting technique, M of (V.17) was set to 10 as for the simulations to reduce the noise's influence on the background measurement. The results are displayed in Fig. V.8 where the PSNRs are given in table V.3 with respect to the reference image of Fig. V.3-(b).

As can be seen by these experimental results, the previous simulations are confirmed with good SPC restored images using the pattern splitting method or proposed SNMF algorithm. The

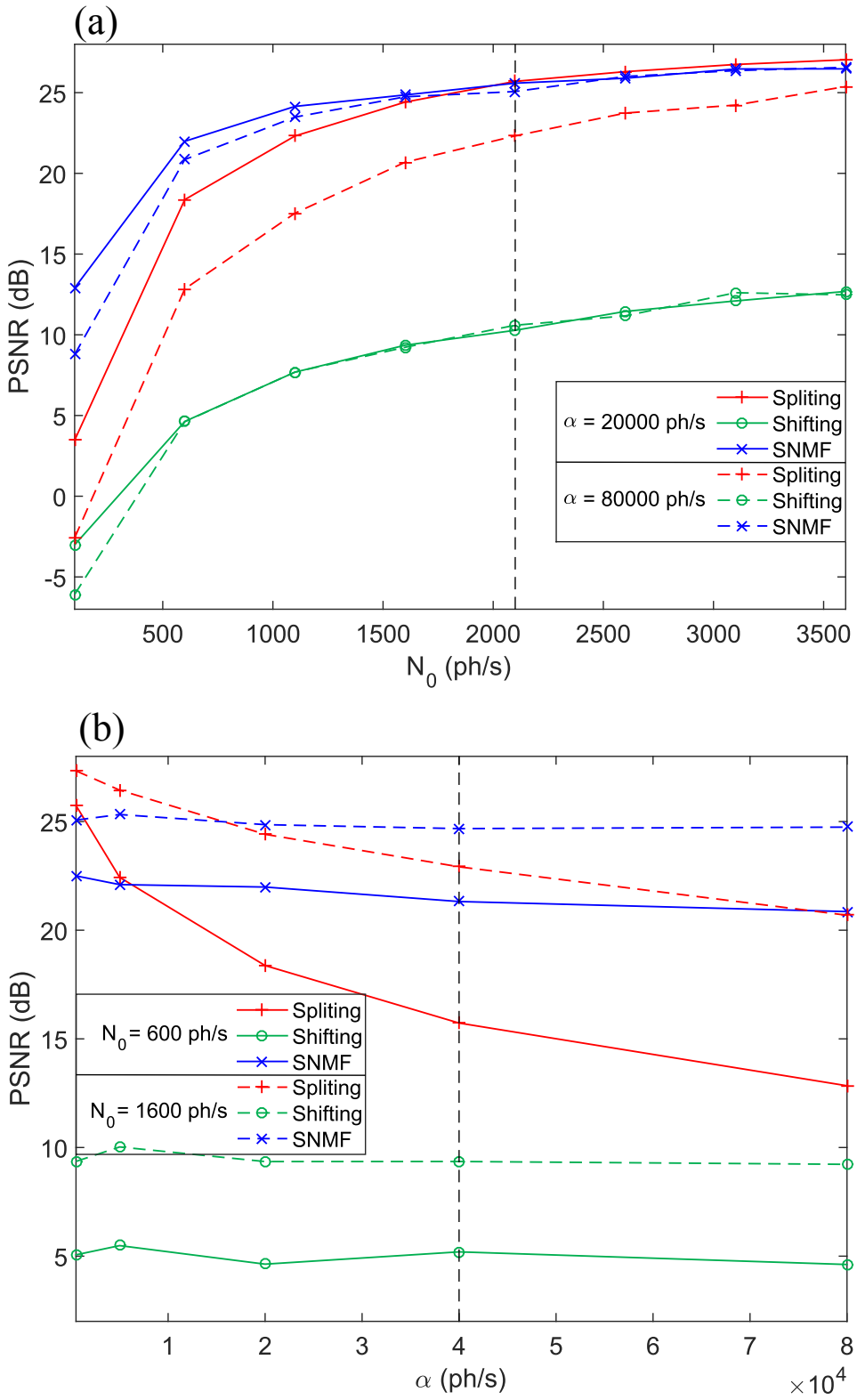

FIGURE V.7 – Jaszczak target and PSNR curves of SPC restored images for (a) (resp. (b)) two fixed values of α (resp. N_0) and increasing values of N_0 (resp. α) for $\Delta t = 1$ s. The dotted black bars correspond to the results displayed in Fig. V.6.

pattern shifting method however fails to restore the object even with the highest N_0 [3].

3. Highest N_0 corresponds to the lowest OD since N_0 decreases if the optical density of the filter increases.

Value of α	Technique	PSNR (dB)							
		$N_0 = 100$	$N_0 = 600$	$N_0 = 1100$	$N_0 = 1600$	$N_0 = 2100$	$N_0 = 2600$	$N_0 = 3100$	$N_0 = 3600$
500	Pattern splitting	**17.56**	**25.74**	**26.95**	**27.33**	**27.63**	**27.77**	**27.83**	**27.94**
	Pattern shifting	-2.41	5.06	7.85	9.36	10.49	11.17	12.94	13.22
	SNMF with $\mathbf{T1}_K \neq \mathbf{0}_I$	16.00	22.63	24.70	25.32	25.90	26.29	26.42	26.81
	SNMF with $\mathbf{T1}_K = \mathbf{0}_I$	15.22	22.50	24.16	25.07	25.68	26.10	26.63	26.68
5000	Pattern splitting	9.34	**22.43**	**25.34**	**26.45**	**26.98**	**27.40**	**27.55**	**27.73**
	Pattern shifting	-2.63	5.49	7.92	10.03	10.18	11.33	12.34	13.36
	SNMF with $\mathbf{T1}_K \neq \mathbf{0}_I$	6.91	19.73	22.93	24.53	25.17	25.87	26.32	26.76
	SNMF with $\mathbf{T1}_K = \mathbf{0}_I$	**14.93**	22.10	24.29	25.32	25.52	26.14	26.40	26.73
20000	Pattern splitting	3.47	18.37	22.31	22.41	**25.70**	**26.30**	**26.75**	**27.04**
	Pattern shifting	-3.01	4.63	7.68	9.35	10.28	11.45	12.10	12.69
	SNMF with $\mathbf{T1}_K \neq \mathbf{0}_I$	-4.58	10.72	15.75	18.74	20.39	21.98	22.83	23.68
	SNMF with $\mathbf{T1}_K = \mathbf{0}_I$	**12.90**	**21.99**	**24.15**	**24.86**	25.59	25.89	26.47	26.47
40000	Pattern splitting	0.91	15.73	19.97	22.92	24.58	25.15	26.03	26.44
	Pattern shifting	-4.91	5.20	7.72	9.36	10.42	11.50	12.30	13.01
	SNMF with $\mathbf{T1}_K \neq \mathbf{0}_I$	-10.51	4.88	10.17	13.26	15.46	17.27	18.68	19.68
	SNMF with $\mathbf{T1}_K = \mathbf{0}_I$	**10.61**	**21.32**	**23.68**	**24.68**	**25.82**	**25.81**	**26.43**	**26.48**
80000	Pattern splitting	-2.57	12.84	17.53	20.69	22.32	23.74	24.23	25.38
	Pattern shifting	-6.08	4.62	7.69	9.23	10.59	11.17	12.61	12.47
	SNMF with $\mathbf{T1}_K \neq \mathbf{0}_I$	-16.62	-1.07	4.18	7.42	9.79	11.54	13.17	14.36
	SNMF with $\mathbf{T1}_K = \mathbf{0}_I$	**8.78**	**20.86**	**23.48**	**24.74**	**25.07**	**26.00**	**26.36**	**26.57**

TABLE V.2 – PSNR values of the SPC restored images for different values of N_0 and α for $\Delta t = 1$. Some cases correspond to the displayed images in Fig. V.6 and curves of Fig. V.7.

V.7 Discussion

The main advantage of our SNMF approach is that it guarantees a low factorization error for a low number of positive patterns, i.e., $K = I + 1$ SLM patterns for I desired patterns. A low factorization error is crucial to get the desired measurements through measurement transformation without introducing model deviation. A low number of patterns K is necessary to limit the number of measurements, hence the acquisition time. Most SNMF methods propose to choose $K << I$ but the factorization error is often important. Here, using the block coordinate descent method (Gillis *et* Kumar, 2015), only $I + 1$ measurements with positive patterns are required to get the I desired measurements, which gives a ratio of almost 1. This is much better than pattern splitting that requires two positive patterns to acquire one data. Overall, the proposed SNMF methods allows to divide by a factor of two the total acquisition time with respect to the conventional pattern splitting approach. As the SNMF method, the pattern shifting method can reach $K = I + 1$. However, it is shown to fail to restore good quality images in most of the cases.

The number of iterations and computation time of the SNMF algorithm depends on the size of the problem. Since the SNMF algorithm updates the rows of $\mathbf{P}$, increasing I (by extension extending K the number of rows of $\mathbf{P}$) has a bigger impact than increasing D (the number of columns of $\mathbf{P}$). This can be seen comparing the computation times of table V.1 for the case $(I, D) = (16, 4096)$ and $(I, D) = (64, 1024)$, for which the matrix $\check{\mathbf{P}}$ has the same number of entries ($I \times D = 65536$). The SNMF algorithm converges more rapidly for the smaller values of I.

For high resolution images (large D and I), the SNMF computation can take up to several mi-

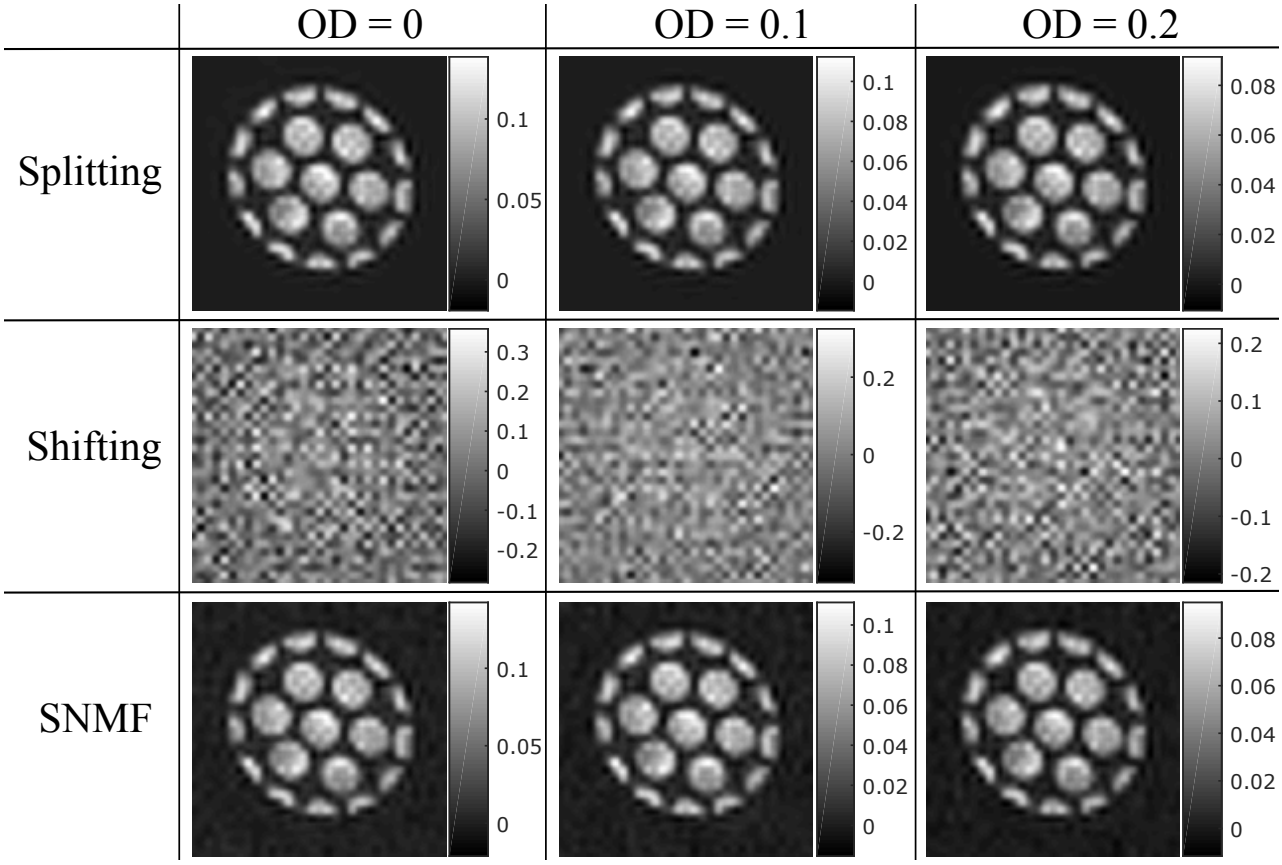

FIGURE V.8 – Experimental acquisitions using the pattern splitting, shifting and proposed SNMF algorithm for three different optical densities (OD). PSNRs with respect to the reference image of Fig. V.3-(b) are given in table V.3.

Technique	**PSNR** (dB)		
	$OD = 0$	$OD = 0.1$	$OD = 0.2$
Pattern splitting	**23.27**	**22.07**	**19.29**
Pattern shifting	4.73	6.25	7.65
SNMF	23.25	21.87	19.22

TABLE V.3 – PSNR values for the images of Fig. V.8 for different optical densities (i.e. different N_0).

nutes. For nonadaptive SPC acquisition (e.g., based on compressed sensing), SNMF can be performed prior to the acquisition. However, long computation times can be a limitation for adaptive acquisition strategies where the set of patterns $\check{\mathbf{P}}$ is determined during acquisition from the knowledge of the previous measurements. Therefore, one must wait that the SNMF algorithm outputs $\mathbf{P}$ and $\mathbf{T}$ before proceeding with the acquisition. In this paper, a computation time of about 4 minutes is required for $I = 1024$ and $D = 4096$, running a Matlab code on a single-core 2.10 GHz CPU. A *C++* implementation running on a GPU would allow to lower significantly these computation times and make them compatible with adaptive acquisition strategies.

The better results of the SNMF method compared to pattern splitting for most cases might be understood looking at the patterns in Fig. V.4. The patterns (j) and (k), obtained from pattern splitting, have many zeros. When α is large with respect to N_0, the useful part of the pattern (i.e., nonzeros) has only a small contribution to the SPC measurement. The SNMF patterns have fe-

wer zeros and such an effect is hence reduced (see patterns (d)–(h)). The pattern shifting method is found to lead to the lowest image quality; only the shape of the target can be recovered (see Fig. V.6). An explanation is that this method is very sensitive to noise since the useful information of the shifted pattern is overwhelmed by the useless information from the background (m). Looking at the shifted pattern (l), it can be seen that all pixels contribute to the measurement, which leads to the collection of many undesired photons in the presence of noise. Overall, the SNMF technique works well when $N_0 \ll \alpha$, i.e., when the dark current cannot be neglected which is always the case in real experiments.

The pattern splitting and SNMF method give close results with a slight edge for pattern splitting for small values of α. A possible explanation regards the construction of the measurement vector. For the proposed SNMF technique, the measurements $\check{\mathbf{m}}$ used for image restoration are obtained from the measurement transformation $\mathbf{Tm}$ (see (V.14)). In the presence of noise, the variance of $\check{\mathbf{m}}$ depends on the sum of the variances of $\mathbf{m}$. While many measurements are combined when the SNMF method is used, only two measurements are combined when pattern splitting is used. Hence pattern splitting is less affected by noise than SNMF. However, compared to pattern splitting, the proposed SNMF method is found to be an excellent compromise that gives an image quality similar to that obtained using pattern splitting, while diving by two the number of measurements.

The experimental acquisitions confirm what has been said up to this point. The visual results of Fig. V.8 are very close using the pattern splitting technique or proposed SNMF algorithm although PSNRs of table V.3 are slightly lower for the SNMF method. The pattern shifting technique is however unusable in practice as measurements get too much corrupted by the noise and no useful image can be obtained from them.

V.8 Conclusion

In this chapter, we introduced a new problem in single-pixel imaging that we refer to as pattern generalization. It consists in determining a set of positive patterns that can be actually loaded on a spatial light modulator. We also show that a second issue that has to be addressed in pattern generalization is dark current removal. Our basis idea is to see the set of desired patterns (having negative entries) as a linear transform of positive patterns.

We report a semi nonnegative factorization technique that is shown to solve the problem. To our knowledge, this is the first time that a SNMF algorithm is employed in the context of single-pixel imaging. It provides an elegant way to dispose of both the positivity constraint induced by the use of a spatial light modulator and the dark current rejection. In the meantime, it allows to reduce the number of measurements compared to the conventional pattern splitting method.

In the future, we will investigate algorithms for which the number of measurements is lower than the number of desired measurements, i.e. $K < I$ in (V.15). This would further compress the data in order to speed up acquisition. The main challenge to perform this is the factorization

error that would be much more important that what can be achieved using Gillis' method with $K = I + 1$. If this error is too big, the desired measurements obtained by (V.14) are partially wrong which could lead to poor image recovery.

While the method ABS-WP of Chapter IV sped up the image restoration side of SPC acquisition/restoration, this SNMF based method allows for faster acquisition with fewer measurements [4]. Acquisitions for real applications can now be considered, in particular for medical applications. The next chapter deals with potential applications in this field with multispectral time-resolved acquisitions.

4. Image restoration is slightly increased since (V.14) as to be performed to get the desired measurements.

CHAPTER VI

APPLICATION TO MULTISPECTRAL TIME-RESOLVED IMAGING

Contents

CHAPTER VI

BIOMEDICAL APPLICATIONS can take advantage of a single-pixel imaging system. In particular, multispectral time-resolved imaging is of interest as SPI allows to obtain good spectral, temporal and spatial resolutions.

In this chapter, we apply the previous developed tools for the acquisition of multispectral and/or time-resolved SPC measurements. Some of these results were presented at the *SPIE Photonics West* conference (Rousset *et al.*, 2017b) in February 2017 and others are expected to be submitted to *Optics Express* in the next months.

VI.1 Introduction

As mentioned in introduction, the SPC has been demonstrated to image through scattering media (Tajahuerce *et al.*, 2014; Duran *et al.*, 2015) such as biological tissues, in ophthalmology (Lochocki *et al.*, 2016, 2017), for skin lesions detection (Gibson *et* Dehghani, 2009) and to characterize tissues with near infrared acquisitions (Torabzadeh *et al.*, 2017). In addition, diffuse optical tomography or fluorescence molecular tomography (D'Andrea *et al.*, 2010; Ducros *et al.*, 2013; Pian *et al.*, 2015; Ducros *et al.*, 2016) with application to oximetry and molecular imaging can be performed by exploiting several SPC images. Another significant advantage of SPC for biomedical applications concerns *time-resolved* (TR) and/or multispectral acquisitions. Coupling the point detector of a SPC with a photon counting board (Pian *et al.*, 2016b,a; Rousset *et al.*, 2017b) results in a low-cost TR system which can benefit to fluorescence lifetime imaging (Becker, 2012). Such a setup was first proposed with application to fluorescence lifetime imaging by Pian *et al.* (2016b,a). It has higher performance compared to time-gated cameras (D'Andrea *et al.*, 2003) since it can combine good temporal and spatial resolutions. Lifetime information can further be supplemented by spectral information adding a spectrometer to the previous TR system (Pian *et al.*, 2016b). The spectral and time information can be exploited to characterize biological tissues that contain several fluorophores with different fluorescence lifetimes. This enables to assess the biological micro-environment (pH, temperature, ion concentration, etc.) of the tissues (Marcu, 2012; Ma *et al.*, 2015) which is an essential parameter for biologists.

In the previous works of Pian *et al.*, a partial basis scan approach with Hadamard patterns was employed, i.e., a subset of the complete basis coefficients are acquired regardless of the object to image (see Section II.3.1). Hence, high compression ratios cannot be reached without dramatic degradation of the image quality. In this chapter, the ability of the ABS-WP technique (Chap-

ter IV) to handle simultaneously TR and multispectral image acquisitions is demonstrated [1] in order to reduce the number of measurements. The use of an *adaptive* basis scan approach over a compressive sensing technique is motivated by the restoration step which is quite crucial when TR measurements are considered. This step should indeed be as fast as possible since a stack of images have to be recovered instead of a single image.

In this chapter, the mathematical modeling of the SPC of Section II.1 is first extended to deal with TR and/or multispectral measurements before detailing the considered phantom and experiments. Results are then proposed for fluorescence lifetime sensing and on multispectral time-resolved acquisitions. It is shown to permit to completely differentiate the different components of the imaged object using both the spectral and temporal information.

VI.2 Methods

VI.2.1 Extension to multispectral time-resolved measurements

Mathematical modeling In order to obtain first a TR system, a pulsed laser is employed as a light source and the detector is coupled with a TCSPC board. The latter one, thanks to its synchronization with the pulse of the laser, enables to obtain a histogram giving the number of photons for different time-of-flights (i.e., time-channels). Then, to obtain a multispectral time-resolved system, the output light of the single-pixel arm is directed towards a spectrometer having Λ parallel single detectors that are coupled to the TCSPC board having T time-channels. This results in a 2D+λ + t image $\mathbf{F} \in \mathbb{R}^{D\times\Lambda T}$ with $\mathbf{F} = \left(\mathbf{f}_{1,1},\ldots,\mathbf{f}_{\lambda,t},\ldots,\mathbf{f}_{\Lambda,T}\right)$. The image $\mathbf{f}_{\lambda,t} \in \mathbb{R}^{D\times 1}$ represents the image in the wavelength channel λ and time channel t with $(\lambda,t) \in \{1,\ldots,\Lambda\}\times\{1,\ldots,T\}$. The spectral and temporal information being acquired simultaneously, the equations (II.4) and (II.5) of Chapter II are therefore slightly changed as

$$\mathbf{m}_k = \left(m_{k,1,1},\ldots,m_{k,\lambda,t},\ldots,m_{k,\Lambda,T}\right)^\top \in \mathbb{R}^{\Lambda T\times 1} \quad \text{with} \quad \mathbf{m}_k^\top = \left(N_0\mathbf{p}_k^\top\mathbf{F} + \alpha\mathbf{1}_{\Lambda T}^\top\right)\Delta t \tag{VI.1}$$

$$\mathbf{M} = \left(\mathbf{m}_1,\ldots,\mathbf{m}_k,\ldots,\mathbf{m}_K\right)^\top \in \mathbb{R}^{K\times\Lambda T} \quad \text{with} \quad \mathbf{M} = \left(N_0\mathbf{P}\mathbf{F} + \alpha\mathbf{1}_{K\times\Lambda T}\right)\Delta t \tag{VI.2}$$

with $\mathbf{1}_{\Lambda T} = (1,\ldots,1)^\top \in \mathbb{R}^{\Lambda T\times 1}$ and $\mathbf{1}_{K\times\Lambda T} \in \mathbb{R}^{K\times\Lambda T}$ the matrix with all entries equal to 1. A measurement vector $\mathbf{m}_k \in \mathbb{R}^{\Lambda T\times 1}$ is directly obtained by the multispectral time-resolved SPC for each pattern $\mathbf{p}_k$, while a scalar measurement is acquired for each pattern of a classical SPC. A matrix of measurements $\mathbf{M} \in \mathbb{R}^{K\times\Lambda T}$ is hence obtained when a sequence of patterns $\mathbf{P} \in \mathbb{R}^{K\times D}$ is considered.

Time or spectral dependent images From the $\Lambda\times T$ restored images, one can extract the T (resp. Λ) images $\mathbf{f}_t$ (resp. $\mathbf{f}_\lambda$) in each time (resp. wavelength) channel by summing $\mathbf{f}_{\lambda,t}$ over λ (resp. t) :

$$\mathbf{f}_\lambda = \sum_{t=1}^{T}\mathbf{f}_{\lambda,t} \qquad \mathbf{f}_t = \sum_{\lambda=1}^{\Lambda}\mathbf{f}_{\lambda,t} \tag{VI.3}$$

1. The SNMF technique presented in Chapter V is not employed for the experimental acquisitions in this chapter since, chronologically, this method was not yet implemented.

The images $\mathbf{f}_t$ (resp. $\mathbf{f}_\lambda$) are equivalent to those that would be obtained without the spectrometer (resp. TCSPC) of the multispectral time-resolved system.

Prediction on CW measurements In the design of our acquisition/restoration scheme ABS-WP of Chapter IV, the prediction step of the significant wavelet coefficients is based on scalar measurement, i.e., on a single image. To perform this prediction, we therefore consider the *continuous-wave* (CW) image $\mathbf{f}$ which is obtained by summing the images $\mathbf{f}_{\lambda,t}$ over λ and t :

$$\mathbf{f} = \sum_{\lambda=1}^{\Lambda} \sum_{t=1}^{T} \mathbf{f}_{\lambda,t} \tag{VI.4}$$

This CW image corresponds to the one that would be acquired without the spectrometer and TCSPC board, i.e., using (II.4) and (II.5) for the image formation model. Note that, when an acquisition/restoration scheme is considered with a linear transform (typically in a basis scan or adaptive basis scan approach), summing the images after the restoration step is equivalent to summing the corresponding measurements before image restoration given the linearity of (VI.1) and (VI.4).

VI.2.2 Exponential fitting of fluorescence decay

Upon excitation at a certain wavelength, a fluorophore is a chemical component able to emit fluorescent light at a different wavelength. The emission of fluorescence is typically modeled by the sum of exponential decays. Here, we assume a mono-exponential decay, i.e., the fluorescence intensity $I(t)$ at t is given by

$$I(t) = Ae^{\frac{-t}{\tau}} \tag{VI.5}$$

where A is the amplitude and τ the lifetime.

After restoration of the images $\mathbf{f}_t$, each pixel $n \in [1, D]$ is assumed to satisfy the model of (VI.5) for each time point of the vector $(t_1, \ldots, t_T)^\top \in \mathbb{R}^{T\times 1}$. The latter vector represents the real time delays in seconds associated to the different time channels of the TCSPC. Using this vector, the model (VI.5) can first be discretized as

$$\mathbf{I}_n = (I_n(t_1), \ldots, I_n(t_T))^\top = \left(A_n e^{\frac{-t_1}{\tau_n}}, \ldots, A_n e^{\frac{-t_T}{\tau_n}}\right)^\top \in \mathbb{R}^{T\times 1} \tag{VI.6}$$

where $n \in [1, D]$ still account for the considered pixel.

An experimental time curve $\widehat{\mathbf{I}}_n \in \mathbb{R}^{T\times 1}$ depicting $\mathbf{I}_n$ of (VI.6) can be obtained for each pixel from $\mathbf{f}_t$, mathematically

$$\widehat{\mathbf{I}}_n = ((\mathbf{f}_1)_n, \ldots, (\mathbf{f}_t)_n, \ldots, (\mathbf{f}_T)_n)^\top \tag{VI.7}$$

The experimental curves $\widehat{\mathbf{I}}_n$ of (VI.7) for each pixel of the image can therefore be fitted to the model $\mathbf{I}_n$ of (VI.6) which enables to obtain the parameters A_n and τ_n. The optimal parameters (A_n^*, τ_n^*) are found minimizing the ℓ_2-norm of the difference between the model function curve $\mathbf{I}_n$ and the experimental curve $\widehat{\mathbf{I}}_n$:

$$\left(A_n^*, \tau_n^*\right) = \arg\min \left\| \widehat{\mathbf{I}}_n - \mathbf{I}_n \right\|_2^2 \tag{VI.8}$$

Here, the Matlab function `lsqcurvefit` is considered to perform this optimization. Repeating the fitting of (VI.8) for each of the $D = N \times N$ pixels of the image permits to finally obtain the amplitude map $\mathbf{A} \in \mathbb{R}^{D\times 1}$ and the lifetime map $\boldsymbol{\tau} \in \mathbb{R}^{D\times 1}$. This process is summarized in Fig. VI.1.

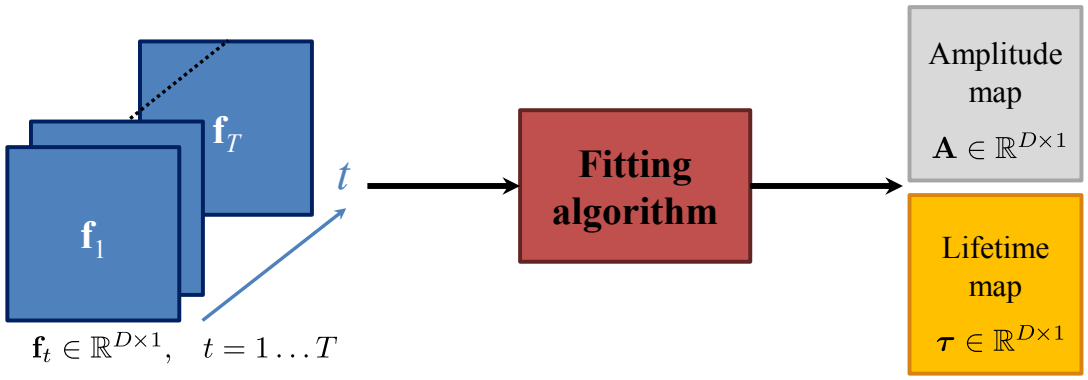

FIGURE VI.1 – Amplitude and lifetime maps obtained by a fitting algorithm using the time-dependent images. Note that the vectors are displayed as images in this scheme.

VI.3 Experiments

VI.3.1 Phantom

Figure VI.3-(a) displays the considered phantom whose different shapes have been created with a paper mask. Approximately, the wave has a 0.7 cm thickness and 2.3 cm height. The circle diameter and square side are about 1 cm. The square (resp. wave) shape is a red (resp. green) fluorescence plastic slide (CHROMA). Painted on a white paper, a solution of DCM dye in ethanol makes the circle shape. A spectral characterization of the fluorophores involved in the phantom is given in table VI.1.

VI.3.2 Experimental setup and conditions

Setup The Polimi setup described in Section III.1 is employed for experimental data acquisitions. The supercontinuum pulsed white light laser source (SuperK Extreme EXW-12, NKT Photonics) serves for uniform illumination of the object. In the fluorescence lifetime imaging re-

Area	Material	Absorption peak	Emission peak
Wave	Green fluorescence plastic slide	464 nm	525 nm
Square	Red fluorescence plastic slide	520 nm	625 nm
Circle	DCM dye painted on a white paper	468 nm	624 nm

TABLE VI.1 – Absorption and emission peaks of the different fluorophores embedded in the phantom.

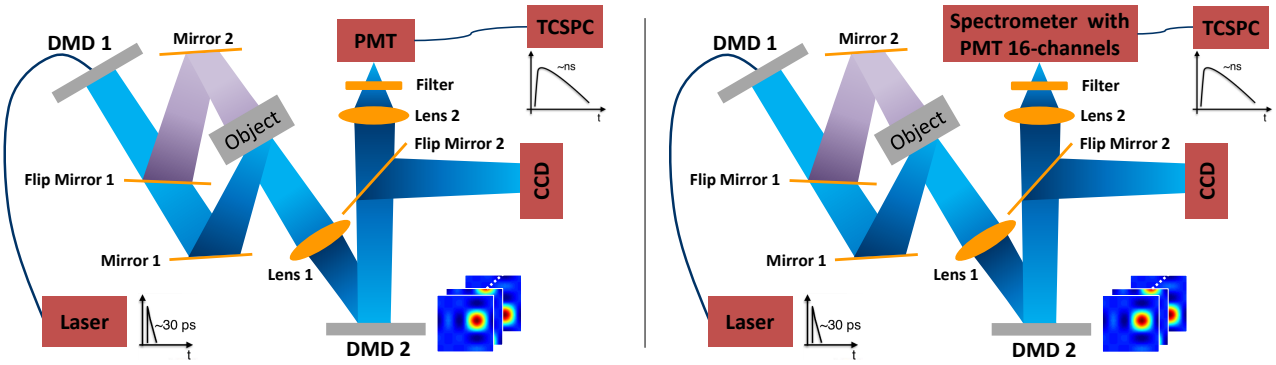

FIGURE VI.2 – Experimental setup at the Polimi with time and spectral information. (Left) Time-resolved SPC and (right) multispectral time-resolved SPC.

sults of Section VI.4.1, the one-channel (spectral channel) PMT (HPM-100-50, Becker & Hickl GmbH) is employed while in the multispectral experiments of Section VI.4.2, a sixteen-channel PMT (PML-16-1, Becker & Hickl GmbH) is used. In both configurations, the detector is coupled to the TCSPC board (SPC-630, Becker & Hickl GmbH). The latter one has a maximum of 4096 available time-channels and the pulse of the laser was repeated at a frequency of 40 MHz. To ensure good SNR while satisfying the statistics constraints of the TCSPC photon counting, an acquisition time $\Delta t = 1$ s was chosen at the detector. Placed before the detection, a long-pass filter (FEL0500, ThorLabs) with the cut-off wavelength at 500 nm selects the emitted fluorescence light based on the phantom's characteristics (see table VI.1). The setup in both configurations is displayed in Fig. VI.2.

Experimental conditions For acquisition/restoration using the SPC, our scheme ABS-WP described in Chapter IV was employed. To deal with the positivity constraint on the patterns and the additive dark current, the classical positive/negative separation presented in Section V.2 was considered since, at this time, the proposed SNMF algorithm reported in Chapter V was not available.

ABS-WP was employed using the Daubechies wavelet with 5 vanishing moments (Db5) (Mallat, 2008; Daubechies, 1992). A compression rate (CR) of 93% was obtained for the set of percentages $\mathcal{P} = \{1; 0.85; 0.075; 0\}$. As mentioned earlier, the prediction step of ABS-WP is based on CW measures (see (VI.4)) gathered by integrating (i.e., summing) the measurements.

VI.4 Results

VI.4.1 Fluorescence lifetime sensing

For these results, illumination of the object was performed in the 450 – 490 nm spectral band. In order to limit noise, the 4096 time-channels of the SPC were partially binned. This led to $T = 72$ time points and a time vector $\mathbf{t}$ ranging from 0 to 21.66 ns with a uniform time step of 0.305 ns.

A photo of the phantom along with different SPC restored images can be seen in Fig. VI.3. From the different images $\mathbf{f}_t$, temporal curves giving the intensity changes within each area of the

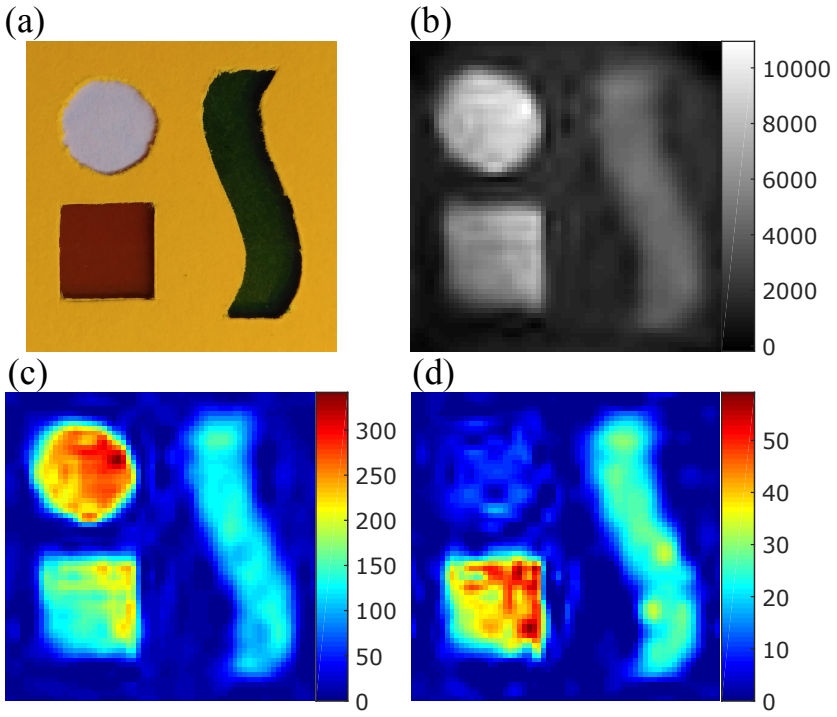

FIGURE VI.3 – Photo of the considered phantom and 64×64 images restored from CW measurements or different time-channels with Daubechies' wavelet (Db5) and $\mathcal{P} = \{1; 0.85; 0.075; 0\}$ giving a CR of 93%. (a) Photo of the phantom, (b) CW image, (c) $\mathbf{f}_t$ restored for $t = 10$ (2.75 ns) and (d) $t = 50$ (14.95 ns).

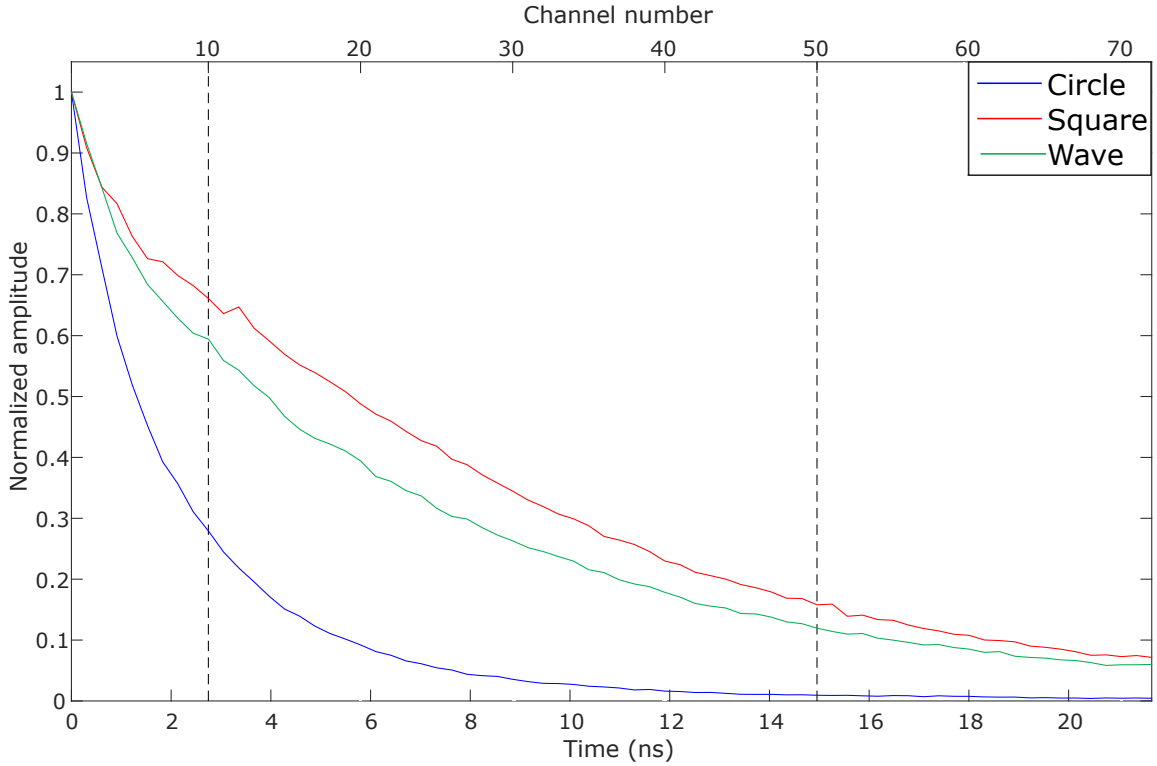

FIGURE VI.4 – Time curves obtained from the restored images $\mathbf{f}_t$ by summing the pixels in each area of the sample for each time channel. The dotted black vertical bars correspond to the time channels of the images (c) and (d) displayed in Fig. VI.3.

phantom can be computed. For this, the pixels within each area are summed for each time point

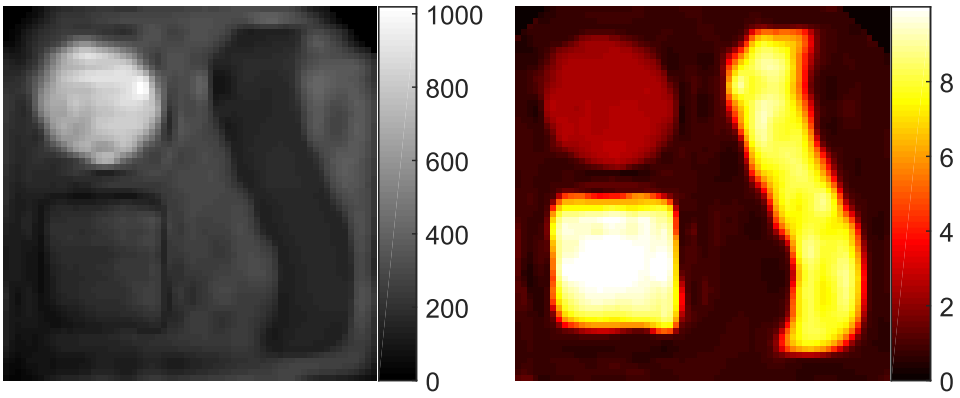

FIGURE VI.5 – Amplitude (arbitrary unit, left) and lifetime (in ns, right) maps obtained by fitting an exponential decay function on the experimental time curves for each pixel.

and then normalized to give the curves of Fig. VI.4. In addition, for each pixel of the image, the fitting of (VI.8) is performed to give the amplitude and lifetime maps of Fig. VI.5.

VI.4.2 Multispectral time-resolved acquisitions

After binning of the TCSPC time-channels, a total of $T = 60$ time-channels was obtained covering times from 0 to 18.00 ns. The object was illuminated in the spectral band $470 - 490$ nm. Regarding the spectrometer's settings, its central wavelength was chosen at $\lambda_c = 575$ nm. The $\Lambda = 16$ spectral channels covered wavelengths from, approximately, 505 ± 5 nm to 655 ± 5 nm with a 10 nm step.

Figure VI.6 displays a photo of the phantom as well as the restored 64×64 CW image $\mathbf{f}$ obtained by (VI.4). It further shows several images $\mathbf{f}_t$ (resp. $\mathbf{f}_\lambda$) in different time (resp. spectral) channels obtained from (VI.3).

Within each area of the phantom, time (resp. spectral) curves are given in Fig. VI.7. They were computed by summing the pixels of $\mathbf{f}_t$ (resp. $\mathbf{f}_\lambda$) of (VI.3) within the different areas of the sample for each time (resp. spectral) channel. The vertical dotted black bars correspond to the restored images displayed in Fig. VI.6.

As it was performed for the TR measurements, if one integrates the spectral information to get $\mathbf{f}_t$ as in (VI.3), the amplitude and lifetime maps can be estimated. Figure VI.8 shows these two maps obtained with the exponential fitting described by (VI.8) using the data from $\mathbf{f}_t$.

VI.5 Discussion

VI.5.1 Fluorescence lifetime sensing

Even with a CR as high as 93%, the results of Fig. VI.3 prove that using our ABS-WP framework, one can acquire a good quality image showing the different shapes of the object. As expected since it is a sum version of the time channels, the CW image presents the three main structures of the phantom. However, Fig. VI.3-(c) and (d) displaying SPC restored images in two time gates do not show exactly the same structures since the lifetimes of the three involved fluorophores are not the

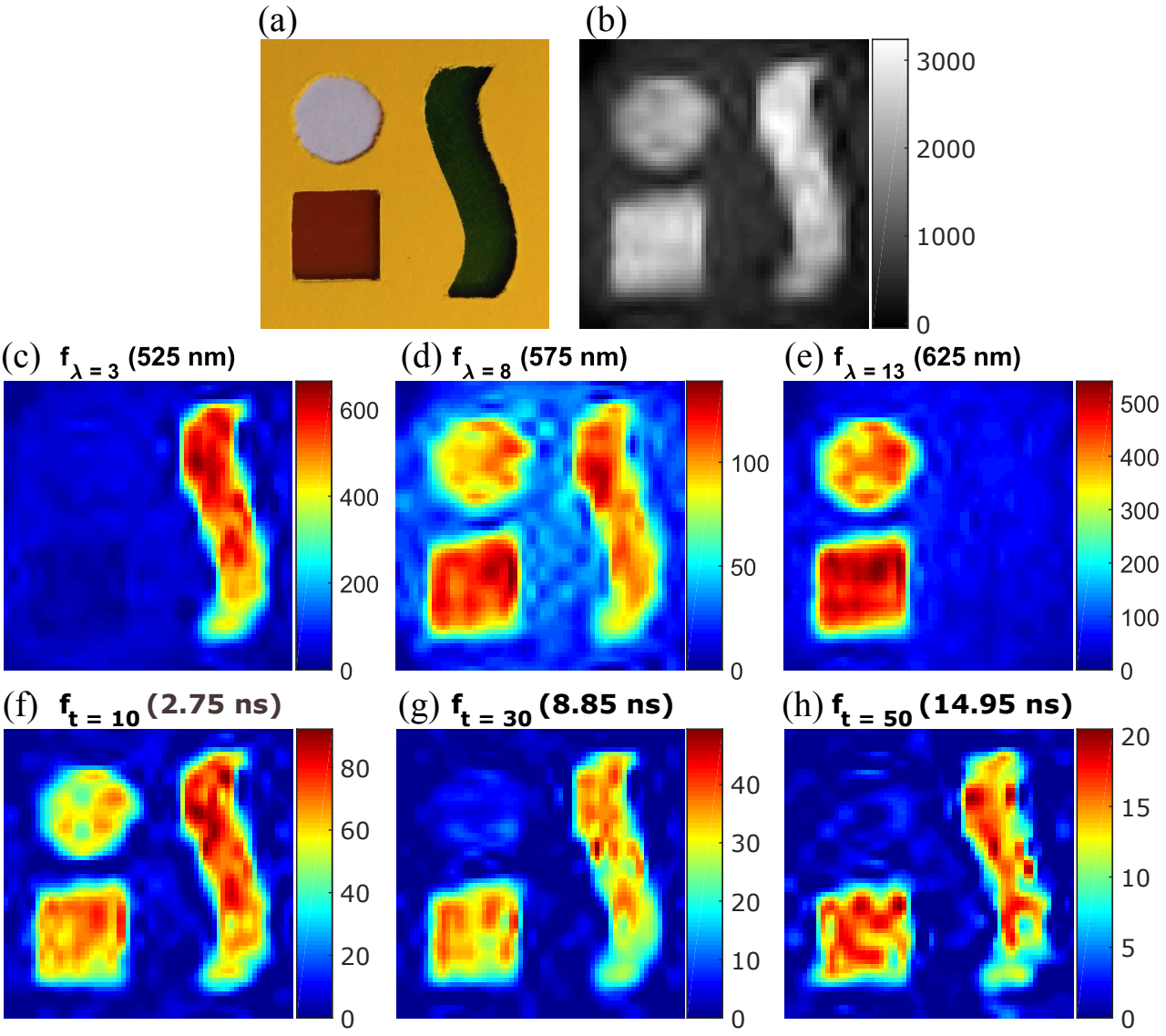

FIGURE VI.6 – Phantom, CW image and SPC restored images in different time or spectral channels using Daubechies' wavelet (Db5). (a) Photo of the phantom, (b) CW image, SPC restored images in (c)–(e) 3 spectral channels and (f)–(h) 3 time channel.

same. In a late gate, the circle shape is almost not present anymore compared to an early gate. The time curves of Fig. VI.4 confirms the difference of lifetime with a much faster exponential decay for the circle compared to the other two structures. Once the fit of (VI.8) is completed, the precise lifetime for the three components can be measured with the results of Fig. VI.5. The DCM dye can therefore be discriminated from the two other components using the time information alone.

Moving on to the system's capabilities, the temporal resolution of the imaging setup is mainly affected by the TCSPC board and detector, which is always better than what can be achieved with an array of detectors. Since only one board is needed in a SPC design, this enables one to choose high-end boards depending on the desired application. In our system, if the total time-window width is strongly reduced, a temporal resolution of tens of picoseconds can be reached which is quite good. Concerning the spatial resolution, it is given by the employed SLM pattern size and the optics which allows for a wide range of possibility, newest DMDs reaching pattern sizes of up

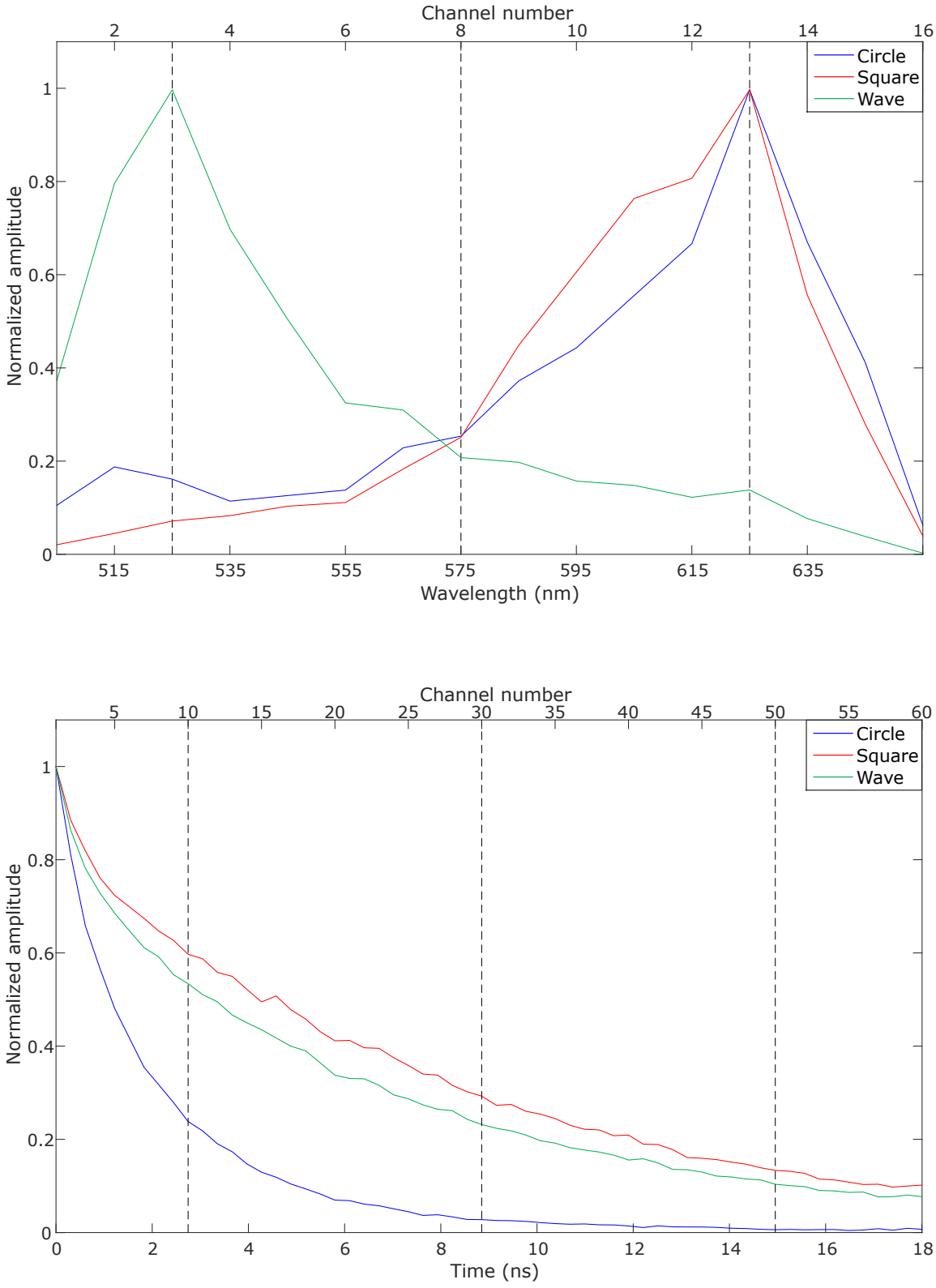

FIGURE VI.7 – Spectrum and time curves obtained from the restored images $\mathbf{f}_\lambda$ and $\mathbf{f}_t$ by summing the pixels in each area of the sample for each wavelength/time channel. The dotted black vertical bars correspond to the time/wavelength channels for the images displayed in Fig. VI.6.

to 1600×2560 pixels. A pixel pitch of about 500 μm was measured in our setup. Consequently, the use of a SPC with a TCSPC board opens the possibility for a system with both high temporal and spatial resolutions. The use of an *adaptive* technique such as ABS-WP permits fast acquisi-

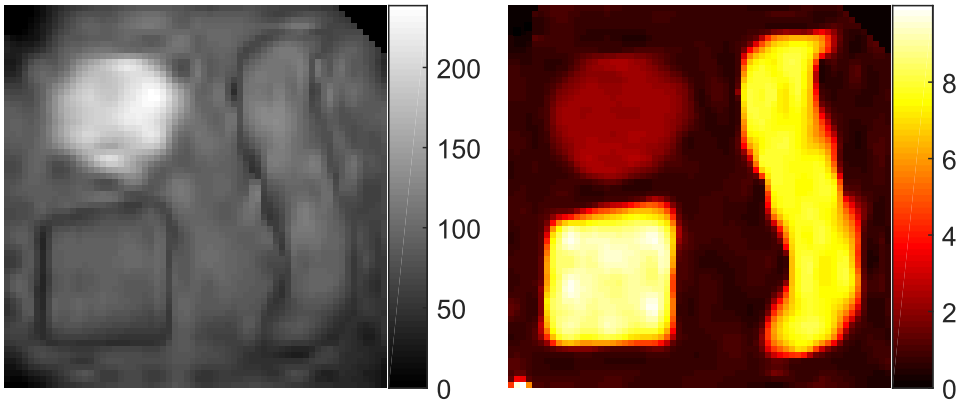

FIGURE VI.8 – Amplitude (arbitrary unit, left) and lifetime (in ns, right) maps obtained from $\mathbf{f}_t$ by fitting an exponential decay function on the experimental time curves for each pixel.

tions with few measurements and straightforward image restoration. The use of the conventional *nonadaptive* CS approach would, in the TR case where T images have to be restored, suffer from long image restoration times, especially for high resolution images.

Overall, our ABS-WP framework coupled to the low cost aspect of the TR SPC makes it an efficient candidate for fluorescence lifetime imaging microscopy. The implementation of a SPC on a microscope using random CS (Rodriguez *et al.*, 2016) or Hadamard patterns (Radwell *et al.*, 2014) has indeed already been shown.

In conclusion, our adaptive wavelet-based acquisition strategy applied to a time-resolved single pixel imaging system was demonstrated. The proposed system allowed for efficient acquisition of TR image with high compression rates and little degradation of the image quality. A possible application in the biomedical field concerns fluorescence lifetime imaging microscopy.

A limitation of the TR setup regards the discrimination of objects having the same lifetime. As shown by the results of Fig. VI.3 and Fig. VI.5, the square and wave shapes almost have the same lifetime and hence cannot be differentiated from each other. Fluorophores, in addition to their lifetime, emit light at different wavelengths. In the next section, a spectrometer is therefore added to the system in order to use both spectral and temporal information to discern the three chemical components.

VI.5.2 Multispectral time-resolved acquisitions

The results of Fig. VI.6 show that our framework ABS-WP permits to recover with a compression rate as high as 93% the stack of $\Lambda \times T$ images in the Λ spectral channels and T time-channels. The use of the CW image of Fig. VI.6-(b) is justified for the prediction step of ABS-WP since it presents the different structures of the phantom. As a result, our strategy finds significant wavelet coefficient for each shapes that are therefore accurately recovered.

If we look at the spectral dependent image $\mathbf{f}_\lambda$ of Fig. VI.6, only the wave stands out for the 525 nm wavelength channel but disappears after the 625 nm wavelength channel. The other way

around happens for the square and circle shapes. This was expected by the characterization of table VI.1 for which the emission peak of the wave fluorophore is at 525 nm and around 625 nm for the other two fluorophores. The detail spectral curves of Fig. VI.7 confirms the results and are in accordance with the characterization of the phantom in table VI.1.

Regarding the time information using the temporal dependent images $\mathbf{f}_t$, similar measurements to what was acquired in Section VI.4.1 are obtained without surprise. The circle has a shorter lifetime compared to the square and wave as shown by Fig. VI.7 and the lifetime map of Fig. VI.8. While the latter one is sensibly the same as the one obtained in Fig. VI.5 with the TR system, the amplitude is slightly different with different number of counts. This is simply because the laser power on the day of these experiments and the experiments before (with the TR system only) was set to a different value. The lifetimes however do not depend on the intensity of the laser and do not change from one experiment to the other.

The addition of the spectral information compared to the results of Section VI.4.1 has a great impact; with the temporal information only, one could not discriminate the square shape from the wave. With the spectral information, the three fluorophores involved in the phantom can be completely differentiated using both spectral and temporal informations. Overall, time-resolved spectral information can provide a way to better discriminate different fluorophores when spectral (or temporal) discrimination is not possible. This can be an important feature in biology to discriminate different structures in tissues.

Moving on to the system's capabilities, a discussion on the spectral side is given since the temporal and spatial resolutions have been discussed in Section VI.5.1. The spectral resolution of the system is given by the employed spectrometer (slit and grating mostly). The SPC can therefore be used to produce images with high spectral resolution at much lower cost than standard imaging devices with array of sensors. Single point spectrometer can indeed provide nanometer resolution for some thousands of euros, where conventional imaging systems with similar resolution would be about 10 times more expensive. The same can be obtained with a single detector with a scan (i.e., rotation) of the grating. However, SPC has the advantages of directly recovering spatial information (without scanning) and there is the possibility to cover a wider spectral range (e.g., infrared).

Overall, SPC acquisition represents a good trade-off between spatial, temporal and spectral resolutions that currently has no equivalent for the same price. Employing an *adaptive* strategy such as ABS-WP in this context is motivated by the speed of acquisition (i.e., high compression rate) and fast image recovery which is crucial when a stack of $\Lambda \times T$ images should be recovered. ABS-WP was shown to perform multispectral time-resolved imaging with high compression rates on a phantom embedding several fluorophores.

VI.6 Conclusion

In this chapter, the applicability of ABS-WP proposed in Chapter IV was demonstrated on a (multispectral) time-resolved imaging system. Unfortunately, at the time of these experiments, the pattern generalization technique proposed in Chapter V was not yet implemented for testing. Experiments have been performed on a phantom embedding fluorophores which emit light at different wavelengths and with their own lifetime. With high-compression rates, our ABS-WP framework allowed to recover both spectral and temporal informations that led to a complete discrimination of the fluorophores.

This is a first step towards medical applications since a multispectral time-resolved imaging system can be exploited to characterize biological tissues. For instance, the biological micro-environment (pH, temperature, ion concentration, etc.) of the tissues (Marcu, 2012; Ma *et al.*, 2015) can be studied which is an essential parameter for biologist.

Overall, the single-pixel camera is an excellent candidate to create multispectral (or hyperspectral) time-resolved system at low costs. The single-point detector indeed allows one to choose high quality photon counting boards (resp. spectrometers) with high temporal (resp. spectral) resolutions. The SPC represents a fine trade-off between spatial, temporal and spectral resolutions that has currently no equivalent for the same price.

CONCLUSION, LIMITATIONS AND PERSPECTIVES

SINGLE-PIXEL IMAGING (SPI) captures the projection of the scene under view onto patterns with an optical setup equipped with a single-point detector. This rather low-cost simple implementation and the non-ionizing aspect of optical imaging make SPI a good candidate for medical applications. Hence, the goal of this thesis was to investigate acquisition/restoration schemes in SPI and their application in biomedical imaging. One of the main limitations of the single-pixel camera regards the relatively low speed of the acquisition and/or image restoration. Real-time applications therefore cannot be considered, which rules out interventional imaging for instance.

Our contributions to speed up acquisition and/or image restoration are threefold :

— a complete framework to control the instruments and data processing in an *adaptive* approach (Chapter III) ;

— the *adaptive basis scan by wavelet prediction* (ABS-WP) technique, which paves the way for the employment of other wavelets than Haar's and it reduces image restoration times compared to compressive sensing based technique (Chapter IV) ;

— the pattern generalization method, which permits to divide by a factor of two the number of measurements compared to conventional acquisitions (Chapter V).

Overall, ABS-WP, implemented with the first contribution, reduces image restoration times (less than a second vs seconds to minutes for compressive sensing) while the pattern generalization algorithm permits to reduce the acquisition times (by a factor of two).

As a proof of concept for medical applications, Chapter VI finally presented multispectral time-resolved measurements on a phantom with the previous contributions. With compression rates as high as 93%, ABS-WP was able to recover both spectral and time informations to completely discriminate the involved fluorophores.

Limitations A first limitation of the contributions of this thesis regards the prediction of the significant wavelet coefficients in our ABS-WP framework. As depicted by the results of table IV.3, our technique finds the correct significant wavelet coefficients with a maximum accuracy of 85%. If this accuracy could reach 100%, the best possible SPC image would be acquired since the non-

linear approximation of the wavelet transform is one of the strongest possible approximations [2].

ABS-WP permits to use any kind of wavelet for which patterns have real floating values. The DMD is hence used in its 8-bit mode to load such patterns which is a second limitation as the DMD's refresh rate is impacted. The DMD can indeed reach its highest frame rate when used in binary mode but this frame rate is reduced when 8 bits are necessary inducing an increase of acquisition times. In our experiments, this was not a problem since the TCSPC board needs acquisitions during a few hundreds ms and our DMD's frequency is 290 Hz in 8-bit. If fast acquisitions are required, one can still employ our strategy with Haar's wavelet which creates binary patterns.

For pattern generalization, a limitation is the combination of several measurements compared to the classical splitting or shifting methods which combines only two measures. In the presence of noise, the variance of the final desired measurement vector for the SNMF algorithm depends on the sum of the variances of the SPC acquired measurements. If the measures are really noisy, this can increase the effect of noise and hence reduce the quality of the recovered image. Such an effect is less visible for the classical splitting and shifting techniques with only two combinations.

While the proposed SNMF algorithm reduces the number of effective measurements and hence acquisition times, a last limitation arises since the positive patterns are computed on the fly for adaptive measurements. Table V.1 shows that, as the dimensions of the problem increases, computation times also increases. During this factorization, no acquisitions can be performed and this therefore increases the total acquisition time (acquisition + computation time) in an adaptive strategy. If a nonadaptive scheme is considered, this is not a limitation since the set of positive patterns can be computed once and for all.

Perspectives A first perspective of this thesis could be an improvement of the prediction strategy in ABS-WP. As mentioned earlier, some significant wavelet coefficients are not acquired which impacts the quality of the restored image. More robust methods for this prediction compared to the employed bicubic interpolation could be considered. This prediction however should be fast enough not to slow down the total acquisition time so only fast techniques should be considered. One idea would be to use deep learning techniques to predict either the value of coefficients or their relevance. Such an approach would be fast since the training part of a neural network can be done a priori on a database of hundreds of images. Then the application of the network on the new data is quite fast.

Another perspective regards the proposed pattern generalization problem. It allows to create K positive patterns from a set of I patterns having positive and negative values. Using the proposed SNMF algorithm, one currently obtains $K = I + 1$. Most matrix factorization algorithms however search for factorization for which $K < I$. Such techniques could therefore be investigated in order to lower the number of effective measurements. A possible problem would be that the factorization error would be more important which could lead to flawed measurements. Having $K < I$ would also permit to combine less measurements to lower the noise of the desired mea-

2. Strongest possible approximation in comparison to a nonlinear approximation in Fourier, DCT or any other basis.

surements. Another possibility to deal with the noise effect in the SNMF algorithm would be to add sparse constraints on the matrix $\mathbf{T}$. If this matrix has zeros, the desired measurement vector would indeed be created from less combinations of measurements. A problem is that the rows of $\mathbf{T}$ should still sum to 0 and adding the sparse constraint might require to increase the value of K.

Regarding the multispectral time-resolved acquisitions of Chapter VI, the prediction step of our ABS-WP framework was based on the continuous-wave measurements which integrates all spectral and time channels. However, some of these channels do not receive much information and hence do not bring much information in the CW measurements. In order to maximize the accuracy of the prediction in ABS-WP, another step could be added just before the prediction. The latter could search for the spectral and time channels which bring the least information in order to discard them in the integration step of the channels to create the CW measure [3].

On the application side, the next step is to apply the developed tools for interventional imaging, e.g, image-guided surgery. This is a completely new work in itself as the tools developed in this manuscript would have to be adapted to video imaging. Exploiting time information with some of the previous perspectives could permit to achieve much higher compression rates (i.e., acquire less measurements) so as to reach video rates.

3. By definition, if some channels are discarded, this would not exactly be CW measurements.

APPENDIX A

DMD IN b-BIT MODE

We note $\mathbf{p} \in \mathbb{R}^{D\times 1}$ the vector representing a DMD pattern and assume it is coded on b bits, i.e., each entry of $\mathbf{p}$ is an integer in $\{0,1,\ldots,2^b-1\}$. Such a pattern can be decomposed as a weighted sum of b different binary patterns noted $\mathbf{b}_i \in \mathbb{R}^{D\times 1}$, with $i = 1\ldots b$, which are referred to as the bit planes of $\mathbf{p}$. Mathematically we have

$$\mathbf{p} = \sum_{i=1}^{b} 2^{i-1}\mathbf{b}_i. \tag{A.1}$$

Note that each bit plane is associated to a weight that is a power of 2, e.g., the first bit plane $\mathbf{b}_1$ correspond to $2^0 = 1$.

Let us take an example for $b = 4$ and the pattern given in Fig. A.1 where each pixel codes a unique integer value in $\{0,1,\ldots,15\}$, hence the obtained pattern size is 4×4. The corresponding 4 bit planes are given in Fig. A.2.

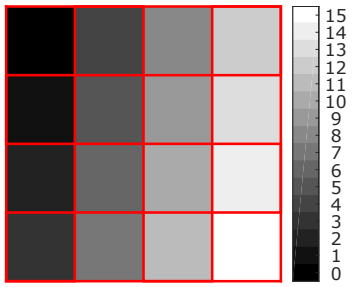

FIGURE A.1 – Considered pattern coded on $b = 4$ bits with each pixel having a unique integer value in the range $[0,15]$. The top left corner pixel has the value 0 while the bottom right one has the value 15. In between, the other pixels pave the remaining pixel values.

For example, the pixel at top right corner of $\mathbf{p}$ in Fig. A.1 corner has a value of 12. This value is coded on 4 bits as $0\times 2^0 + 0\times 2^1 + 1\times 2^2 + 1\times 2^3$ hence the same pixel has the value 0 (resp. 1) in $\mathbf{b}_0$ and $\mathbf{b}_1$ (resp. $\mathbf{b}_2$ and $\mathbf{b}_3$) in Fig. A.2.

At this stage, the DMD can work with the binary patterns $\mathbf{b}_i$ with the 0 (resp. 1) corresponding to the OFF (resp. ON) sate of the DMD. To recreate a pattern on b-bits, the power of 2 of (A.1) are divided by 2^b-1 so as to give the weights

$$w_i = \frac{2^{i-1}}{2^b-1} \quad \text{with} \quad \sum_{i=1}^{b} w_i = 1. \tag{A.2}$$

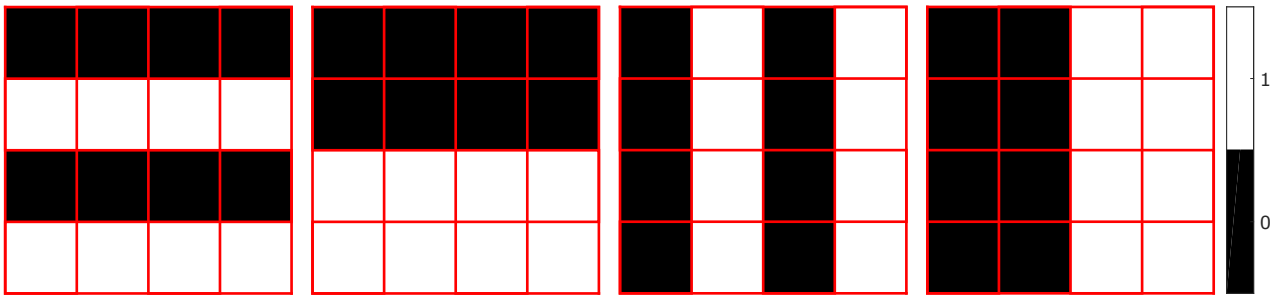

FIGURE A.2 – The four bit planes of the pattern displayed in Fig. A.1. From left to right, bit planes $\mathbf{b}_0$ to $\mathbf{b}_3$.

These weights can be encoded as the display time of each bit plane $\mathbf{b}_i$ in order to recreate the pattern of (A.1) [1]. For instance, if the DMD's frame rate is set to f in Hz, then the total display time of a b-bit plane is $t_d = 1/f$ and each bit plane is allocated a display time of $t_i = w_i t_d$ to form the b-bit pattern. For instance, in our previous example, we have the display times t_i given in Fig. A.3.

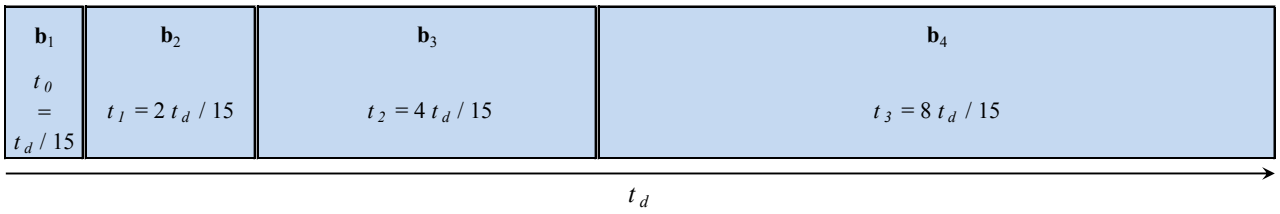

FIGURE A.3 – Display time of the four bit planes to recreate a four bit pattern.

Note that in the DMD employed in the experimental acquisitions of this thesis, the ALP library provided with the DMD manages itself the splitting of the b-bits patterns on its bit planes and associates automatically the display time. Only the DMD's frame rate is chosen which corresponds to the frequency at which a new pattern can be loaded.

1. Up to the scalar factor $\frac{1}{2^b-1}$.

APPENDIX B

COMPLEMENTS TO CHAPTER V

Below are some complements of Chapter V leading to the final matrix $\mathbf{T}$ and $\mathbf{P}$ employed in the SNMF algorithm. For the matrix and vector derivatives used below, we refer the reader to the Matrix Cookbook Petersen *et al.* (2008).

B.1 Dual problem to solve for T

As a reminder of what was exposed in Chapter V, the problem to solve to find the solution for $\mathbf{T}$ is the following :

$$\min_{\mathbf{T}} \left\| \check{\mathbf{P}} - \mathbf{TP} \right\|_{\mathrm{F}}^2 \quad \text{such that} \quad \mathbf{T}\mathbf{1}_K = \mathbf{0}_I. \tag{B.1}$$

To solve the dual problem, we first write the Lagrange function $\mathcal{L}$:

$$\mathcal{L}(\mathbf{T}, \boldsymbol{\lambda}) = \left\| \check{\mathbf{P}} - \mathbf{TP} \right\|_{\mathrm{F}}^2 + \boldsymbol{\lambda}^\top \mathbf{T}\mathbf{1}_K$$

$$\mathcal{L}(\mathbf{T}, \boldsymbol{\lambda}) = \mathrm{tr}\left(\left(\check{\mathbf{P}} - \mathbf{TP} \right) \left(\check{\mathbf{P}} - \mathbf{TP} \right)^\top \right) + \boldsymbol{\lambda}^\top \mathbf{T}\mathbf{1}_K$$

$$= \mathrm{tr}\left(\mathbf{TPP}^\top \mathbf{T}^\top - \mathbf{TP}\check{\mathbf{P}}^\top - \check{\mathbf{P}}\mathbf{P}^\top \mathbf{T}^\top + \check{\mathbf{P}}\check{\mathbf{P}}^\top \right) + \boldsymbol{\lambda}^\top \mathbf{T}\mathbf{1}_K \tag{B.2}$$

where $\boldsymbol{\lambda} = (\lambda_1, ..., \lambda_I)^\top \in \mathbb{R}^{I \times 1}$ are the Lagrange multipliers. We now write the dual function $\mathcal{D}$:

$$\mathcal{D}(\boldsymbol{\lambda}) = \min_{\mathbf{T}} \mathcal{L}(\mathbf{T}, \boldsymbol{\lambda}) = \mathcal{L}(\mathbf{T}(\boldsymbol{\lambda}), \boldsymbol{\lambda})$$

with $\mathbf{T}(\boldsymbol{\lambda}) = \arg\min_{\mathbf{T}} \mathcal{L}(\mathbf{T}, \boldsymbol{\lambda})$ for $\boldsymbol{\lambda}$ fixed. If the dual function $\mathcal{D}$ is differentiable, then $\mathbf{T}(\boldsymbol{\lambda}^*) = \mathbf{T}$, with if $\boldsymbol{\lambda}^* = \arg\max_{\boldsymbol{\lambda}} \mathcal{D}(\boldsymbol{\lambda})$, is the solution of the primal problem (V.19).

First, we search $\mathbf{T}(\boldsymbol{\lambda}) = \arg\min_{\mathbf{T}} \mathcal{L}(\mathbf{T}, \boldsymbol{\lambda})$ by expressing the derivative of $\mathcal{L}$, using (B.2) :

$$\frac{\partial \mathcal{L}(\mathbf{T}, \boldsymbol{\lambda})}{\partial \mathbf{T}} = 2\mathbf{TPP}^\top - 2\check{\mathbf{P}}\mathbf{P}^\top + \boldsymbol{\lambda}\mathbf{1}_K{}^\top \tag{B.3}$$

$\mathbf{T}(\boldsymbol{\lambda})$ is found when (B.3) is null. This gives

$$\mathbf{T}(\boldsymbol{\lambda}) = \left(\check{\mathbf{P}}\mathbf{P}^\top - \frac{1}{2}\boldsymbol{\lambda}\mathbf{1}_K{}^\top \right) \left(\mathbf{PP}^\top \right)^{-1} \tag{B.4}$$

We now use (B.4) in the equality constraint (V.13) to get the optimal Lagrange multipliers $\boldsymbol{\lambda}^*$:

$$\mathbf{T}(\boldsymbol{\lambda}^*)\mathbf{1}_K = \mathbf{0} \Rightarrow \left(\check{\mathbf{P}}\mathbf{P}^\top - \frac{1}{2}\boldsymbol{\lambda}^* {\mathbf{1}_K}^\top\right)\left(\mathbf{P}\mathbf{P}^\top\right)^{-1}\mathbf{1}_K = \mathbf{0}$$

leading to

$$\boldsymbol{\lambda}^* = \frac{2}{{\mathbf{1}_K}^\top\left(\mathbf{P}\mathbf{P}^\top\right)^{-1}\mathbf{1}_K}\check{\mathbf{P}}\mathbf{P}^\top\left(\mathbf{P}\mathbf{P}^\top\right)^{-1}\mathbf{1}_K \tag{B.5}$$

Finally, one can get the final expression of $\mathbf{T}$ solving the problem (V.19) by replacing (B.5) in (B.4) :

$$\mathbf{T} = \check{\mathbf{P}}\mathbf{P}^\top\left(\mathbf{P}\mathbf{P}^\top\right)^{-1}\left(\mathbf{I} - \frac{1}{{\mathbf{1}_K}^\top\left(\mathbf{P}\mathbf{P}^\top\right)^{-1}\mathbf{1}_K}\mathbf{1}_{K\times K}\left(\mathbf{P}\mathbf{P}^\top\right)^{-1}\right) \tag{B.6}$$

where $\mathbf{I}$ is the identity matrix of size $K \times K$ and $\mathbf{1}_{K\times K} = \mathbf{1}_K {\mathbf{1}_K}^\top$ is the matrix of size $K \times K$ with all entries equal to one.

B.2 Block coordinate descent for P

This time, $\mathbf{T}$ is considered fixed and the problem to solve is

$$\min_{\mathbf{p}_k} \mathcal{F}(\mathbf{P}_{-k}, \mathbf{p}_k) \quad \text{such that} \quad \mathbf{p}_k \geq 0 \tag{B.7}$$

with

$$\mathcal{F}(\mathbf{P}_{-k}, \mathbf{p}_k) = \left\|\check{\mathbf{P}} - \mathbf{T}_{|k}\mathbf{P}_{-k} - \mathbf{t}_k\mathbf{p}_k^\top\right\|_{\mathrm{F}}^2 = \left\|\boldsymbol{\Sigma} - \mathbf{t}_k\mathbf{p}_k^\top\right\|_{\mathrm{F}}^2 \tag{B.8}$$

where $\boldsymbol{\Sigma} = \check{\mathbf{P}} - \mathbf{T}_{|k}\mathbf{P}_{-k}$, $\mathbf{T}_{|k}$ (resp. $\mathbf{P}_{-k}$) is the matrix $\mathbf{T}$ (resp. $\mathbf{P}$) deprived of its column (resp. row) k and $\mathbf{t}_k \in \mathbb{R}^{I\times 1}$ (resp. $\mathbf{p}_k \in \mathbb{R}^{D\times 1}$) is the k-th column (resp. row) of $\mathbf{T}$ (resp. $\mathbf{P}$).
Let us rewrite $\mathcal{F}(\mathbf{P}_{-k}, \mathbf{p}_k)$ as

$$\left\|\boldsymbol{\Sigma} - \mathbf{t}_k\mathbf{p}_k^\top\right\|_{\mathrm{F}}^2 = \mathrm{tr}\left(\left(\boldsymbol{\Sigma} - \mathbf{t}_k\mathbf{p}_k^\top\right)\left(\boldsymbol{\Sigma} - \mathbf{t}_k\mathbf{p}_k^\top\right)^\top\right)$$

for which we now take its derivative with respect to $\mathbf{p}_k$:

$$\frac{\partial\mathcal{F}(\mathbf{P}_{-k}, \mathbf{p}_k)}{\partial\mathbf{p}_k} = 2\mathbf{p}_k{\mathbf{t}_k}^\top\mathbf{t}_k - 2\boldsymbol{\Sigma}^\top\mathbf{t}_k = 2\left(\mathbf{p}_k\|\mathbf{t}_k\|_2^2 - \boldsymbol{\Sigma}^\top\mathbf{t}_k\right). \tag{B.9}$$

The minimum of (B.7) is found when (B.9) is null and adding the projection operation onto the feasible set $\mathbb{R}_+^{D\times 1}$ leads to the solution

$$\mathbf{p}_k = \max\left(\mathbf{0}_D, \frac{\boldsymbol{\Sigma}^\top\mathbf{t}_k}{\|\mathbf{t}_k\|_2^2}\right) \tag{B.10}$$

with the max function applied to each entry of both vectors.

APPENDIX C

RÉSUMÉ ÉTENDU EN FRANÇAIS

Table des matières

Introduction

La caméra mono-pixel (*single-pixel camera*, SPC) est un dispositif émergent permettant l'acquisition d'images à bas coût. En effet, l'architecture de cette caméra comporte seulement deux éléments, un modulateur spatial de la lumière (*spatial light modulator*, SLM) et un détecteur ponctuel (*single point detecteur*, SPD). L'idée est de moduler la scène à imager avec des motifs chargés au niveau du SLM et la mesure correspondante est obtenue par le détecteur ponctuel. Le post-traitement d'une séquence de mesures obtenue pour différent motifs permet de restaurer l'image de la scène observée.

Les premières images par une SPC ont été obtenues à l'Université de Rice en 2006. A l'époque, les idées pionnières de l'acquisition comprimée (*compressive sensing*, CS) proposées par Donoho ont rendu possible l'utilisation de motifs aléatoires et la restauration d'images par minimisation ℓ_1 pour la SPC par Takhar *et al.*. Depuis, de nouvelles stratégies d'acquisitions ont été proposées et la SPC a trouvé de nombreuses applications.

A première vue, avoir un seul pixel peut sembler contre-productif puisque la plupart des caméras actuelles contiennent des millions de pixels acquis simultanément. Cependant, plusieurs avantages ressortent quand la SPC est comparée avec les architectures de caméras CCD ou CMOS. Tout d'abord, les détecteurs ponctuels ont souvent un haut rendement si bien qu'ils sont capables de détecter de très faibles changement d'intensité lumineuse (Hadfield, 2009). Pour des applications médicales, ceci peut être très utile puisque l'absorption des tissus est bien souvent élevée (Jacques, 2013). Le second avantage est la compression réalisée au niveau matériel (i.e. un détecteur donc une donnée), peu de mémoire de stockage est ainsi nécessaire. Ceci est un point clé pour des applications comme l'imagerie à distance (e.g. télédétection aérospatiale) où le taux de transmission des données est relativement faible (Ma, 2009b,a). Enfin, un détecteur ponctuel est généralement moins couteux qu'une matrice de capteurs. La SPC devient alors un candidat parfait pour l'imagerie infrarouge (Shin *et al.*, 2016) pour laquelle un imageur conventionnel fonctionnant à ces longueurs d'ondes serait onéreux (Rogalski, 2012).

Tous ces avantages et la nature non-ionisante de l'imagerie optique rendent la SPC très attrayante pour des applications en imagerie médicale. Par exemple, un système résolu en temps à bas coût est bénéfique pour l'imagerie du temps de vie de fluorescence (Becker, 2012) en couplant le détecteur à une carte de comptage des photons (Pian *et al.*, 2016a; Rousset *et al.*, 2017b). L'ajout d'un spectromètre (Pian *et al.*, 2016b) permet d'obtenir une information spectrale supplémentaire pour étudier le micro-environnement (pH par exmple) des tissus biologiques. D'autres applications dans le domaine médical sont possibles parmi lesquelles l'imagerie à travers des milieux diffusants (Tajahuerce *et al.*, 2014; Duran *et al.*, 2015), l'imagerie optique diffuse (e.g. intra-

opératoire ou la détection des lésions de la peau (Gibson *et* Dehghani, 2009)), l'ophtalmologie (Lochocki *et al.*, 2016, 2017), la tomographie optique diffuse (D'Andrea *et al.*, 2010; Ducros *et al.*, 2013; Pian *et al.*, 2015; Ducros *et al.*, 2016) (e.g. oximétrie et imagerie moléculaire), ou encore la caractérisation des propriétés des tissus par illumination infrarouge (Torabzadeh *et al.*, 2017).

Le but de cette thèse est l'étude de techniques pour l'acquisitions d'images SPC à visée médicale. Une des principales limitations de ce système optique dans les travaux cités précédemment est la durée de l'acquisition et/ou de la restauration d'images. Dans ces cas, des applications en temps réel ne peuvent être considérées, excluant ainsi l'imagerie interventionnelle par exemple. Il est alors souhaitable d'avoir des techniques plus rapides pour l'acquisition et/ou la restauration par SPC pour l'imagerie médicale.

Pour parvenir à ces objectifs, nous avons proposé une nouvelle stratégie d'acquisition SPC pour réduire le temps de restauration ainsi qu'une technique innovante pour réduire les temps d'acquisitions d'un autre côté. L'applicabilité de ces méthodes pour l'imagerie biomédicale a été démontrée par des mesures multispectrales résolues en temps.

Ce travail a été réalisé dans le cadre d'une cotutelle entre l'INSA de Lyon et le Politecnico di Milano. Les parties expérimentales de cette thèse ont été réalisées à Milan où une SPC est disponible. Les méthodes et algorithmes ont quant à eux été développés au sein du laboratoire CREATIS.

Ce manuscrit de thèse est divisé en six chapitres. Les deux premiers donnent l'état de l'art de la SPC alors que les quatre suivants répondent à la problématique de cette thèse avec ses différentes contributions.

Au Chaptitre I, le concept de la SPC et son implémentation matérielle sont présentés.

Au Chaptitre II, l'état de l'art concernant l'implémentation logicielle de la SPC est cette fois ci détaillée. Deux grandes catégories de techniques existent séparant les approches *non-adaptatives* des approches *adaptatives*.

Au Chaptitre III, les deux systèmes expérimentaux ayant servis à la validation expérimentale des algorithmes développés sont présentés. Le premier système est celui existant au Politecnico de Milan et le second est celui récemment monté au laboratoire CREATIS.

Au Chaptitre IV, notre stratégie d'acquisition *Adaptive Basis Scan by Wavelet Prediction* (ABS-WP) est expliquée. Cette méthode permet d'acquérir une image directement dans le domaine d'ondelettes et compare favorablement par rapport à d'autres méthodes d'acquisitions d'images par SPC. Ce chapitre contient principalement un article de revue publié dans *IEEE Transactions on Computational Imaging* en 2017 (Rousset *et al.*, 2017a).

Au Chaptitre V, une méthode pour diviser par deux le nombre de mesures est proposé. Cette méthode a été inventée pour contourner le fait que des motifs ayant à la fois des valeurs positives et négatives ne peuvent être mis en œuvre sur un SLM. Nous proposons dans ce chapitre une solution générale au problème qui peut être solutionnée par un algorithme de factorisation en matrices semi non-négatives. Les résultats de ce chapitre ont été déposés sous forme de brevet (Rousset *et al.*, 2017c) et soumis à *IEEE Transactions on Image Processing* (Rousset *et al.*, 2017d).

Au Chaptitre VI, la SPC avec les techniques des chapitres précédents est employée pour des

applications susceptibles d'être bénéfiques pour l'imagerie médicale. Une dimension temporelle et spectrale est ajoutée à la SPC afin d'obtenir des mesures multispectrales résolues en temps. Ceci permet d'imager un fantôme avec différents fluorophores afin d'en déduire leurs caractéristiques. Une partie de ces résultats ont été présentés à la conférence *SPIE Photonics West* (Rousset *et al.*, 2017b) en Février 2017.

C.1 CHAPITRE I - IMAGERIE MONO-PIXEL

Sous le nom imagerie mono-pixel se cachent différentes mises en œuvre optiques possibles pour lesquelles existent plusieurs stratégies d'acquisitions/restaurations. Ce chapitre donne le concept de la SPC puis regroupe la plupart de ses configurations matérielles existantes.

C.1.1 Concept

La théorie et les résultats de Donoho en 2006 sur l'acquisition comprimée (*compressive sensing*, CS) ont montré qu'un signal peut être restauré à partir d'un faible nombre de projections. Ceci a permis à Takhar *et al.* de proposer la même année une nouvelle architecture de caméra basée sur un simple détecteur ponctuel afin de produire un système d'imagerie compressive (Duarte *et al.*, 2008; Baraniuk *et al.*, 2014; Miao *et* Amirparviz, 2015).

Un tel système mesure une donnée 1D au lieu d'une information classique 2D obtenue par une matrice de capteurs conventionnelle (e.g. cameras CCD ou CMOS). Un modulateur spatial de la lumière (*spatial light modulator*, SLM) est placé entre la scène à imager et le détecteur ponctuel (i.e. pixel unique) de façon à moduler la lumière émanant de la scène et d'obtenir la projection correspondante au niveau du détecteur. Une séquence de mesures est prise avec différents motifs chargés sur le SLM qui, après post-traitement, permet de restaurer l'image de la scène. La

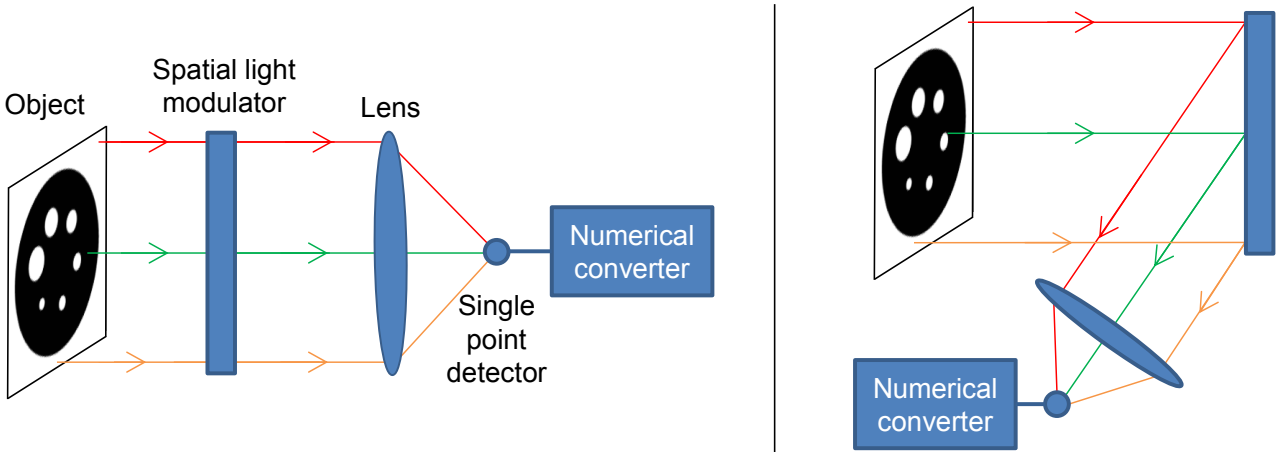

FIGURE C.1 – Montage optique d'une caméra mono-pixel en géométrie de transmission (gauche) ou de réflexion (droit).

mise en œuvre la plus simple d'une SPC peut être schématisée selon la Fig. C.1 où le SLM est soit un appareil réfléchissant, soit un système transmissif selon la technologie utilisée. L'image

de l'objet est formée dans le plan du SLM et une lentille est ajoutée afin de concentrer les rayons lumineux modulés au niveau du détecteur ponctuel. Un convertisseur numérique est enfin utilisé afin d'obtenir des données scalaires à partir du détecteur. Il est à noter que l'objet et le SLM sont complètement interchangeables. Si le SLM est placé avant [1] l'objet, on dit que la lumière est modulée en illumination, si placé après, le côté détection est modulé.

C.1.2 Configurations matérielles

A travers les années, plusieurs configurations matérielles de la SPC ont été proposées. Suivant l'application visée, une technologie spécifique devrait être choisie afin d'en tirer le meilleur. Cette section donne des exemples [2] de SLM et détecteurs ponctuels les plus employés ainsi que les différentes technologies pour obtenir des mesures numériques.

Modulateur spatial de la lumière Les travaux originels de Takhar *et al.* et Duarte *et al.* utilisent une matrice de micro-miroirs (*digital micromirror device*, DMD) inventée par Hornbeck à *Texas Instruments* en 1987. Ce dispositif comporte des milliers de petits miroirs arrangés sous forme de matrice de taille $H \times W$. Chacun de ces miroirs peut être indépendamment basculé dans deux positions. L'état ON à +12° réfléchit la lumière vers le détecteur qui est donc collectée. A −12°, l'état OFF envoie la lumière dans la direction opposée. Le DMD peut donc charger des motifs binaires pour lesquelles une valeur 0 (resp. 1) correspond à l'état OFF (resp. ON). Des motifs sur b-bits [3] peuvent également être chargés en utilisant le principe de modulation de largeur d'impulsion. Pour cela, un motif sur b-bits est décomposé en ses b motifs binaires (*bit planes*). A chacun d'eux est associé un certain temps de chargement sur le DMD, temps multiple d'une puissance de 2, ce qui permet de recréer un motif sur b-bits (voir Annexe A pour plus de détails).

En 2013, Huang *et al.* utilisent un écran à cristaux liquides (*liquid crystal display*, LCD) en tant que modulateur en géométrie de transmission [4]. Ce dispositif emploie des filtres polarisant et les propriétés d'orientation des cristaux liquides contrôlées par un courant électrique. Un état ON (resp. OFF) correspond ici à un élément transparent (resp. opaque) laissant passer (resp. bloquant) la lumière.

Contrairement aux précédents modulateurs d'intensité, un écran à cristaux liquides sur silicium (*liquid crystal on silicon*, LCoS) peut moduler la phase des rayons lumineux. Comme pour le LCD, un courant électrique contrôle les cristaux pour créer des motifs binaires. Ce dispositif est utilisé dans Clemente *et al.* (2013) pour faire de l'holographie compressée.

Détecteur ponctuel Une photodiode est classiquement employée dans la mise en œuvre de la SPC du fait de son prix généralement très bon marché. Elle est en effet simplement constituée d'un semi-conducteur capable de recevoir des photons et de les convertir en courant électrique.

1. Dans la direction de la lumière.
2. Liste non-exhaustive.
3. Suivant les modèles, b peut varier de 4 à 12 bits.
4. Des LCD en réflexion existent aussi mais ne sont pas présentés ici car les performances des DMDs sont bien meilleures.

Un autre détecteur ponctuel souvent utilisé est le photomultiplicateur qui permet également la détection des photons et leur conversion en courant électrique. La différence est que les photons captés lâchent des électrons dont le nombre peut être multiplié par application d'un courant électrique.

Convertisseur numérique Le signal électrique donné par la photodiode ou photomultiplicateur peut être digitalisé par un convertisseur analogique numérique (CAN). La valeur échantillonnée est proportionnelle à l'amplitude de l'intensité ou tension appliquée au CAN.

Certains détecteurs peuvent être couplés à une carte de comptage des photons (*time-correlated single photon counting*, TCSPC) employée en lien avec un laser pulsé illuminant l'objet. Un tel dispositif compte le nombre de photons et ceci pour différents canaux temporels suivant le temps de vol des photons grâce à la référence donnée par le laser pulsé. Dans ce cas, la mesure SPC n'est pas une simple donnée scalaire mais un vecteur de données scalaires pour chaque canal temporel.

C.1.3 Conclusion du chapitre

Ce chapitre a présenté les idées principales derrière la SPC et ses configurations matérielles possibles. Ces dernières peuvent prendre plusieurs formes, que ce soit en géométrie de transmission ou de réflexion. L'avantage principal de ce système est l'aspect bas coût du montage optique qui réalise une compression directement pendant l'acquisition.

Le côté matériel ayant été présenté dans ce chapitre, de nombreuses questions essentielles n'ont pas encore trouvé réponse : comment obtenir une image à partir de mesures sur un détecteur ponctuel? Quels sont les concepts et outils mathématiques derrière la SPC? Ces questions sont étudiées dans le prochain chapitre qui présente les différentes techniques d'acquisition et de restauration d'images par une SPC.

C.2 CHAPITRE II - TECHNIQUES D'ACQUISITION/RESTAURATION DES IMAGES

Contrairement à une matrice de capteurs type CCD ou CMOS où chaque pixel de l'image est acquis en parallèle, une acquisition SPC nécessite le traitement de plusieurs mesures afin de remonter à l'information spatiale de l'image. Différentes stratégies d'acquisition et de restauration des images par une SPC existent que l'on peut principalement séparer en deux catégories, les méthodes *non-adaptatives* et les méthodes *adaptatives*. Avant de détailler ces deux techniques, la modélisation mathématique d'une acquisition par une SPC est donnée.

C.2.1 Modélisation mathématique

On note N_0 (en photons par seconde, ph/s) la puissance émise par la source lumineuse et α (en ph/s) le courant d'obscurité mesuré au niveau du capteur quand $N_0 = 0$ ph/s. Soit $\mathbf{f} \in \mathbb{R}^{D\times 1}$ l'image $H \times W$ de la scène observée avec $D = H \times W$. La mesure m_k (ph) obtenue au niveau du détecteur durant le temps d'intégration Δt (en s) peut-être modélisée par

$$m_k = \Delta t \left(N_0 \mathbf{p}_k^\top \mathbf{f} + \alpha \right) \tag{C.1}$$

où $\mathbf{p}_k \in \mathbb{R}_+^{D\times 1}$ est un motif chargé sur le SLM. On note $\mathbf{P} = \left(\mathbf{p}_1, \ldots, \mathbf{p}_K\right)^\top \in \mathbb{R}_+^{K\times D}$ la matrice regroupant la séquence de K motifs à charger sur le SLM. Le vecteur de mesure $\mathbf{m} = (m_1, \ldots, m_K)^\top \in \mathbb{R}_+^{K\times 1}$ (ph) contient la séquence des K mesures correspondantes obtenues. Mathématiquement,

$$\mathbf{m} = \Delta t \left(N_0 \mathbf{P}\mathbf{f} + \alpha \mathbf{1}_K \right) \tag{C.2}$$

avec $\mathbf{1}_K = (1, \ldots, 1)^\top \in \mathbb{R}^{K\times 1}$.

Deux problèmes interviennent suite à l'écriture de ce modèle. Le premier concerne le choix de la séquence de motifs $\mathbf{P}$ alors que le second cherche à restaurer l'image $\mathbf{f}$ connaissant le vecteur de mesure $\mathbf{m}$ et les motifs $\mathbf{P}$.

C.2.2 Implémentation logicielle

Méthodes non-adaptatives Les premières méthodes de type *non-adaptatives* reposent sur la théorie de l'acquisition comprimée (*compressive sensing*, CS) (Donoho, 2006). L'idée est que la plupart des signaux sont compressibles dans une certaine base et ils peuvent ainsi être obtenus à partir d'un faible nombre de projections, i.e. $K << D$ mesures SPC. Les premières mesures CS par une SPC ont été proposées par Takhar *et al.* in 2006. La séquence de motifs $\mathbf{P}$ est alors choisie en tant que motifs aléatoires dont les valeurs sont ± 1 ce qui est bien adapté à la technologie ON/OFF des DMD par exemple. L'étape de restauration des images fait ensuite intervenir un algorithme de minimisation de la norme ℓ_1 afin de remonter, à partir des mesures $\mathbf{m}$, à l'image $\mathbf{f}$. Sous certaines conditions, il est possible de montrer que l'image $\mathbf{f}$ peut être parfaitement restaurée. L'avantage de cette méthode est le faible nombre de mesures $K << D$. En revanche, l'étape de restauration est lourde en calculs et peut prendre plusieurs minutes pour des images hautes résolutions.

Une autre possibilité *non-adaptative* est l'acquisition complète d'une image dans une certaine base (Hadamard, Fourier, ondelettes, transformée en cosinus, etc.), on parle alors de *basis scan*. La séquence de motifs est alors choisie comme $\mathbf{P} = \mathbf{B} \in \mathbb{R}^{D\times D}$ où $\mathbf{B}$ représente l'opérateur de transformation dans la base choisie. L'image est alors restaurée de façon directe avec l'opérateur de transformée inverse $\mathbf{B}^{-1}$. Par exemple, si la base choisie est celle de Fourier, les coefficients de Fourier sont acquis par la SPC dans le vecteur $\mathbf{m}$ auquel est appliqué la transformée de Fourier inverse pour obtenir l'image $\mathbf{f}$ de l'objet. L'avantage de cette méthode est donc l'étape de restauration qui est extrêmement rapide puisqu'elle ne nécessite aucune optimisation par rapport à l'approche CS. En revanche $K = D$ mesures doivent être acquises ce qui est trop long en pratique.

En résumé, les méthodes *non-adaptatives* peuvent être schématisées selon la Fig. C.2. Le choix de la séquence de motif est la même quelle que soit l'image observée d'où le nom de ces approches.

FIGURE C.2 – Schématisation d'une méthode d'acquisition non-adaptative.

Méthodes adaptatives Les méthodes *adaptatives* réalisent l'acquisition de l'image en plusieurs itérations j avec $1 \leq j \leq J$. Les mesures à l'itération j sont basées sur l'étude des mesures effectuées à l'étape $j-1$ d'où le nom *adaptatif*. L'idée principale est que, dans la plupart des bases, une image est compressible, c'est-à-dire que seuls $K << D$ coefficients sont nécessaires afin de remonter à l'image. La difficulté est qu'avec une SPC, l'image n'est a priori pas connue et les K coefficients à acquérir ne sont donc pas connus. Un schéma itératif permet ainsi de procéder à une première série de mesure $\mathbf{m}^{(j)}$ avec un sous ensemble $\mathbf{B}^{(j)} \in \mathbb{R}^{K^{(j)} \times D}$ de la base $\mathbf{B} \in \mathbb{R}^{D \times D}$ avec $K^{(j)} << D$. Cette série de mesures $\mathbf{m}^{(j)}$ est traitée afin de *prédire* l'ensemble $\mathcal{I}^{(j+1)}$ des prochains $K^{(j+1)}$ coefficients à acquérir à l'itération $j+1$. Au final, J itérations sont effectuées afin d'obtenir $K = \sum_{j=1}^{J} K^{(j)}$ coefficients avec $K << D$. L'image est alors restaurée en utilisant la transformée inverse $\mathbf{B}^{-1}$ de la base choisie comme dans le cas du *basis scan*. On parle ici d'*adaptive basis scan* qui tire avantage de la restauration rapide de l'image tout en effectuant que très peu de mesures. L'inconvénient est l'étape de prédiction qui doit être fiable pour prédire les bons coefficients significatifs dans la base $\mathbf{B}$ [5]. Cette étape doit également être rapide afin de ne pas perdre de temps lors de l'acquisition. La Fig. C.3 résume ce type d'approche.

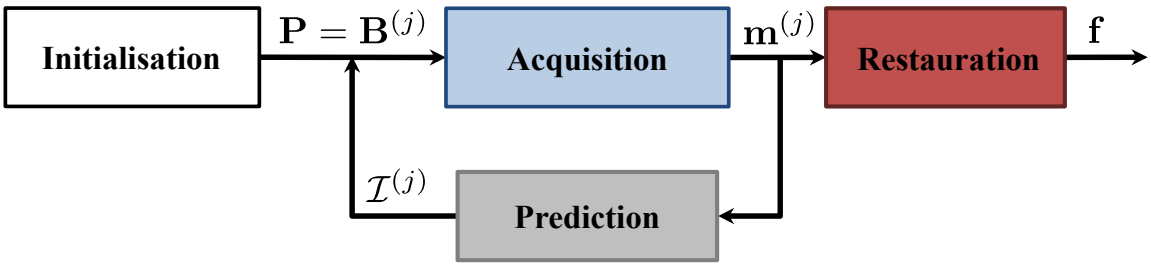

FIGURE C.3 – Schématisation d'une méthode d'acquisition adaptative.

C.2.3 Conclusion du chapitre

Nous avons vu dans ce chapitre les principales méthodes d'acquisition et de restauration des images par une caméra mono-pixel. Trois techniques principales existent qui sont résumées dans le tableau C.1.

En résumé, ABS est la méthode la plus favorable puisqu'elle nécessite peu de mesures K et la restauration des images par transformée inverse est extrêmement rapide. Ce sont pour ces raisons qu'une méthode *adaptative* est considérée dans le Chaptitre IV.

La fin de ce chapitre marque une rupture entre la bibliographie des caméras mono-pixel présentée jusqu'à ce chapitre et les chapitres suivants qui rapportent les contributions de ce travail

5. Les K coefficients ayant la plus forte magnitude.

Approche	Adaptatif?	Motifs	# de motifs K	Restauration de l'image
Acquisition comprimée (CS)	Non	Aléatoires	$K << D$	Minimisation ℓ_1
Basis Scan (BS)	Non	Ceux de la base	$K = D$	Transformée inverse
Adaptive Basis Scan (ABS)	Oui	Ceux de la base	$K << D$	Transformée inverse

TABLEAU C.1 – Comparaison des caractéristiques principales des techniques d'acquisition et restauration des images par une SPC.

de thèse. Avant de détailler la technique *adaptative* choisie, les systèmes expérimentaux sur lesquels sont réalisés des tests en conditions réelles sont présentés.

C.3 CHAPITRE III - SYSTÈMES EXPÉRIMENTAUX

Les acquisitions expérimentales sont essentielles à la conception de nouveaux algorithmes puisqu'elles permettent de valider et/ou d'ajuster les développements. Ce chapitre décrit deux systèmes expérimentaux sur lesquels ont été testées les méthodes développées dans les chapitres suivants. Le premier est le montage SPC déjà existant du Politecnico di Milano auquel quelques améliorations ont été apportées. Le second a été monté récemment au laboratoire CREATIS. Un logiciel pour contrôler ces dispositifs optiques de manière *adaptative* est également proposé.

C.3.1 Montage au Politecnico di Milano

Le système présent au Politecnico di Milano a initialement été conçu pour faire de la tomographie optique diffuse (D'Andrea *et al.*, 2010; Ducros *et al.*, 2013, 2016) en utilisant un DMD pour de l'illumination structurée et une caméra CCD en place du détecteur ponctuel. Plus tard, un second DMD a été ajouté ainsi qu'un détecteur ponctuel pour obtenir le système complet de la Fig. C.4.

Les contributions de cette thèse sur ce système couvrent deux parties. En premier lieu, un spectromètre a été ajouté pour obtenir des mesures multispectrales. Dans un second temps, un logiciel permettant de contrôler les différents éléments de manière *adaptative* a été implémenté puisque une technique d'acquisition/restauration des images *adaptative* est considérée dans les prochains chapitres.

Système Le système est composé d'une source laser à impulsions supercontinues (SC-450, Fianium ou SuperK Extreme EXW-12, NKT Photonics). L'objet étant généralement illuminé dans une bande spectrale particulière, un filtre (ThorLabs) est ajouté sur le chemin du laser si le SC-450 est employé. Quand le SuperK Extreme est utilisé, un filtre à longueur d'onde ajustable (SuperK Select, NKT Photonics) est couplé au laser afin de choisir une ou plusieurs (jusqu'à 8) bandes spectrales pour l'illumination de l'objet.

Un premier DMD (DLP7000-V7001, Vialux GmbH) de taille 768×1024 est employé pour l'illumination de l'objet. La lumière issue de ce DMD peut éclairer l'objet en transmission ou réflexion grâce au jeu de miroirs (mirror 1, 2 et flip mirror 1). L'image de l'objet est ensuite formée par la première lentille sur le second DMD (DLP7000-V7001, Vialux GmbH) également de taille 768×1024.

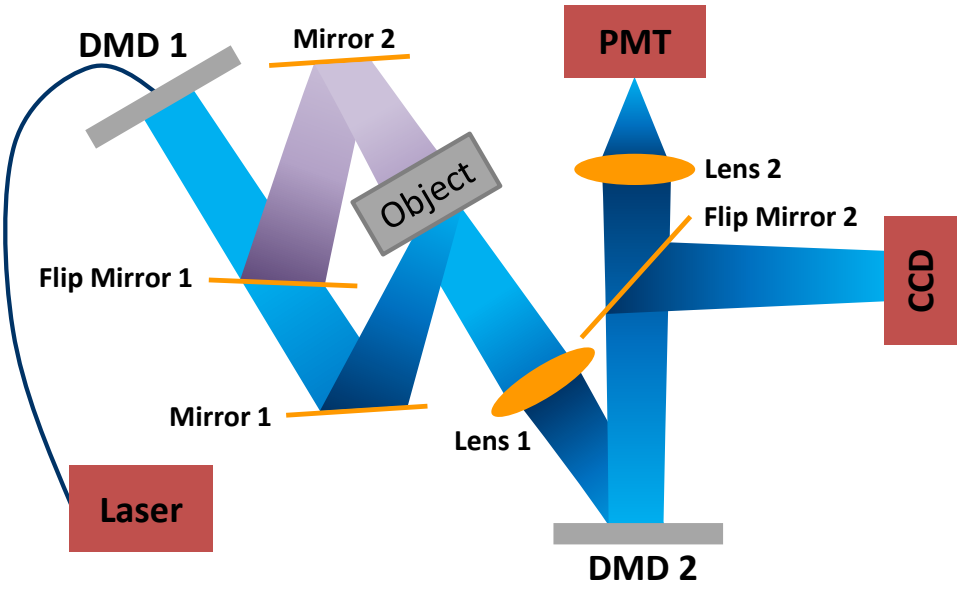

FIGURE C.4 – Système expérimental du Politecnico di Milano.

Pour nos expériences, le DMD 1 sera toujours chargé avec un motif blanc afin d'avoir une illumination uniforme de l'objet et le DMD 2 sert à la modulation.

Enfin, par action sur le second miroir à bascule (flip mirror 2), la lumière réfléchie du DMD 2 peut être imagée sur une caméra CCD (Versarray 512, Princeton Instruments) ou est concentrée sur un PMT (HPM-100-50, Becker & Hickl GmbH) grâce à la seconde lentille.

Mesures résolues en temps Afin d'obtenir un système résolu en temps, une carte de comptage des photons (SPC-130 or SPC-630, Becker & Hickl GmbH), *time-correlated single photon counting* board (TCSPC), est couplée au PMT. Un tel dispositif est synchronisé avec l'impulsion du laser de sorte que la TCSPC puisse estimer le temps de vol de chacun des photons détectés. Après un certain temps d'intégration, la carte donne un histogramme des temps de vols des photons i.e. elle donne le nombre de photons détectés dans T canaux temporels. En place d'une simple mesure scalaire par une SPC classique, un vecteur de taille T est à présent directement obtenu quand un motif est envoyé au SLM. Cela donne la possibilité de restaurer une image par canal temporel [6].

Mesures multispectrales Des mesures multispectrales peuvent également être réalisées en remplaçant le détecteur ponctuel par un spectromètre. En quelques mots, la lumière issue de la seconde lentille est renvoyée dans le spectromètre où un prisme disperse cette dernière. La dispersion entraîne une séparation de la lumière en différents rayons lumineux correspondants à différentes bandes spectrales (i.e. plages de longueur d'onde). Une barrette de Λ détecteurs ponctuels en parallèle collecte alors ces différents rayons lumineux. Chaque détecteur mesure ainsi une information spectrale différente. Dans notre montage, un PMT de $\Lambda = 16$ canaux spectraux (PML-16-1, Becker & Hickl GmbH) est utilisé. Ces détecteurs sont toujours couplés à la TCSPC (SPC-630, Becker & Hickl GmbH) qui permet d'obtenir un histogramme de temps de vol des photons pour

6. La modélisation mathématique de ces acquisitions est donnée au Chaptitre VI.

chacun des Λ canaux spectraux. La mesure scalaire d'une SPC classique devient cette fois-ci un vecteur de taille $(\Lambda \times T)$ pour un motif envoyé au SLM [7].

C.3.2 Montage au laboratoire CREATIS

Un montage expérimental plus simple a été monté au laboratoire CREATIS pendant la thèse afin de valider les expériences du Chaptitre V. A notre connaissance, outre les travaux de Studer *et al.* datant de 2012, aucune autre plateforme SPC n'est disponible en France. Le montage est schématisé en Fig. C.5.

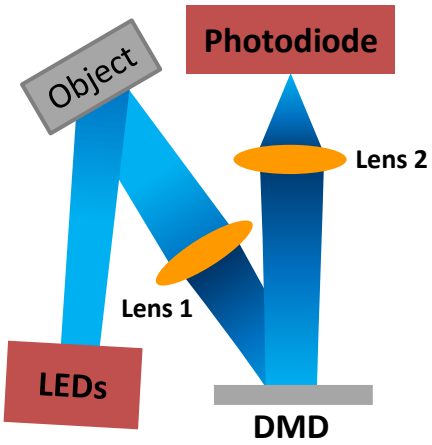

FIGURE C.5 – Montage expérimental à CREATIS.

Ce dernier est composé d'un lampe à LED blanche (LIUCWHA, ThorLabs) pour l'illumination de l'objet. Une roue contenant différents filtres de densité (NEXXB, ThorLabs) est placée devant la LED afin de contrôler l'intensité de l'illumination (paramètre N_0 introduit en (C.2)).

L'image de l'objet est formé par la première lentille dans le plan du SLM. Ce dernier est un DMD de taille 768×1024 (DLP700-V7001,Vialux) exploité pour moduler spatialement l'image avec la possibilité de charger des motifs sur 8-bits.

La lumière réfléchie du DMD est enfin concentrée, grâce à la seconde lentille, sur la partie sensible d'un photo-détecteur (PDA36A-EC, ThorLabs) couplé à un convertisseur analogique numérique (USB-6210, National Instruments).

C.3.3 Contrôle logiciel

Comme mentionné dans la conclusion du Chaptitre II, une approche *adaptative* est considérée dans cette thèse. Ceci signifie que les motifs envoyés au SLM sont choisis en se basant sur les mesures précédentes. Une communication entre le contrôle de l'instrumentation avec Labview et l'algorithme adaptatif codé en Matlab est donc nécessaire.

Labview pour l'instrumentation Comme c'est souvent le cas pour le contrôle de dispositifs optiques et électroniques, Labview peut être utilisé. Un logiciel a donc été implémenté dans ce langage pour commander le DMD, la caméra, le détecteur ponctuel et le convertisseur numérique.

7. La modélisation mathématique de ces acquisitions est donnée au Chaptitre VI.

L'interface graphique permet de réaliser plusieurs acquisitions en réglant manuellement les différents paramètres de ces instruments.

Matlab pour traiter les données Matlab est de son côté employé pour créer les motifs à envoyer au SLM et implémenter la technique d'acquisition/restoration des images en traitant les données sauvegardées par le logiciel précédent codé sur Labview. Une fois les mesures réalisées par Labview, Matlab peut donc commencer le traitement des données afin de restaurer une image ou décider des prochaines mesures à effectuer.

Communication Matlab/Labview Les deux programmes précédents travaillent indépendamment et doivent être lancés manuellement l'un après l'autre pour effectuer un jeu complet de mesures et restaurer une image. Afin de mettre en œuvre une méthode *adaptative*, une étape de communication entre les deux programmes a été ajoutée. Le choix a été fait de choisir Matlab comme "maître", c'est-à-dire que tous les paramètres sont choisis dans le script Matlab. Le principe de cette implémentation est imagée en Fig. C.6. Un ordinateur avec le programme Labview contrôle les instruments et un autre contrôle l'algorithme adaptatif en Matlab. Des dossiers partagés sur un réseau commun permettent à Matlab de donner à Labview les paramètres (fichiers *Parameters_j.txt*). Le fichier *Matlab_done.txt* (resp. *Labview_done.txt*) permet au programme Labview (resp. Matlab) de connaitre quand Matlab (resp. Labview) a terminé sa tâche et celui-ci peut alors prendre le relais.

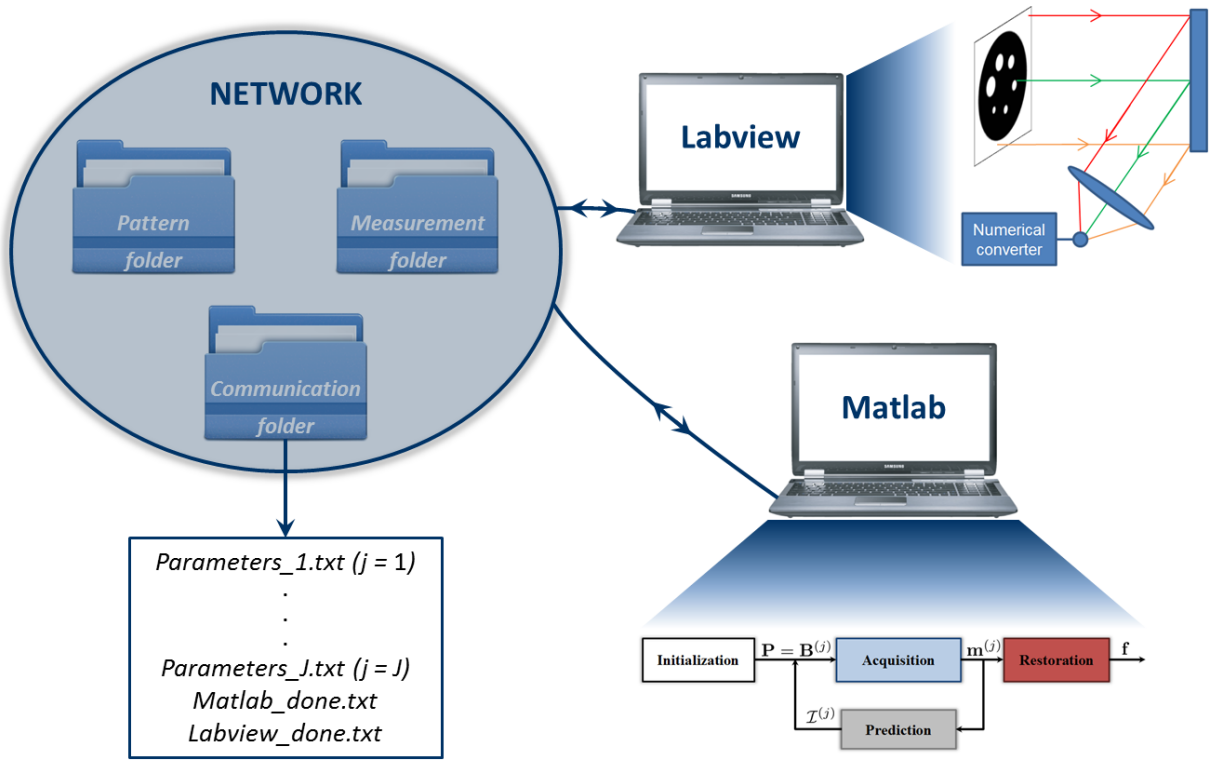

FIGURE C.6 – Fonctionnement de la communication entre Matlab et Labview.

C.3.4 Conclusion du chapitre

Ce chapitre a présenté les systèmes expérimentaux qui sont employés pour des acquisitions réelles dans les prochains chapitres. Le système de Milan est très complet puisqu'il permet d'avoir des mesures multispectrales résolues en temps avec une SPC. Au laboratoire CREATIS, le système est plus basique mais constitue une plateforme SPC unique en France.

Comme mentionné en fin de Chaptitre II, les méthodes *adaptive basis scans* sont les plus efficaces pour l'acquisition et la restauration d'images SPC. Les systèmes décrits dans ce chapitre permettent de mettre en œuvre la technique adaptative proposée dans le chapitre suivant.

C.4 CHAPITRE IV - TECHNIQUE ABS-WP

Les acquisitions adaptatives pour l'imagerie mono-pixel exploitent l'ensemble de mesures acquises à une itération précédente pour décider des prochains motifs SLM à envoyer, i.e. décider les nouvelles mesures à réaliser. En particulier, les méthodes *adaptive basis scan* (ABS) sont performantes avec un faible nombre de mesures et une restauration d'image très rapide. Une base d'ondelettes est souvent choisie car la plupart des images ont une représentation parcimonieuse dans cette base.

Dans ce chapitre, nous proposons une méthode complète pour l'imagerie mono-pixel en utilisant une nouvelle technique appelée *adaptive basis scan by wavelet prediction* (ABS-WP). Notre approche bénéficie de deux caractéristiques. Dans un premier temps, une étape de prédiction sans seuillage est proposée, étape inspirée par l'approximation non-linéaire de la transformée en ondelettes. La seconde caractéristique est la possibilité d'utiliser n'importe quelle ondelette ce qui permet de mieux compresser les données. On présente dans un premier temps la technique ABS-WP avant de donner des résultats simulés et expérimentaux. Une comparaison avec l'acquisition comprimée (CS) et une autre stratégie ABS est également donnée avant d'ouvrir une discussion sur les résultats.

Certains résultats de ce chapitre viennent de deux papiers de conférences, *IEEE EMBC 2015* (Rousset *et al.*, 2015) où une stratégie de prédiction légèrement différente a été présentée et *IEEE ISBI 2016* (Rousset *et al.*, 2016) où une comparaison avec le CS a été donnée. Il contient également en grande partie un article publié dans *IEEE Transactions on Computational Imaging* en 2017a (Rousset *et al.*, 2017a).

C.4.1 Méthodes

Transformée en ondelettes La transformée en ondelettes fonctionnant sur des images carrés dont la taille est une puissance de 2, on considère à présent une image $\mathbf{f} \in \mathbb{R}^{D\times 1}$ de taille $N \times N = D$. On note $\widetilde{\mathbf{f}} \in \mathbb{R}^{D\times 1}$ les coefficients d'ondelettes de $\mathbf{f}$ pour une ondelette donnée :

$$\widetilde{\mathbf{f}} = \mathbf{B}\mathbf{f} \tag{C.3}$$

avec $\mathbf{B} \in \mathbb{R}^{D\times D}$ un opérateur orthonormal (Daubechies, 1992) traduisant la transformée en ondelettes. La valeur $j = 1 \dots J$ représente l'échelle à laquelle l'image $\mathbf{f}$ est observée avec J le niveau de décomposition. Une position d'un coefficient d'ondelettes dans un niveau j est spécifiée par le vecteur $\mathbf{i}$ tel que

$$\mathbf{i} = (i_1, i_2)^\top \in \left\{1, \dots, 2^\ell\right\}^2 \quad \text{with} \quad \ell = R - j,\, R = \log_2(N) \tag{C.4}$$

Ainsi, chaque élément de $\widetilde{\mathbf{f}}$ peut être complètement identifié et positionné par son unique triplet k tel que

$$k = \{o, j, \mathbf{i}\} \tag{C.5}$$

où $o = 0$, 1, 2 or 3 correspond aux coefficients d'approximation, verticaux, horizontaux et diagonaux, respectivement. De plus, chaque ligne de $\mathbf{B}$ correspond à un unique triplet k. L'image $\mathbf{f}$ peut être parfaitement restaurée avec $\widetilde{\mathbf{f}}$ en utilisant la transformée en ondelettes inverse :

$$\mathbf{f} = \mathbf{B}^{-1}\widetilde{\mathbf{f}} \tag{C.6}$$

Stratégie d'acquisition La transformée en ondelettes donnant des signaux parcimonieux, il est possible de ne pas prendre en compte les plus faibles coefficients (en magnitude) de $\widetilde{\mathbf{f}}$ lors de l'étape de restauration (Mallat, 2008). Notre méthode ABS-WP cherche ainsi à trouver les coefficients d'ondelettes dits significatifs, i.e. ayant une forte magnitude. On cherche donc à prédire les triplets k de chacun de ses éléments afin de remplir la matrice $\mathbf{P} = \left(\mathbf{p}_1, \dots, \mathbf{p}_k, \dots, \mathbf{p}_K\right)^\top$ de (C.2) avec les lignes de $\mathbf{B}$ correspondantes aux triplets k prédits, notés $\bar{k}$. Comme nous n'avons pas accès à toute l'image, une méthode itérative est proposée.

Pour plus de simplicité et comprendre les tailles des images mises en jeu dans notre technique, la notation vectorielle $\mathbf{f} \in \mathbb{R}^{D\times 1}$, $D = N \times N$, de l'image est temporairement remplacée par sa notation matricielle $\mathbf{F} \in \mathbb{R}^{N\times N}$. De même, $\widetilde{\mathbf{F}} \in \mathbb{R}^{N\times N}$ représente la transformée en ondelettes de $\mathbf{F}$. Notre stratégie se décompose en 5 étapes principales :

1. L'image d'approximation $\mathbf{A}_j$ à l'échelle grossière $j = J$ est complètement acquise. Cette image est de taille $2^\ell \times 2^\ell$ avec $\ell = R - j$.
2. $\mathbf{A}_j \in \mathbb{R}^{2^\ell \times 2^\ell}$ est sur-échantillonnée par un facteur 2 en utilisant une interpolation bicubique $\mathcal{S}$. Ceci mène à une image haute résolution $\mathbf{H}_j = \mathcal{S}(\mathbf{A}_j) \in \mathbb{R}^{2^{\ell+1}\times 2^{\ell+1}}$.
3. L'image $\mathbf{H}_j$ est transformée en ondelettes sur 1 niveau afin de donner $\widetilde{\mathbf{H}}_j \in \mathbb{R}^{2^{\ell+1}\times 2^{\ell+1}}$. Ceci donne les coefficient d'ondelettes de détails *predits* à l'échelle j.
4. Pour obtenir les triplets $\bar{k}$ des plus forts éléments prédits, une approximation non-linéaire est réalisée en retenant un pourcentage p_j des plus forts coefficients de détails de $\widetilde{\mathbf{H}}_j$. Ceci mène à l'obtention des éléments significatifs prédits et de leurs triplets correspondants prédits $\bar{k}$.
5. Ces coefficients sont finalement acquis expérimentalement en choisissant comme motifs SLM les lignes de $\mathbf{B}$ correspondantes aux triplets $\bar{k}$.

La description ci-dessus marche pour un niveau de décomposition de la transformée en ondelettes mais peut facilement être étendue à plusieurs niveaux. A l'étape 1, au lieu d'acquérir

l'image grossière à $j = J$, l'image $\mathbf{A}_j$ est retrouvée par transformée en ondelettes inverse des coefficients acquis jusqu'alors. Les étapes 2 à 5 sont inchangées, seule une valeur différente de p_j est utilisée pour chaque échelle donnant le jeu de pourcentage final suivant :

$$\mathcal{P} = \{p_J, p_{J-1}, ..., p_1\}. \tag{C.7}$$

Taux de compression L'acquisition complète de l'image d'approximation $\mathbf{A}_j$ à l'échelle $j = J$ obtient $n_0 = 2^{2L} = 4^L$ coefficients d'ondelettes avec $L = R - J$. Ensuite, un pourcentage p_j des plus forts coefficients de détails est acquis. Ainsi, le nombre de mesures à chaque échelle j est donné $n_j = 3 \times 2^{2^\ell} \times p_j = 3 \times 4^\ell \times p_j$ avec $\ell = R - j$. Le nombre total n d'éléments acquis est donc contrôlé par le jeu de pourcentage $\mathcal{P}$ de (C.7). On peut montrer que n est donné par

$$n = 4^L \left[1 + 3 \sum_{j=1}^{J} 4^{J-j} p_j \right]. \tag{C.8}$$

Le taux de compression (TC), correspondant à une quantité normalisée entre 0 et 1, est défini comme

$$\text{TC} = 1 - \frac{n}{D} \tag{C.9}$$

C.4.2 Expériences

Simulations Pour les simulations, trois images sont considérées : l'image de Lena et peppers souvent utilisées en traitement du signal et une image de bioluminescence d'une souris (Kerami-das *et al.*, 2010) superposée à l'image en lumière ambiante (Fig. C.7). Notre méthode ABS-WP est comparée à l'acquisition comprimée (CS) en restaurant directement **f** à partir des mesures **m** par minimisation TV (Total Variation) (Takhar *et al.*, 2006; Duarte *et al.*, 2008). Nous nous comparons également à une autre méthode adaptative dans le domaine ondelette, EWT-ACS (*adaptive compressed sampling by extended wavelet trees*) proposée par Dai *et al.*. Cette méthode est dérivée de l'ondelette de Haar et un seuil doit être choisi pour prédire les coefficients significatifs à acquérir.

Montage expérimental Le montage expérimental du Politecnico di Milano présenté au Chaptitre III sert pour les acquisitions réelles. Le DMD 1 sert à illuminer l'objet uniformément et le DMD 2 charge les motifs d'ondelettes donnés par ABS-WP.

C.4.3 Résultats et discussion

Résultats Le tableau C.2 donne les PSNRs des images SPC restaurées par CS, EWT-ACS et ABS-WP pour les trois images de simulation. Pour notre technique ABS-WP, l'ondelette de Le Gall est employée car, dans la plupart des cas, elle est la plus efficace.

La Fig. C.7 présente un cas visuel de restauration d'image par ABS-WP sur une image de bioluminescence d'une souris. Cette image étant plutôt lisse, de forts taux de compression peuvent être obtenus.

Des acquisitions SPC réelles sur la cible de Jaszczak avec ABS-WP et CS sont présentées en Fig. C.8. Dans le cas de notre technique, les ondelettes de Haar et de Le Gall sont employées pour montrer la capacité du DMD à charger des motifs sur 8 bits.

Image	**TC**	**PSNR** (dB)			**Seuils**
		CS	*EWT-ACS*	*ABS-WP*	**pour EWT-ACS**
Lena (256 × 256)	80	29.55	29.90	**30.33**	11.52
	85	27.89	28.49	**29.59**	16.63
Peppers (256 × 256)	80	34.70	35.06	**35.35**	7.71
	85	32.96	33.42	**34.83**	11.77
Mouse (128 × 128)	80	45.36	47.65	**49.23**	385.65
	85	42.18	45.83	**49.13**	851.10

TABLEAU C.2 – PSNRs obtenus pour différentes stratégies d'acquisition SPC à deux taux de compression. Les seuils pour la méthode EWT-ACS de Dai *et al.* sont donnés dans la dernière colonne. Pour ABS-WP, les motifs de Le Gall sont utilisés avec $\mathcal{P} = \{0.90, 0.80, 0.71, 0.02\}$ et $\mathcal{P} = \{0.90, 0.80, 0.45, 0.019\}$ pour donner des taux de compression TC de 80% et 85%.

Discussion Les résultats du tableau C.2 où notre méthode ABS-WP est comparée au CS et EWT-ACS, des résultats numériques proches ou meilleurs sont obtenus pour ABS-WP. Les seuils d'EWT-ACS montrent qu'ils dépendent de l'image et doivent être adaptés pour chaque objet. En comparaison, pour ABS-WP et un taux de compression fixe, le même jeu de pourcentages $\mathcal{P}$ est utilisé pour chaque image. Bien que les trois images en simulation soient différentes, notre stratégie donne toujours une très bonne qualité d'image. ABS-WP s'adapte ainsi à l'image et aucun seuil ne doit être ajusté. Pour le cas du CS, de nombreux paramètres doivent être choisis pour l'étape

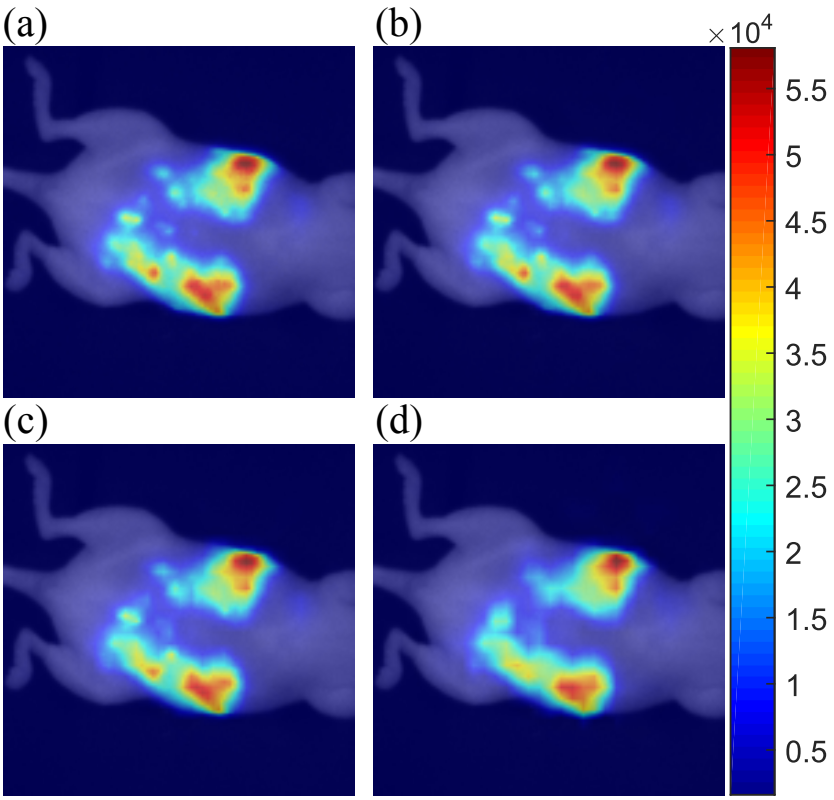

FIGURE C.7 – Acquisition SPC avec ABS-WP sur une image 128 × 128 de bioluminescence de souris. (a) Image de référence, images restaurées avec Le Gall pour un TC de (b) 90%, (c) 95% et (d) 98%. Respectivement, les PSNRs par rapport à l'image de référence sont 48.25 dB, 41.48 dB et 35.37 dB.

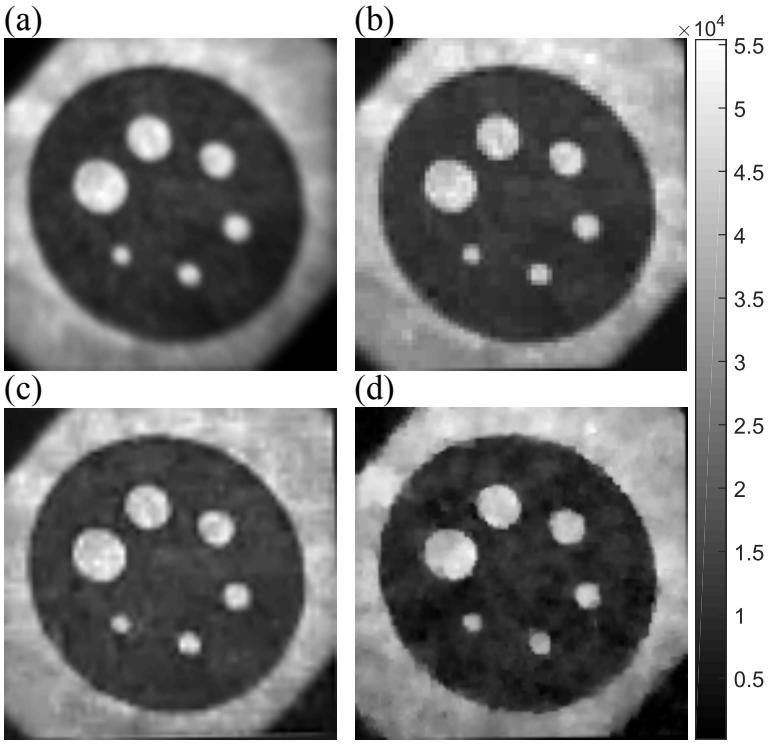

FIGURE C.8 – Acquisitions experimentales avec la SPC sur la cible de Jaszczak. (a) Image CCD expérimentale de la cible, images 128 × 128 restaurées avec un TC de 85% (b) pour ABS-WP avec Haar, (c) pour ABS-WP avec Le Gall et (d) par CS. Respectivement, les PSNRs obtenus par rapport à l'image CCD sont 21.99 dB, 21.65 dB et 21.20 dB.

de minimisation TV. Suivant ces choix, la qualité de l'image peut être gravement affectée.

Même avec un TC aussi haut que 98%, les résultats de la Fig. C.7 montrent qu'ABS-WP restaure des images d'excellentes qualités dans le cas d'objets lisses. Pour ce type d'images typiques en imagerie de fluorescence, peu de coefficients d'ondelettes sont en effet nécessaires pour retrouver l'image originale.

Si l'on regarde les données expérimentales de la Fig. C.8, celles-ci montrent qu'une ondelette plus sophistiquée comme celle de Le Gall peut être utilisée par rapport aux acquisitions classiques avec Haar. Elle permet de donner de meilleurs résultats visuels avec une image plus lisse par rapport au cas Haar qui a tendance à pixéliser l'image. Le choix de l'ondelette est ainsi un paramètre important de notre méthode. En effet, suivant l'objet imagé, certaines ondelettes sont meilleures pour capturer l'information de l'image avec moins de coefficients. Si l'on regarde l'objet restauré par CS sur la Fig. C.8, on peut apercevoir des sortes de tâches dues à la minimisation TV.

C.4.4 Conclusion du chapitre

Dans ce chapitre, nous avons décrit une nouvelle méthode pour l'imagerie mono-pixel. Les coefficients significatifs qui devraient être acquis sont prédits par une interpolation bicubique alors que les autres coefficients ne sont pas pris en compte à l'étape de restauration de l'image. A notre connaissance, des données expérimentales obtenues avec une autre ondelette qu'Haar n'avaient jamais été présentées auparavant.

Un problème qui n'a pas été détaillé dans ce chapitre concerne les valeurs positives et négatives que contiennent les motifs d'ondelettes. De tels motifs ne peuvent pas être implémentés directement sur un SLM puisque les photons ne peuvent être comptés négativement. Un recours possible est de séparer le motif en sa partie positive et partie négative prise en valeur absolue. La soustraction des deux mesures correspondantes donne la mesure finale, doublant ainsi le nombre de mesures nécessaires. Au chapitre suivant, nous généralisons le problème qui peut être solutionné par un algorithme de factorisation de matrices et qui permet de réduire le nombre de mesures à effectuer.

C.5 CHAPITRE V - GÉNÉRALISATION DES MOTIFS

Quelle que soit la technique d'acquisition/restauration des images employée, deux problèmes expérimentaux apparaissent. Le premier concerne les motifs à envoyer au SLM qui comportent des valeurs négatives ce qui ne peut pas être physiquement mis en œuvre sur un SLM. Le second problème est le courant d'obscurité au niveau du détecteur qui perturbe les mesures et qui doit être éliminé.

Pour palier ce problème, nous proposons de créer des motifs à valeurs positives qui, combinés linéairement, donnent les motifs désirés à valeurs positives et négatives. Nous montrons que ceux-ci peuvent être obtenus par un algorithme de factorisation en matrices semi non-négatives (*semi nonnegative matrix factorization*, SNMF) qui permet de décomposer une matrice en un produit de deux autres matrices dont l'une n'a que des éléments positifs (Lee *et* Seung, 1999; Ding *et al.*, 2010; Gillis *et* Kumar, 2015).

Ce chapitre présente les méthodes classiques permettant de contourner le problème de positivité des motifs et d'élimination du courant d'obscurité. Une formulation générale du problème est ensuite donnée avant d'en proposer une solution par un algorithme SNMF. Des résultats en simulation montrent les avantages de cette méthode par rapport aux solutions conventionnelles.

Ces résultats ont été déposés sous forme de brevet (Rousset *et al.*, 2017c) et soumis à *IEEE Transactions on Image Processing* (Rousset *et al.*, 2017d).

C.5.1 Méthodes ad'hoc pour contourner le problème

On note $\check{\mathbf{P}} = \left(\check{\mathbf{p}}_1, \ldots, \check{\mathbf{p}}_I\right)^\top \in \mathbb{R}^{I\times D}$ la matrice contenant I motifs désirés $\check{\mathbf{p}}_i \in \mathbb{R}^{D\times 1}$, c'est-à-dire ayant des valeurs positives et négatives. On note $\check{\mathbf{m}} = (\check{m}_1, \ldots, \check{m}_I)^\top \in \mathbb{R}^{I\times 1}$ le vecteur contenant les mesures désirées correspondantes :

$$\check{\mathbf{m}} = N_0 \Delta t \check{\mathbf{P}} \mathbf{f} \tag{C.10}$$

Il est à noter que le terme additif $\Delta t \alpha \mathbf{1}_K$ de (C.2) est supprimé de cette équation puisque qu'il ajoute une information supplémentaire dans (C.2) qui perturbe les mesures.

Méthode *pos/neg* Cette méthode naturelle consiste à séparer chaque motif désiré $\check{\mathbf{p}} \in \mathbb{R}^{D\times 1}$ en sa partie positive $\mathbf{p}_+ \in \mathbb{R}_+^{D\times 1}$ et sa partie négative prise en valeur absolue $\mathbf{p}_- \in \mathbb{R}_+^{D\times 1}$ (Dai *et al.*, 2014; Rousset *et al.*, 2017a), i.e.,

$$\check{\mathbf{p}} = \mathbf{p}_+ - \mathbf{p}_- \quad \text{with} \begin{cases} \mathbf{p}_+ = \max(\mathbf{0}_D, \check{\mathbf{p}}) \\ \mathbf{p}_- = |\min(\mathbf{0}_D, \check{\mathbf{p}})| \end{cases} \tag{C.11}$$

où les fonctions $\max(.)$ et $\min(.)$ sont appliquées sur chaque entrée des deux vecteurs, $\mathbf{0}_D$ étant le vecteur nul de taille D. Ensuite, les mesures m_+ et m_- acquises avec $\mathbf{p}_+$ et $\mathbf{p}_-$, respectivement, sont soustraites pour donner $\check{m}$. En effet, nous avons

$$m_+ - m_- = \left(N_0 \mathbf{p}_+^\top \mathbf{f} + \alpha\right)\Delta t - \left(N_0 \mathbf{p}_-^\top \mathbf{f} + \alpha\right)\Delta t = \check{m}. \tag{C.12}$$

Il est important de noter que le courant d'obscurité $\alpha\Delta t$ est bien annulé par cette technique. L'inconvénient est que $K = 2I$ mesures SPC doivent être réalisées pour obtenir les I mesures désirées, augmentant ainsi les temps d'acquisition.

Méthode *shift* Une seconde approche consiste à décaler chaque motif désiré $\check{\mathbf{p}} \in \mathbb{R}^{D\times 1}$ vers des valeurs positives (Duarte *et al.*, 2008). Mathématiquement

$$\check{\mathbf{p}} = \mathbf{p}_\mathrm{s} - \mathbf{p}_\mathrm{b} \quad \text{with} \begin{cases} \mathbf{p}_\mathrm{s} = \check{\mathbf{p}} + \mathbf{p}_\mathrm{b} \in \mathbb{R}_+^{D\times 1} \\ \mathbf{p}_\mathrm{b} = (b, \ldots, b)^\top \in \mathbb{R}_+^{D\times 1} \end{cases} \tag{C.13}$$

où b est la valeur d'arrière plan choisie telle que $b \geq |\min(\check{\mathbf{p}})| \in \mathbb{R}_+$. Comme pour la méthode pos/neg, la soustraction des deux mesures SPC correspondantes donne la mesure désirée en annulant le courant d'obscurité. Contrairement à la méthode pos/neg, il n'est pas nécessaire de doubler le nombre de mesures. En effet, en choisissant b assez grand, cette valeur peut être la même pour tous les I motifs désirés. Seulement $K = I + 1$ mesures sont donc nécessaires. Cependant, nous montrerons plus tard que cette méthode souffre du bruit de mesure.

C.5.2 Méthode proposée basée sur des motifs généralisés

Transformation des motifs Pour obtenir une solution générale et robuste au problème de positivité, notre idée est de factoriser la matrice $\check{\mathbf{P}}$ en un produit de deux matrices $\mathbf{T}$ et $\mathbf{P}$ telles que

$$\check{\mathbf{P}} = \mathbf{T}\mathbf{P} \tag{C.14}$$

où $\mathbf{P} \in \mathbb{R}_+^{K\times D}$ contient une séquence de motifs positifs et $\mathbf{T} \in \mathbb{R}^{I\times K}$ est une matrice de transformation permettant de combiner les motifs de $\mathbf{P}$ pour retrouver ceux de $\check{\mathbf{P}}$. Si une telle factorisation peut se trouver, l'idée est alors d'appliquer la même matrice de transformation $\mathbf{T}$ sur le vecteur de mesure $\mathbf{m}$ pour obtenir $\check{\mathbf{m}}$, soit

$$\check{\mathbf{m}} = \mathbf{T}\mathbf{m}. \tag{C.15}$$

Les mesures désirées sont donc obtenues par la combinaison linéaire de mesures réalisables avec les motifs positifs de $\mathbf{P}$. Or, si l'on développe $\mathbf{Tm}$ en utilisant (C.2), on obtient :

$$\mathbf{Tm} = \Delta t(N_0\mathbf{TPf} + \alpha\mathbf{T1}_K) = N_0\Delta t\check{\mathbf{P}}\mathbf{f} + \alpha\Delta t\mathbf{T1}_K \tag{C.16}$$

Afin d'obtenir (C.10) par (C.15), le second terme de (C.16) doit s'annuler. Nous choisissons ainsi d'imposer la contrainte suivante :

$$\mathbf{T1}_K = \mathbf{0}_I \tag{C.17}$$

où $\mathbf{0}_I = (0,\dots,0)^\top \in \mathbb{R}^{I\times 1}$.

En résumé, pour une séquence de motifs désirés $\check{\mathbf{P}} \in \mathbb{R}^{I\times D}$, la problème de généralisation des motifs que nous adressons et le suivant :

$$\text{Trouver } \mathbf{T} \in \mathbb{R}^{I\times K} \text{ et } \mathbf{P} \in \mathbb{R}^{K\times D} \text{ tels que } \begin{cases} \check{\mathbf{P}} = \mathbf{TP} \\ \mathbf{P} \geq 0 \\ \mathbf{T1}_K = \mathbf{0}_I \end{cases} \tag{C.18}$$

où $\mathbf{P} \geq 0$ signifie que $(\mathbf{P})_{k,n} \geq 0$, $\forall (k,n)$.

Formulation du problème Afin de trouver une solution à (C.14), nous proposons de résoudre le système suivant :

$$\min_{\mathbf{T},\mathbf{P}} \left\|\check{\mathbf{P}} - \mathbf{TP}\right\|_{\mathrm{F}}^2 \quad \text{tel que} \quad \mathbf{P} \geq 0 \text{ and } \mathbf{T1}_K = \mathbf{0}_I \tag{C.19}$$

où $\mathbf{P} \geq 0$ signifie que $\forall\,(k,n) \in (1\dots K)\times(1\dots D)$, $(\mathbf{P})_{k,n} \geq 0$ et $\|\mathbf{M}\|_{\mathrm{F}}$ est la norme de Frobenius de la matrice $\mathbf{M}$.

C.5.3 Solution par algorithme SNMF

Algorithme SNMF Le problème (C.19) peut-être résolu par un algorithme de factorisation en matrice semi non-négatives. En pratique, notre but est d'avoir une valeur de K la plus petite possible afin de limiter le nombre de mesures nécessaires tout en ayant une faible erreur de factorisation. Étant donné que les deux matrices $\mathbf{P}$ et $\mathbf{T}$ sont inconnues, la plupart des méthodes sont itératives et résolvent (C.19) alternativement pour $\mathbf{P}$ puis $\mathbf{T}$ avec leurs contraintes respectives $\mathbf{P} \geq 0$ et $\mathbf{T1}_K = \mathbf{0}_I$. Afin d'avoir un calcul et une convergence rapides, nous considérons une méthode basée sur les moindres carrés pour résoudre (C.19).

Solution pour T La résolution de (C.19) pour $\mathbf{T}$ considère $\mathbf{P}$ fixe, il s'agit donc de résoudre

$$\min_{\mathbf{T}} \left\|\check{\mathbf{P}} - \mathbf{TP}\right\|_{\mathrm{F}}^2 \qquad \text{tel que} \qquad \mathbf{T1}_K = \mathbf{0}_I. \tag{C.20}$$

La condition (C.17) donne un problème d'optimisation sous contrainte d'égalité dont la solution analytique à (C.20) trouvée en utilisant la propriété de dualité est donnée par :

$$\mathbf{T} = \check{\mathbf{P}}\mathbf{P}^\top\left(\mathbf{P}\mathbf{P}^\top\right)^{-1}\left(\mathbf{I} - \frac{1}{\mathbf{1}_K^\top\left(\mathbf{P}\mathbf{P}^\top\right)^{-1}\mathbf{1}_K}\mathbf{1}_{K\times K}\left(\mathbf{P}\mathbf{P}^\top\right)^{-1}\right) \tag{C.21}$$

avec $\mathbf{I}$ la matrice identité de taille $K\times K$, $\mathbf{1}_K^\top(\mathbf{P}\mathbf{P}^\top)^{-1}\mathbf{1}_K \in \mathbb{R}$ et $\mathbf{1}_{K\times K} = \mathbf{1}_K\mathbf{1}_K^\top$ est la matrice de taille $K\times K$ dont tous les éléments sont égaux à 1. Si $(\mathbf{P}\mathbf{P}^\top)$ n'est pas inversible, la matrice pseudo-inverse de Moore-Penrose est employée.

Solution pour P On cherche à présent à trouver une solution à (C.19) pour **P** considérant **T** fixe, on cherche donc

$$\min_{\mathbf{P}} \left\| \check{\mathbf{P}} - \mathbf{TP} \right\|_{\mathrm{F}}^2 \qquad \text{tel que} \qquad \mathbf{P} \geq 0. \tag{C.22}$$

Ce problème n'ayant pas de solution explicite, Gillis a proposé dans Gillis *et* Kumar (2015) un algorithme de descente par blocs sur les lignes de **P** qui amène à une solution analytique pour minimiser chaque ligne et un calcul rapide en choisissant $K = I + 1$.

Pour résoudre ce problème par la méthode de Gillis, la fonction coût $\mathcal{F}(\mathbf{P}) = \left\| \check{\mathbf{P}} - \mathbf{TP} \right\|_{\mathrm{F}}^2$ est réécrite de la manière suivante :

$$\mathcal{F}(\mathbf{p}_k) = \left\| \check{\mathbf{P}} - \mathbf{TP} \right\|_{\mathrm{F}}^2 = \left\| \check{\mathbf{P}} - \mathbf{T}_{|k}\mathbf{P}_{-k} - \mathbf{t}_k \mathbf{p}_k^\top \right\|_{\mathrm{F}}^2 \tag{C.23}$$

où $\mathbf{T}_{|k}$ (resp. $\mathbf{P}_{-k}$) est la matrice **T** (resp. **P**) privée de sa colonne (resp. ligne) k et $\mathbf{t}_k \in \mathbb{R}^{I \times 1}$ (resp. $\mathbf{p}_k \in \mathbb{R}^{D \times 1}$) est la k-ième colonne (resp. ligne) de **T** (resp. **P**). On montre que la solution analytique minimisant (C.23) est donnée par :

$$\mathbf{p}_k = \max\left(\mathbf{0}_D, \frac{(\check{\mathbf{P}} - \mathbf{T}_{|k}\mathbf{P}_{-k})^\top \mathbf{t}_k}{\|\mathbf{t}_k\|_2^2} \right) \tag{C.24}$$

où la fonction max(.) s'applique sur chaque composante des deux vecteurs et $\mathbf{0}_D$ est le vecteur nul de taille D. Une solution partielle au problème (C.22) est finalement obtenue en itérant une fois (C.24) sur chaque ligne de **P** [8].

Algorithme final En utilisant la solution analytique **T** de (C.21) et celle de (C.24) pour minimiser chaque ligne de **P**, l'algorithme complet peut maintenant être écrit suivant l'algorithme 4.

Algorithme 4 Trouver $\check{\mathbf{P}} \approx \mathbf{TP}$ suivant (C.19)

Initialisation : Prendre $K = I + 1$ et $\mathbf{P} = \mathrm{rand}(K, D)$
while $\left\| \check{\mathbf{P}} - \mathbf{TP} \right\|_{\mathrm{F}}^2 > \epsilon$ **do**
  1 : Mettre à jour **T** avec (C.21)
  2 : Mettre à jour **P**
    for $k = 1 : K$ **do**
      2.1 : $\mathbf{p}_k \leftarrow \max\left(\mathbf{0}_D, \frac{(\check{\mathbf{P}} - \mathbf{T}_{|k}\mathbf{P}_{-k})^\top \mathbf{t}_k}{\|\mathbf{t}_k\|_2^2} \right)$
      2.2 : Mettre à jour la k-ième ligne de **P** avec $\mathbf{p}_k$
    end for
end while

C.5.4 Résultats et discussion

Résultats Pour juger des performances de la méthode SNMF proposée, nous comparons les images SPC obtenues par cette technique avec les méthodes *pos/neg* et *shift* présentées en Section C.5.1. La factorisation de la même matrice $\check{\mathbf{P}}$ en **TP** est donc effectuée de trois manières différentes.

8. Plusieurs passages de l'algorithme sur les lignes de **P** amèneraient à une solution au problème (C.22). Ici, un passage suffit puisque l'algorithme 4 est inclus dans une autre boucle ce qui revient, quand celui-ci commence à converger, à résoudre (C.22).

Les simulations suivantes ont été corrompues par un bruit de Poisson, bruit généralement obtenu sur une mesure optique. Ce dernier est appliqué sur le vecteur de mesure **m** de (C.2).

On donne en Fig. C.9, les courbes du PSNR des images restaurées par ABS-WP avec les trois techniques (SNMF, *pos/neg*, *shift*) en fonction de différentes valeurs N_0 et deux valeurs du courant d'obscurité α. Pour ces cas, Δt est fixé à 1 s et l'image test choisie est la cible de Jaszczak.

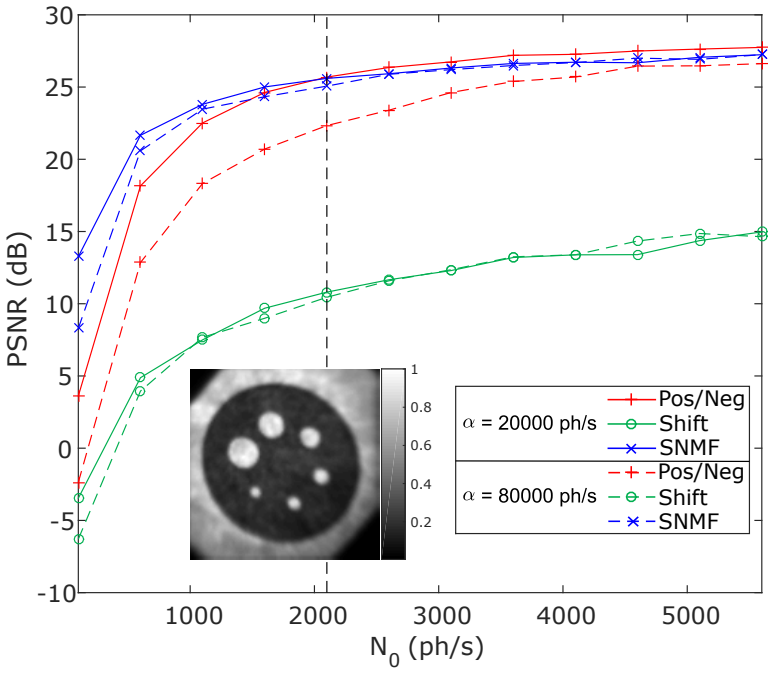

FIGURE C.9 – Image test et courbes du PSNR des images restaurées en fonction de N_0 pour $\Delta t = 1$ s avec deux valeurs de α. La barre en pointillée correspond aux résultats de la Fig. C.10.

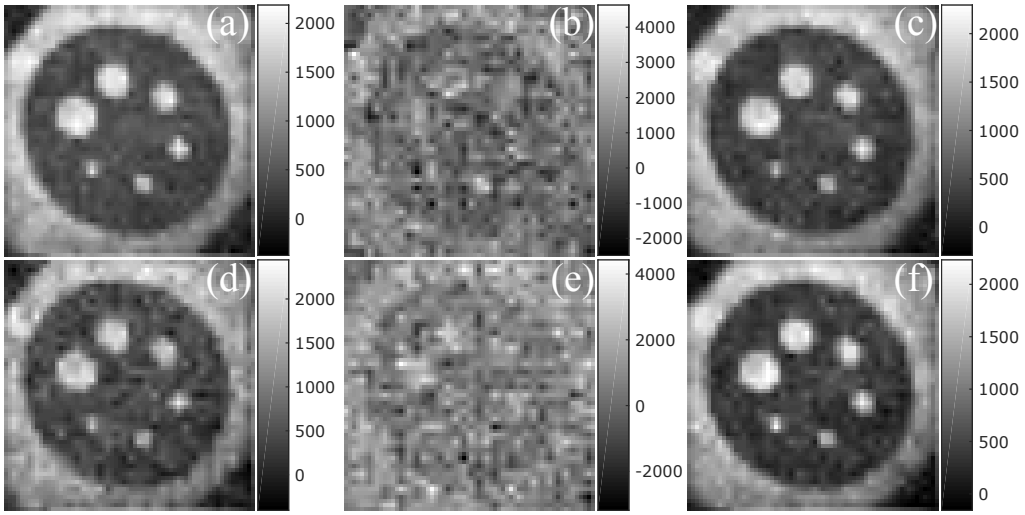

FIGURE C.10 – Images restaurées par ABS-WP pour les trois techniques de factorisation pour $N_0 = 2100$ ph/s et $\Delta t = 1$ s sur l'image test de la Fig. C.9. Images obtenues pour $\alpha = 20000$ ph/s avec (a) *pos/neg*, (b) shift, (c) SNMF et pour $\alpha = 80000$ ph/s avec (d) *pos/neg*, (e) *shift*, (f) SNMF. Les PSNRs correspondants peuvent être lus sur la Fig. C.9 (barre en pointillée).

La Fig. C.10 montre les 6 images 64×64 restaurées par ABS-WP pour le cas $N_0 = 2100$ ph/s de la Fig. C.9.

Discussion L'avantage principal de l'algorithme SNMF proposé par rapport au cas *pos/neg* est le nombre K de motifs créés qui est égal à $I+1$ pour SNMF alors qu'il vaut $2I$ pour *pos/neg*, les acquisitions sont donc plus rapides avec notre méthode. Pour la technique *shift*, $K = I+1$ peut également être obtenu mais les résultats des deux figures suivantes montrent que cette méthode souffre énormément du bruit de mesure.

Ceci peut être vu sur la Fig. C.9 où la méthode *shift* donne toujours des restaurations d'images de qualité bien inférieure aux deux autres techniques. Une explication est que l'information utile du motif décalé est en quelque sorte noyée dans celle ajoutée par l'arrière-plan. La méthode SNMF quant à elle donne de très bons résultats et ceci quelle que soit la valeur de la composante continue α. La technique *pos/neg* est impactée par cette composante pour des valeurs faibles de N_0. Ceci s'explique par le fait que les motifs *pos/neg* ont de nombreux coefficients nuls et une composante continue α importante diminue l'effet des parties actives (i.e. coefficients non nuls) du motif, effet moins présent pour SNMF où la partie active est plus considérable.

Ces résultats numériques sont confirmés par les images restaurées visibles en Fig. C.10 où la méthode *shift* donne des images très bruitées ((b) et (e)). SNMF et *pos/neg* donne des résultats similaires avec un avantage certain pour SNMF où le nombre de mesures effectives est quasiment égal au nombre de mesures désirées.

C.5.5 Conclusion du chapitre

En conclusion, nous avons proposé une technique de factorisation en matrice semi non-négatives pour contourner deux contraintes expérimentales de positivité lors de l'acquisition d'images par une SPC. La méthode permet de ne pas doubler le nombre de mesures comme la méthode *pos/neg* et est peu affectée par le bruit de mesure contrairement à la technique *shift*.

C.6 CHAPITRE VI - APPLICATION À L'IMAGERIE MULTISPECTRALE RÉSOLUE EN TEMPS

Les applications biomédicales peuvent tirer profit d'une SPC comme mentionné en introduction. Un avantage certain pour le domaine médical concerne les acquisitions multispectrales résolues en temps. En effet, les informations spectrales et temporelles peuvent être utilisées pour caractériser des tissus biologiques comportant différents fluorophores afin d'étudier leur micro-environnement (pH, température, etc.) qui est un élément essentiel pour les biologistes.

Une SPC multispectrale résolue en temps peut être obtenue en remplaçant le détecteur ponctuel de la SPC classique par un spectromètre ayant plusieurs détecteurs ponctuels en parallèle et en couplant chacun de ces détecteurs à une carte de comptage des photons (TCSPC) (Pian *et al.*, 2016b,a). Dans ses travaux, l'équipe d'Intes (Pian *et al.*, 2016b,a) utilise une méthode d'acquisition/restoration des images *non-adaptative* avec des motifs d'Hadamard.

Dans ce chapitre, la capacité de notre technique ABS-WP (Chaptitre IV) pour manipuler des données multispectrales résolues en temps est démontrée [9]. Une partie de ces résultats ont été

9. La technique SNMF presentée au Chaptitre V n'est pas utilisée ici car, chronologiquement, cette méthode

présentés à la conférence *SPIE Photonics West* en Février 2017 (Rousset *et al.*, 2017b). Nous étendons dans un premier temps les méthodes pour traiter les données avec l'apport de la dimension spectrale et temporelle avant de détailler les expériences et résultats.

C.6.1 Méthodes

Extension aux mesures multispectrales résolues en temps L'ajout d'une dimension spectrale à la SPC se fait en remplaçant le détecteur ponctuel par un spectromètre comportant Λ détecteurs ponctuels parallèles. Ceux-ci sont de plus couplés à une carte de comptage des photons (*time-correlated single photon counting*, TCSPC) avec T canaux temporels. Cette dernière est de plus synchronisée avec l'impulsion du laser qui sert de référence pour classer chaque photon selon son temps de vol (i.e. temps entre son émission par le laser et son arrivée au détecteur). Au final, une SPC multispectrale résolue en temps est donc obtenue.

Une image $\mathbf{F} \in \mathbb{R}^{D\times\Lambda T}$ (2D+λ+t) peut ainsi être acquise avec $\mathbf{F} = \left(\mathbf{f}_{1,1},\dots,\mathbf{f}_{\lambda,t},\dots,\mathbf{f}_{\Lambda,T}\right)$. L'image $\mathbf{f}_{\lambda,t} \in \mathbb{R}^{D\times 1}$ représente l'image dans le canal spectral λ et canal temporel t avec $(\lambda,t) \in [1,\Lambda]\times[1,T]$. Les informations spectrales et temporelles étant acquises simultanément, les équations (C.1) et (C.2) du Chaptitre II sont ainsi changées en

$$\mathbf{m}_k = \left(m_{k,1,1},\dots,m_{k,\lambda,t},\dots,m_{k,\Lambda,T}\right)^\top \in \mathbb{R}^{\Lambda T\times 1} \quad \text{with} \quad \mathbf{m}_k^\top = \left(N_0\mathbf{p}_k^\top\mathbf{F} + \alpha\mathbf{1}_{\Lambda T}^\top\right)\Delta t \tag{C.25}$$

$$\mathbf{M} = \left(\mathbf{m}_1,\dots,\mathbf{m}_k,\dots,\mathbf{m}_K\right)^\top \in \mathbb{R}^{K\times\Lambda T} \quad \text{with} \quad \mathbf{M} = \left(N_0\mathbf{P}\mathbf{F} + \alpha\mathbf{1}_{K\times\Lambda T}\right)\Delta t \tag{C.26}$$

avec $\mathbf{1}_{\Lambda T} = (1,\dots,1)^\top \in \mathbb{R}^{\Lambda T\times 1}$ et $\mathbf{1}_{K\times\Lambda T} \in \mathbb{R}^{K\times\Lambda T}$ la matrice dont tous les éléments valent 1. Un vecteur de mesures $\mathbf{m}_k \in \mathbb{R}^{\Lambda T\times 1}$ est directement obtenu par la SPC multispectrale résolue en temps pour un motif $\mathbf{p}_k$. Une matrice de mesures $\mathbf{M} \in \mathbb{R}^{K\times\Lambda T}$ est acquise quand une séquence de motifs $\mathbf{P} \in \mathbb{R}^{K\times D}$ est considérée.

Images dépendant uniquement du temps ou de la longueur d'onde A partir des $\Lambda\times T$ images restaurées, il est possible d'extraire T (resp. Λ) images $\mathbf{f}_t$ (resp. $\mathbf{f}_\lambda$) dans chaque canal temporel (resp. spectral) en intégrant $\mathbf{f}_{\lambda,t}$ suivant λ (resp. t) :

$$\mathbf{f}_\lambda = \sum_{t=1}^{T}\mathbf{f}_{\lambda,t} \qquad \mathbf{f}_t = \sum_{\lambda=1}^{\Lambda}\mathbf{f}_{\lambda,t} \tag{C.27}$$

Les images $\mathbf{f}_t$ (resp. $\mathbf{f}_\lambda$) sont équivalentes à celles qui auraient été obtenues sans le spectromètre (resp. TCSPC) de la SPC multispectrale résolue en temps.

Prédiction sur les mesures CW Notre méthode d'acquisition/restauration des images ABS-WP du Chaptitre IV repose sur une étape de prédiction basée sur des mesures scalaires. Pour effectuer cette étape sur les mesures (C.25), nous considérons alors l'image $\mathbf{f}$ en onde continue (*continuous-wave*, CW) obtenue en intégrant $\mathbf{f}_{\lambda,t}$ suivant λ et t :

$$\mathbf{f} = \sum_{\lambda=1}^{\Lambda}\sum_{t=1}^{T}\mathbf{f}_{\lambda,t} \tag{C.28}$$

n'était pas encore implémentée.

Area	Material	Absorption peak	Emission peak
Wave	Green fluorescence plastic slide	464 nm	525 nm
Square	Red fluorescence plastic slide	520 nm	625 nm
Circle	DCM dye painted on a white paper	468 nm	624 nm

TABLEAU C.3 – Pic d'émission et d'absorption des fluorophores constituant le fantôme.

C.6.2 Expériences

Fantôme La Fig. C.11-(a) montre le fantôme considéré pour lequel les différentes formes ont été créées avec un masque en papier orange. Le carré (resp. la vague) est une plaque auto-fluorescente en plastique rouge (resp. verte) de CHROMA. Le rond est quant à lui une solution de DCM dilué dans de l'éthanol et peinte sur une feuille blanche. Une caractérisation spectrale de ces trois fluorophores est donnée au tableau C.3.

Système expérimental Le système expérimental du Politecnico di Milano décrit en Section III.1 est employé. Un PMT à $\Lambda = 16$ canaux spectraux sert de détecteur (PML-16-1, Becker & Hickl GmbH) couplé à une TCSPC (SPC-630, Becker & Hickl GmbH) ayant 4096 canaux temporels. Après binning de ces canaux, un total de $T = 60$ canaux temporels sont obtenus qui couvrent des temps de 0 à 18.00 ns avec un pas de 0.305 ns. L'objet est illuminé dans la bande spectrale $470 - 490$ nm et un filtre passe-haut (FEL0500, ThorLabs) à 500 nm est placé devant le détecteur afin d'observer la lumière fluorescente émise par l'objet. Concernant les paramètres du spectromètre, sa longueur d'onde centrale est choisie à $\lambda_c = 575$ nm de manière à ce que les $\Lambda = 16$ canaux spectraux couvrent la plage de longueur d'onde de 505 ± 5 nm à 655 ± 5 nm avec un pas de 10 nm.

C.6.3 Résultats et discussion

Résultats La Fig. C.11 donne une photo du fantôme et l'image 64×64 CW restaurée selon (C.28). Elle montre aussi plusieurs images $\mathbf{f}_t$ (resp. $\mathbf{f}_\lambda$) dans différent canaux temporels (resp. spectraux) obtenues par (C.27). Les acquisitions ont été réalisées avec ABS-WP pour l'ondelette de Daubechies avec 5 moments nuls (Db5) (Mallat, 2008; Daubechies, 1992). Un taux de compression (TC) de 93% a été obtenu pour $\mathcal{P} = \{1; 0.85; 0.075; 0\}$.

Les courbes temporelles (resp. spectrales) dans chaque zone du fantôme sont données en Fig. C.12. Celles-ci sont calculées en sommant les pixels de $\mathbf{f}_t$ (resp. $\mathbf{f}_\lambda$) de (C.27) dans chaque zone de l'objet pour chaque canal temporel (resp. spectral).

A partir des images $\mathbf{f}_t$ de (C.27), les cartes d'amplitude et de temps de vie des fluorophores peuvent être estimées par ajustement de courbe d'une fonction exponentielle sur les données expérimentales. La Fig. C.13 montre ces deux cartes.

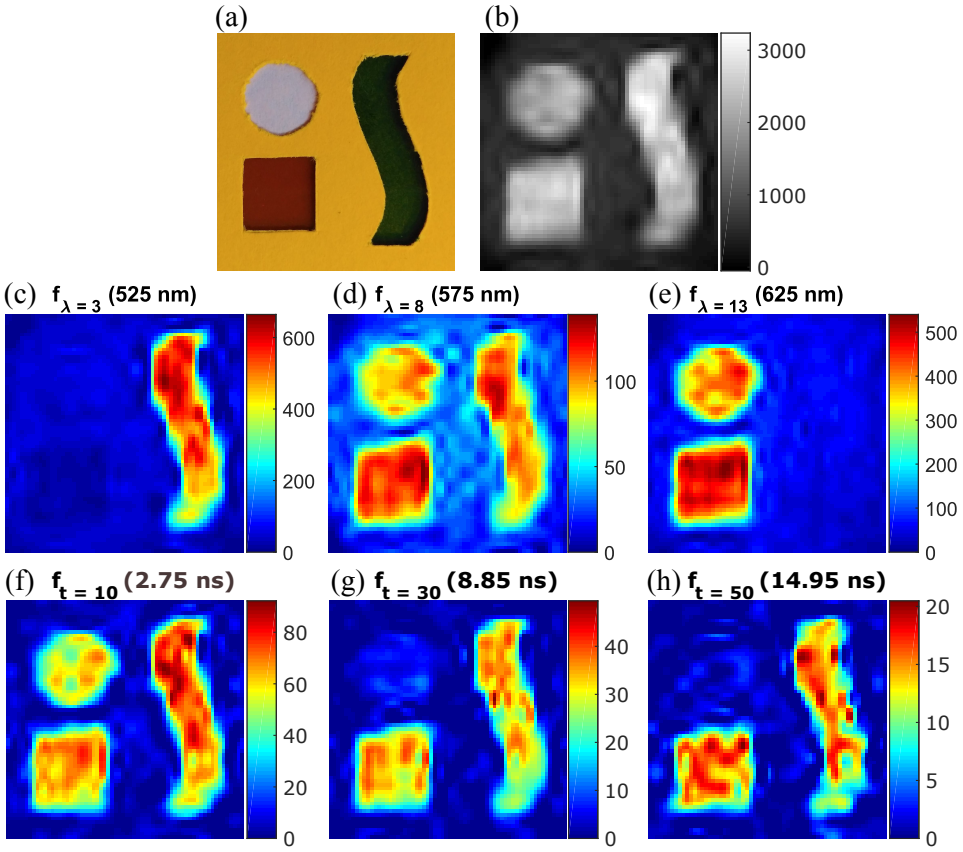

FIGURE C.11 – Fantôme, image CW et images SPC restaurées dans différents canaux temporels et spectraux. (a) Photo du fantôme, (b) image CW, image SPC restaurée dans (c)–(e) 3 canaux spectraux et (f)–(h) 3 canaux temporels.

Discussion Les résultats de la Fig. C.11 montrent que notre méthode ABS-WP permet de restaurer la pile de $\Lambda \times T$ images avec un taux de compression de 93%. L'utilisation de l'image CW (Fig. C.11-(b)) pour l'étape de prédiction est justifiée puisque cette image montre les différentes structures de notre fantôme. ABS-WP va donc chercher les coefficients d'ondelettes significatifs pour chaque zone de l'objet.

Si nous regardons les images $\mathbf{f}_\lambda$ dépendant de la longueur d'onde uniquement, seule la vague ressort dans la canal 525 nm et disparaît dans le canal 625 nm. L'effet inverse se produit pour le carré et le cercle. Les courbes spectrales plus détaillées de la Fig. C.12 confirment également ces résultats qui sont en accord avec le tableau C.3.

Concernant l'information temporelle en utilisant les images $\mathbf{f}_t$ dépendantes du temps, le rond montre un temps de vie plus court que les deux autres fluorophores puisqu'il disparait au cours du temps sur les images $\mathbf{f}_t$ de la Fig. C.11 et la décroissance exponentielle sur la Fig. C.12 est plus marquée. Ceci est confirmé par les résultats de la Fig. C.13 où la carte de temps de vie révèle un temps beaucoup plus court pour le rond que pour les deux autres fluorophores.

Au final, l'utilisation de l'information spectrale ou temporelle seule ne permet pas de différentier les trois composantes du fantôme. En revanche, quand ces deux informations sont présentes comme c'est le cas sur notre système, les trois fluorophores sont différentiables : le rond se différencie de la vague et du carré par un temps de vie beaucoup plus court alors que la vague se différencie par son contenu spectral.

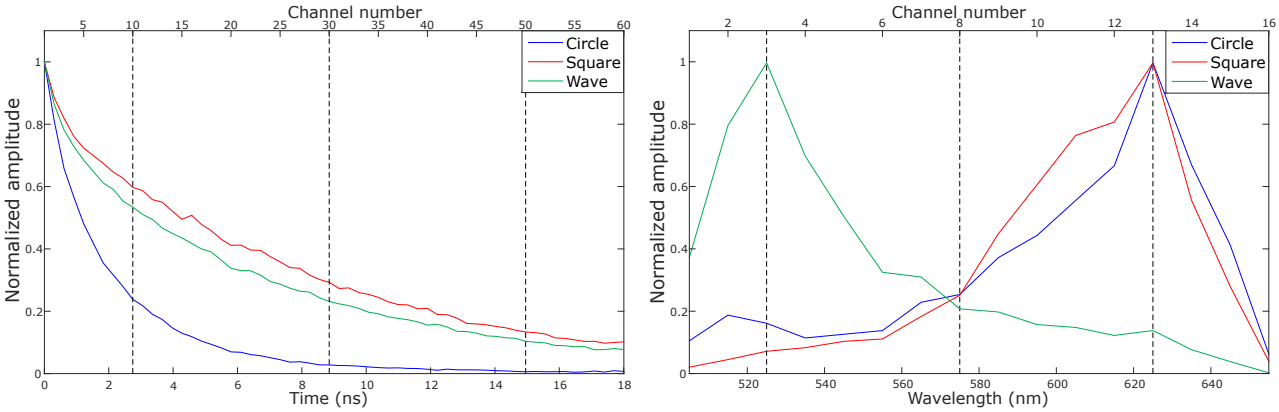

FIGURE C.12 – Courbes spectrales et temporelles obtenues depuis les images $\mathbf{f}_\lambda$ et $\mathbf{f}_t$ en sommant chaque pixel des différentes zones de l'objet. Les barres verticales en pointillée correspondent à différents canaux temporels/spectraux dont les images restaurées sont données en Fig. C.11.

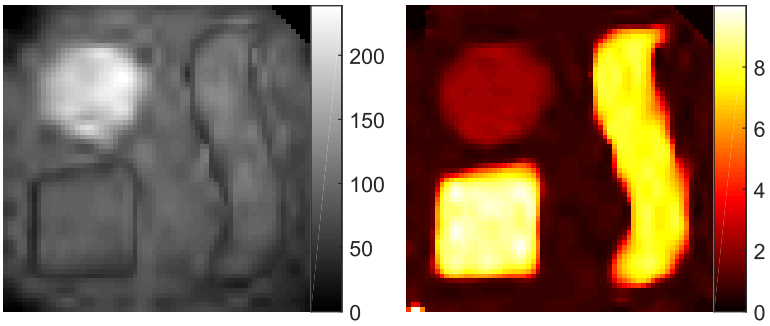

FIGURE C.13 – Cartes d'amplitude (en photons, gauche) et de temps de vie (en ns, droite) de l'objet considéré.

C.6.4 Conclusion du chapitre

Nous avons reporté dans ce chapitre la capacité de notre technique ABS-WP à fonctionner sur une caméro mono-pixel multispectrale résolue en temps. Le système permet d'acquérir efficacement l'information spectrale et temporelle avec de forts taux de compression. La SPC est un excellent compris pour obtenir de bonnes résolutions spatiales, temporelles et spectrales et n'a aucun équivalent similaire actuellement pour le même prix.

Conclusion, limites et perspectives

L'imagerie mono-pixel permet de mesurer la projection de la scène observée sur des motifs à l'aide d'un montage optique équipé d'un simple détecteur ponctuel. Cette implémentation particulière rend ce type d'imagerie intéressante pour des applications médicales, applications visées par cette thèse. La limitation actuelle de la caméra mono-pixel sont les temps d'acquisition et/ou de restauration de l'image qui sont généralement longs. Des applications temps réel ne peuvent alors être considérées telles que l'imagerie interventionnelle (e.g. la chirurgie de fluorescence).

Après avoir détaillé l'état de l'art au niveau matériel (Chaptitre I) et logiciel (Chaptitre II), les contributions de cette thèse ont été exposées.

Dans un premier temps, deux systèmes expérimentaux ont été présentés au Chaptitre III avec

l'ajout d'un logiciel de communication entre Labview qui contrôle les instruments et Matlab pour traiter les données. Ceci permet l'implémentation de la technique d'imagerie ABS-WP présentée au Chaptitre IV qui permet d'acquérir les coefficients d'ondelettes significatifs de l'image observée. Outre des forts taux de compression, cette méthode permet une restauration de l'image directe par transformée en ondelettes inverse. Au Chaptitre V, une méthode par factorisation de matrices est proposée afin de palier deux contraintes expérimentales. La méthode permet, par rapport aux méthodes classiques, de réduire le nombre de mesures et donc d'accélérer les temps d'acquisition. Enfin, au Chaptitre VI, des acquisitions multispectrales résolues en temps donnent une preuve de concept pour aller vers des applications médicales.

En résumé, le but principal de cette thèse d'accélérer les temps d'acquisition et/ou de restauration des images par une SPC est atteint. En effet, la méthode ABS-WP permet de réduire le temps de restauration de l'image alors que la méthode par factorisation de matrices réduit ceux d'acquisitions.

Limites Une première limite des contributions de cette thèse concerne l'étape de prédiction des coefficients d'ondelettes dans ABS-WP. Les résultats montrent une précision maximum de 85% pour trouver les coefficients significatifs. Si cette précision pouvait atteindre 100%, la meilleure image SPC possible serait acquise puisque l'approximation non-linéaire de la transformée en ondelettes est la meilleure possible [10]

ABS-WP permet d'utiliser n'importe quelle ondelette pour laquelle les motifs ont des valeurs réelles flottantes. Le DMD est alors utilisé dans son mode 8-bit ce qui est une seconde limitation puisque le taux de rafraichissement du DMD est impacté. En effet, ce dernier peut atteindre son plus haut taux de rafraichissement quand il fonctionne en mode binaire, ce taux est donc réduit quand 8 bits sont nécessaires, augmentant ainsi les temps d'acquisition. Pour nos acquisitions réelles, ceci n'était pas un problème car la carte de comptage des photons a besoin d'un temps d'acquisition plus long que le taux de rafraichissement du DMD en mode 8-bit. Si des acquisitions rapides sont nécessaires, il est toujours possible d'utiliser notre méthode ABS-WP avec l'ondelette de Haar qui crée des motifs binaires.

Si l'on passe à la méthode de généralisation des motifs, une limite est la combinaison de plusieurs mesures par rapport aux méthodes classiques *pos/neg* et *shift* qui combinent seulement deux mesures. En présence de bruit, la variance de nos mesures désirées finales pour l'algorithme SNMF dépend ainsi d'une somme de variance des mesures SPC acquises. Ceci peut alors accroitre l'effet du bruit et réduire la qualité de l'image restaurée. Cet effet est moins visible avec les méthodes classiques puisque le bruit ne dépend que d'une somme de deux variances.

Perspectives Une première perspective de ce travail de thèse serait d'améliorer la stratégie de prédiction d'ABS-WP. Comme mentionné plus tôt, certains coefficients significatifs d'ondelettes ne sont pas acquis ce qui impacte la qualité de l'image restaurée. Des méthodes plus robustes pour cette prédiction par rapport à l'interpolation bi-cubique pourraient donc être envisagées. Cette étape doit cependant rester assez rapide afin de ne pas ralentir le temps total d'acquisition.

10. En comparaison avec le même genre d'approximation dans Fourier ou une autre base.

Une idée serait d'utiliser les techniques récentes de *deep learning* afin de prédire soit la valeur d'un coefficient d'ondelettes directement ou s'il est significatif ou non. Une telle approche serait rapide puisque la partie d'entrainement d'un réseau de neurones peut se faire a priori sur une base de données de centaines d'images. L'application du réseau sur les nouvelles données est ensuite rapide et pourrait permettre d'augmenter la précision de prédiction.

Une autre perspective concerne la méthode de généralisation des motifs. Cette dernière permet de créer K motifs positifs à partir d'un ensemble de I motifs réels. Avec l'algorithme proposé, une valeur de $K = I + 1$ est actuellement obtenue. Cependant, la plupart des algorithmes de factorisation de matrice cherchent une factorisation avec $K < I$. Ces techniques pourraient alors être envisagées afin de réduire le nombre de mesures SPC effectives. Un problème possible serait l'erreur de factorisation qui deviendrait plus importante et les mesures seraient alors erronées. Avoir $K < I$ permettrait également de combiner moins de mesures afin de réduire l'influence du bruit sur les mesures désirées. Une autre possibilité pour palier l'effet du bruit serait d'ajouter une contrainte de parcimonie sur la matrice $\mathbf{T}$. Si cette matrice a des zéros, le vecteur des mesures désirées serait ainsi créé avec moins de combinaisons de mesures SPC.

Au niveau des acquisitions multispectrales résolue en temps du Chaptitre VI, l'étape de prédiction de ABS-WP était basée sur les mesures en onde-continue qui intègrent tous les canaux spectraux et temporels. Cependant, certains de ces canaux ne reçoivent pas beaucoup d'information et n'apportent ainsi que très peu d'information aux mesures CW. Afin de maximiser la précision de l'étape de prédiction, une étape préliminaire juste avant celle-ci pourrait être ajoutée. Cette nouvelle étape chercherait les canaux spectraux et temporels qui amènent le moins d'information afin de ne pas les intégrer pour créer la mesure CW [11].

Du côté des applications, la prochaine marche serait d'appliquer les méthodes développées dans cette thèse pour l'imagerie interventionnelle, e.g. la chirurgie guidée par fluorescence pour la résection de tumeurs au cerveau imagées par une SPC hyperspectrale. Ceci est un travail complet en soi puisque les techniques de cette thèse devraient être adaptées pour l'imagerie vidéo. L'exploitation de la donnée temporelle (i.e. la frame à $t + 1$ ressemble à celle à t) et l'utilisation de certaines des autres perspectives mentionnées plus tôt pourraient permettre de compresser encore plus les données afin d'atteindre des images à des taux vidéos [12]. Une fois l'extension d'ABS-WP aux vidéos faite, la SPC couplée à un spectromètre dernier cri devrait permettre de discerner les marges tumorales des tissus sains.

11. Par définition, si certains canaux ne sont pas pris en compte, cette mesure ne serait pas une mesure CW à proprement parler.

12. Pour la chirurgie guidée par fluorescence, 1 Hz peut être considéré comme temps réel.

APPENDIX D

LIST OF PERSONAL PUBLICATIONS

D.1 Journal

[J1] Rousset, F., Ducros, N., Farina, A., Valentini, G., D'Andrea, C., Peyrin, F., March 2017. Adaptive basis scan by wavelet prediction for single-pixel imaging. IEEE Transactions on Computational Imaging 3 (1), 36-46.

[J2] Rousset, F., Peyrin, F., Ducros, N. A Semi Nonnegative Matrix Factorization Method for Pattern Generalization in Single-Pixel Imaging. IEEE Transactions on Computational Imaging, submitted.

[J3] Rousset, F., Ducros, N., Farina, A., Valentini, G., D'Andrea, C., Peyrin, F. Adaptive single-pixel camera acquisitions on a time-resolved multispectral system. Optics Express, to be submitted.

D.2 Pattent

[P1] Rousset, F., Ducros, N., Peyrin, F., 2017. Caméra mono-pixel. FR Patent 1751515 filed the 02/24/2017.

D.3 International conferences (with proceedings)

[C1] Rousset, F., Ducros, N., D'Andrea, C., Peyrin, F., August 2015. Single pixel camera : An acquisition strategy based on the non-linear wavelet approximation. 2015 37th Annual International Conference of the IEEE Engineering in Medicine and Biology Society (EMBC), 6240–6243

[C2] Rousset, F., Ducros, N., Farina, A., Valentini, G., D'Andrea, C., Peyrin, F., April 2016. Adaptive acquisitions in biomedical optical imaging based on single pixel camera : Comparison with compressive sensing. 2016 IEEE 13th International Symposium on Biomedical Imaging (ISBI), 680–683.

[C3] Rousset, F., Ducros, N., Farina, A., Valentini, G., D'Andrea, C., Peyrin, F., February 2017. Time-resolved wavelet-based acquisitions using a single-pixel camera. Proc. SPIE. Vol. 10070, 1007016–1007016–7.

D.4 National communications

[N1] Rousset, F., Ducros, N., D'Andrea, C., Peyrin, F., Mars 2015. A wavelet-based non-linear acquisition strategy for single pixel camera acquisitions. Journées RITS 2015, Dourdan, France, 144-145, 2015.

[N2] Rousset F., Ducros, N., Peyrin, F., Mars 2015. Single-pixel camera : stratégie d'acquisition non linéaire basée sur les ondelettes. 10e Journées Imagerie Optique Non Conventionnelle, Paris, France, 2015.

[N3] Rousset, F., Ducros, N., Andrea, F., D'Andrea, C., Peyrin, F., Mars 2016. Acquisition adaptative pour single-pixel caméra : comparaison avec l'acquisition comprimée. 11e Journées Imagerie Optique Non Conventionnelle, Paris, France, 2016.

[N4] Rousset, F., Ducros, N., Farina, A., Gianluca, V., D'Andrea, C., et Peyrin, F., Mars 2017. Acquisitions adaptatives multispectrales et résolues en temps par une caméra mono-pixel. 12e Journées Imagerie Optique Non Conventionnelle, Paris, France, 2017.

[N5] Rousset, F., Ducros, N., Farina, A., D'Andrea, C., Peyrin, F., Mars 2017. Fluorescence lifetime imaging using a multispectral time-resolved wavelet-based single pixel imaging system. Journées RITS 2017, Lyon, France, 2017.

[N6] Rousset, F., Ducros, N., Peyrin, F., Septembre 2017. Technique de factorisation en matrices semi non-négatives pour acquisition d'images par caméra mono-pixel. GRETSI 2017, Juan-les-pins, France.

BIBLIOGRAPHY

Allier, C. P., Hiernard, G., Poher, V., Dinten, J. M., Oct 2010. Bacteria detection with thin wetting film lensless imaging. Biomed. Opt. Express 1 (3), 762–770. 17

Asif, M. S., Ayremlou, A., Sankaranarayanan, A. C., Veeraraghavan, A., Baraniuk, R. G., 2015a. Flatcam : Thin, bare-sensor cameras using coded aperture and computation. CoRR abs/1509.00116. 17

Asif, M. S., Ayremlou, A., Veeraraghavan, A., Baraniuk, R., Sankaranarayanan, A., Dec 2015b. Flatcam : Replacing lenses with masks and computation. In : 2015 IEEE International Conference on Computer Vision Workshop (ICCVW). pp. 663–666. 17

Aßmann, M., Bayer, M., 2013. Compressive adaptive computational ghost imaging. Scientific Reports 3 (1545). 13

Averbuch, A., Dekel, S., Deutsch, S., 2012. Adaptive compressed image sensing using dictionaries. SIAM Journal on Imaging Sciences 5 (1), 57–89. 32, 69, 76

Baraniuk, R., 2007. Compressive sensing. IEEE Signal Processing Mag, 118–120. 23

Baraniuk, R., Baron, D., Duarte, M., Kelly, K., Lane, C., Laska, J., Takhar, D., Wakin, M., Sep. 30 2014. Method and apparatus for compressive imaging device. US Patent 8848091. 7, 118

Baraniuk, R., Davenport, M., Devore, R., Wakin, M., 2007. A simple proof of the restricted isometry property for random matrices. Constr. Approx 2008. 24

Baraniuk, R. G., Cevher, V., Duarte, M. F., Hegde, C., April 2010. Model-based compressive sensing. IEEE Transactions on Information Theory 56 (4), 1982–2001. 23

Baraniuk, R. G., Goldstein, T., Sankaranarayanan, A. C., Studer, C., Veeraraghavan, A., Wakin, M. B., Jan 2017. Compressive video sensing : Algorithms, architectures, and applications. IEEE Signal Processing Magazine 34 (1), 52–66. 16

Becker, W., 2012. Fluorescence lifetime imaging – techniques and applications. Journal of Microscopy 247 (2), 119–136. 2, 95, 116

Ben-Yosef, N., Sirat, G., 1982. Real-time spatial filtering utilizing the piezoelectric-elasto-optic effect. Optica Acta : International Journal of Optics 29 (4), 419–423. 1

Bernal, E., Mestha, L., Austin, P., Loce, R., Nov. 17 2015. Single-pixel camera architecture with simultaneous multi-band acquisition. US Patent 9188785. 14

Berry, M. W., Browne, M., Langville, A. N., Pauca, V. P., Plemmons, R. J., 2006. Algorithms and applications for approximate nonnegative matrix factorization. In : Computational Statistics and Data Analysis. pp. 155–173. 76, 80

Bian, L., Suo, J., Hu, X., Chen, F., Dai, Q., 2016a. Efficient single pixel imaging in fourier space. Journal of Optics 18 (8), 085704. 28

Bian, L., Suo, J., Situ, G., Li, Z., Fan, J., Chen, F., Dai, Q., 2016b. Multispectral imaging using a single bucket detector. Scientific Reports 6 (24752). 14, 15

Bonaccorso, F., Sun, Z., Hasan, T., Ferrari, A., 2010. Graphene photonics and optoelectronics. Nature photonics 4 (9), 611–622. 18

Boominathan, V., Adams, J. K., Asif, M. S., Avants, B. W., Robinson, J. T., Baraniuk, R. G., Sankaranarayanan, A. C., Veeraraghavan, A., Sept 2016. Lensless imaging : A computational renaissance. IEEE Signal Processing Magazine 33 (5), 23–35. 17

Bucak, S. S., Gunsel, B., Sept 2007. Video content representation by incremental non-negative matrix factorization. In : 2007 IEEE International Conference on Image Processing. Vol. 2. pp. II – 113–II – 116. 76

Candes, E., Romberg, J., 2005. l1-magic : Recovery of sparse signals via convex programming. 24

Candes, E., Romberg, J., Tao, T., Feb 2006. Robust uncertainty principles : exact signal reconstruction from highly incomplete frequency information. Information Theory, IEEE Transactions on 52 (2), 489–509. 23, 24, 25

Candes, E., Tao, T., Dec 2006. Near-optimal signal recovery from random projections : Universal encoding strategies? Information Theory, IEEE Transactions on 52 (12), 5406–5425. 24

Chan, W. L., Charan, K., Takhar, D., Kelly, K. F., Baraniuk, R. G., Mittleman, D. M., 2008. A single-pixel terahertz imaging system based on compressed sensing. Applied Physics Letters 93 (12). 13, 25

Chen, H., Xi, N., Song, B., Chen, L., Lai, K. W. C., Oct 2011. Single pixel infrared camera using a carbon nanotube photodetector. In : Sensors, 2011 IEEE. pp. 1362–1366. 17

Chen, L., Zhou, Z., Xi, N., Yang, R., Song, B., Sun, Z., Su, C., Nov 2014. Super resolution infrared camera using single carbon nanotube photodetector. In : SENSORS, 2014 IEEE. pp. 1038–1041. 17

Cichocki, A., Zdunek, R., Amari, S., May 2006. New algorithms for non-negative matrix factorization in applications to blind source separation. In : 2006 IEEE International Conference on Acoustics Speech and Signal Processing Proceedings. Vol. 5. pp. V–V. 76

Clemente, P., Durán, V., Tajahuerce, E., Andrés, P., Climent, V., Lancis, J., Jul 2013. Compressive holography with a single-pixel detector. Opt. Lett. 38 (14), 2524–2527. 9, 119

Cohen, A., Daubechies, I., Feauveau, J. C., 1992. Biorthogonal bases of compactly supported wavelets. Communications on Pure and Applied Mathematics 45 (5), 485–560. 61

Coifman, R., Geshwind, F., Meyer, Y., 2001. Noiselets. Applied and Computational Harmonic Analysis 10 (1), 27–44. 34

Dai, H., Gu, G., He, W., Liao, F., Zhuang, J., Liu, X., Chen, Q., Oct 2014. Adaptive compressed sampling based on extended wavelet trees. Appl. Opt. 53 (29), 6619–6628. 32, 33, 61, 64, 65, 69, 75, 76, 77, 129, 130, 133

Dai, H., Gu, G., He, W., Ye, L., Mao, T., Chen, Q., Nov 2016. Adaptive compressed photon counting 3d imaging based on wavelet trees and depth map sparse representation. Opt. Express 24 (23), 26080–26096. 16

D'Andrea, C., Comelli, D., Pifferi, A., Torricelli, A., Valentini, G., Cubeddu, R., 2003. Time-resolved optical imaging through turbid media using a fast data acquisition system based on a gated ccd camera. Journal of Physics D : Applied Physics 36 (14), 1675–1681. 95

D'Andrea, C., Ducros, N., Bassi, A., Arridge, S., Valentini, G., 2010. Fast 3d optical reconstruction in turbid media using spatially modulated light. Biomed. Opt. Express 1 (2), 471–481. 2, 41, 95, 117, 123

Daubechies, I., 1992. Ten Lectures on Wavelets. Society for Industrial and Applied Mathematics. 55, 56, 99, 128, 139

Davenport, M. A., Arias-Castro, E., July 2012. Compressive binary search. In : Information Theory Proceedings (ISIT), 2012 IEEE International Symposium on. pp. 1827–1831. 36

de Fréin, R., Drakakis, K., Rickard, S., Cichocki, A., 2008. Analysis of financial data using non-negative matrix factorization. In : International Mathematical Forum. Vol. 3. Journals of Hikari Ltd, pp. 1853–1870. 76

Deutsch, S., Averbush, A., Dekel, S., May 2009. Adaptive compressed image sensing based on wavelet modeling and direct sampling. In : Laurent Fesquet and Bruno Torrésani (Ed.), SAMPTA'09. Marseille, France, p. General session. 31, 32, 69, 76

Ding, C., Li, T., Jordan, M., Jan 2010. Convex and semi-nonnegative matrix factorizations. IEEE Transactions on Pattern Analysis and Machine Intelligence 32 (1), 45–55. 76, 132

Donoho, D. L., 2006. Compressed sensing. IEEE Trans. Inform. Theory 52, 1289–1306. 1, 7, 23, 24, 35, 116, 118, 121

Duan, P., Wang, Y., Xu, D., Yan, C., Yang, Z., Xu, W., Shi, W., Yao, J., May 2016. Single pixel imaging with tunable terahertz parametric oscillator. Appl. Opt. 55 (13), 3670–3675. 14

Duarte, M., Davenport, M., Takhar, D., Laska, J., Sun, T., Kelly, K., Baraniuk, R., March 2008. Single-pixel imaging via compressive sampling. Signal Processing Magazine, IEEE 25 (2), 83–91. 7, 8, 12, 13, 22, 24, 25, 26, 61, 75, 77, 118, 119, 129, 133

Ducros, N., Bassi, A., Valentini, G., Canti, G., Arridge, S., D'Andrea, C., 2013. Fluorescence molecular tomography of an animal model using structured light rotating view acquisition. Journal of Biomedical Optics 18 (2), 020503–020503. 2, 41, 95, 117, 123

Ducros, N., Correia, T., Bassi, A., Valentini, G., Arridge, S., D'Andrea, C., 2016. Reconstruction of an optical inhomogeneity map improves fluorescence diffuse optical tomography. Biomedical Physics & Engineering Express 2 (5), 055020. 2, 41, 95, 117, 123

Duran, V., Soldevila, F., Irles, E., Clemente, P., Tajahuerce, E., Andrés, P., Lancis, J., Jun 2015. Compressive imaging in scattering media. Opt. Express 23 (11), 14424–14433. 2, 25, 95, 116

Edgar, M. P., Gibson, G. M., Bowman, R. W., Sun, B., Radwell, N., Mitchell, K. J., Welsh, S. S., Padgett, M. J., 2015. Simultaneous real-time visible and infrared video with single-pixel detectors. Scientific reports 5. 13, 16, 25

Foucart, S., Rauhut, H., 2013. A mathematical introduction to compressive sensing. Vol. 1. Springer. 24, 29

Fursich, B., Bamler, R., Augustin, S., Hubers, H. W., Zhu, X. X., Sept 2016. Towards single-pixel fmcw radar reconstruction. In : 2016 4th International Workshop on Compressed Sensing Theory and its Applications to Radar, Sonar and Remote Sensing (CoSeRa). pp. 95–99. 14

Gall, D. L., Tabatabai, A., April 1988. Sub-band coding of digital images using symmetric short kernel filters and arithmetic coding techniques. International Conferance on Acoustics, Speech, and Signal Processing 2, 761–764. 61

Gibson, A., Dehghani, H., 2009. Diffuse optical imaging. Philosophical Transactions of the Royal Society of London A : Mathematical, Physical and Engineering Sciences 367 (1900), 3055–3072. 2, 95, 117

Gibson, G. M., Sun, B., Edgar, M. P., Phillips, D. B., Hempler, N., Maker, G. T., Malcolm, G. P. A., Padgett, M. J., Feb 2017. Real-time imaging of methane gas leaks using a single-pixel camera. Opt. Express 25 (4), 2998–3005. 13, 16

Gillis, N., 2014. The why and how of nonnegative matrix factorization. In : Regularization, Optimization, Kernels, and Support Vector Machines. Chapman and Hall/CRC, pp. 257–291. 76, 80

Gillis, N., Kumar, A., 2015. Exact and heuristic algorithms for semi-nonnegative matrix factorization. SIAM Journal on Matrix Analysis and Applications 36 (4), 1404–1424. 81, 88, 132, 135

Goldstein, T., Xu, L., Kelly, K. F., Baraniuk, R., Dec 2015. The stone transform : Multi-resolution image enhancement and compressive video. IEEE Transactions on Image Processing 24 (12), 5581–5593. 16

Hadfield, R. H., 2009. Single-photon detectors for optical quantum information applications. Nature photonics 3 (12), 696–705. 1, 12, 116

Hahn, J., Debes, C., Leigsnering, M., Zoubir, A. M., 2014. Compressive sensing and adaptive direct sampling in hyperspectral imaging. Digital Signal Processing 26, 113 – 126. 14, 32, 76

Herman, M. A., Weston, T., McMackin, L., Li, Y., Chen, J., Kelly, K. F., 2015. Recent results in single-pixel compressive imaging using selective measurement strategies. Vol. 9484. pp. 94840A–94840A–18. 35, 36

Hornbeck, L., Oct. 29 1991. Spatial light modulator and method. US Patent 5061049. 8, 119

Howland, G. A., Lum, D. J., Ware, M. R., Howell, J. C., Oct 2013. Photon counting compressive depth mapping. Opt. Express 21 (20), 23822–23837. 16

Huang, G., Jiang, H., Matthews, K., Wilford, P., Sept 2013. Lensless imaging by compressive sensing. In : 2013 IEEE International Conference on Image Processing. pp. 2101–2105. 8, 11, 17, 119

Huo, Y.-R., He, H.-J., Chen, F., Tai, H.-M., Jan 2017. Adaptive single-pixel imaging based on guided coefficients. J. Opt. Soc. Am. A 34 (1), 39–51. 32, 69, 76

Huynh, N., Zhang, E., Betcke, M., Arridge, S., Beard, P., Cox, B., Jan 2016. Single-pixel optical camera for video rate ultrasonic imaging. Optica 3 (1), 26–29. 16

Indyk, P., Price, E., Woodruff, D. P., Oct 2011. On the power of adaptivity in sparse recovery. In : Foundations of Computer Science (FOCS), 2011 IEEE 52nd Annual Symposium on. pp. 285–294. 36

Jacques, S. L., 2013. Optical properties of biological tissues : a review. Physics in Medicine and Biology 58 (11), R37. 1, 116

Keramidas, M., Josserand, V., Righini, C. A., Wenk, C., Faure, C., Coll, J. L., 2010. Intraoperative near-infrared image-guided surgery for peritoneal carcinomatosis in a preclinical experimental model. British Journal of Surgery 97 (5), 737–743. 61, 129

Keys, R., Dec 1981. Cubic convolution interpolation for digital image processing. Acoustics, Speech and Signal Processing, IEEE Transactions on 29 (6), 1153–1160. 63

Kirmani, A., Colaço, A., Wong, F. N. C., Goyal, V. K., Oct 2011. Exploiting sparsity in time-of-flight range acquisition using a single time-resolved sensor. Opt. Express 19 (22), 21485–21507. 15

Kuo, D. M.-T., Fang, A., Chang, Y., 2001. Theoretical modeling of dark current and photo-response for quantum well and quantum dot infrared detectors. Infrared Physics & Technology 42 (35), 433 – 442. 17

Lee, D. D., Seung, H. S., 1999. Learning the parts of objects by nonnegative matrix factorization. Nature 401, 788–791. 76, 80, 132

Lee, D. D., Seung, H. S., 2001. Algorithms for non-negative matrix factorization. In : NIPS. MIT Press, pp. 556–562. 76, 80

Li, C., 2009. An efficient algorithm for total variation regularization with applications to the single pixel camera and compressive sensing. Ph.D. thesis, Rice University. 25, 61

Li, G., Wang, W., Wang, Y., Yang, W., Liu, L., Jan 2016. Single-pixel camera with one graphene photodetector. Opt. Express 24 (1), 400–408. 17, 18

Li, X., Orchard, M., Oct 2001. New edge-directed interpolation. Image Processing, IEEE Transactions on 10 (10), 1521–1527. 63

Li, Z., Suo, J., Hu, X., Deng, C., Fan, J., Dai, Q., 2017. Efficient single-pixel multispectral imaging via non-mechanical spatio-spectral modulation. Scientific Reports 7. 15

Lin, C.-J., Oct. 2007. Projected gradient methods for nonnegative matrix factorization. Neural Comput. 19 (10), 2756–2779. 76, 80

Liu, B.-L., Yang, Z.-H., Liu, X., Wu, L.-A., 2017. Coloured computational imaging with single-pixel detectors based on a 2d discrete cosine transform. Journal of Modern Optics 64 (3), 259–264. 29, 76

Lochocki, B., Gambín, A., Manzanera, S., Irles, E., Tajahuerce, E., Lancis, J., Artal, P., Oct 2016. Single pixel camera ophthalmoscope. Optica 3 (10), 1056–1059. 2, 95, 117

Lochocki, B., Gambin, A., Manzanera, S., Irles, E., Tajahuerce, E., Lancis, J., Artal, P., 2017. A single pixel camera video ophthalmoscope. In : Proc. SPIE. Vol. 10057. pp. 100570M–100570M–7. 2, 95, 117

Ma, D., Bec, J., Gorpas, D., Yankelevich, D., Marcu, L., Mar 2015. Technique for real-time tissue characterization based on scanning multispectral fluorescence lifetime spectroscopy (ms-trfs). Biomed. Opt. Express 6 (3), 987–1002.
URL http://www.osapublishing.org/boe/abstract.cfm?URI=boe-6-3-987 95, 106

Ma, J., Oct 2009a. A single-pixel imaging system for remote sensing by two-step iterative curvelet thresholding. IEEE Geoscience and Remote Sensing Letters 6 (4), 676–680. 1, 25, 116

Ma, J., April 2009b. Single-pixel remote sensing. IEEE Geoscience and Remote Sensing Letters 6 (2), 199–203. 1, 25, 116

Ma, Y., Grant, J., Saha, S., Cumming, D. R. S., May 2012. Terahertz single pixel imaging based on a nipkow disk. Opt. Lett. 37 (9), 1484–1486. 14

Magalhaes, F., Abolbashari, M., Araujo, F. M., Correia, M. V., Farahi, F., 2012. High-resolution hyperspectral single-pixel imaging system based on compressive sensing. Optical Engineering 51 (7), 071406–1–071406–6. 14, 25

Magalhaes, F., Araujo, F. M., Correia, M. V., Abolbashari, M., Farahi, F., Feb 2011. Active illumination single-pixel camera based on compressive sensing. Appl. Opt. 50 (4), 405–414. 25

Mallat, S., Jul 1989. A theory for multiresolution signal decomposition : the wavelet representation. Pattern Analysis and Machine Intelligence, IEEE Transactions on 11 (7), 674–693. 32, 54

Mallat, S., Dec. 2008. A Wavelet Tour of Signal Processing, Third Edition : The Sparse Way, 3rd Edition. Academic Press. 32, 53, 54, 57, 68, 99, 128, 139

Malloy, M. L., Nowak, R. D., July 2014. Near-optimal adaptive compressed sensing. IEEE Transactions on Information Theory 60 (7), 4001–4012. 36

Marcu, L., 2012. Fluorescence lifetime techniques in medical applications. Annals of Biomedical Engineering 40 (2), 304–331. 95, 106

Martínez-León, L., Clemente, P., Mori, Y., Climent, V., Lancis, J., Tajahuerce, E., Mar 2017. Single-pixel digital holography with phase-encoded illumination. Opt. Express 25 (5), 4975–4984. 14

Miao, X., Amirparviz, B., Jun. 30 2015. Single pixel camera. US Patent 9071739. 7, 118

Nystrom, P., Mestha, L., Bernal, E., Wen, X., Gulvin, P., Feb. 2 2016. Hyperspectral single pixel imager with fabry perot filter. US Patent 9253420. 14

Onose, S., Takahashi, M., Mizutani, Y., Yasui, T., Yamamoto, H., 2016. Single pixel imaging with a high-frame-rate led array. In : JSAP-OSA Joint Symposia 2016 Abstracts. Optical Society of America, pp. 13a–C301–10. 13

Ozcan, A., McLeod, E., 2016. Lensless imaging and sensing. Annual Review of Biomedical Engineering 18, 77–102. 17

Paatero, P., Tapper, U., 1994. Positive matrix factorization : A non-negative factor model with optimal utilization of error estimates of data values. Environmetrics 5 (2), 111–126. 76, 80

Park, S. C., Park, M. K., Kang, M. G., 2003. Super-resolution image reconstruction : a technical overview. Signal Processing Magazine, IEEE 20 (3), 21–36. 68

Petersen, K. B., Pedersen, M. S., *et al.*, 2008. The matrix cookbook. Technical University of Denmark 7, 15. 113

Petrovici, M. A., Damian, C., Udrea, C., Garoi, F., Coltuc, D., June 2016. Single pixel camera with compressive sensing by non-uniform sampling. In : 2016 International Conference on Communications (COMM). pp. 443–448. 36

Phillips, D. B., Sun, M.-J., Taylor, J. M., Edgar, M. P., Barnett, S. M., Gibson, G. G., Padgett, M. J., 2016. Adaptive foveated single-pixel imaging with dynamic super-sampling. arXiv preprint arXiv :1607.08236. 16

Pian, Q., Yao, R., Intes, X., 2016a. Time-resolved hyperspectral single-pixel camera implementation for compressive wide-field fluorescence lifetime imaging. In : Proc. SPIE. Vol. 9701. pp. 970115–970115–6. 2, 95, 116, 137

Pian, Q., Yao, R., Sinsuebphon, N., Intes, X., 2016b. Hyperspectral compressive single-pixel imager for fluorescence lifetime sensing. In : Biomedical Optics 2016. Optical Society of America, p. OTu2C.7. 2, 95, 116, 137

Pian, Q., Yao, R., Zhao, L., Intes, X., 2015. Hyperspectral time-resolved wide-field fluorescence molecular tomography based on structured light and single-pixel detection. Optics Letters 40, 431–434. 2, 95, 117

Pratt, W., Kane, J., Andrews, H. C., Jan 1969. Hadamard transform image coding. Proceedings of the IEEE 57 (1), 58–68. 27

Radwell, N., Mitchell, K. J., Gibson, G. M., Edgar, M. P., Bowman, R., Padgett, M. J., Nov 2014. Single-pixel infrared and visible microscope. Optica 1 (5), 285–289. 2, 13, 14, 34, 36, 76, 104

Rodriguez, A., Clemente, P., Tajahuerce, E., Lancis, J., 2016. Dual-mode optical microscope based on single-pixel imaging. Optics and Lasers in Engineering 82, 87 – 94. 2, 14, 25, 104

Rogalski, A., 2012. History of infrared detectors. Opto-Electronics Review 20 (3), 279–308. 1, 12, 116

Rousset, F., Ducros, N., D'Andrea, C., Peyrin, F., Aug 2015. Single pixel camera : An acquisition strategy based on the non-linear wavelet approximation. In : 2015 37th Annual International Conference of the IEEE Engineering in Medicine and Biology Society (EMBC). pp. 6240–6243. 53, 127

Rousset, F., Ducros, N., Farina, A., Valentini, G., D'Andrea, C., Peyrin, F., April 2016. Adaptive acquisitions in biomedical optical imaging based on single pixel camera : Comparison with compressive sensing. In : 2016 IEEE 13th International Symposium on Biomedical Imaging (ISBI). pp. 680–683. 53, 127

Rousset, F., Ducros, N., Farina, A., Valentini, G., D'Andrea, C., Peyrin, F., March 2017a. Adaptive basis scan by wavelet prediction for single-pixel imaging. IEEE Transactions on Computational Imaging 3 (1), 36–46. 3, 41, 53, 75, 76, 77, 82, 117, 127, 133

Rousset, F., Ducros, N., Farina, A., Valentini, G., D'Andrea, C., Peyrin, F., 2017b. Time-resolved wavelet-based acquisitions using a single-pixel camera. In : Proc. SPIE. Vol. 10070. pp. 1007016–1007016–7. 2, 3, 41, 95, 116, 118, 138

Rousset, F., Ducros, N., Peyrin, F., 2017c. Caméra mono-pixel. FR Patent 1751515 filed the 02/24/2017. 3, 75, 117, 132

Rousset, F., Peyrin, F., Ducros, N., 2017d. A semi nonnegative matrix factorization technique for pattern generalization in single-pixel imaging. IEEE Transactions on Computational Imaging, Submitted. 3, 75, 117, 132

Salvador-Balaguer, E., Clemente, P., Tajahuerce, E., Pla, F., Lancis, J., Apr 2016. Full-color stereoscopic imaging with a single-pixel photodetector. J. Display Technol. 12 (4), 417–422. 13, 15

Sankaranarayanan, A. C., Herman, M. A., Turaga, P., Kelly, K. F., Sept 2016. Enhanced compressive imaging using model-based acquisition : Smarter sampling by incorporating domain knowledge. IEEE Signal Processing Magazine 33 (5), 81–94. 16, 35, 36

Sankaranarayanan, A. C., Xu, L., Studer, C., Li, Y., Kelly, K. F., Baraniuk, R. G., 2015. Video compressive sensing for spatial multiplexing cameras using motion-flow models. SIAM Journal on Imaging Sciences 8 (3), 1489–1518. 16

Shapiro, J. H., Dec 2008. Computational ghost imaging. Phys. Rev. A 78, 061802. 13

Shapiro, J. M., Dec 1993. Embedded image coding using zerotrees of wavelet coefficients. Signal Processing, IEEE Transactions on 41 (12), 3445–3462. 32

Shin, J., Bosworth, B. T., Foster, M. A., Mar 2016. Single-pixel imaging using compressed sensing and wavelength-dependent scattering. Opt. Lett. 41 (5), 886–889. 1, 13, 116

Shin, J., Bosworth, B. T., Foster, M. A., Jan 2017. Compressive fluorescence imaging using a multicore fiber and spatially dependent scattering. Opt. Lett. 42 (1), 109–112. 13

Shrekenhamer, D., Watts, C. M., Padilla, W. J., May 2013. Terahertz single pixel imaging with an optically controlled dynamic spatial light modulator. Opt. Express 21 (10), 12507–12518. 14

Soldevila, F., Salvador-Balaguer, E., Clemente, P., Tajahuerce, E., Lancis, J., 09 2015. High-resolution adaptive imaging with a single photodiode. Scientific Reports (5). 34, 35, 36

Starling, D. J., Storer, I., Howland, G. A., Jul 2016. Compressive sensing spectroscopy with a single pixel camera. Appl. Opt. 55 (19), 5198–5202. 15

Stork, D. G., Gill, P. R., 2013. Lensless ultra-miniature cmos computational imagers and sensors. In : International Conference on Sensor Technologies and Applications. Citeseer, pp. 186–190. 17

Studer, V., Bobin, J., Chahid, M., Shams Mousavi, H., Candes, E., Dahan, M., 2012. Compressive fluorescence microscopy for biological and hyperspectral imaging. In : Proceedings of the National Academy of Sciences of the USA. Vol. 109 (26). pp. E1679–E1687. 2, 14, 25, 44, 125

Sun, B., Edgar, M. P., Bowman, R., Vittert, L. E., Welsh, S., Bowman, A., Padgett, M. J., 2013. 3d computational imaging with single-pixel detectors. Science 340 (6134), 844–847. 15

Sun, M.-J., Edgar, M. P., Gibson, G. M., Sun, B., Radwell, N., Lamb, R., Padgett, M. J., 2016a. Single-pixel three-dimensional imaging with time-based depth resolution. Nature Communications 7. 15

Sun, M.-J., Edgar, M. P., Phillips, D. B., Gibson, G. M., Padgett, M. J., May 2016b. Improving the signal-to-noise ratio of single-pixel imaging using digital microscanning. Opt. Express 24 (10), 10476–10485. 27

Tajahuerce, E., Durán, V., Clemente, P., Irles, E., Soldevila, F., Andrés, P., Lancis, J., Jul 2014. Image transmission through dynamic scattering media by single-pixel photodetection. Opt. Express 22 (14), 16945–16955. 2, 25, 95, 116

Takhar, D., Laska, J. N., Wakin, M. B., Duarte, M. F., Baron, D., Sarvotham, S., Kelly, K. F., Baraniuk, R. G., 2006. A new compressive imaging camera architecture using optical-domain compression. In : in Proc. of Computational Imaging IV at SPIE Electronic Imaging. pp. 43–52. 1, 7, 8, 12, 18, 22, 23, 24, 25, 26, 61, 116, 118, 119, 121, 129

Taubman, D. S., Marcellin, M. W., 2001. JPEG 2000 : Image Compression Fundamentals, Standards and Practice. Kluwer Academic Publishers, Norwell, MA, USA. 53, 54

Temizel, A., Vlachos, T., Feb 2005. Wavelet domain image resolution enhancement using cycle-spinning. Electronics Letters 41 (3), 119–121. 63

Torabzadeh, M., Park, I.-Y., Bartels, R. A., Durkin, A. J., Tromberg, B. J., 2017. Compressed single pixel imaging in the spatial frequency domain. Journal of Biomedical Optics 22 (3), 030501. 2, 35, 36, 95, 117

Wahl, M., 2014. Time-correlated single photon counting. Tech. rep., PicoQuant GmbH.
URL http://www.picoquant.com 43

Wang, D., Li, T., Zhu, S., Ding, C., 2008. Multi-document summarization via sentence-level semantic analysis and symmetric matrix factorization. In : Proceedings of the 31st Annual International ACM SIGIR Conference on Research and Development in Information Retrieval. SIGIR '08. ACM, New York, NY, USA, pp. 307–314. 76

Wang, Y. X., Zhang, Y. J., June 2013. Nonnegative matrix factorization : A comprehensive review. IEEE Transactions on Knowledge and Data Engineering 25 (6), 1336–1353. 76, 80

Watts, C. M., Shrekenhamer, D., Montoya, J., Lipworth, G., Hunt, J., Sleasman, T., Krishna, S., Smith, D. R., Padilla, W. J., 2014. Terahertz compressive imaging with metamaterial spatial light modulators. Nature Photonics 8 (8), 605–609. 9, 14

Welsh, S. S., Edgar, M. P., Bowman, R., Jonathan, P., Sun, B., Padgett, M. J., Oct 2013. Fast full-color computational imaging with single-pixel detectors. Opt. Express 21 (20), 23068–23074. 12, 13, 25

Welsh, S. S., Edgar, M. P., Bowman, R., Sun, B., Padgett, M. J., 2015. Near video-rate linear stokes imaging with single-pixel detectors. Journal of Optics 17 (2), 025705. 27

Xia, F., Mueller, T., Lin, Y.-m., Valdes-Garcia, A., Avouris, P., 2009. Ultrafast graphene photodetector. Nature nanotechnology 4 (12), 839–843. 18

Yu, W.-K., Li, M.-F., Yao, X.-R., Liu, X.-F., Wu, L.-A., Zhai, G.-J., Mar 2014a. Adaptive compressive ghost imaging based on wavelet trees and sparse representation. Opt. Express 22 (6), 7133–7144. 13, 34, 36, 69

Yu, W.-K., Liu, X.-F., Yao, X.-R., Wang, C., Zhai, Y., Zhai, G.-J., 2014b. Complementary compressive imaging for the telescopic system. Scientific reports 4, 5834. 14

Yu, W.-K., Yao, X.-R., Liu, X.-F., Li, L.-Z., Zhai, G.-J., Jan 2015. Three-dimensional single-pixel compressive reflectivity imaging based on complementary modulation. Appl. Opt. 54 (3), 363–367. 15

Zhang, Y., Edgar, M. P., Sun, B., Radwell, N., Gibson, G. M., Padgett, M. J., 2016. 3d single-pixel video. Journal of Optics 18 (3), 035203. 15, 16, 25

Zhang, Z., Ma, X., Zhong, J., 2015. Single-pixel imaging by means of fourier spectrum acquisition. Nature communications 6. 28, 76

Zhang, Z., Zhong, J., Jun 2016. Three-dimensional single-pixel imaging with far fewer measurements than effective image pixels. Opt. Lett. 41 (11), 2497–2500. 15, 28, 76

Zhao, M., Liu, J., Chen, S., Kang, C., Xu, W., 2015. Single-pixel imaging with deterministic complex-valued sensing matrices. Journal of the European Optical Society-Rapid publications 10. 34, 36